Single-Chain Origami – En Route to Artificial Proteins?

Zur Erlangung des akademischen Grades eines
DOKTORS DER NATURWISSENSCHAFTEN
(Dr. rer. nat.)

von der KIT-Fakultät für Chemie und Biowissenschaften
des Karlsruher Instituts für Technologie (KIT)

genehmigte
DISSERTATION
von

Johannes Willenbacher

aus
Kirchheimbolanden, Deutschland

KIT-Dekan:	Prof. Willem M. Klopper
Referent:	Prof. Christopher Barner-Kowollik
Koreferent:	Prof. Peter W. Roesky
Tag der Mündlichen Prüfung:	18.12.2015

Die vorliegende Arbeit wurde von Oktober 2012 bis Dezember 2015 unter Anleitung von Prof. Dr. Christopher Barner-Kowollik am Karlsruher Institut für Technologie (KIT) angefertigt.

Ein Blatt Papier wird erst zum Kranich wenn du's faltest.

Marten Laciny

Abstract

The rapidly evolving field of single-chain technology, with its ultimate goal to mimic the structure and function of naturally occuring proteins with synthetic polymers, lays the foundation for the current thesis. New platform technologies on the basis of metal complexation and the reversible host/guest complexation are introduced for the folding of single polymer chains akin to biomacromolecules. Based on the concept of metal complexation, catalytically active palladium(II)-loaded single-chain nanoparticles (SCNPs) are synthesized. Furthermore, advanced photochemical ligation protocols are applied for the facile preparation of functional SCNPs under mild reaction conditions. Especially the use of the nitrile imine-mediated tetrazole-ene cycloaddition (NITEC) presents a powerful way to produce functional, (pro)fluorescent SCNPs with a potential application as novel transporting agents. Due to their ability of a triggered payload release, stimulus responsive water-soluble SCNPs are investigated as well.

The current thesis is segmented into two parts, which group the individual projects in accordance to the synthetic approach that was applied. The synthetically more demanding, but therefore more sophisticated selective point folding approach is discussed initially in two projects. Both studies address the cyclization of synthetic polymer chains, which can be regarded as the simplest form of folding and is used to showcase the viability of the targeted mode of folding for the construction of more complex architectures in the future. In a first study, synthetic polymers on the basis of polystyrene are folded by means of metal-ligand complexation. The cyclic folded structures are analyzed by size exclusion chromatography (SEC), dynamic light scattering (DLS), and ^{1}H, as well as ^{31}P nuclear magnetic resonance (NMR) spectroscopy. To transfer the concept of selective point folding into aqueous environments, a water-soluble α, ω-functional polymer is designed in a second project, with the ability to undergo reversible folding driven by host/guest inclusion. Diffusion ordered spectroscopy (DOSY) is applied to identify the concentration

of the single-chain regime. The temperature responsive reversible selective point folding is investigated by DLS and Nuclear Overhauser Enhancement spectroscopy (NOESY) at ambient and elevated temperatures.

The second part of the thesis is devoted to the preparation of single-chain nanoparticles (SCNPs) following the repeating unit approach and starts with the formation of metal-ion containing single-chain nanoparticles (M-SCNPs). The successful synthesis is initially evidenced by SEC, DLS, ^{1}H, as well as ^{31}P NMR spectroscopy, and X-ray photoelectron spectroscopy (XPS). In addition, analysis of the transversal relaxation time by NMR, and log-normal distribution (LND) simulations of the SEC data, provide detailed information about the intramolecular crosslinking. The potential application of such M-SCNPs in homogeneous catalysis is presented in an exemplary Sonogashira coupling reaction. In the following, two projects that address mild and efficient photochemical intramolecular crosslinking methodologies are presented. For one, the photo-triggered NITEC reaction is applied for the synthesis of a set of inherently (pro)fluorescent SCNPs with the potential application as novel transporting agents. The SCNPs are characterized by SEC, DLS, atomic force microscopy (AFM), and additionally by ultraviolet/visible (UV/vis) and fluorescence spectroscopy. Remaining (surface) exposed tetrazole units of the SCNPs are utilized to demonstrate their ability of being able to be further functionalized. On the other hand, a photo-induced Diels–Alder reaction is employed to fabricate a range of mono-alkyne functional SCNPs. The successful synthesis of sub-20 nm sized SCNPs is evidenced by SEC, DLS, and AFM. The functionalization ability of these SCNPs is indicated by the exemplary synthesis of mono-poly(ethyleneglycol)-tethered tadpole-like SCNPs. Finally, preliminary results from the synthesis of pH-responsive water-soluble SCNPs are presented, for which a payload release in an acidic environment is envisioned.

In conclusion, the presented concepts for the controlled folding of single polymer chains, and for the straight forward synthesis of application oriented single-chain nanoparticles constitute a major step forward towards the long-term goal of artificial proteins.

Zusammenfassung der Doktorarbeit

Das sich schnell entwickelnde Feld der Polymereinzelkettentechnologie, mit dem langfristigen Ziel die Struktur und Funktion von natürlich auftretenden Proteinen mit synthetischen Polymeren nachzuahmen, stellt die Grundlage dieser Dissertation dar. Basierend auf der Chemie der Metallkomplexe und dem Prinzip der reversiblen Wirt/Gast Komplexierung werden neue Konzepte vorgestellt um einzelne Polymerketten, in gleicher Weise wie Biomakromoleküle, zu falten. Metallkomplexierung wird darüber hinaus verwendet um Palladium(II)-haltige, und damit katalytisch aktive Einzelkettennanopartikel (engl. single-chain nanoparticles, SCNPs) herzustellen. Des Weiteren werden moderne photochemische Reaktionen für die einfache Darstellung von funktionellen Einzelkettennanopartikeln herangezogen. Besonders die Anwendung der Nitrilimin-vermittelten Tetrazol-En Cycloaddition (engl. nitrile imine-mediated tetrazole-ene cycloaddition, NITEC) stellt eine leistungsstarke Methode dar, um funktionelle, fluoreszierende Einzelkettennanopartikel zu synthetisieren, die potentiell Anwendung als neuartige Transportmoleküle finden könnten. Aufgrund ihrer Eigenschaft auf einen Auslöseimpuls hin ein kleines Molekül freizusetzen, werden weiterhin Stimulus responsive Einzelkettennanopartikel untersucht.

Die vorliegende Arbeit ist in zwei Themenkomplexe geteil, die die individuellen Projekte nach der zugrundeliegenden synthetischen Strategie gruppieren. Zuerst wird der synthetisch anspruchsvollere, aber auch elegantere Weg der selektiven Punktfaltung anhand von zwei Projekten diskutiert. Beide Studien befassen sich mit der Zyklisierung von synthetischen Polymeren, welches als die einfachste Form von Faltung angesehen werden kann. Anhand dieses einfachen Models soll vorerst die Funktionsfähigkeit des angestrebten Faltungsmechanismus demonstriert werden, um in Zukunft komplexere Strukturen realisieren zu können. In einem ersten Projekt werden synthetische Polymere auf Styrolbasis durch Metallkomplexbildung gefaltet. Die zyklisch gefalteten Strukturen werden mit Hilfe der Größenausschlusschromatographie (engl. size exclusion chromatography, SEC),

dynamischer Lichtstreuung (engl. dynamic light scattering, DLS) und sowohl [1]H- als auch ^{31}P-Kernspinresonanzspektroskopie (engl. nuclear magnetic resonance, NMR) analysiert. Um das Konzept der selektiven Punktfaltung in wässrige Lösung zu übertragen, wird im zweiten Projekt ein wasserlösliches α,ω-funktionalisiertes Polymer entwickelt. Die Polymerenden sind aufgrund der Ausbildung eines Wirt/Gast Einschlusskomplexes in der Lage eine reversible Faltung der Kette durchzuführen. Mittels DOSY (engl. diffusion ordered spectroscopy) Messungen wird daraufhin die Konzentration bestimmt, bei der das Einzelkettenregime erreicht ist. Die temperaturabhängige Faltung und Entfaltung wird anschließend durch DLS und NOESY (engl. Nuclear Overhauser Enhancement Spectroscopy) bei Umgebungstemperatur und erhöhten Temperaturen untersucht.

Der zweite Teil der Arbeit befasst sich mit der Synthese von Einzelkettennanopartikeln basierend auf dem Prinzip der Wiederholeinheiten-Methode und beginnt mit der Darstellung von metallionhaltigen SCNPs. Die erfolgreiche Synthese wird vorerst durch SEC, DLS, ^{1}H- als auch ^{31}P-NMR Spektroskopie und Röntgenphotoelektronenspektroskopie (engl. X-ray photoelectron spectroscopy, XPS) nachgewiesen. Zusätzlich liefern die Analyse der transversalen Relaxationszeit durch NMR, sowie die Simulation der SEC Kurven durch Log-Normalverteilungen (engl. log-normal distribution, LND) detaillierte Informationen über die intramolekulare Vernetzung. Die potentielle Anwendung solcher metallionhaltingen SCNPs in der homogenen Katalyse wird beispielhaft an einer Sonogashira-Kupplung demonstriert. Darauffolgend werden zwei Projekte vorgestellt die sich mit der milden und effizienten photochemischen Synthese von funktionellen Einzelkettennanopartikeln befassen. Zum einen findet die NITEC Reaktion Anwendung für die Darstellung von einer Reihe von inhärent (pro)fluoreszierenden SCNPs, die sich potentiell als neuartige Transportmoleküle eignen. Die SCNPs werden durch SEC, DLS, Rasterkraftmikroskopie (engl. atomic force microscopy, AFM), und zusätzlich durch UV/vis- und Fluoreszenzspektroskopie Messungen charakterisiert. Nach dem Vernetzen überschüssige Tetrazol-Einheiten der SCNPs werden genutzt, um deren Funktionalisierbarkeit zu zeigen. Zum anderen wird eine lichtinduzierte Diels–Alder Reaktion ausgenutzt, um eine Reihe von mono-Alkin-funktionalisierten SCNPs darzustellen. Die erfolgreiche Synthese der sub-20 nm SCNPs wird durch SEC, DLS und AFM bestätigt. Im Falle dieser SCNPs wird die Funktionalisierbarkeit durch die exemplarische Synthese von mono-poly(ethyleneglycol)-funktionalisierten kaulquappenförmigen SCNPs gezeigt. Abschließend werden erste

Ergebnisse der Synthese von pH-responsiven, wasserlöslichen SCNPs gezeigt, für die eine Wirkstoff-Freisetzung im sauren Milieu angestrebt wird.

Alle hier vorgestellten Konzepte zum Falten von einzelnen Polymerketten und für die effiziente Synthese von anwendungsorientierten Einzelkettennanopartikeln stellen einen großen Schritt in Richtung des langfristigen Ziels dar, künstliche Proteine zu erzeugen.

Contents

1 | Introduction

Since the dawn of mankind humans try to mimic what they observe in their surroundings. A very prominent and early example for biomimetics are the designs of Leonardo da Vinci's flying machines, which were derived from studies of birds.

Pursuing Nature as an inspiring example has lead to a large output of practical materials, *e.g.*, the *lotus effect* for self-cleaning surfaces, the *adhesive mechanism of gecko feet* for dry adhesive tape, the *antireflective properties of eyes and wings of insects* for solar panels, the *tooth like scales of shark skin* for lowering the hydrodynamic drag of ships and for the use in pipelines and *spidersilk* for generating fibers tougher than Kevlar.[1,2]

One aspect which is of particular interest to modern polymer chemists is the ability of organisms to synthesize macromolecules with a precisely controlled sequence of monomer units and specific three dimensional shape as found in proteins or DNA. Proteins are monodisperse biomacromolecules and are crucial for living organisms. The delicate, dynamic three dimensional structure of proteins - to a large extend - determines their function.[3] This structure is stabilized by non-covalent (hydrogen bonding, ionic interaction, van-der-Waals forces, hydrophobic stacking), or (dynamic-)covalent (disulfide bridges) interactions between functional groups that are precisely located along the biopolymer chain.[4,5] The three dimensional structure of a protein is the product of a folding process, aided by a living cell's enzymatic machinery. The final structure can be devided into three to four substructures, which are illustrated in Scheme 1.1.

Proteins are known to be the main actors in cells, with roles defined by the information encoded in genes.[7] The best-known role of proteins in the cell is as enzymes, which catalyze chemical reactions. Their application as very efficient and specific catalysts makes enzymes extremely interesting for the utilization in industrial applications. Owing to the elaborate and costly downstream process of enzyme purification, enzyme-catalyzed reactions are typically conducted as biotransformations using wild-type whole cells, recombinant whole
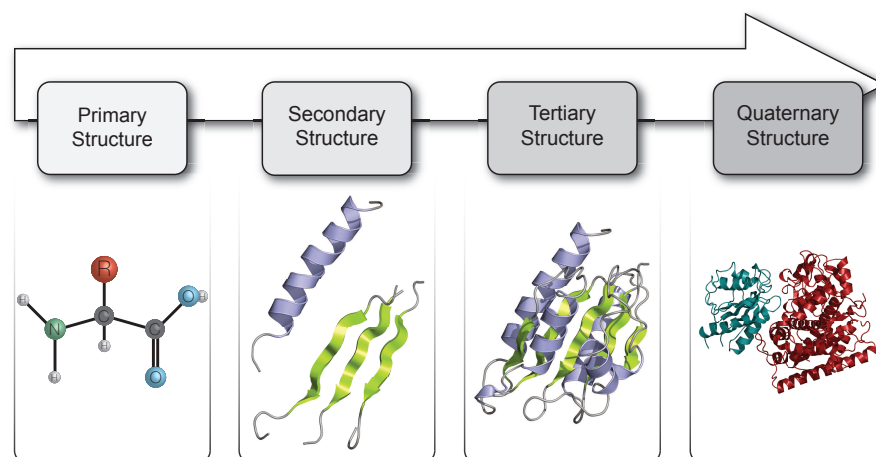
Scheme 1.1 The structure of a protein is divided into three to four levels. The primary structure is the unique sequence in which the amino acids appear in the protein backbone. This sequence defines the final structure and function of the protein. The main secondary structural elements are the α-helix and β-sheet, which resemble local sub-structures along the peptide chain. The folding of these substructures into a compact entity leads to the tertiary structure. Many functional proteins are constituted of several peptide chains. Their spatial arrangement is called the quarternary structure. The shown structures are taken from the complex of the heme and FMN-binding domains of the cytochrome P450 (BM-3). RCSB: 1BVY.[6]

cells or cell free crude extract.[8] Applying wild-type whole cells has the disadvantage of low protein expression, which is accompanied by a significant increase of side reactions. Very significant advances in molecular biology eliminate this drawback by allowing the overexpression of enzymes in recombinant whole cells.[9] One of the milestones in industrial microbial biotransformations is the synthesis of acrylamide from acrylonitrile using a nitrile hydratase in the wild-type whole cells of *Rhodococcus* sp.[10] It is estimated that this process produces 400 000 t of acrylamide per year (stand 2012).[8]

Nevertheless, the major drawback of natural enzymes is their fragile nature and thus, the choice of solvent, pH- and temperature range is limited (typically to physiological conditions). These drawbacks and also the cost-intensive protein purification can eventually be overcome by artificial proteins, which are envisioned in current research.

The sequence controlled synthesis of enzymes on the laboratory scale is mostly realized by Merrifield's solid phase peptide synthesis (SPPS), which is limited to relatively short peptide chains and suffers low yields. Instead of sticking to the proteinogenic α-amino acids found in natural proteins, research addressing protein mimics has also considered β-amino acids,[11] vinylogous amino acids,[12] aminosulfonic acids,[13] and *N*-substituted glycines, known as peptoids in their polymeric form,[14] for the synthesis of protein-like

structures with alternative backbones. First sequence controlled synthetic polymers have also been reported, but are accompanied by similar drawbacks as the SPPS.[15–24]

An alternative take on artificial protein mimics is followed in the field of single-chain technology. By using synthetic macromolecules, the field is fundamentally different to the existing strategies listed above. Since sequence controlled synthetic polymers, at least for now, seem out of reach in the near future, the idea behind current approaches is to directly impart a certain tertiary structure to synthetic polymer chains by either placing a few mutually orthogonal recognition units along the polymer backbone (selective point folding) or by collapsing single polymer chains into so-called single-chain nanoparticles (repeating unit approach). The concept, especially the selective point folding approach, is supported by recent all atom simulations that suggest a unique conformation of the chain segments in between a pair of recognition units for a certain chain length.[25] The single-chain technology approaches have the potential of delivering comparably high yields in relatively simple processes, which may make the envisioned protein mimics applicable as nanoreactors or in nano-medicine, catalysis, or sensors.

The current thesis aims at providing novel platform technologies for the precise folding of synthetic polymers as well as facile routes for the synthesis of application oriented single-chain nanoparticles. The most adequate and advanced characterization methods are matched to the chosen chemistry. Potential applications, *e.g.*, in catalysis or nano-medicine, will be discussed or exemplary demonstrated. Scheme 1.2 outlines the addressed projects, divided into two synthetic approaches: the selective point folding approach and the repeating unit approach. The selective point folding is for the first time attempted by metal complexation. The same concept is translated to the intramolecular crosslinking of linear polymer chains to form catalytically active single-chain nanoparticles (SCNPs). In addtition, two photochemical reactions are adapted to fabricate SCNPs with novel properties. Finally, new strategies for single-chain architectures in water are developed for each approach, an imperative step on the route to artificial proteins.
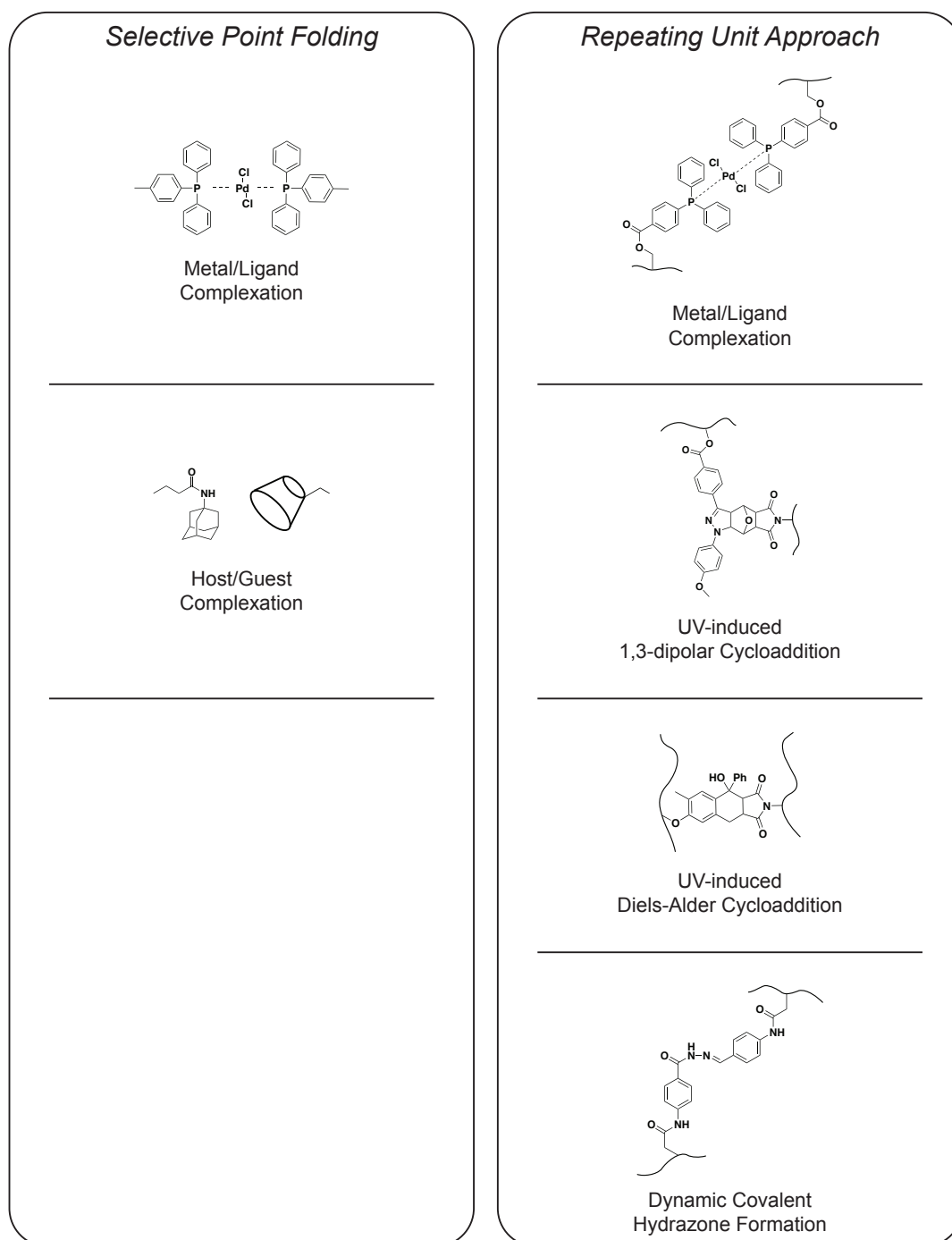
Scheme 1.2 Overview of the different (cross)linking strategies that are addressed within the projects of the current thesis, divided according to the chosen synthetic strategy for the preparation of the single-chain architectures.

2 | Single-Chain Technology: A Literature Overview

Interestingly, the first example of single-chain nanoparticles has been reported in 1955,[26] but the field, with a few exceptions, lay dormant afterwards. Only with the advent of novel polymerization techniques (*e.g.*, atom transfer radical polymerization (ARTP), reversible addition-fragmentation chain transfer (RAFT) polymerization, nitroxide mediated polymerization (NMP)),[27–31] and the ready availability of the important characterization techniques around the turn of the last century, the research area picked up pace again.

Consequently, the field has since produced an enormous output in the form of scientific articles, which have been collated in several extensive review articles in the past years.[32–38] Thus, the current chapter can merely cover the most important aspects that are essential to follow the scientific discussions in the subsequent chapters. The first section will introduce the different approaches for the construction of single-chain architectures. In the following sections it will be discussed how the new polymerization techniques in combination with chemical ligation tools can be utilized to prepare single-chain architectures. The final section will then present the most important analytical techniques which are required to verify the successful synthesis.

2.1 Selective Point Folding *vs.* Repeating Unit Approach

In general, two main approaches are conceivable for giving a tertiary structure to single polymer chains. The synthetic strategies can be divided into the selective point folding approach and the repeating unit approach, which are fundamentally different (see Scheme 2.1). In the selective point folding approach orthogonal recognition unit pairs are placed at distinct positions along the polymeric backbone, which leads to a

controlled folding of the chain segments in between. In the repeating unit approach on the other hand, the reactive groups are either introduced into the parent polymer during a copolymerization of one or more functional monomers, or they are grafted to the backbone in a postpolymerization modification. In case of the repeating unit approach however, the placement, as well as the intramolecular crosslinking, are non-directed and lead to random connections between the chain segments in the so-called single-chain nanoparticles (SCNPs). Both approaches bear their own advantages and drawbacks. The major gain of the selective point folding is the precise positioning of the recognition units and thus a better understanding of the folding process when compared with the random intra-chain collapse. Unfortunately, this advantage is the result of a demanding synthesis process, especially when it comes to installing more than one or two pairs of recognition units. In contrast, the repeating unit approach is characterized by considerably less synthetic effort. Therefore, it is not surprising that the majority of studies is centered around the repeating unit approach. Hence, the selective point folding approach will be introduced in the current section, while the repeating unit approach will be presented separately.

Schmidt *et al.* demonstrated the selective point folding of synthetic polymer chains into various geometries, including tadpole (P-shaped), pseudocyclic (Q-shaped), bicyclic (8-shaped), and knotted (α-shaped) architectures.[39] By introducing alkyne-functional maleimides to a running styrene polymerization at defined points in time, they were able to position alkyne moieties at varying places along the polymer chain. After an endgroup transformation of these ATRP-based polymers, they applied the highly effective copper(I)-catalyzed azide-alkyne cycloaddition (CuAAC) reaction to produce the aforementioned architectures.

In another work of the group of Lutz, the same approach was chosen for the introduction of functional groups to produce complex single-chain polymer topologies locked by positionable twin disulfide cyclic bridges.[40] This time, active-ester-functional maleimides were added to a running nitroxide mediated polymerization (NMP) at defined points in time. The chosen reactive groups to fold the polymer chain were short tripeptide cysteine–arginine–cysteine (CRC) sequences. The trityl-protected thiols had to be deprotected by trifluoroacetic acid (TFA) prior to the folding reaction, which was performed by simply oxidizing the thiol groups of the CRC sequence to form cyclic disulfide bridges between the two CRC moieties. In contrast to the first attempt of folding single polymer
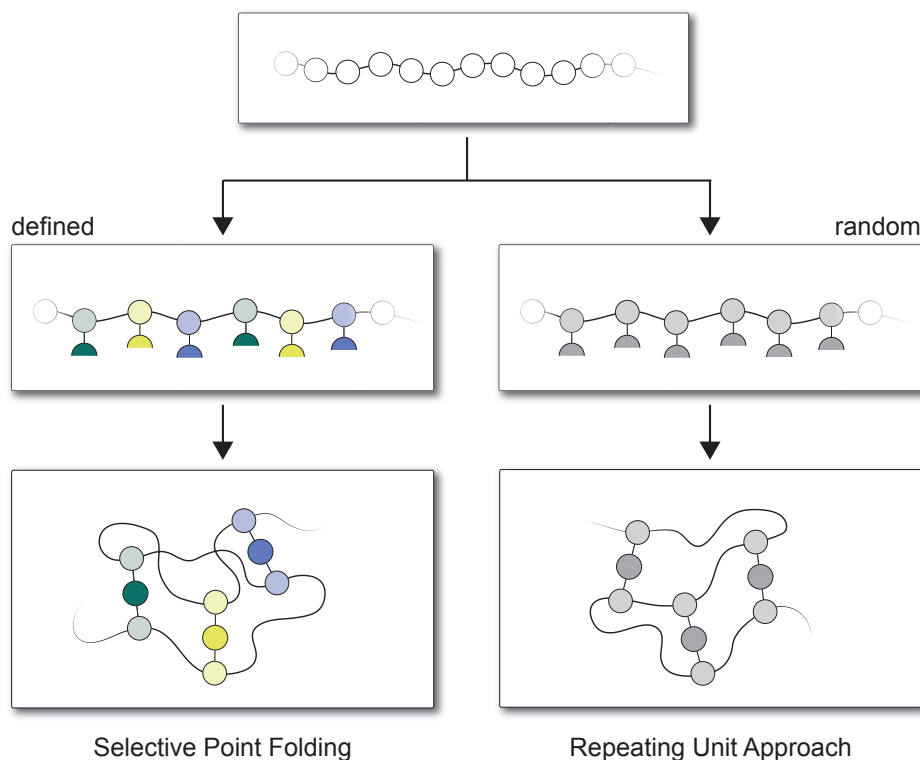
Scheme 2.1 Illustration of two fundamentally different synthetic strategies for the construction of single-chain architectures. The defined placement of mutually orthogonal recognition units leads to a controlled folding of the polymer chain, whereas the random placement of recognition units leads to a statistical intramolecular crosslinking of the polymer chain, which thereby collapses into a single-chain nanoparticle (SCNP).

chains by Lutz and coworkers, the CRC-folded rings have the potential to be reversibly unfolded by reducing the disulfide bridges. Such dynamic-covalent bonds are important characteristics that are needed for synthetic proteins.

An alternative dynamic system that is typical for proteins and should be adapted is based on hydrogen bonds. In a series of publications by the Barner-Kowollik group, the selective point folding of single polymer chains based on hydrogen bonds has been evaluated. The earliest examples studied α,ω-functionalized styrene chains that carry the respective recognition units at their chain ends. The hydrogen bonding pairs that were chosen to drive the folding process were the Hamilton-wedge/cyanuric acid pair, and the thymine/diaminopyridine pair.[41,42] In each case, the folding could be disrupted by the addition of a competing hydrogen bond donor/acceptor (*e.g.*, methanol). An interesting aspect of these recognition unit pairs is caused by the arrangement of the hydrogen bond donor and acceptor atoms. Due to the positioning of the donors (D) and acceptors (A),
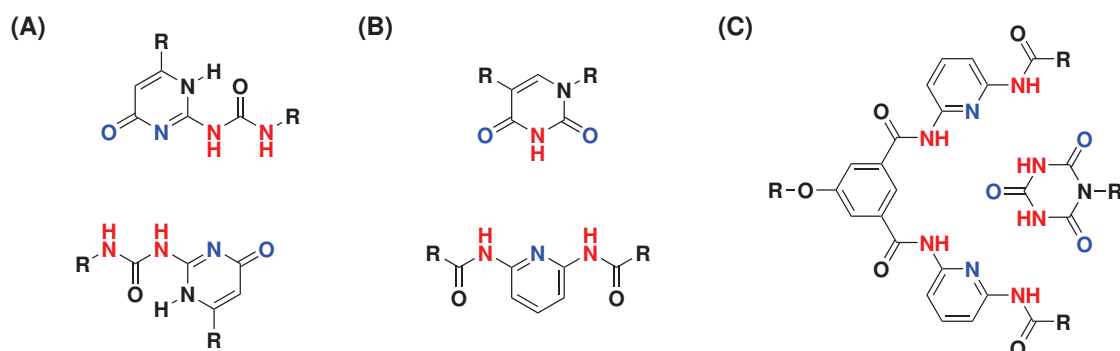
Scheme 2.2 Various hydrogen bonding motifs that are applied for supramolecular interactions. (A) The A-A-D-D arrangement in the ureidopyrimidinone (upy) motif leads to dimerization. (B) The A-D-A/D-A-D arrangement in the thymine/diaminopyridine system leads to only cross-interaction. (C) The same is true for the D-A-D-D-A-D/A-D-A-A-D-A geometry in the Hamilton-wedge/cyanuric acid motif.

the seperate elements of the recognition unit pairs are not able to dimerize, as it is the case for another widely used hydrogen bonding motif, the ureidopyrimidinone (upy) dimer (see Scheme 2.2).

A ^{1}H NMR study revealed that the three-point interaction of the thymine/diaminopyridine and the six-point interaction of the Hamilton-wedge/cyanuric acid motif are orthogonal to each other.[43] These findings resulted in the follow-up study of the dual selective point folding of single styrene-based polymer chains.[44] The recognition units, which led to a two-point folding in diluted solution, were positioned along the polymer backbone in the order: cyanuric acid, thymine, diaminopyridine, and Hamilton-wedge. The same concept was also employed in another study of the dual selective point folding of a single polymer chain, this time of a block copolymer of styrene and *n*-butyl acrylate.[45] Therein, the recognition units were positioned along the block copolymer backbone in the order: cyanuric acid, Hamilton-wedge, thymine, and diaminopyridine. This led to a slightly different geometry of the dual folded system.

There exists a plethora of examples for cyclic polymers known in literature which have been thoroughly reviewed.[46–48] However, the main concern in these investigations is the cyclic architecture itself, whereas in the light of the current thesis, the cyclic architecture is just seen as the simplest form of folding and is therefore only applied as a model system to demonstrate the targeted folding mechanisms. Since the interactions that fold a protein are of dynamic and supramolecular nature, there is still room for the development of new ways to conduct the selective point folding of synthetic polymers.

Although commonly applied in the construction of supramolecular polymers,[49–56] the concept of metal complexation for example has not yet been translated to the realm of selective point folding. Since a large number of proteins/enzymes carry metal ion cofactors (*e.g.*, hemoglobin, cytochrome P450, and nitrogenase),[57,58] it is a logical step to explore whether metal-based selective point folding systems can be synthetically realized. Compared to alternative reversible non-covalent interactions characteristic for supramolecular chemistry, metal-ligand coordination has proven to be one of the most prominent supramolecular motifs, due to its ease of accessibility and strong binding constants.[50,59] Therefore, the selective point folding of synthetic polymers driven by metal complexation is investigated in the current thesis (see Section 3.1).

A further aspect to consider when aiming at emulating the structures or even the functions of natural macromolecules in the future is the environment in which these systems work: water. Thus, it is mandatory to move synthetic single-chain architectures into aqueous systems. The prominent motif of cyclodextrin (CD) host-guest chemistry has been applied in the fabrication of a plethora of supramolecular structures (*e.g.*, block copolymers, star polymers, brush polymers), as well as branched polymers, and gels.[60] However, there are only two examples of CD host-guest complexation driven selective point folding in the literature, yet they are limited to a poly(ethylene glycol) platform.[61,62] Similarly, the cucurbit[8]uril (CB[8]) host was employed in the fabrication of supramolecular cyclic polymers. CB[8] is able to host for example two anthracene units. Therefore, a dianthracene functional poly(ethylene glycol) precursor was synthesized, which underwent cyclization in diluted solution when CB[8] is present.[63] The supramolecular assembly can be locked into place by linking the two anthracene moieties in a photo-induced dimerization reaction. As a consequence of the limitations of the PEG platform, a more versatile approach for the selective-point folding based on supramolecular host/guest chemistry in water is investigated in Section 3.2.

2.2 Crosslinking Strategies in the Single-Chain Realm: A Synthetic Point of View

There is a vast variety of reactions to choose from when it comes to realizing the crosslinks in single-chain nanoparticles. Three general strategies have emerged for collapsing single

polymer chains into SCNPs: (I) In the homofunctional coupling two functionalities of the same kind form the crosslink. (II) In the heterofunctional coupling two complementary groups react to form the crosslink (*e.g.*, in the copper(I)-catalyzed azide-alkyne cycloaddition). (III) A bifunctional crosslinker is added to induce the chain collapse by crosslinking two other functionalities along the backbone of the parent polymer.

The following subsections will give a short overview of various crosslinking strategies that have been employed in recent literature and it will highlight the strategies that have been chosen in the research projects of the current thesis. The subsections are ordered according to increasing complexity of the crosslinking bond. Starting with covalent bonds the complexity is increased with dynamic-covalent bonds, which represent the transition to the most complex form, the supramolecular bonds.

2.2.1 Covalent Chemistry

The vast majority of reported single-chain nanoparticles is based on covalent crosslinking.[32] Many of the earlier examples applied harsh reaction conditions (*e.g.*, high temperatures) to facilitate the intramolecular crosslinking.[64,65] One of the strategies to overcome this issue is the application of photochemical reactions. Such reactions are of particular interest not only because of their exceptional spatial and temporal resolution, but also because of their efficiency.

The [2+2] photo-dimerization of cinnamoyl groups has been applied multiple times for the preparation of tadpole structured single-chain nanoparticles.[66–68] An interesting strategy for achieving such structures was recently published by Chen and coworkers.[69] They sparsely grafted poly(ethylene oxide)-*block*-poly(2-cinnamoylethyl methacrylate) chains to the surface of silica spheres. Upon UV-irradiation, the cinnamoyl-functional block collapses to form tadpole structured SCNPs on the silica sphere surface. Due to the chosen strategy of grafting the blockcopolymers to the surface, it is was possible to obtain mono-functional tadpole-SCNPs after HF-etching of the silica spheres. In a subsequent ligation reaction, the tadpole-SCNPs were reacted with poly(2-(dimethylamino)ethyl methacrylate)-N_3 (PDMAEMA-N_3), which was prepared by the RAFT process. Finally, to showcase the full potential of the system, the RAFT groups were aminolyzed, which resulted in the dimerization of the functional SCNPs.

Another unusual architecture utilizing the cinnamoyl photo-crosslinking was presented by Hecht and Khan,[70] who prepared organic nanotubes by intramolecularly crosslinking a helical polymer.

Returning to the synthesis of single-chain nanoparticles, an alternative photochemical approach, namely the photo-dimerization of pendant anthracene units, was introduced by Berda and coworkers.[71] The group recently applied their photo-dimerization strategy for the synthesis of SCNPs that carry a single $[(\mu\text{-}S_2C_2H_4NR)Fe_2(CO)_6]$ complex and thus mimic the structure of the [FeFe]-hydrogenase enzyme.[72]

Since two of the research projects of the current thesis are also based on photochemical intramolecular ligations, the underlying photochemical reactions shall shortly be discussed in the following paragraphs.

Nitrile Imine-Mediated Tetrazole-Ene Cycloaddition (NITEC)

Huisgen *et al.* discovered the reaction of tetrazoles in 1,3-dipolar cycloadditions.[73,74] Later on, Huisgen and others were able to verify the nitrile imine as the reactive intermediate of these reactions, which led to the term NITEC, short for nitrile imine-mediated tetrazole-ene cycloaddition.[75–79] The general reaction scheme of a light-induced NITEC reaction is presented in Scheme 2.3.
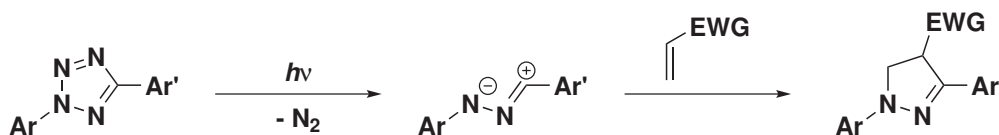
Scheme 2.3 General reaction of the nitrile imine-mediated tetrazole-ene cycloaddition (NITEC). When a diaryl substituted tetrazole molecule is irradiated with light of a certain wavelength, nitrogen is expelled and a very reactive 1,3-dipole, a nitrile imine, is formed. Reactions with suitable double bonds lead to fluorescent pyrazoline derivatives.

Lin and coworkers pioneered the application of the photo-induced NITEC process in the field of biochemistry. Besides the synthesis of diversely functionalized tetrazoles, they mainly focused on the bio-orthogonal functionalization of proteins.[80–85] Picking up this concept, Arndt *et al.* synthesized a tetrazole functional DNA building block, which allows for postsynthetic labeling, *e.g.*, with a maleimide-modified sulfo-Cy3 dye.[86]

Research investigating the tetrazole chemistry in the group of Barner-Kowollik is concerned with the spatially resolved functionalization of various substrates,[87–90] but also

with traditional aspects of polymer chemistry, such as the formation of blockcopolymers,[91] network formation,[92] or the step growth polymerization of tetrazole-ene functional A-B-monomers.[93]

An aspect that makes the NITEC reaction especially interesting is the fact that the profluorescent tetrazole reacts to a fluorescent pyrazoline derivative. The fluorescent reaction product brings many inherent advantages. For one, the reaction process, *i.e.*, the kinetics, can be monitored by fluorescence spectroscopy. Furthermore, the broad fluorescence band in the visible spectral range might be utilized to follow transport processes in cells. In one project of the current thesis, the NITEC reaction is employed to synthesize inherently fluorescent single-chain nanoparticles. An example for fluorescent SCNPs was indeed already presented by Oria *et al.* in 2010.[94] However, the fluorescence properties had to be imparted by employing a suitable crosslinker, and the fluorescence (391 and 410 nm), which has to be excited at $\lambda_{exc} = 390\,\text{nm}$, is not suitable for biological applications as it is the case for the fluorescence of the pyrazoline derivative.

Photoenol Chemistry

The basic principle of the photoenol chemistry as depicted in Scheme 2.4 was first mentioned in 1971.[95] The technique is based on *ortho*-methyl benzaldehyde or *ortho*-methyl benzophenone derivatives that form *ortho*-quino dimethanes, *i.e.*, photoenols, when irradiated with UV-light. Suitable reaction partners for these highly reactive dienes are electron deficient alkenes, *e.g.*, maleimides or acrylates. The Diels–Alder cycloaddition of these photoenols is an irreversible process. If, however, no dienophile is present, the photoenol can return to its ground state without forming any by-products.
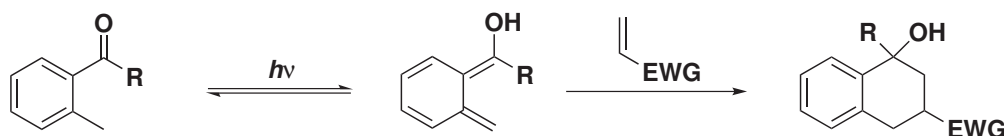
Scheme 2.4   General reaction of a photoenol. An *ortho*-methyl benzaldehyde or *ortho*-methyl benzophenone derivative forms an *ortho*-quino dimethane - a so-called photoenol - upon irradiation. In the presence of a suitable double bond, a rapid Diels–Alder reaction ensues.

Surprisingly, it took more than 40 years until the photo-induced DA cycloaddition was adapted to polymer science by the group of Barner-Kowollik. Similar to the studies employing the NITEC reaction, the photoenol chemistry was also utilized to functionalize

various substrates in a spatially resolved manner.[96–101] Again, the photoenol chemistry is also a powerful ligation tool for the synthesis of for instance cyclic polymers,[102–104] or blockcopolymers.[105–107] In addition to the widely applied strategy for block formation, where both blocks need to be functionalized with the complementary reactive counterparts, the photoenol process opened the door for a much more elegant approach. The photoenol that is generated upon irradiation is sufficiently reactive to even react with the unactivated C-S double bond of the RAFT-agent 2-cyanopropyl dithiobenzoate (CPDB) in a hetero-Diels–Alder (HDA) reaction.[108] Since CPDB is commercially available and applicable for the controlled polymerization of a large number of monomers, the photoenol-RAFT-HDA concept is well suited for the facile preparation of blockcopolymers, but also for the endgroup modification of RAFT-polymers.

2.2.2 Dynamic-Covalent Chemistry

Dynamic covalent bonds display all the characteristics of a regular covalent bond, yet are able to break and reform as a response to an external stimulus, for example a change in pH or an oxidation/reduction.[109,110] The dynamic nature of the crosslinking bond additionally allows the loading and releasing of components. Such SCNPs have the potential of being utilized for the controlled drug release in the future.

Disulfide bonds are ubiquitous in the structure of proteins, and it is therefore not surprising that disulfide bridges have been used as crosslinks for single-chain nanoparticles. The disulfide bond is responsive towards oxidation and reduction processes. Oxidation leads to bond formation, whereas reduction (*e.g.*, with dithiothreitol, DTT) leads to bond scission. Early examples showed the formation of disulfide crosslinked SCNPs and their reversion to the parent polymers in organic solvents.[111,112] Lately, Thayumanavan and coworkers realized disulfide based SCNPs in aqueous environment.[113] In their work they also presented the encapsulation of hydrophobic probes inside the SCNP. Upon the addition of DTT, a controlled release of the encapsulated molecules was achieved.

A more unusual form of dynamic covalent chemistry is the photo-dimerization of coumarin. He *et al.* presented the formation of SCNPs by irradiating a parent copolymer, composed of *N,N*-dimethylaminoethyl methacrylate (DMAEMA) and CMA (short for 4-methyl-[7-(methacryloyl)oxy-ethyl-oxy]coumarin), with UV-light of $\lambda > 310$ nm in dilute

solution.[114] Irradiation at $\lambda < 260$ nm led to a partial reversion of the dimerization, with the degree of crosslinking decreasing from 75 % to 38 %. Building upon this work, the same group designed a biodegradable and biocompatible polyester that carries coumarin moieties in the main chain.[115] When irradiated with UV-light of $\lambda = 254$ nm, the SCNPs were photo-degraded into smaller fragments by cleavage of the coumarin-4-yl methyl esters.

Pomposo and coworkers made use of the enamine chemistry to fabricate pH-responsive single-chain nanoparticles.[116,117] Another example for pH-responsive dynamic covalent chemistry (DCC) is the formation of hydrazones. As one of the projects of the current thesis also employs hydrazone crosslinking, this form of DCC will be discussed in more detail in the following paragraph.

Hydrazone Formation

Hydrazones are formed in condensation reactions of a ketone or an aldehyde with a hydrazine compound. The hydrazone exchange proceeds at acidic pH at ambient temperature and can be turned off by adjusting the pH to neutral/basic conditions, where kinetically stable products are present.[109] Mostly acylhydrazones are used, since without the acyl or another similar electron withdrawing group, the hydrazone is mostly too stable to undergo exchange reactions.[110] Lehn and coworkers have applied hydrazone formation for the preparation of dynamic covalent polymers and foldamers.[118–120]

In the field of single-chain nanoparticles, hydrazone formation has only been applied by Fulton and coworkers. In an initial project, they synthesized single-chain nanoparticles with hydrazone crosslinks in organic solvents.[121] The parent polymers, which carried benzaldehyde units along the backbone, were crosslinked with a bifunctional hydrazine crosslinker in diluted solution to form the SCNPs. In addition, the loading of these SCNPs with a range of low molecular weight organic hydrazines and alkoxyamines was demonstrated by utilizing residual aldehyde moieties along the polymer backbone. The group of Fulton extended their strategy to aqueous systems by simply exchanging the monomer type of the parent polymer from styrene to oligo(ethylene glycol) methacrylate (OEGMA).[122] The SCNP formation was again realized by crosslinking the parent polymers in a dilute solution with a suitable bifunctional hydrazine crosslinker. Due to the thermoresposive

nature of the employed polymers, it was possible to form a macroscopic hydrogel by heating a solution containing the SCNPs over their lower critical solution temperature (LCST). When cooled back to ambient temperature, the hydrogel transformed back into the sol state, and very slowly into the SCNP state (3 to 60 days).

2.2.3 Supramolecular Chemistry

As already alluded to in the introduction, supramolecular bonds (such as hydrogen bonds, ionic interactions, van-der-Waals forces, hydrophobic stacking) play a major role in nature.

Hydrogen bonds are a widely utilized motif for directed self-assembly.[123] In the realm of single-chain nanoparticles, the dimerization of ureidopyrimidinone (upy) constitutes an often applied crosslinking strategy.[124–127] Similarly, the dimerization of 2-ureido-5-deazapteridines was also recently reported as a crosslinking motif for the formation of pH-responsive SCNPs.[128]

The groups of Palmans and Meijer have made the chiral benzene-1,3,5-tricarboxamide (BTA) moiety their recognition unit of choice. BTA self-assembles into helical stacks stabilized by threefold intermolecular hydrogen bonding.[129] SCNPs based on the interaction of pendant BTA units have been intensively investigated by both groups.[130–133]

Exploiting their strategy, the groups were able to collapse a parent polymer around a catalyst in various examples, thus mimicking an enzyme on a basic level. In an initial project, an A-B-A type blockcopolymer was synthesized as the linear precursor for the SCNP. The A blocks contained only chiral BTA-bearing methacrylate (BTAMA) and poly(ethylene glycol) methyl ether methacrylate (PEGMA), while the B block, besides BTAMA and PEGMA, also comprised a ruthenium complex of diphenylphosphinostyrene (SDP).[134] When a diluted aqueous solution of this parent polymer is prepared, the BTA units form a helical, hydrophobic core around the Ru-based catalyst. The prepared SCNPs showed catalytic activity in the reduction of cyclohexanone to cyclohexanol, or the reduction of acetophenone. In a similar work, A-B-A blockcopolymers that carry BTAMA and PEGMA in the A blocks and BTAMA, PEGMA, and SDP in the B block were synthesized by RAFT polymerization. In addition, A-B-A blockcopolymers in which the BTA units were replaced by hydrophobic lauryl residues of a lauryl methacrylate (LMA) comonomer were synthesized.[135] In these cases, the Ru-catalyst loading was performed

in a second step. Catalytic experiments of the transfer hydrogenation of cyclohexanone derivatives showed that the BTA self-assembly is not required for the stabilization of the hydrophobic pocket when SDP-Ru complexes are present.

Moving away from transition metal-based catalysts, the groups prepared water-soluble methacrylate random copolymers containing oligo(ethylene glycol) (OEG) units, L-proline as catalytic units, and chiral (*S*)-BTAs as structuring elements.[136] The catalytic activity of the resulting SCNPs was assessed in a model aldol reaction between *p*-nitrobenzaldehyde and cyclohexanone. As a control experiment, they also employed copolymers where n-dodecyl chains were inserted as a BTA surrogate for the catalysis. Their findings showed that the BTA as a structuring unit is indeed necessary for successful catalysis. Building upon their works, the groups next designed random copolymers composed of oligo(ethylene glycol) methacrylate (OEGMA) and BTAMA, which are able to collapse into well defined SCNPs in diluted aqueous solution.[137] Functionality was incorporated into these SCNPs following a modular approach. Therefore, functional groups (a fluorescent 1,8-naphthalimide derivative in BTA-dye, and an organocatalyst in (*S*)-BTA-L-Pro) were added to "free" BTA units. When these functional BTA units were added to solutions of the prior prepared SCNPs, the free BTAs readily incorporated into the helical core of the BTAs, which was monitored by fluorescence spectroscopy in the case of BTA-dye. Catalytically active SCNPs were achieved after the incorporation of (*S*)-BTA-L-Pro. The catalytic activity was again investigated with the aldol reaction between *p*-nitrobenzaldehyde and cyclohexanone. In contrast to their first findings, the catalytic activity of the modular SCNP was higher than that of the SCNP with covalently bound L-proline. The modular approach now also allowed for the easy control over the local concentration of L-proline, which led to an improved catalytic activity. An alternative modular approach was just recently developed by Meijer and coworkers.[138] Liu *et al.* synthesized poly(pentafluorophenyl acrylate) (pPFPA) *via* the RAFT process as their starting polymer. The active esters in the side groups of pPFPA are very reactive towards amines, which enables the facile introduction of various sidegroups. In the presented case, polyetheramines and BTA-amines were utilized to provide water-solubility and self-assembly, respectively. Functionality was added by introducing either metal binding ligands (mono(benzimidazoylmethyl)-bis(pyridylmethyl) (Bimpy), phenanthroline (Phen), or 2,2-bipyridine (BiPy), or porphyrins, which can be applied as novel photosensitizers

that can produce singlet oxygen. By incorporating Cu(I)-ions into the Bimpy and Phen functional SCNPs the group was able to catalyze the well-known CuAAC. Complexation of Pd(II) by the Bipy-SCNPs led to catalytically active Pd-SCNPs capable of catalyzing depropargylation reactions.

Functionalized BTA units were also utilized by Palmans and coworkers, who synthesized 3,3-bis(acylamino)-2,2-bipyridine-substituted benzene-1,3,5-tricarboxamide (BiPy-BTA) grafted polynorbornene polymers *via* ring-opening metathesis polymerization.[139] The BiPy-BTA units along the polymeric backbone led to a collapse of single polymer chains, this time driven by π-π interactions in diluted solution. The π-π interactions led to an inherent fluorescence of the SCNPs, a fact that can be exploited as a chemical sensor. The BiPy-BTA moieties not only lead to the intrachain collapse, they also show a strong binding affinity towards copper(II)-ions. Accordingly, the self-assembly was disrupted upon Cu(II) complexation, which led to a decrease in fluorescence.

In another case of π-π stacking, the interactions between phenyl and pentafluorophenyl residues have been exploited by Weck and coworkers to mimic β-hairpin-like structures on a simple level.[140] Therefore, a polystyrene-*b*-poly(dimethyl acrylamide)-*b*-poly(pentafluoro-styrene) ABC triblockcopolymer was synthesized *via* the RAFT process. In dilute solution the quadrupole interaction between electron-rich (phenyl) and electron-deficient (pentafluorophenyl) aromatic systems led to the folding of the blockcopolymer into a sheet like structure between the A and C block, while the B block forms the loop region that is typical for β-hairpins. Applying a similar strategy, the same group also synthesized β-sheet mimics by folding an ABC triblockcopolymer carrying the complementary hydrogen bonding recognition pair ureidoguanosine-diaminonaphthyridine (UG-DAN).[141]

Other supramolecular binding motifs are metal complexation and host/guest complexation. Since three of the research projects of the current thesis are based on such systems, they will be discussed in more detail in the following paragraphs.

Metal Complexation

The concept of metal complexation can be applied to fabricate a variety of structures from main chain to side chain metallo-polymers and star-shaped assemblies. The binding forces in these structures can range from static binding to labile bonds that allow for

the construction of dynamic, supramolecular arrangements.[142] A myriad of metal-ligand combinations is available to choose from. An often employed ligand is terpyridine.[143,144] Since metallo-polymers feature the processing characteristics of polymers as well as the fucntionality provided by the metal-ions, they have potential applications in sensors, memory and light-emitting devices, solar cells, nanolithography, photonic crystal displays, controlled release, and catalysis.[145]

An early example for metal-ion containing SCNPs was presented by Odriozola and coworkers.[146] However, the Gd(III)-ions that potentially make the SCNPs applicable as magnetic resonance imaging (MRI) contrasting agents were loaded to the particles after SCNP formation. The intramolecular crosslinking was achieved by reacting an azide containing precursor polymer in diluted solution with a dialkyne crosslinker, which had a diethylenetriaminepentaacetic acid (DTPA) group incorporated into its structure. The Gd(III) loading was afterwards achieved in aqueous solutions.

Sanchez-Sanchez *et al.* utilized β-ketoester moieties along the polymeric backbone to form 2:1 complexes with copper(II)-ions, thus leading to the formation of SCNPs *via* the intramolecular crosslinking of the parent polymers by metal-ligand complexation. Following this strategy, methyl methacrylate (MMA) and 2-(acetoacetoxy)ethyl methacrylate (AEMA) copolymers were synthesized and subsequently crosslinked with Cu(II)-ions in diluted solution.[147] The enzyme-mimetic, catalytic properties of these metallo-SCNPs (M-SCNPs) were evaluated in the transformation of terminal acetylenes into 1,3-diynes *via* oxidative coupling. Indeed, the SCNPs showed excellent catalytic selectivity towards the homocoupling products when a mixture of terminal acetylenes was employed as the starting material, while $CuCl_2$ gives homo- as well as hetero-coupled products under the same conditions. In another work of the group, water-soluble poly(OEGMA-*co*-AEMA) precursors were intramolecularly crosslinked with Cu(II)-ions in diluted solution. The polymerase-like activity of these SCNPs was tested during the controlled polymer synthesis in aqueous media by either the ATRP or RAFT process.[148] By adapting reaction conditions of di Lena and co-workers,[149,150] but replacing the laccase enzyme by the copper-containing SCNPs, Pomposo and coworkers were able to successfully polymerize OEGMA, acrylic acid (AA), and AA-*co*-*N*-isopropyl acrylamide (NIPAM).

Another strategy involving copper-ions was presented by Paik and coworkers.[151] Linear precursor polymers were collapsed by intramolecular copper-phthalocyanine formation,

which resulted in colored SCNPs. The parent polymers were synthesized *via* a random RAFT copolymerization of styrene and 4-((4-vinylbenzyl)oxy)phthalonitrile (VBOP). The Cu-SCNPs were formed by cyclotetramerization of the VBOP moieties of the parent polymer with CuCl and free phthalonitrile in benzyl alcohol. In the absence of additional phthalonitrile, the Cu-SCNPs were formed inefficiently due to the bulky copper-phthalocyanine crosslinking units, which reduce the free volume in the single-chain nanoparticles.

The group of Lemcoff and coworkers investigated the synthesis of M-SCNPs based on polycyclooctadiene (polyCOD) precursors. In an intial study, such parent polymers were reacted with the commercially available chlorobis(ethylene)rhodium(I) dimer in diluted solution to form Rh(I) containing SCNPs.[152] The size of the SCNPs was tunable by varying the amount of precursor complex, *i.e.*, crosslinker, used for the chain collapse. The complexation of Rh(I) by polyCOD could be reversed by adding a competing ligand (2-(diphenylphosphino) benzaldehyde (PCHO)) to the solution of the Rh-SCNPs. Next to polyCOD, the corresponding acyl hydride derivative was obtained through oxidative addition of PCHO to the metal.

Expanding their strategy, Lemcoff and coworkers next synthesized mono- and bimetallic SCNPs containing rhodium(I), iridium(I), and nickel(0) on the basis of polyCOD precursors.[153] The complex $[IrCl(COE)_2]_2$ (COE = *cis*-cyclooctene) was utilized as the precursor complex for the Ir-SCNPs, while nickel(II) acetylacetonate was employed for the Ni-SCNPs. Since the Ni(0) complexes are less stable than the analogous rhodium(I) and iridium(I)/diene complexes, the *in situ* reduction of nickel(II) acetylacetonate with diisobutylaluminiumhydrid (DIBAL-H) in the presence of polyCOD afforded the targeted Ni-SCNPs. Bimetallic Rh,Ir-SCNPs were generated by reacting polyCOD in diluted solution first with appropriate amounts of $[RhCl(C_2H_4)_2]_2$ and then with $[IrCl(COE)_2]_2$, or *vice versa*. Finally, some preliminary tests for the application of the synthesized M-SCNPs in catalysis were presented. The Ir-SCNPs for instance were employed in the reduction of benzyl benzamide. In this case, however, the Ir-SCNPs only acted as the metal supplier for the known catalytic reduction of secondary amides by an iridium silane complex. In the allylation reaction of acetophenone with allyl boronic acid pinacol ester the Ir-SCNPs this time acted as the catalytically active species and smoothly afforded the expected allylated product. The isolated Ir-SCNPs could be recycled three times without loosing any of

their catalytic activity. The Rh-SCNPs were intended to be utilized as the catalyst in the cross-coupling reaction of 4-nitrobenzaldehyde and phenyl boronic acid. Interestingly, not the cross-coupled product, but biphenyl was found as the major product. By introducing N-heterocyclic carbenes (NHCs) into the Rh-SCNP structure *via* a simple ligand exchange reaction, the authors were able to significantly improve the yield of cross-coupled product.

Host/Guest Complexation

Inclusion complexes of guest molecules in a certain host are stabilized by non-covalent interactions (such as hydrophobic complexes, hydrogen bonds, π, π-interactions, ion-ion-interactions). Similar to metal complexes, the concept of host/guest complexation as well provides a plethora of motifs and manifold combinations of host/guest complexes. Well studied host molecules are for instance cyclodextrins,[154] calixarenes,[155] and crown ethers.[156]

Macrocylic host molecules of the cucurbit[n]uril family (CB[n];n = 5-8, 10) are highly selective and feature exceptionally high binding constants in water (K_a up to 10^{15} M^{-1}).[157] Sherman and coworkers introduced two examples for SCNP systems based on the supramolecular chemistry of these macrocyclic hosts. *nor-seco*-CB[10] (*ns*-CB[10]) contains two identical cavities capable to bind one guest each, forming 2 : 1 ternary complexes.[158] The group around Sherman synthesized water-soluble copolymers with pendant methyl viologen (MV) moieties, suitable guests for *ns*-CB[10] ternary complexes. A linear contraction of the hydrodynamic radius was observed when a diluted solution of the copolymer was titrated with *ns*-CB[10]. In another study of the same group parent, water-soluble polymers with pendant viologen (MV) and naphthyl (Np) residues where synthesized.[159] The MV and Np moieties are excellent guests for cucurbit[8]uril (CB[8]), so the addition of CB[8] to a diluted solution of the parent polymer led to the formation of SCNPs.

2.3 Characterization Methods in the Single-Chain Realm: An Analytical Point of View

Regardless of the selected synthetic approach, the analysis of the targeted single-chain architectures is a critical aspect. In addition to the techniques that have been employed for the research projects of the current thesis, the following paragraphs will also outline

some other common analytical methods for the sake of completeness. In theory, none of the following analytical methods is sufficiently powerful to verify the existence of a single-chain architecture in a standalone measurement. However, the careful choice of conditions and comparisons to the linear precursor polymers provide all the information for an in-depth analysis. Typically, complementary analysis techniques are utilized to support each other.

2.3.1 Size Exlusion Chromatography (SEC)

Size exclusion chromatography (SEC) is a chromatographic method to separate macromolecules in solution according to their size, or more accurately their hydrodynamic volume. SEC has become the standard technique in polymer science to determine the molecular weight distribution (MWD) of a polymer sample. In an SEC measurement a diluted solution of the polymer is pumped through one or more columns that are filled with a macroporous gel. These gels are typically made from crosslinked polystyrene, dextrane, polyacrylamide, cellulose, or silica particles. Most of these gels swell in the solvent that is used as the eluent. At sufficiently low flow rates ($\approx 1\,\mathrm{mL\,min}^{-1}$) a chromatographic behavior is expected. The total volume of the gel is composed of the volume of the gel-scaffold, the inner volume of the gel V_i and the outer volume between the gel particles V_0. The outer volume V_0 is identical with the elution volume V_e of a substance with a size, or better hydrodynamic volume, that is above the exclusion limit. Such substances cannot diffuse into the pores of the gel and thus elute without a delay. Hence, $V_e = V_0$ for large molecules. Very small molecules for which all pores are completely accessible, the elution volume is $V_e = V_0 + V_i$. For molecules with sizes in between, which can access only a fraction K_d ($0 < K_d < 1$) of the pores, the SEC equation (Equation 2.1) describes the elution volume.

$$V_e = V_0 + K_d V_i \tag{2.1}$$

The constant K_d mainly depends on the size (hydrodynamic volume) of the molecule, but also on the size of the pores and the kind of gel, the solvent, the temperature, and the degree of branching of the molecule. Due to these complicated dependencies it is not possible to calculate K_d as a function of the molecular weight. Thus, a calibration of the

SEC system using known standards with narrow MWDs is necessary. At this point, the interested reader is referred to standard textbooks which explain the calibration and how the MWDs are deduced.[160–162]

Already from the qualitative discussion above, it becomes apparent that size exclusion chromatography is an excellent tool for the analysis of single-chain architectures, since the transition from the random coil to the more compact structure leads to a reduction in the hydrodynamic volume and thus leads to prolonged retention times compared to the linear precursors.[64]

Pomposo and coworkers derived power-laws to describe the apparent molecular weight (M_{app}) and dispersity ($Đ_{\mathrm{app}}$) of SCNPs.[163] By assuming that the intramolecular crosslinking leads to fractal, soft nanoobjects they arrived at Equations 2.2 and 2.3.

$$M_{\mathrm{app}} = cM^{\beta} \tag{2.2}$$

$$Đ_{\mathrm{app}} = Đ^{\beta^2} \tag{2.3}$$

Here, c is a constant and the power-law exponent is $\beta = \frac{1+\alpha_{\mathrm{F}}}{1+\alpha_{\mathrm{L}}}$, where α_{L} is one of the Mark–Houwink–Sakurada constants, and $\alpha_{\mathrm{L}} \geq 0$ is a measure for the fractal nature of the SCNP and describes its discrepancy from the ideal "hard-sphere" state. The power law for $Đ_{\mathrm{app}}$ is based on the assumption that the MWD of the linear precursor follows a log-normal function. The concept of Pomposo and coworkers enables the quantification of the reduction in the (apparent) molecular weight and dispersity based on experimentally obtained SEC data.

Another power-law was derived by the group of Mays, which allows for the determination of hydrodynamic and thermodynamic properties of well-defined linear polymers in solution.[164] The authors selected data of various types of polymers (1,4-polybutadiene, 1,4-polyisoprene, polyisobutylene, polystyrene, and poly(α-methylstyrene)) and deduced power laws for the intrinsic viscosity, the radius of gyration, the hydrodynamic radius, and the second virial coefficient. In the context of the current thesis, the most interesting property is the hydrodynamic radius in the case of polystyrene dissolved in tetrahydrofurane (THF). Here the power-law is given by Equation 2.4.

$$R_{\mathrm{h}}^{\mathrm{THF}} = 1.44 \cdot 10^{-2} M^{0.561} \tag{2.4}$$

The above power-law, with M being the molecular weight according to SEC, allows for the prediction of the hydrodynamic radii of linear precursors as well as the single-chain nanoparticles. Although very practical, the obtained data should be taken with care, since the power-law is based on empirical data from homopolymers of styrene, which are certainly not the best representation of the functional linear precursors that are employed for SCNP formation.

2.3.1.1 Log-normal Distribution (LND) Simulations

As discussed earlier, the reduction of the hydrodynamic volume and therefore longer retention times in SEC experiments have become the most widely applied method for analyzing single-chain architectures. Monteiro and coworkers established a way to analyze experimental molecular weight distributions (MWD) with log-normal distrubutions (LND) based on the works of Cabaniss and coworkers.[165] The LND method determines the MWD by the summation of many narrow MWDs, thus allowing for the quantification of, *e.g.*, the amount of dead polymer in a reversible-deactivation radical polymerization (RDRP), or the amount of cyclic polymer in a ring-closure reaction.[46,166,167]

Typically, MWDs can be described by a Gaussian (or normal) distribution, given by Equation 2.5, where M is the molar mass, $\overline{M}$ is the median molar mass of the distribution, and σ is the standard deviation.

$$n(M) = \frac{exp(-(M - \overline{M})^2 / 2\sigma^2)}{(2\pi\sigma^2)^{0.5}} \tag{2.5}$$

The main problem of a Gaussian distribution is its failure to describe broad distributions, since an increase in σ would lead to negative values for M.[168] The use of a log-normal distribution avoids this problem. Assuming the weight-distribution, $w(M)$, is symmetrical about the median on an lnM axis, leads to the log-normal distribution (Equation 2.6).

$$w(M) = \frac{exp(-(lnM - ln\overline{M})^2 / 2\sigma^2)}{M(2\pi\sigma^2)^{0.5}} \tag{2.6}$$

The two parameters of the LND equation, the median $\overline{M}$ and the standard deviation σ, are related to the SEC data by the following equations.

$$M_n = \overline{M}exp(-\sigma^2/2) \tag{2.7}$$

$$M_w = \overline{M}exp(\sigma^2/2) \tag{2.8}$$

$$Đ = exp(\sigma^2) \tag{2.9}$$

From equations (2.7) and (2.8) a value for the median can be obtained.

$$\overline{M} = \sqrt{(M_\mathrm{n}M_\mathrm{w})} \tag{2.10}$$

An experimental MWD can be fitted with multiple distributions, each of which is generated from Equation 2.6 with predetermined values for M_n and $Đ$. The final simulated MWD is then produced from Equation 2.11.

$$w(M)_\mathrm{final} = \sum_i w_{p,i}w(M)_i \tag{2.11}$$

Here, $w_{p,i}$ is the weight fraction of distribution i and $w(M)_i$ is the weight at molecular weight M. When a good fit between the experimental and simulated MWD is achieved, analysis of the weight fractions enables the determination of, *e.g.*, residual linear polymer after cyclization reactions.[167] The same concept can also be applied for the analysis of SEC traces of single-chain nanoparticles. Compared to cyclizations, where there is only one reaction that leads to a reduction in the hydrodynamic volume (HDV), the random intramolecular crosslinking during SCNP formation leads to various species with reduced HDV. Consequently, several MWDs need to be considered in order to achieve a good fit. The M_n values that are utilized for the simulated MWDs can be regarded as a measure for the change in HDV, when the M_n of the linear starting material is used as the reference.

2.3.2 Dynamic Light Scattering (DLS)

Dynamic light scattering, or photon correlation spectroscopy, is a technique that can be utilized to determine the mean hydrodynamic diameter of a molecule in solution.[169] The light source for DLS analysis is usually a laser, which produces a monochromatic and coherent light beam. When the size of the investigated particles is small compared to the laser wavelength, light is scattered into all directions. This phenomenon is termed Rayleigh scattering and results from the electric polarizability of the particle. The oscillating electromagnetic field of the incoming light wave causes the electrons of the particle to oscillate at the same frequency. Thus, the scattered light that is detected thus is the light that is emitted by the oscillating electrons of the particle. In principle, the diffusion of particles could be monitored by experimentally determining the optical spectrum of the scattered light with an interferometer, but the speed of the moving particles however is so small compared to the speed of light that the interferometer encounters experimental difficulties.[160]

The optical Doppler-shift-spectrum $S(q, \omega)$ is a complicated sum of Lorentz-functions, which among others contains the form-factor $P_{k,m}(X, m)$, and the argument of the Doppler-shift spectrum $G_{k,m}(q, M)$. The form-factor or scattering function $P_{k,m}(X, m)$, as well as $G_{k,m}(q, M)$ depend on the shape of the scattering molecule and are different for, *e.g.*, coils, rods, and spheres. For a sphere $X = qR$, $G_{k,m} = q^2 D$, and $P_{k,m} \longrightarrow k = m = 0$ applies. Here R is the radius of the sphere, D is the translational diffusion coefficient, and $q = (4\pi n/\lambda)\sin\theta/2$ with n being the refractive index of the solvent and θ the angle at which the scattered light is detected.

The net scattering intensity that arrives at the detector, which is typically located at a 90° angle to the incident beam, is the result of an interference of many individual scattered waves. Due to the Brownian motion of the particles and the resulting Doppler-shift, the net intensity arriving at the detector fluctuates in time. The timescale of these fluctuations depends on the size of the particles and can be determined much more exactly, *e.g.*, with a photon-counter.

To obtain quantitative information about the diffusing particles from the timely fluctuation of the net scattering intensity an autocorrelation function is necessary, which is given in Equation 2.12 for monodisperse systems.

$$g_1(q,t) \equiv g_1(t) = < X(\tau)X^*(\tau+t) > = \lim_{T\to\infty} \frac{1}{2T} \int_{-T}^{T} X(\tau)X^*(\tau+t)d\tau \qquad (2.12)$$

The connection between the optical spectrum and the autocorrelation function is given by the Wiener-Khinchine theorem (see Equation 2.13). After Fourier transformation Equation 2.14 is deduced.

$$S(q,\omega) = \int_{0}^{\infty} g_1(t)exp(-i\omega t)dt \qquad (2.13)$$

$$g_1(t) = \sum_{k,m} P_{k,m}(X,m)exp(-G_{k,m}(q,M)t) \qquad (2.14)$$

In the case of only translational diffusion, Equation 2.14 simplifies dramatically (see Equation 2.15) and the correlation to the diffusion coefficient becomes apparent. Accordingly, the hydrodynamic radius is accessible *via* the Stokes-Einstein equation (see Equation 2.16).

$$g_1(t) = P_{0,0}(X,m)exp(-q^2 Dt) \qquad (2.15)$$

$$D = \frac{k_B T}{6\pi\eta R_h} \qquad (2.16)$$

So far, only monodispers systems were considered. In the case of dispers samples, a probability-density-function $G(\Gamma)$ is defined, which leads to a new autocorrelation function as shown in Equation 2.17.

$$g_1(t) = \int_{0}^{\infty} G(\Gamma)exp(-\Gamma t)d\Gamma \qquad (2.17)$$

To obtain the diffusion coefficients and their distribution from this new autocorrelation function is not an easy task and mathematically complicated. Typically, DLS instruments apply an inverse-Laplace transformation to extract the information. At the end it should be noted that most commercial DLS instruments use the homodyn-procedure to determine

the intensity autocorrelation function $g_2(t)$. The Siegert-relation (see Equation 2.18) establishes the connection to $g_1(t)$.

$$g_2(t) = A + B[g_1(t)]^2 \qquad (2.18)$$

The primary data that is collected during an DLS measurement delivers the intensity-weighted size distribution of the molecules in a sample, all other distributions (volume- and number-weighted) are generated from that initial distribution. The distribution of choice for the interpretation of DLS results obtained during the course of the current thesis is the number-weighted distribution, since it best represents the situation within the sample. One of the reasons is the fact that larger particles (or aggregates) scatter much more light than small particles. According to Rayleigh's approximations, the scattering intensity is proportional to the sixth power of the diameter. Thus, the small particles that are investigated in the single-chain realm would produce only a tiny amount of scattering intensity in the presence of only a small fraction of larger particles, which sometimes is unavoidable due to some formation of multi-chain nanoparticles.

Comparing the hydrodynamic diameters of the linear precursor polymers and the corresponding single-chain nanoparticles has become a common procedure.[71,111,158,170] Naturally, the technique is also suitable for the analysis of structures that have been synthesized following the selective point folding approach.

2.3.3 Small Angle Neutron/X-Ray Scattering (SANS/SAXS)

Other scattering techniques that are often applied for the characterization of single-chain nanoparticles are small angle neutron scattering (SANS) and small angle X-ray scattering (SAXS). Both techniques deliver information about the solution morphology of the sample of interest. SANS and SAXS may provide information about the radius of gyration R_g or the form factor of the SCNPs.[33]

Meijer and coworkers obtained values for the radius of gyration R_g and the excluded volume parameter ν from the fitting of SAXS data and found reduced values for both, indicating a compacted structure after the intramolecular crosslinking.[134,171]

SANS results for methyl methacrylate based SCNPs obtained by Pomposo and coworkers suggest a morphology similar to those of disordered multidomain proteins, which was also

backed up by complementary molecular dynamics (MD) simulations.[172] Another study of the same group revealed form factors (scaling exponent ν) for the SCNPs more similar to those of a Gaussian chain ($\nu = 1$) than to that of a spherical object ($\nu = 0.5$).[173] Yet again their findings were supported by MD simulations. Stals *et al.* investigated the dependency of the chainlenght of the linear precursor on the structure of their BTA-collapsed SCNPs by SANS.[132] With increasing degree of polymerization the SCNPs preferentially expanded in one direction, leading to ellipsoidal particles. In a recent viewpoint article Pomposo *et al.* reviewed literature data and pointed out that current SCNPs do not feature a compact, globular morphology, but rather adopt the structure of chains in a θ-solvent or intrinsically disordered proteins.[174]

2.3.4 Nuclear Magnetic Resonance (NMR) Spectroscopy Methods

Nuclear magnetic resonance (NMR) spectroscopy is typically employed to determine the molecular structure of molecules and to verify the existence of functional groups. The most widely applied techniques for that matter are the one-dimensional proton and carbon experiments. However, in the realm of single-chain technology these techniques can only provide information about bond formation during the crosslinking event, but not about the intra- or intermolecular nature of those bonds. Nevertheless, some more specialized experiments can provide useful insights into the crosslinking process and the structure of single-chain architectures. A few examples for such techniques are covered in the following paragraphs. For the basic knowledge about NMR physics that is required to understand the discussed pulse sequences the reader is referred to NMR textbooks.[175,176] The coordinate system that is used in the following paragraphs is presented in Scheme 2.5.

2.3.4.1 Analysis of the Transversal Relaxation Delay

There are two types of processes that govern the relaxation of a magnetic spin. On the one hand, there is the longitudinal, or spin-lattice, relaxation, which is characterized by the spin-lattice relaxation time T_1. On the other hand, there is the transversal, or spin-spin, relaxation, which is characterized by the spin-spin relaxation time T_2. The longitudinal relaxation describes the return of the component of the magnetization vector along the direction of the static magnetic field to its thermal equilibrium with its surroundings,
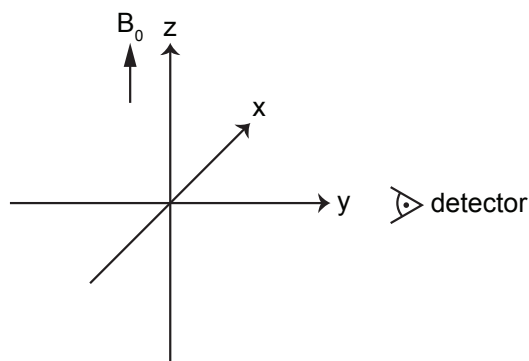
Scheme 2.5 Coordinate system used for the following discussions. The static magnetic field B_0 is applied along the z-axis. Typically, the pulses are applied from the x-direction and the detector is aligned with the y-axis.

the lattice, after it was flipped into the magnetic transverse x,y-plane by a 90° pulse. T_1 can be determined in an Inversion-Recovery-Experiment. Therefore, first a 180° pulse is applied, which rotates the magnetization into the -z-direction. After a certain time τ a 90° pulse is applied, which moves the remaining magnetization into the x,y-plane and a spectrum is recorded. The intensities of the signals are now proportional to the residual magnetization after the interval τ. To obtain T_1, experiments with different τ values are performed and an exponential decay function is fitted to the signal intensities. The spin-lattice relaxation is caused by fluctuating, local magnetic fields that originate from the motion of the molecules. These fluctuations can induce transitions between the two spin-niveaus and therefore lead to equilibration.

In contrast, the spin-spin relaxation relates to the phase of the rotating spins. After a 90° pulse, all spins rotate in phase in the x,y-plane with the Larmor frequency, *i.e.*, phase coherence exists. Already after a short amount of time the spins start to dephase and magnetization is lost. The dephasing is for one caused by inhomogeneities of the magnetic field, which are caused by local magnetic fields generated by other spins. During the flipping of the magnetization into the x,y-plane each vector component experiences a slightly different magnetic field strength due to their position. Thus, even at equal shielding constants, a distribution of Larmor frequencies is generated and the system starts to dephase. As already mentioned, the other mechanism contributing to the dephasing is the spin-spin relaxation. The spin-spin relaxation is an entropic process, during which the distribution of spins between the upper and lower states is not changed. The relaxation
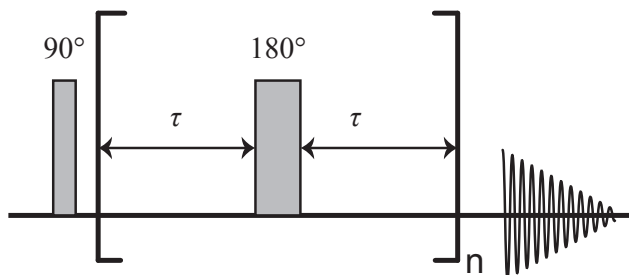
Scheme 2.6　Illustration of the Carr-Purcell-Meiboom-Gill (CPMG) pulse sequence. Adapted with permission from Reference [177]. Copyright 1958, AIP Publishing LLC.

process is simply an energy exchange between two nuclei. Nuclei in an excited state can relax and transfer their energy to a nucleus in its ground state and *vice versa.* Since these processes are spontaneous, it is unlikely that a certain nucleus returns to the excited state with the same phase as it initially had. Therefore, the phase coherence is lost. Hence, the magnetization in the x,y-plane decays with a compounded time constant T_2^*, which matches the sum of the individual processes T_2 and $T_{2,\text{inhomogeneous}}$.

To measure T_2 the Carr-Purcell-Meiboom-Gill (CPMG) pulse sequence is usually applied (see Scheme 2.6).[177] The CPMG sequence eliminates the influence of field inhomogeneities and enables the determination of T_2. The technique is based on Hahns spin-echo experiment.[178] Initially, a 90° pulse is applied, which flips the magnetization into the x,y-plane. Due to their different Larmor frequencies the spins start to dephase, *i.e.*, some precess slower and some precess faster. After a certain time interval τ a 180° pulse is applied to invert the spins, which keep their individual Larmor frequency. After another interval τ the spins thus refocus and the spin-echo is recorded. Due to the spin inversion after the 180° pulse, effects of an inhomogeneous field are compensated and the intensity of the recorded echo only decays because of spin-spin relaxation effects. The CPMG-pulse train records several such echos after different numbers n of τ-180°-τ cycles. T_2 is then determined by fitting an exponential decay function to the decreasing intensities of the spin-echos.

During the transition from a random coil to the more compacted structure of the single-chain nanoparticle a reduction of the mobility of the chain segments takes place. Consequently, the spin-spin relaxation becomes more effective and the transversal relax-

ation time decreases. Therefore, the decreasing T_2 time can be interpreted as a sign for SCNP formation.[114]

2.3.4.2 Diffusion Ordered Spectroscopy (DOSY)

As the name implies, diffusion ordered spectroscopy (DOSY) is a NMR technique to measure the translational diffusion coefficient of a molecule in solution.[179] The diffusion coefficient of a spherical particle with the radius R_h in a continuous medium with the viscosity η is given by the Stokes-Einstein equation (see Equation 2.19).

$$D = \frac{k_B T}{6\pi\eta R_h} \tag{2.19}$$

Here, k_B and T are the Boltzmann constant and the absolute temperature, respectively. Already at this point in the discussion it becomes apparent that DOSY provides an excellent tool for the characterization of SCNPs, since the contraction of the parent polymer will lead to an increased diffusion coefficient. Analogous to DLS, a hydrodynamic diameter can be calculated by employing the Stokes-Einstein equation. Loinaz and coworkers applied DOSY to demonstrate the reduction in hydrodynamic diameter of a linear precurosr polymer after the intramolecular crosslinking.[180] In addition to demonstrating the transition from the parent polymer to the single-chain architecture, DOSY can also be applied to identify the single-chain regime of dynamic systems.

The basis of every DOSY experiment is the fact that the position of a spin can be indirectly labeled with a pulsed magnetic field *via* its Larmor frequency. After the first gradient pulse, the molecule is allowed to diffuse for a given time Δ. A second gradient pulse can then be used to decode the new position of the molecule. The measured signal intensity will decrease depending on the diffusion time Δ and the gradient parameters G (strength), and δ (duration). The signal attenuation is given by Equation 2.20, where γ is the gyromagnetic constant of the observed nucleus. For the complete mathematical derivation the interested reader is referred to the comprehensive reviews of Johnson Jr. and Price.[181–183]

$$I = I_0 exp[-\gamma^2 G^2 \delta^2 (\Delta - \frac{\delta}{3})D] \tag{2.20}$$

The basic principle is best explained using the simple Stejskal and Tanner, or pulsed field gradient (PFG), sequence as shown in Scheme 2.7. To understand the effect of a gradient on a nuclear spin, the Larmor equation (see Equation 2.21) is needed.

$$\omega_0 = \gamma B_0 \tag{2.21}$$

ω_0 is the Larmor frequency, γ is the gyromagnetic ratio, and B_0 is the strength of the static magnetic field, which shall be oriented in the z-direction and spatially homogeneous. Hence, ω is the same throughout the sample. However, when there is a spatially dependent magnetic field gradient G in addition to B_0, ω becomes spatially dependent. In DOSY experiments the gradient is typically oriented parallel to B_0 along the z-axis. In the case of a single gradient, the magnitude of G is only a function of the position on the z-axis. For a single spin the cumulative phase shift is given by Equation 2.22.

$$\Phi(t) = \gamma B_0 t + \gamma \int_0^t G(t')z(t')dt' \tag{2.22}$$

The first term on the right hand side of Equation 2.22 corresponds to the phase shift due to the static field, while the second term is the phase shift resulting from the effects of the gradient. This second term shows that the degree of dephasing is proportional to the gradient strength, the duration of the gradient, and the displacement of the spin along the z-axis.
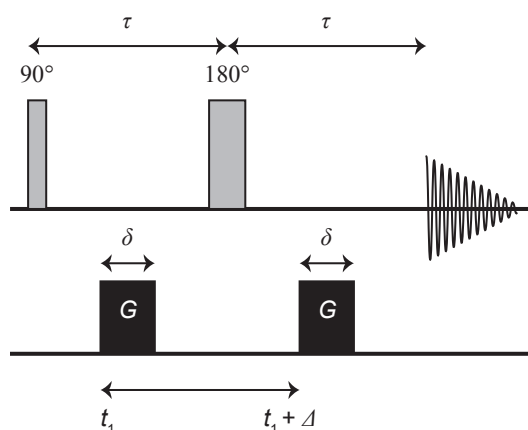
Scheme 2.7   Illustration of the Stejskal and Tanner, or pulsed field gradient (PFG), sequence. Adapted from Reference [183]. Copyright (1999), with permission from Elsevier.
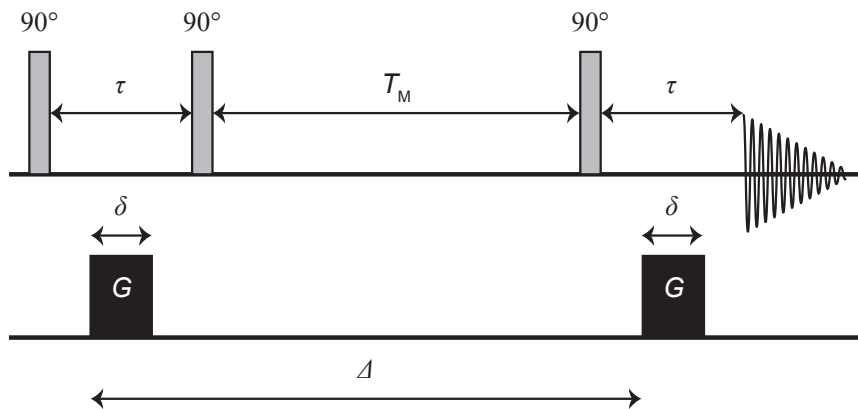
Scheme 2.8 Illustration of the stimulated echo (STE) pulse sequence. Adapted from Reference [183]. Copyright (1999), with permission from Elsevier.

The following paragraph will qualitatively explain how the PFG method works. As presented in Scheme 2.7, a 90° pulse rotates the magnetization into the x,y-plane. During the first τ period at time t_1, a gradient pulse of duration δ and magnitude G is applied so that at the end of the first τ period, spin i experiences the following phase shift:

$$\Phi_i(\tau) = \gamma B_0 \tau + \gamma G \int_{t_1}^{t_1 + \Delta} z_i(t) dt \tag{2.23}$$

Here, G has been taken out of the integral, since a constant amplitude gradient is considered. After the first τ period, a 180° pulse is applied, which leads to a reversal of the precession direction. At time $t_1 + \Delta$, a second gradient pulse (of equal magnitude and duration) is applied. If the spins did not diffuse along the z-axis during that time, the effect of the two applied gradient pulses would cancel out and all spins would refocus, leading to maximum signal intensity. However, if the spins have moved along the z-axis, the degree of dephasing due to the applied gradient is proportional to the displacement in the period Δ. The second gradient now is not able to refocus all spins, which leads to an attenuated signal.

A major disadvantage of the PFG sequence is the long time that the magnetization stays in the transverse (x,y) plane. During that time the magnetization is subject to transversal relaxation and J-modulation. Especially for macromolecules T_2 can be short, which results in a loss of signal. Incomplete refocusing due to J-modulation can occur when hard

pulses exchange the spin states of nuclei that are coupled to the monitored nucleus. To circumvent these problems a finding of Hahn can be applied, who showed that a sequence of three 90° pulses can generate up to five echos.[178] The first of these echos is the so-called stimulated echo (STE) and can be used for diffusion analysis. The second 90° pulse in the STE sequence (Scheme 2.8) stores the magnetization by flipping only the y-components back into the z-direction. The remaining x-component stays in the transverse plane and can contribute to the primary and secondary echoes. Finally, after the storage period T_M, the third 90° pulse moves the magnetization back into the transverse plane, where it is refocused by the second gradient and detected as the stimulated echo. Since the periods τ, where the magnetization is in the transverse plane, can be kept short in the STE sequence, relaxation is primarily based on T_1, which is way longer than T_2 and thus results in little loss of signal. Even though the STE sequence provides an improvement of the PFG sequence, the short τ periods may lead to a new problem: eddy currents.

Eddy currents, which arise from the rapid changes in pulse gradients, produce a magnetic field that interferes with the originally applied field. Since the quality of the applied gradient pulse is a very important aspect that influences the accuracy of a diffusion experiment, additional adjustments to the STE sequence have to be made. An advanced sequence is the longitudinal eddy current delay (LED) sequence as depicted in Scheme 2.9. In contrast to the STE sequence, here two additional 90° pulses, which are seperated by a time T_e, are added after the second τ period. The first of these new 90° pulses again stores the magnetization in the longitudinal direction, while the eddy currents can decay
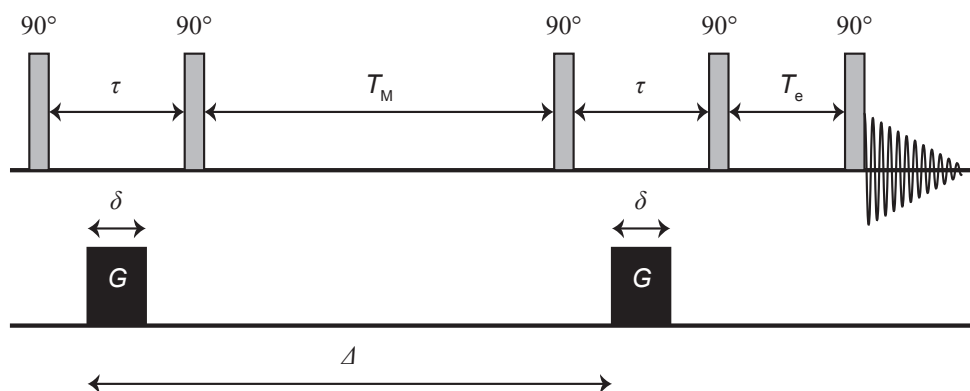
Scheme 2.9   Illustration of the longitudinal eddy current delay (LED) pulse sequence. Adapted from Reference [183]. Copyright (1999), with permission from Elsevier.
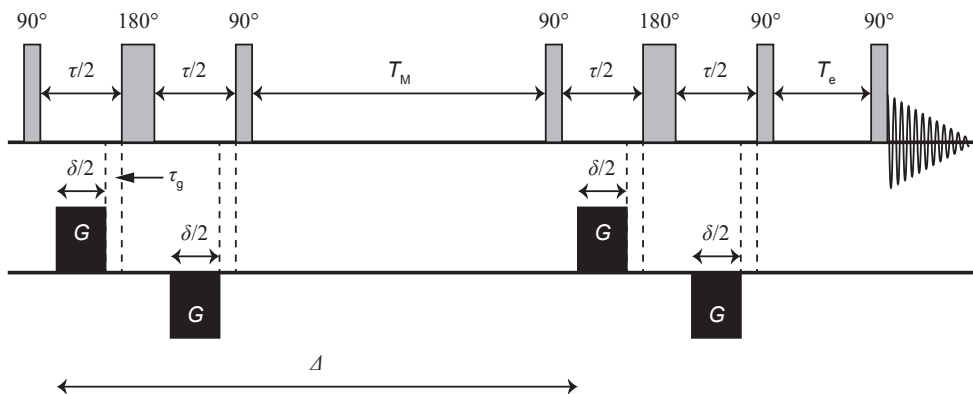
Scheme 2.10 Illustration of the bi-polar longitudinal eddy current delay (BPLED) pulse sequence. Adapted from Reference [183]. Copyright (1999), with permission from Elsevier.

during the settling time T_e. The last 90° pulse rotates the magnetization back into the x,y-plane where the echo can be detected.

An alternative way to suppress eddy currents even more effectively is to employ the bi-polar longitudinal eddy current delay (BPLED) sequence (see Scheme 2.10).[184]

In the BPLED sequence two gradient pulses (G) with opposite polarity ($+G$ and $-G$), which are divided by a 180° pulse, are applied. The $(+G)$-$(180°)$-$(-G)$ sequence cancels out the eddy currents.[185] Since eddy currents typically have settling times of the order of hundreds of milliseconds, the eddy currents generated by the first pulse (positive polarity) are canceled by the effects of the second gradient pulse (negative polarity), which follows only a few milliseconds later.[182] When the BPLED sequence is applied, adjustment of formula 2.20 by a correction factor is necessary, which leads to Equation 2.24.

$$I = I_0 exp[-\gamma^2 G^2 \delta^2 (\Delta - \frac{\delta}{3} - \frac{\tau_g}{2})D]$$ (2.24)

2.3.4.3 Nuclear Overhauser Enhancement Spectroscopy (NOESY)

Nuclear Overhauser Enhancement Spectroscopy, short NOESY, is an NMR technique based on the Nuclear Overhauser Effect (NOE), which was theoretically described and experimentally verified by Anderson and Freeman in 1962.[186] The NOE is a result of the dipolar interaction of two spin-$\frac{1}{2}$ nuclei through space and depends on the orientation of the two dipoles.[187] The dipolar interaction arises from precessing nuclei in close proximity, since the nuclear magnetic moment μ of one nucleus will influence the field that is felt by
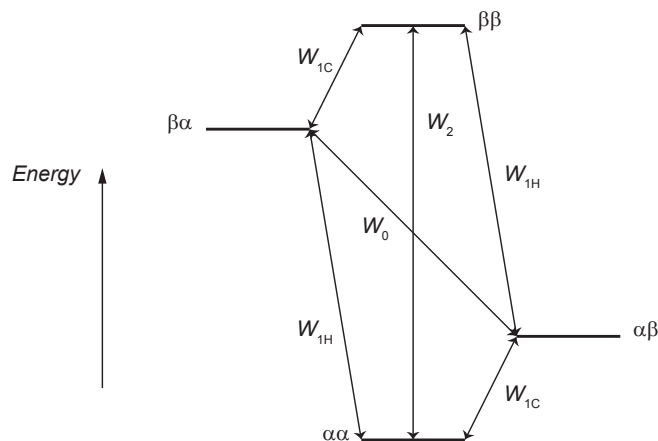
Scheme 2.11 Energy diagram of the four allowed spin state combinations of the ^{1}H-^{13}C pair. The first greek letter is the spin state of ^{1}H, the second the spin state of ^{13}C. W_0, W_{1H}, W_{1C}, and W_2 are the dipolar relaxation rate constants. Adapted from Reference [187] with permission from Elsevier.

the nearby nucleus, which affects the relaxation of spins. The dipolar relaxation pathway shall be discussed on the simple example of an isolated heteronuclear two-spin system (^{1}H-^{13}C). Here, four combinations for the spin state are possible (see Scheme 2.11).

The equilibrium population of the spin states is governed by the Boltzmann equation. The spin state of the ^{1}H has a bigger effect on the energy, hence $E(\alpha\beta)<E(\beta\alpha)$. The spin state combinations are linked to each other by a relaxation pathway with a unique dipolar relaxation rate constant W. The subscripts on the rate constants in Scheme 2.11 denote which spin needs to undergo a spin flip (quantum transition) during that particular relaxation pathway. The single quantum transitions (W_1) constitute the spin-lattice relaxation process. The zero (W_0) or double (W_2) quantum transitions are spectroscopically forbidden and can thus not be excited by electromagnetic radiation. In relaxation, however, they are allowed. Transitions between these states are only efficient when sufficient spectral density, which compensates the energy difference of the transition, is present. The way how energy spreads as a function of frequency is given by the spectral density function $J(\nu)$ (see Equation 2.25).

$$J(\nu) = \frac{2\tau_c}{1 + 4\pi^2\nu^2\tau_c^2} \tag{2.25}$$

Here, τ_c is a variable called correlation time, which is the time it takes for a molecule to diffuse one molecular diameter or rotate one radian. For small values of $\nu^2\tau_c^2$ Equation 2.25
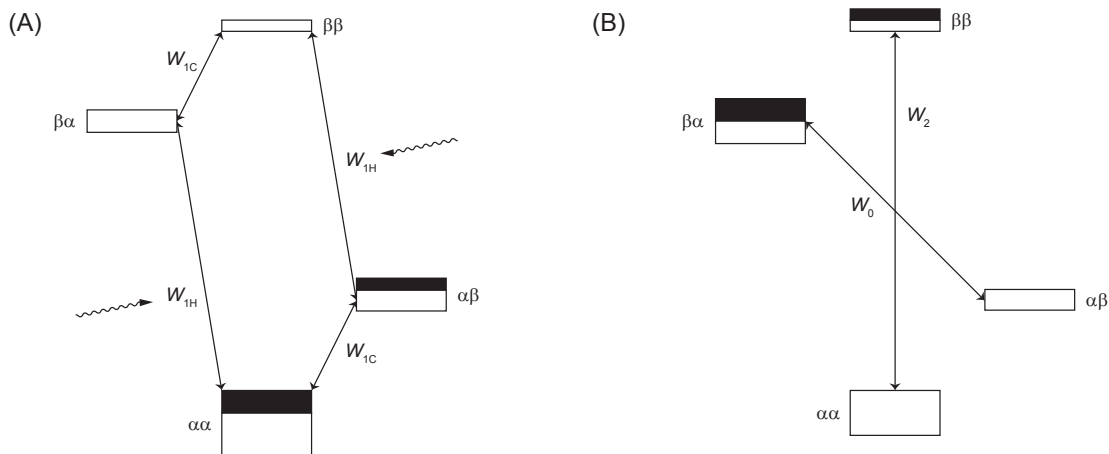
Scheme 2.12 Energy diagram of the four allowed spin state combinations before (A) and after decoupling (B). The relative thickness of the boxes represent the populations of the spin states. Adapted with permission from Reference [175]. Copyright Wiley-VCH Verlag GmbH & Co. KGaA.

simplifies to $J(\nu)=2\tau_c^2$, and for large values of $\nu^2\tau_c^2$ it approaches 0. A transition will not occur when the spectral density function drops to 0 at the frequency of the given transition. For short τ_c (fast-exchange limit) the ratio of relaxation rate constants $W_0\!:\!W_1\!:\!W_2$ is 2:3:12. Since the calculations of the relative values are complicated and would go beyond the scope of this introduction, the interested reader is referred to additional sources.[188,189] However, since W_2 involves the greatest change in spin states and brings the biggest gain in energy (see Scheme 2.11) it makes sense that it is the largest of the three rate constants.

A qualitative understanding of the NOE can be obtained when the saturation, or decoupling, of the ^{1}H transition is considered, which equalizes the spin populations in $\alpha\alpha$ and $\beta\alpha$, and $\alpha\beta$ and $\beta\beta$, respectively (see Scheme 2.12). The allowed relaxation processes W_0 and W_2 lead to a new equilibrium distribution. Relaxation *via* W_2 results in an increase in the population differences between the states $\alpha\alpha$ and $\alpha\beta$, as well as $\beta\alpha$ and $\beta\beta$, respectively, which determine the intensity of the C-transitions. Thus, the signal intensity is increased. Conversely, the W_0 relaxation reduces the signal intensities. The sum of these opposing relaxation processes is what can be observed as the Nuclear Overhauser Effect.[175] As a result, the NOE can lead to a signal increase or decrease, and it can also lead to the disappearance of a signal. For small molecules with short correlation times τ_c the NOE is positive, as W_2 predominates. For macromolecules with a large τ_c W_0 has the greater effect and the NOE is negative. The dependence of W on the correlation times becomes apparent when looking at the fluctuating magnetic fields needed to induce

the transitions. For the double quantum transitions, the magnetic fields must contain frequencies close to the sum of the Larmor frequencies ν_H and ν_C, whereas for the W_0 transitions much lower frequencies are needed.

The Nuclear Overhauser Enhancement therefore is a direct result of dipol-dipol relaxation. Since dipolar coupling decreases with r^{-6}, the NOE too depends on the internuclear distance r. Thus, the NOE can be utilized for structure determinations of proteins or to prove inclusion complexes in supramolecular systems. The two-dimensional NOESY experiment provides qualitative information for these structure determinations. Such spectra allow the direct mapping of all through-space interactions for every resonance of interest.

The 2D NOESY sequence is illustrated in Scheme 2.13. In the following, a homonuclear system in which the nuclei A and X are both protons is considered. Furthermore, the protons shall belong to the same molecule, have no scalar coupling and be close neighbors.

The first 90° pulse rotates the magnetization of A and X into the transverse plane, were they precess with their individual Larmor frequency. After t_1, the second 90° pulse moves all y-components of the magnetization back into the z-direction. During the subsequent mixing time τ_m, besides longitudinal relaxation, also cross-relaxation between the nuclei A and X, and *vice versa* is occurring. To generate different starting points for the mixing time, t_1 is changed in increments. The final 90° pulse then turns the resulting magnetization again into the transverse plane, and the free induction decay (FID) is recorded.

Fourier transformation with regard to t_1 and t_2 leads to the two-dimensional spectrum, which features resonances at (ν_A, ν_A) and (ν_X, ν_X) (the diagonal peaks), and at (ν_A, ν_X) and (ν_X, ν_A) (the cross-correlation peaks). These cross-correlation peaks, as a result of
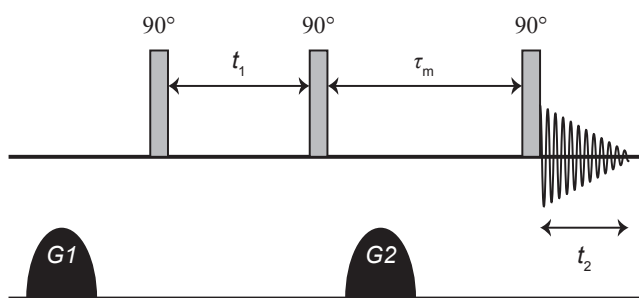
Scheme 2.13 Illustration of the two-dimensional NOESY pulse sequence. Adapted with permission from Reference [175]. Copyright Wiley-VCH Verlag GmbH & Co. KGaA.
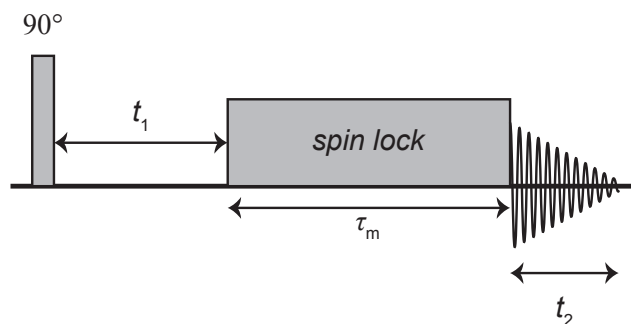
Scheme 2.14 Illustration of the two-dimensional ROESY pulse sequence. Adapted with permission from Reference [175]. Copyright Wiley-VCH Verlag GmbH & Co. KGaA.

the NOE, indicate the close proximity of the protons, which can usually be observed over distances of up to ≈ 5 Å.

The gradient pulses G_1 and G_2 (see Scheme 2.13) are very similar in their purpose. In the NOE sequence, these pulses are employed to disperse any transverse magnetization during the mixing time or before the next t_1 increment. G_2 is necessary, since any remaining transverse magnetization after τ_m would lead to unwanted artefacts or contribution to the cross-correlation peaks in the final spectrum. G_1 helps to decrease the overall experiment duration, as normally a long delay time between each t_1 increment would be needed to ensure complete relaxation of the spin system to avoid residual transverse relaxation.

As already implied, there is a critical correlation time $\tau_\mathrm{c}^\mathrm{crit}$ for which no NOE is detectable. Such correlation times are typically found for molecules with molar masses between 1000 and 2000 Da, depending on the solution conditions and spectrometer frequency.[188] For smaller molecules with small correlation times, the signs of the amplitudes of the cross-correlation peaks and the diagonal peaks are opposite. For larger macromolecules, the signs of cross-correlation and diagonal peaks have the same positive sign. To get structural information about the molecules with intermediate sizes, the rotating-frame NOE spectroscopy (ROESY) experiment was developed.[190,191] The respective pulse sequence is given in Scheme 2.14.

Here again a homonuclear system in which the nuclei A and X are both protons (not scalar-coupled) is considered. Like in the NOESY experiment the magnetization in the x,y-plane develops according to the different Larmor frequencies of the nuclei during the time t_1. Subsequently, a strong constant magnetic field, which contains the Larmor

frequencies of both nuclei A and X, is applied for the time τ_{m}. The effect of this spin-lock field B_1 keeps the remaining magnetization vectors aligned along the direction of B_1 in the x,y-plane during the mixing time τ_{m}, were they still decay with the transverse relaxation constant T_2. Since these magnetization components have the same frequency in the rotating frame, cross-relaxation is possible. Thus, cross-relaxation in the case of ROE occurs between transverse magnetization components.

The fact that $\gamma B_1 \ll \gamma B_0$ has the consequence that for all realistic values of τ_{c} cross-correlation peaks can be observed. A two-dimensional spectrum is obtained in the same way as for the NOESY experiment. Regardless of τ_{c} all cross-correlation peaks will have the opposite sign as the diagonal peaks.

2.3.5 Atomic Force Microscopy (AFM) and Transmission Electron Microscopy (TEM)

So far, the discussed methods characterized the single-chain architectures in solution. Solution-free microscopy techniques, such as atomic force microscopy (AFM) or transmission electron microscopy (TEM), are often applied to obtain information about the shape and size of the single-chain structure in the solid state.

AFM is a high resolution form of scanning probe microscopy (SPM).[192] During the scanning process of AFM the tip (probe), which is connected to the end of the cantilever, is moved across the sample surface. The structure of the surface leads to a position-dependent deflection of the cantilever due to forces between the tip and the sample according to Hooke's law.[193] The forces that cause the deflection are van der Waals forces, capillary forces, chemical bonding, electrostatic forces, and others. Usually a laser beam that is reflected from the top of the cantilever is utilized to determine the magnitude of the deflection. To avoid collisions with the surface when moving the tip at a constant height, a feedback mechanism is used instead to keep a constant force between the tip and the sample by adjusting the tip-to-sample distance with piezoelectric elements. The point by point registration of the deflection or force provides a map of the surface structure. Depending on the roughness of the examined surface, the lateral resolution can be as low as 0,1 to 10 nm. The resolution mainly depends on the radius of curvature of the tip (10 to 20 nm).

Numerous groups have utilized AFM to image their single-chain nanoparticles.[173,194,195] The sample preparation needs to be carefully performed, since dewetting effects and evaporative self-assembly, which has been described in the literature,[196,197] may lead to the formation of aggregates during the casting process. Cherian *et al.* were able to follow the progress of SNCP formation by analyzing samples taken at different time points of the intramolecular crosslinking process by AFM.[198] Meijer and coworkers performed a series of studies on the AFM analysis of SCNPs. For example, they studied the aggregation behavior of SCNPs crosslinked by upy dimerization. When the solvent of a dilute solution of the SCNPs was slowly evaporated, they found aggregation of the SCNPs similar to other synthetic nanoparticles or proteins.[124] In another study, similar upy crosslinked SCNPs were investigated. High resolution scans of individual SCNPs showed a "fried egg" structure of the particles on the mica surface.[125] By casting such SNCPs from solutions of different concentration, aggregation was observed similar to the aforementioned drying mediated self-assembly. Next, the group investigated the dependency of the molecular weight of the precursor polymers on the size of the SCNP according to AFM, by analyzing high and low molecular weight fractions of the same precursor polymer.[126] The AFM results of their upy crosslinked SCNPs confirmed the expected trend that low molecular weight precursors will result in smaller SCNPs than high molecular weight precursors.

In TEM an electron beam, which is transmitted through a thin layer of the sample, is employed for imaging. It is possible to achieve a much better resolution with transmission electron microscopes than with traditional light microscopes, as the resolution is limited by the wavelength of the photons used to examine the sample. In contrast to traditional light sources, electrons posses a very small de-Broglie wavelength, which leads to the high resolution. Like AFM, TEM has been employed to image and determine solid state diameters of SCNPs by various groups.[111,114,134,199–201]

3 | The Selective Point Folding Approach

As discussed earlier, there exist two synthetic approaches resulting in a three dimensionally linked polymer structure, one of which is the selective point folding approach. In order to design complex geometries, several orthogonal recognition unit pairs are required to selectively connect the chain segments. Due to the synthetic effort, not many examples for the selective point folding exist in current literature. Thus, the following chapter will investigate novel methodologies for the selective point folding of single polymer chains based on supramolecular recognition units. Since the cyclization of a polymer chain can be regarded as the simplest form of folding, employing only one pair of precisely installed recognition units, it is viewed here as a model system to showcase the viability of the targeted mode of folding.

Inspired by the large number of proteins/enzymes that carry metal ion cofactors (*e.g.*, hemoglobin, cytochrome P450, and nitrogenase),[57,58] it will be investigated if the complexation of a metal-ion can be utilized for the selective point folding of synthetic macromolecules (see Section 3.1). As a consequence of trying to mimic biological macromolecules, the synthetic approaches need to be moved into aqueous environment. Hence, Section 3.2 will discuss a strategy for the folding of single polymer chains in water, driven by the formation of a host/guest inlusion complex. A summary of the employed modes of folding is given in Scheme 3.1.
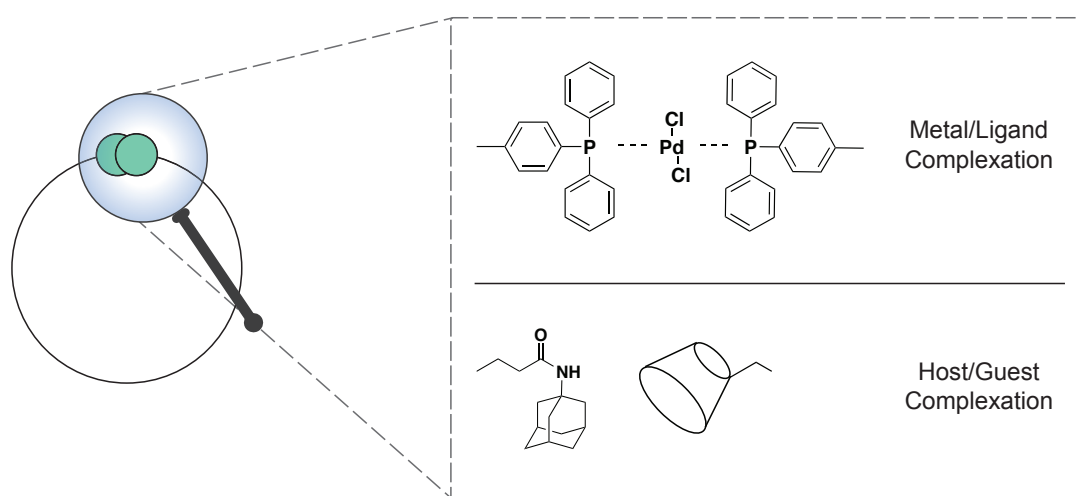
Scheme 3.1 Illustrative summary of the selective point folding strategies that are investigated in the current chapter.

3.1 Metal Complexation Driven Single-Chain Folding

The current section presents the folding of single polymer chains by metal complexation (see Scheme 3.2).* Therefore, homotelechelic bis-triphenylphosphine macroligands (MLs) with variable chain lengths were synthesized by a combination of the activator regenerated by electron transfer (ARGET) ATRP of styrene with a symmetrical, bifunctional initiator and subsequent copper(I)-catalyzed azide-alkyne cycloaddition (CuAAC) of a novel alkyne-bearing triarylphosphine ligand with the azide-terminated symmetrical polystyrene. In high dilution, cyclic complexes were formed with the $PdCl_2$ precursor complex dichloro(1,5-cyclooctadiene)palladium(II) [Pd(COD)Cl$_2$]. The complexation-driven selective point folding, resulting in single-chain metal complexes (SCMCs), was verified by ^{1}H and ^{31}P{^{1}H} NMR spectroscopy, size exclusion chromatography (SEC), and dynamic light scattering (DLS).
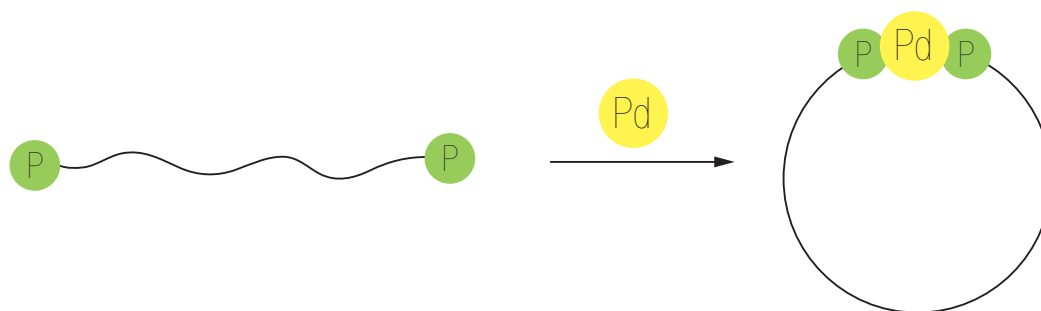
Scheme 3.2 Illustration of the controlled folding of single polymer chains induced by metal-ligand complexation.

Synthesis of the Linear Precursor Polymers

For the synthesis of a homotelechelic bis-triarylphosphine polymeric-macroligand, the strategy in Scheme 3.3 was designed. The symmetrical ATRP initiator ethylene bis(2-bromoisobutyrate) was utilized in the ARGET ATRP of styrene to generate symmetrical macromolecules with a bromine atom at the α- and ω-ends of the polymer chain. Subse-
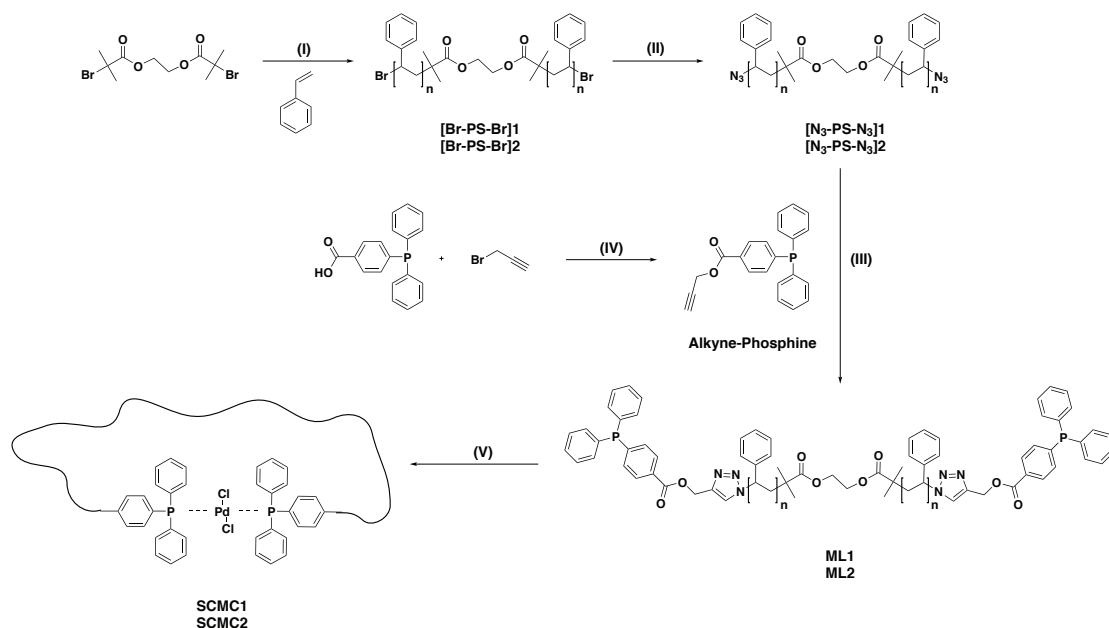
Scheme 3.3 Synthetic strategy for the preparation of single-chain metal complexes. (I) $CuBr_2$/Me_6TREN/$Sn(EH)_2$, anisole, 90 °C; (II) NaN_3, DMF, a.t., 24 h; (III) CuBr/PMDETA, DMF, a.t., 24 h; (IV) K_2CO_3, DMF, a.t., 24 h; (V) $[Pd(COD)Cl_2]$, CH_2Cl_2, a.t., 24 h. Adapted with permission from Reference [202] ©2013 WILEY-VCH Verlag GmbH & Co. KGaA, Weinheim.

quent end-group transformation by nucleophilic substitution with NaN_3 led to α,ω-azido functional polystyrene. The substitution was quantitative as verified within the limits of ^{1}H NMR spectroscopy: the resonance of the proton neighboring the bromine (4.35 - 4.66 ppm) completely shifted upfield (3.84 - 4.09 ppm) due to the quantitative substitution of bromine by azide (see Figure 3.1).

To introduce the palladium(II) complexing moiety, an alkyne-bearing triarylphosphine ligand was synthesized *via* esterification of 4-(diphenylphosphino) benzoic acid and propargyl bromide. The ^{1}H NMR spectrum of the novel triarylphosphine ligand (Alkyne-Phosphine) displays the resonance of the alkyne proton at 2.51 ppm and the resonances of the two $COO-CH_2-C{\equiv}CH$ protons at 4.92 ppm (see Figure 3.2).

The CuAAC between the ligand (Alkyne-Phosphine) and the di-azido functional polystyrene was performed in DMF employing CuBr/PMDETA as the catalytic system. The reaction was quantitative as verified within the boundaries of ^{1}H NMR spectroscopy (see Figure 3.1). The resonance of the two $CH-N_3$ protons (3.84 - 4.09 ppm) completely disappeared in the product ^{1}H NMR spectrum. New resonances emerged for the two $CH-$triazole (4.88 - 5.16 ppm) and the four CH_2-triazole-protons (5.20 - 5.45 ppm) in
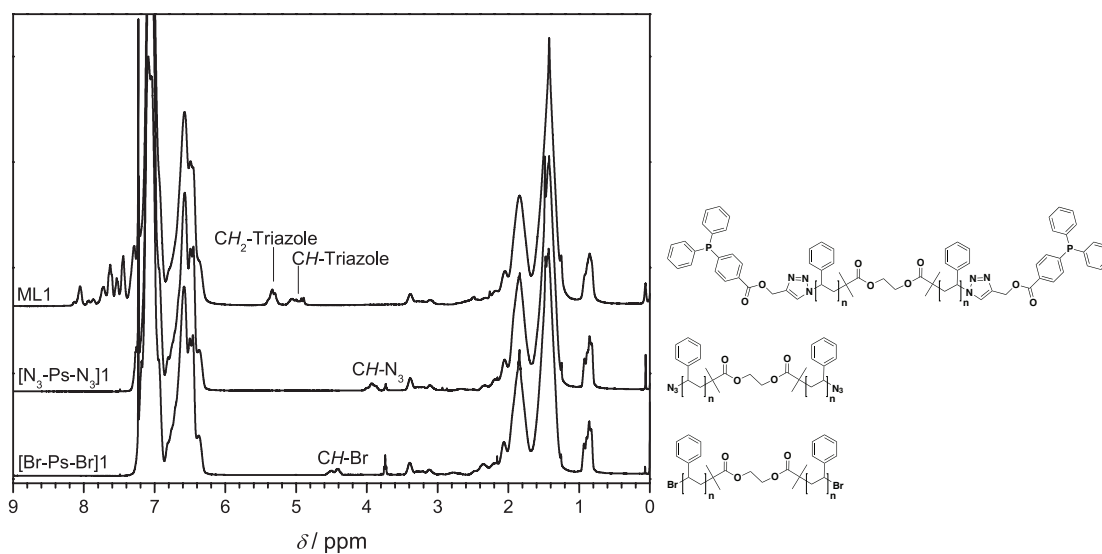
Figure 3.1 Normalized ^{1}H NMR spectra (400 MHz, CDCl$_3$) of the polymers [Br-PS-Br]1, [N$_3$-PS-N$_3$]1 and the telechelic bis-triarylphosphine macroligand ML1 at 25 °C. Adapted with permission from Reference [202] ©2013 WILEY-VCH Verlag GmbH & Co. KGaA, Weinheim.
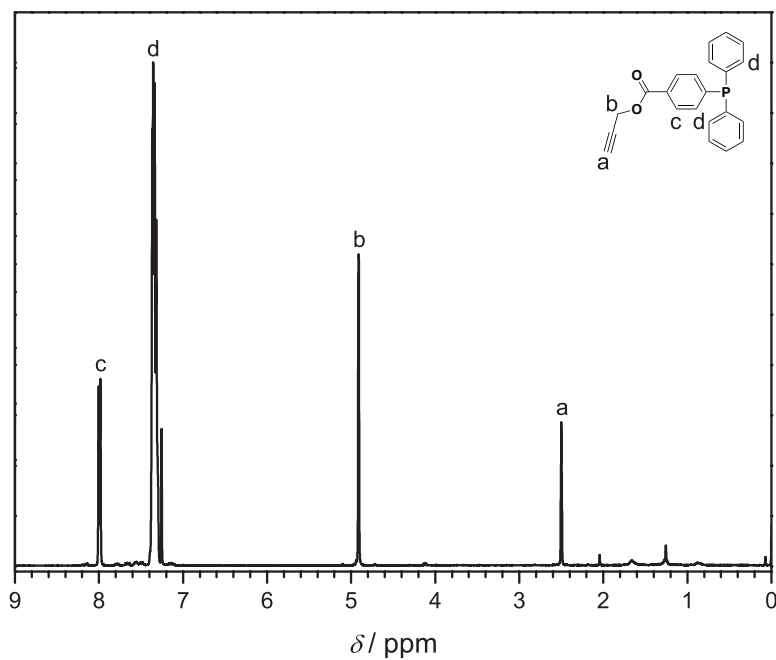
Figure 3.2 Normalized ^{1}H NMR spectrum (400 MHz, CDCl$_3$) of prop-2-yn-1-yl 4-(diphenylphosphino)benzoate (Alkyne-Phosphine, see Scheme 3.3) at 25 °C. Adapted with permission from Reference [202] ©2013 WILEY-VCH Verlag GmbH & Co. KGaA, Weinheim.
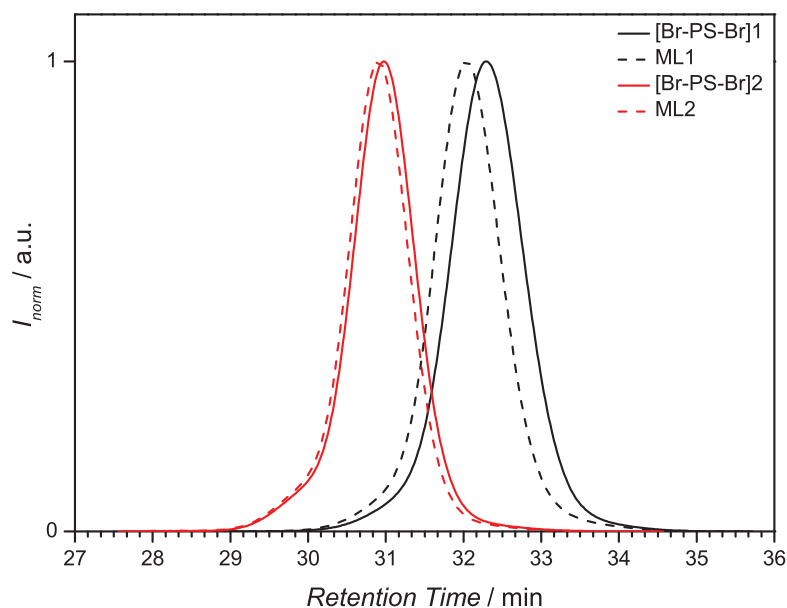
Figure 3.3 Normalized SEC traces of the α,ω-bromine functional polystyrene (solid lines) and the corresponding homotelechelic bistriphenylphosphine macroligands (dashed lines) in THF at 35 °C. A set of two macroligands (ML1, ML2) with varying molar mass were synthesized. Adapted with permission from Reference [202] ©2013 WILEY-VCH Verlag GmbH & Co. KGaA, Weinheim.

the downfield region. Additionally, the SEC traces of the conjugated products shifted to shorter retention times, which is related to an increase in molar mass (see Figure 3.3).

Preparation of the Single-Chain Metal Complexes

For the generation of the cyclic single-chain palladium(II) complexes, a highly diluted solution of the homotelechelic bis-triarylphosphine polymeric-macroligand in CH_2Cl_2 was slowly added at approximately $0.16\,mL\,min^{-1}$ to a highly diluted solution of a precursor complex in CH_2Cl_2 . Dichloro(1,5-cyclooctadiene)palladium(II) [Pd(COD)Cl$_2$] is an ideal candidate, since 1,5-cyclooctadiene constitutes a good leaving group in the ligand-exchange reaction.[203,204] The stereochemistry of the Pd-complexes in SCMC1 and SCMC2 is unknown. Usually, the arrangement of the ligands (*cis vs. trans*) in [Pd(PR$_3$)$_2$Cl$_2$] complexes is driven by the large cone angle of the phosphine ligand.[204] In contrast, chelating ligands with a small bite angle form *cis*-configured complexes. Since the triphenylphosphine complex [Pd(PPh$_3$)$_2$Cl$_2$] has a *trans*-configuration and the macroligands can form large rings, *trans*-configuration of the metal in SCMC1 and SCMC2 is suggested.[205,206] The palladium(II) complexation was monitored by ^{1}H NMR and ^{31}P{^{1}H} NMR spectroscopy (see Figure 3.4).
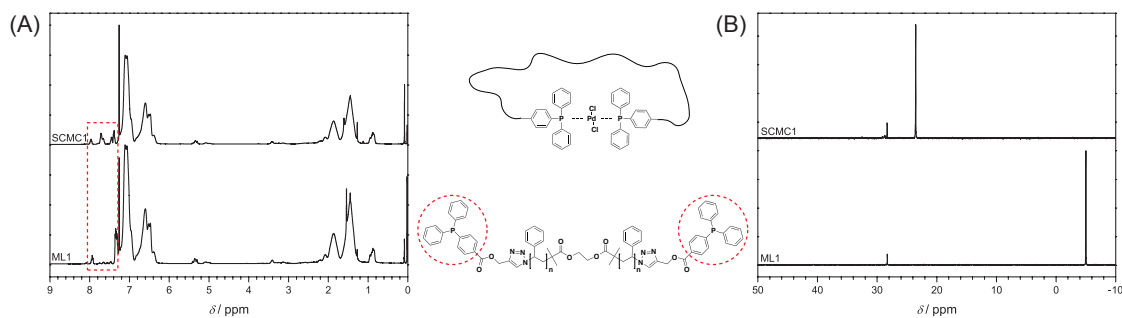
Figure 3.4 Normalized ^{1}H (A) and ^{31}P$\{^1$H$\}$ (B) NMR spectra of the telechelic bistriphenylphosphine macroligand ML1 and the corresponding single-chain palladium(II) complex SCMC1 in CDCl$_3$. The proton resonances in the dashed box (A) are assigned to the aromatic protons of the triarylphosphine moiety, which shift downfield upon complexation. Adapted with permission from Reference [202] ©2013 WILEY-VCH Verlag GmbH & Co. KGaA, Weinheim.

Table 3.1 SEC (THF, RI) results of the homotelechelic bis-triarylphosphine macroligand (ML) and the corresponding single-chain metal complex (SCMC) with PdCl$_2$.

Species	M_n(ML)/g mol^{-1}	M_n(SCMC)/g mol^{-1}	Collapse/%
1	6600	5600	15.0
2	12800	10300	19.5

The proton resonances of the aromatic protons of the triarylphosphine moieties are significantly shifted to lower field, indicating complexation. The ^{31}P$\{^1$H$\}$ NMR resonance of the macroligand (-4.99 ppm) completely shifts downfield (23.53 ppm) after the complex formation, evidencing quantitative complexation based on the ^{31}P$\{^1$H$\}$ NMR data of [Pd(PPh$_3$)$_2$Cl$_2$], where the phosphor resonance appears at 23.88 ppm.[207] The ^{31}P$\{^1$H$\}$ NMR spectra of the macroligands and SCMCs exhibit a resonance close to 28 ppm, which is assigned to the oxidized phosphine moiety (P=O).[57] Although the phosphine oxides will not participate in the complexation, their presence is likely of minor importance, since the DLS distributions of the SCMCs do not show any residual macroligands. The oxidation of the macroligands presumably takes place during the workup of the CuAAC conjugation.

The complexation-driven single-chain folding was evidenced by SEC and DLS. The more compact topology of a cyclic polymer – compared to its linear precursor – results in a smaller hydrodynamic diameter, which was unambiguously verified by DLS (see Figure 3.5B, Table 3.1 and 3.2).
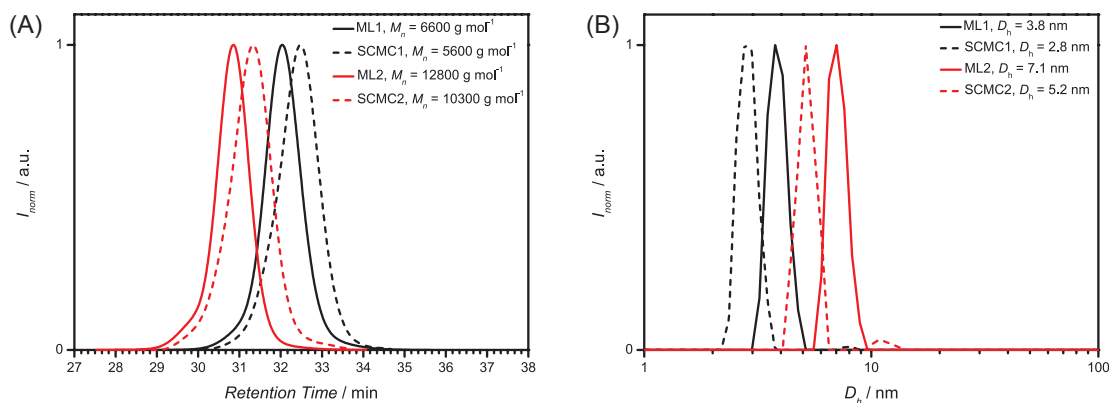
Figure 3.5 (A) Normalized SEC traces of the macroligands (solid lines) and the corresponding single-chain metal complexes (dashed lines) in THF at 35 °C. (B) Number-averaged particle size distributions of the macroligands (solid lines) and the corresponding single-chain metal complexes (dashed lines) in THF at 25 °C. Adapted with permission from Reference [202] ©2013 WILEY-VCH Verlag GmbH & Co. KGaA, Weinheim.

Table 3.2 DLS (THF) results of the homotelechelic bis-triarylphosphine macroligand (ML) and the corresponding single-chain metal complex (SCMC) with $PdCl_2$.

Species	D_h(ML)/nm	D_h(SCMC)/nm	Collapse/%
1	3.8 ± 0.4	2.8 ± 0.3	26.0
2	7.1 ± 0.8	5.2 ± 0.5	27.0

The mean hydrodynamic diameters for SCMC1 and SCMC2 decreased by 26 % and 27 %, respectively, compared to the corresponding macroligands ML1 and ML2. The DLS results for the single-chain metal complexes (SCMCs) both show small populations at slightly larger mean hydrodynamic diameters as the main distributions, which are attributed to minor intermolecular complexation. In SEC experiments, the cyclization manifests itself in the apparent loss of molar mass, which correlates with a shift of the SEC trace to longer retention times, since the SEC columns separate analytes based on their hydrodynamic volume (see Figure 3.5A and Table 3.1 and 3.2).

The fact that the SEC trace is completely shifted to longer retention times in both cases indicates an efficient complexation of the macroligands. The apparent change in molar mass for SCMC1 and SCMC2 amounts to 15 % and 19.5 %, respectively.

3.2 Host/Guest Complexation Driven Single-Chain Folding

In order to transfer the selective point folding concept into the aqueous environment, the current section introduces a new platform technology for the reversible folding of single polymer chains on the basis of cyclodextrin (CD) host-guest chemistry and reversible-deactivation radical polymerization (RDRP) protocols (see Scheme 3.4).[†] The strategy thus allows the application of a wide range of water-soluble monomers. The folding of adamantyl-β-CD α-ω-functionalized poly(*N,N*-dimethylacrylamide) and its reversion at elevated temperatures were monitored by dynamic light scattering (DLS) and nuclear Overhauser enhancement spectroscopy (NOESY).
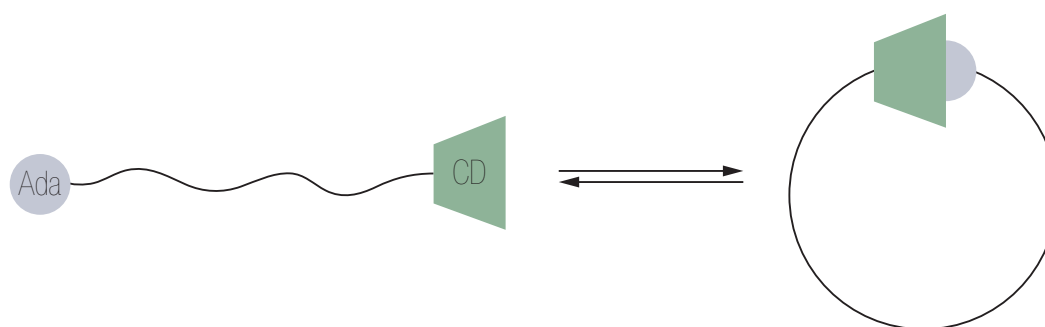
Scheme 3.4 Illustration of the β-cyclodextrin/adamantyl host-guest complexation driven reversible selective point folding in highly diluted aqueous solution.

Synthesis of the Linear Precursor Polymer

A synthetic route for a water-soluble polymer, namely poly(*N,N*-dimethylacrylamide), carrying the host (β-CD) and guest (adamantyl) moiety at the chain ends was designed (see Scheme 3.5).

The adamantyl (Ada) guest, which is known to form strong inclusion complexes with β-CD in aqueous solution with association constants of up to 10^5 M^{-1}, was introduced to the R-group of the novel chain transfer agent (CTA) Alkyne-CTA-COOH to obtain Alkyne-CTA-Ada, which carries an additional alkyne functionality in the Z-group to allow

Scheme 3.5 Synthetic route to α,ω-host-guest-functionalized poly(N,N-dimethylacrylamide). (I) EDC/DMAP, CH$_2$Cl$_2$ (dry), a.t., 24 h; (II) AIBN, DMF, 60 °C, 4 h; (III) CuI/DIPEA, DMF, a.t., 24 h. Adapted from Reference [208] by permission of The Royal Society of Chemistry.

**Table 3.3** Theoretical and experimental m/z of poly(DMAa) polymerized with Alkyne-CTA-Ada.

Species	m/z_theo	m/z_exp	$\Delta m/z$
■ [CTA(DMAa)$_{19}$ + 2 Na]$^{2+}$	1240.74	1240.64	0.10
● [CTA(DMAa)$_{31}$ + 3 Na]$^{3+}$	1231.10	1231.04	0.06

its modification *via* the copper(I)-catalyzed azide-alkyne cycloaddition (CuAAC). The complete characterization of the CTAs can be found in the experimental section of the current chapter (see Section 3.4). After the RAFT polymerization of *N*,*N*-dimethylacrylamide (DMAa) with Alkyne-CTA-Ada, the host moiety was attached to the chain end by CuAAC conjugation of the Alkyne-PDMAa-Ada polymer ($M_\mathrm{n,SEC} = 11\,000\,\mathrm{g\,mol^{-1}}$, $M_\mathrm{n,NMR} = 16\,900\,\mathrm{g\,mol^{-1}}$, $Đ = 1.19$) with 6-monoazido-6-monodeoxy-β-cyclodextrin (β-CD-azide).

The NMR spectrum of the Alkyne-PDMAa-Ada in Figure 3.6 features the resonances of the adamantyl-unit (e, f, g) and also the resonance for the alkyne endgroup (a) is clearly visible. Mass spectrometric analysis of a Alkyne-PDMAa-Ada polymer of lower molar mass (for better ionization) shows only one distribution in several ionization states (see Figure 3.7). The individual peaks of the distribution can unambiguously be assigned to the targeted structure (see Figure 3.8 and Table 3.3). In summary, these findings indicate a successful synthesis of the targeted structure.

The successful incorporation of the CD moiety was confirmed by ^{1}H NMR spectroscopy (see Figure 3.9). The resonance associated with the proton of the triazole unit (a, set
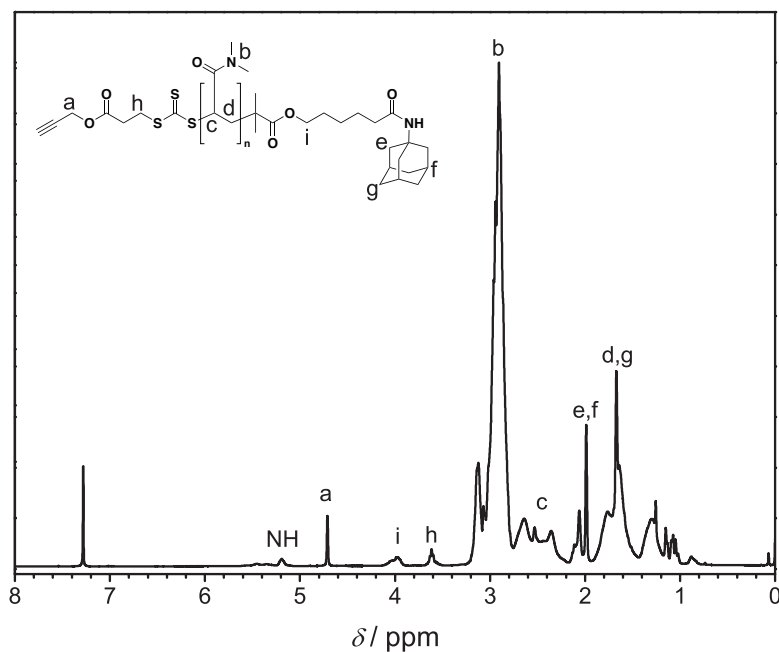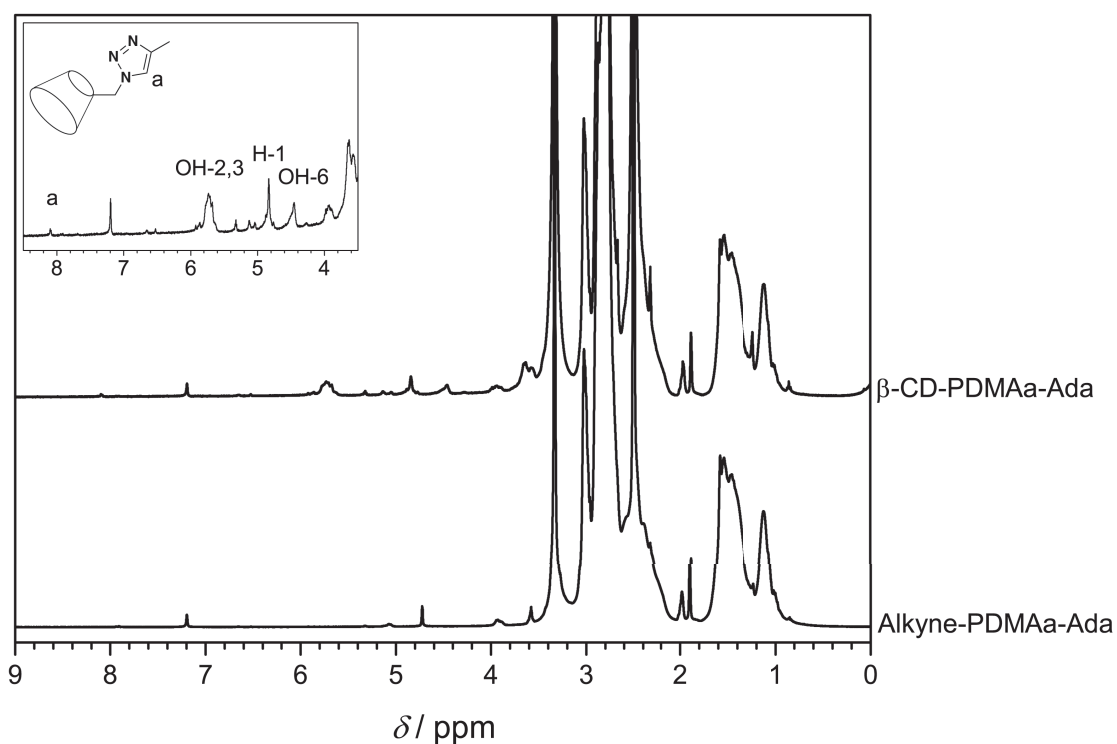
Figure 3.6 Normalized ^{1}H NMR spectrum (400 MHz, CDCl$_3$) of Alkyne-PDMAa-Ada at 25 °C. Adapted from Reference [208] by permission of The Royal Society of Chemistry.
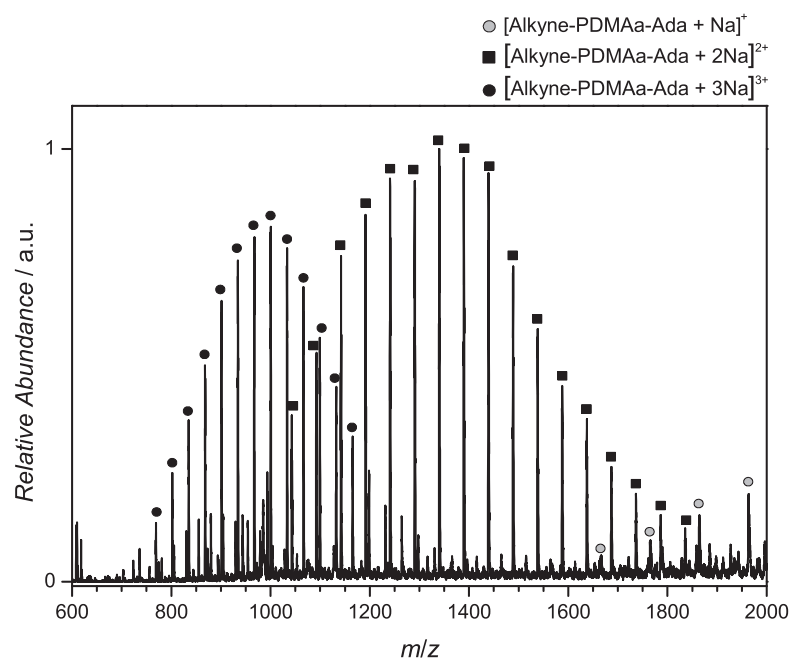

Figure 3.7 ESI-MS spectrum of Alkyne-PDMAa-Ada ($M_{n,SEC} = 5000 \, \text{g mol}^{-1}$, $M_{m,SEC} = 5250 \, \text{g mol}^{-1}$, $Đ = 1.06$). Reused from Reference [208] by permission of The Royal Society of Chemistry.
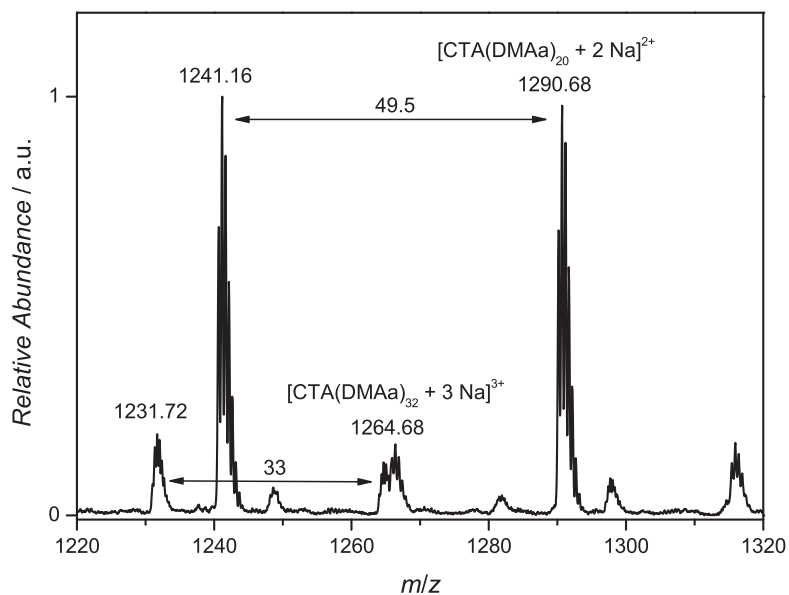
Figure 3.8 Section of the ESI-MS spectrum of Alkyne-PDMAa-Ada ($M_{\mathrm{n,SEC}} = 5000\,\mathrm{g\,mol^{-1}}$, $M_{\mathrm{m,SEC}} = 5250\,\mathrm{g\,mol^{-1}}$, $Đ = 1.06$). Reused from Reference [208] by permission of The Royal Society of Chemistry.

Figure 3.9 ^{1}H NMR spectra (400 MHz, DMSO$-d_6$) of β-CD-PDMAa-Ada (top) and Alkyne-PDMAa-Ada (bottom) at 25 °C. Adapted from Reference [208] by permission of The Royal Society of Chemistry.
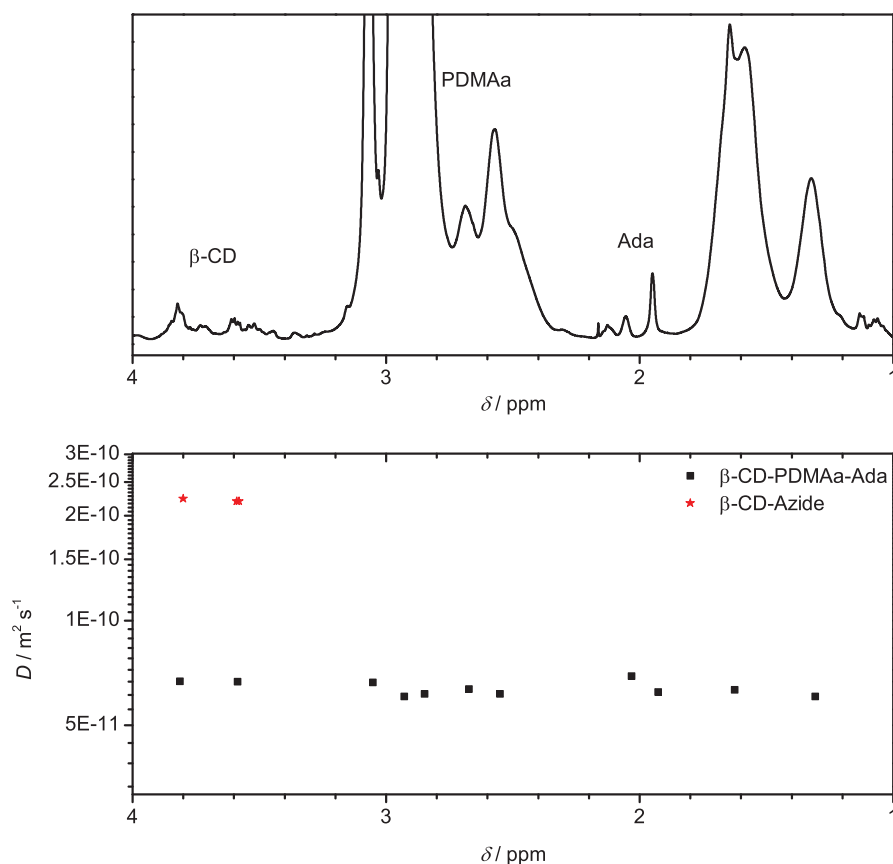
Figure 3.10 Top: Partial ^{1}H NMR spectrum (400 MHz, D$_2$O) of β-CD-PDMAa-Ada. Bottom: Diffusion coefficients corresponding to various resonances of the ^{1}H NMR spectrum of β-CD-PDMAa-Ada. For comparison the diffusion coefficients of β-CD-azide are plotted. Reused from Reference [208] by permission of The Royal Society of Chemistry.

to 1) at 8.10 ppm is in due proportion with the resonances corresponding to the CD moiety at 5.73 ppm (OH-2,3), 4.83 ppm (H-1) and 4.45 ppm (OH-6) (integral ratios: 1 : 13.33, 7.41, 6.78). In addition, diffusion ordered spectroscopy (DOSY) measurements evidence that the CD end group exhibits the same diffusion coefficient as the polymeric backbone, which indicates a successful incorporation of the host moiety (see Figure 3.10).

The SEC trace of the β-CD-PDMAa-Ada polymer ($M_{n,SEC} = 11\,600\,\mathrm{g\,mol^{-1}}$, Đ = 1.20) exhibits a small shoulder at shorter retention times, which might be attributed to the reaction product of two Alkyne-PDMAa-Ada polymers with difunctional β-CD-azide (see Figure 3.11).
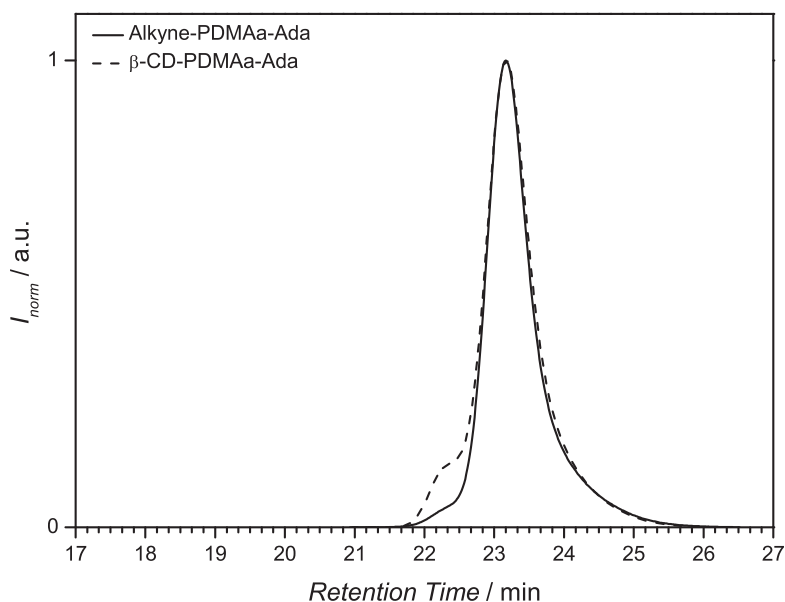
Figure 3.11 Normalized SEC traces (DMAc, RI) of Alkyne-PDMAa-Ada (solid line) and β-CD-PDMAa-Ada (dashed line). Reused from Reference [208] by permission of The Royal Society of Chemistry.

**Investigation of the Reversible Selective Point Folding**

The folding of β-CD-PDMAa-Ada and its reversion in diluted aqueous solution were monitored by DLS and NOESY NMR at ambient and elevated temperatures. DLS experiments with different concentrations of β-CD-PDMAa-Ada evidence that the polymer chains tend to aggregate or form intermolecular inclusion complexes at higher concentrations (see Figure 3.12). At elevated temperature, however, the inclusion complex is not stable, which leads to the observation of a constant hydrodynamic diameter, independent of the concentration, which is attributed to the open chain configuration (see Figure 3.12).

Only at high dilution the single-chain regime is reached. The concentration necessary for single-chain folding was established *via* DOSY experiments by varying the concentration of the β-CD-PDMAa-Ada polymer. The diffusion coefficient starts leveling below a concentration of $\approx 0.6\,\mathrm{mmol\,L^{-1}}$ (see Figure 3.13), thus the single-chain regime is reached. With increasing concentration the diffusion coefficient decreases, which underpins the assumption of a shift of the ring-chain-equilibrium to the open chain or even oligomer side (see also caption of Figure 3.13). However, step growth polymers are likely not observable, due to the low association constant compared to hydrogen bonds or metal complexes, for instance.[53,209] At a concentration of $0.57\,\mathrm{mmol\,L^{-1}}$, the number-weighted mean
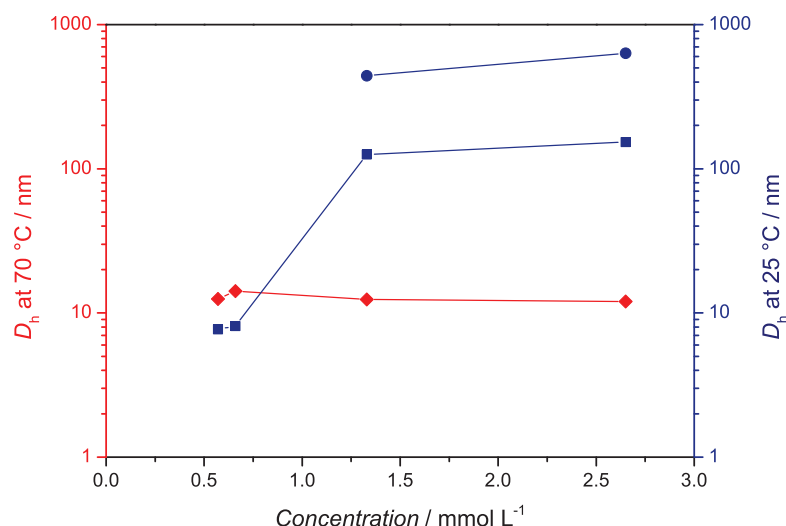
Figure 3.12 Number-weighted mean hydrodynamic diameter of β-CD-PDMAa-Ada at variable concentrations in water at 25 °C (blue) and 70 °C (red) according to DLS. The blue dots represent the mean hydrodynamic diameter of a second population. The lines are drawn to guide the eye. Adapted from Reference [208] by permission of The Royal Society of Chemistry.
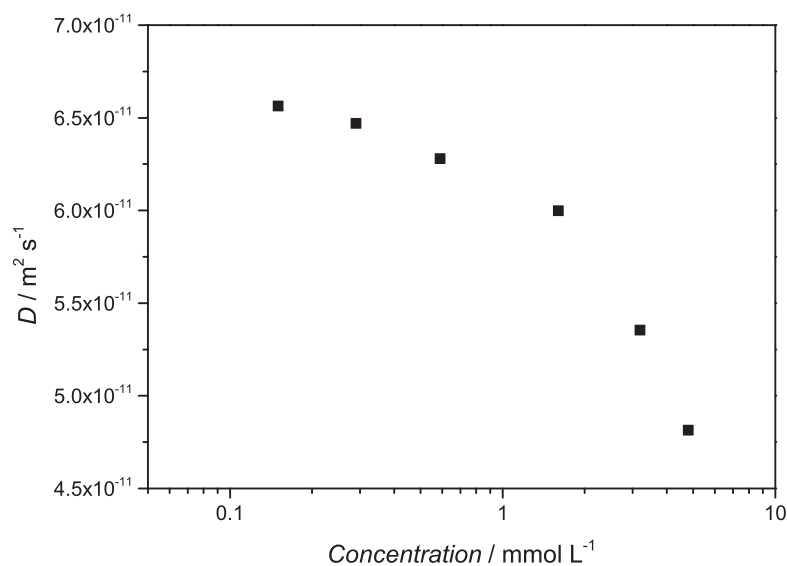
Figure 3.13 Averaged diffusion coefficient D plotted against the concentration of β-CD-PDMAa-Ada in D_2O. Taking into account the 5 % change in the diffusion coefficient of D_2O from the sample with the lowest to the sample with the highest concentration, the averaged diffusion coefficient at the highest concentration can be corrected to prevent an error potentially occurring due to changes in the solvent viscosity. With the corrected value of the averaged diffusion coefficient at the highest concentration, an averaged relative hydrodynamic radius between the lowest and highest concentration was estimated. With a value of 1.28 for the averaged relative hydrodynamic radius, the DOSY data leads to the assumption that oligomers are formed at higher concentrations. Reused from Reference [208] by permission of The Royal Society of Chemistry.
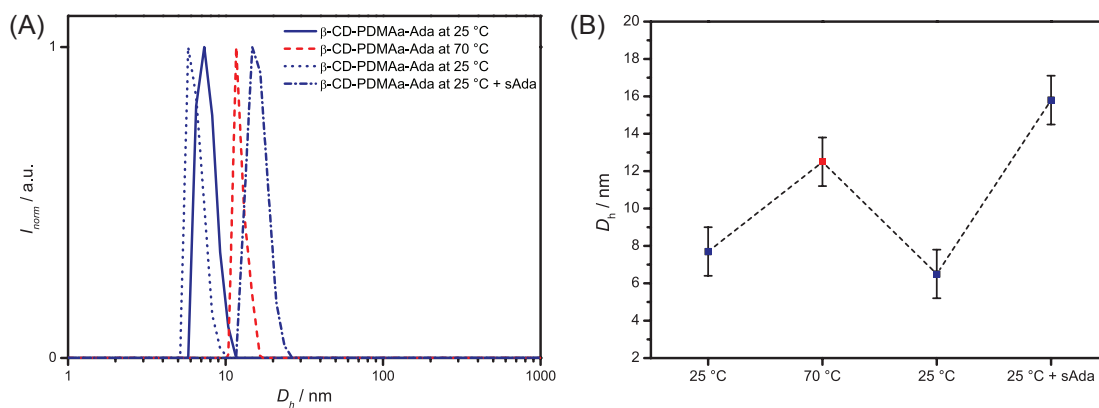
Figure 3.14 Dynamic light scattering results for the selective point folding of β-CD-PDMAa-Ada. (A) Number-weighted size distributions of β-CD-PDMAa-Ada in aqueous solution (c = 0.57 mmol L^{-1}). (B) Number-weighted mean hydrodynamic diameters (the lines are drawn to guide the eye). Adapted from Reference [208] by permission of The Royal Society of Chemistry.

hydrodynamic diameter (D_{h}) of the folded polymer chain at 25 °C is 7.7 nm. Previous studies have shown that inclusion complexes between CD and Ada can reversibly be opened at temperatures of approximately 70 °C.[210] Consequently, D_{h} increases to 12.5 nm when the temperature is increased. After cooling to ambient temperature and 24 h of equilibration time, the mean hydrodynamic diameter returns to a value of 6.5 nm, which is in good agreement with the initial value (see Figure 3.14).

In a displacement experiment, an excess of 1-adamantylamine hydrochloride (sAda) was added to the diluted β-CD-PDMAa-Ada solution, heated to 70 °C for 1 h and subsequently left to cool to ambient temperature for 24 h. The excess of sAda should then have replaced the α-Ada chain-end of the polymer, leading to an increased hydrodynamic volume, compared to the folded state at ambient temperature. As anticipated, the mean hydrodynamic diameter increased to 15.8 nm (see Figure 3.14). The slightly larger hydrodynamic diameter compared to the value at 70 °C hints at a more effective unfolding of the chain by the displacement of α-Ada.

Nuclear Overhauser enhancement spectroscopy (NOESY) can be applied to determine the formation of the β-CD and Ada inclusion complex formation.[210] The NMR sample was prepared in D$_2$O with the same concentration as the DLS sample (0.57 mmol L^{-1}) to ensure single-chain folding. The NOESY NMR spectrum of β-CD-PDMAa-Ada in D$_2$O at 25 °C clearly features cross-correlation peaks that correspond to the protons of the Ada
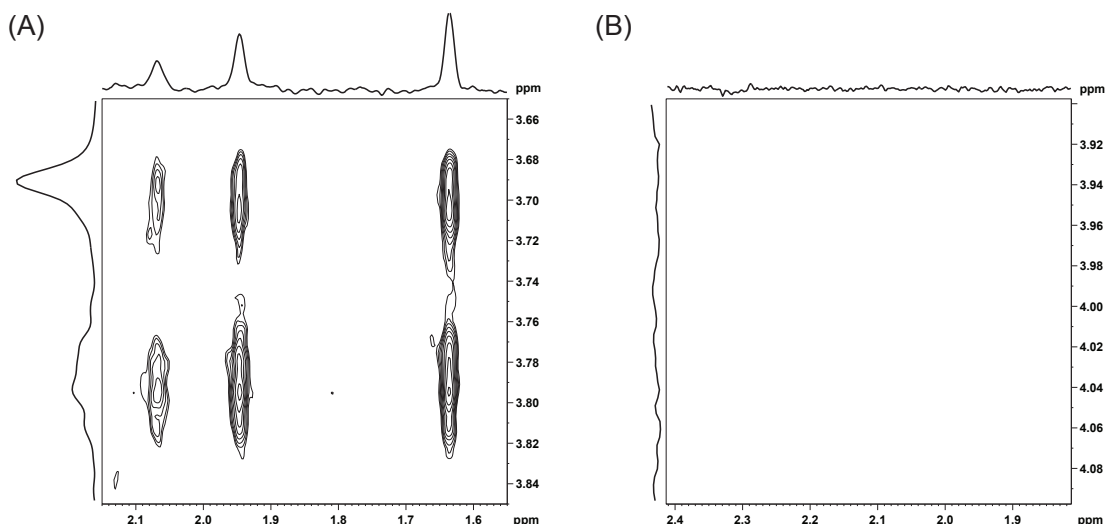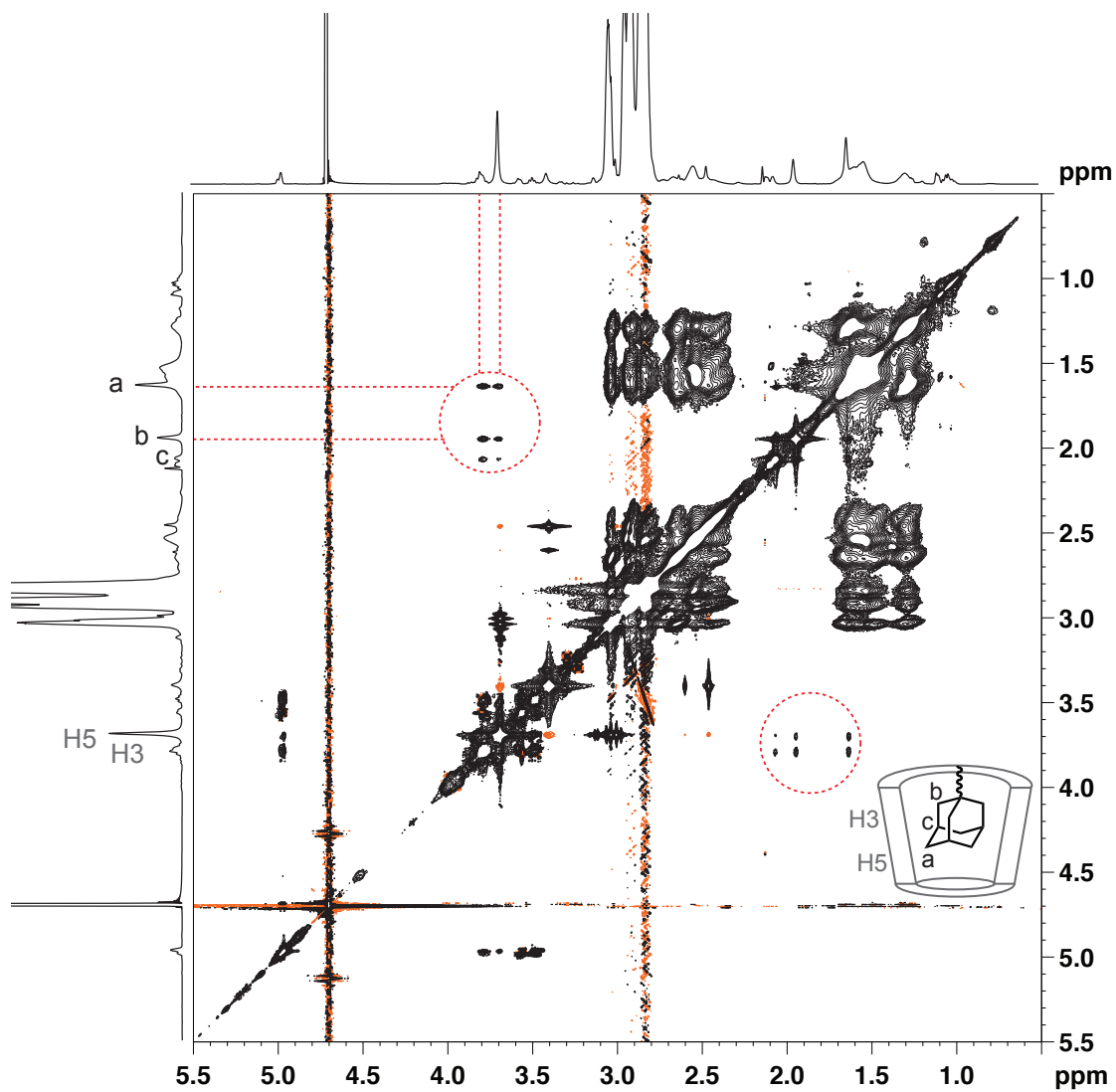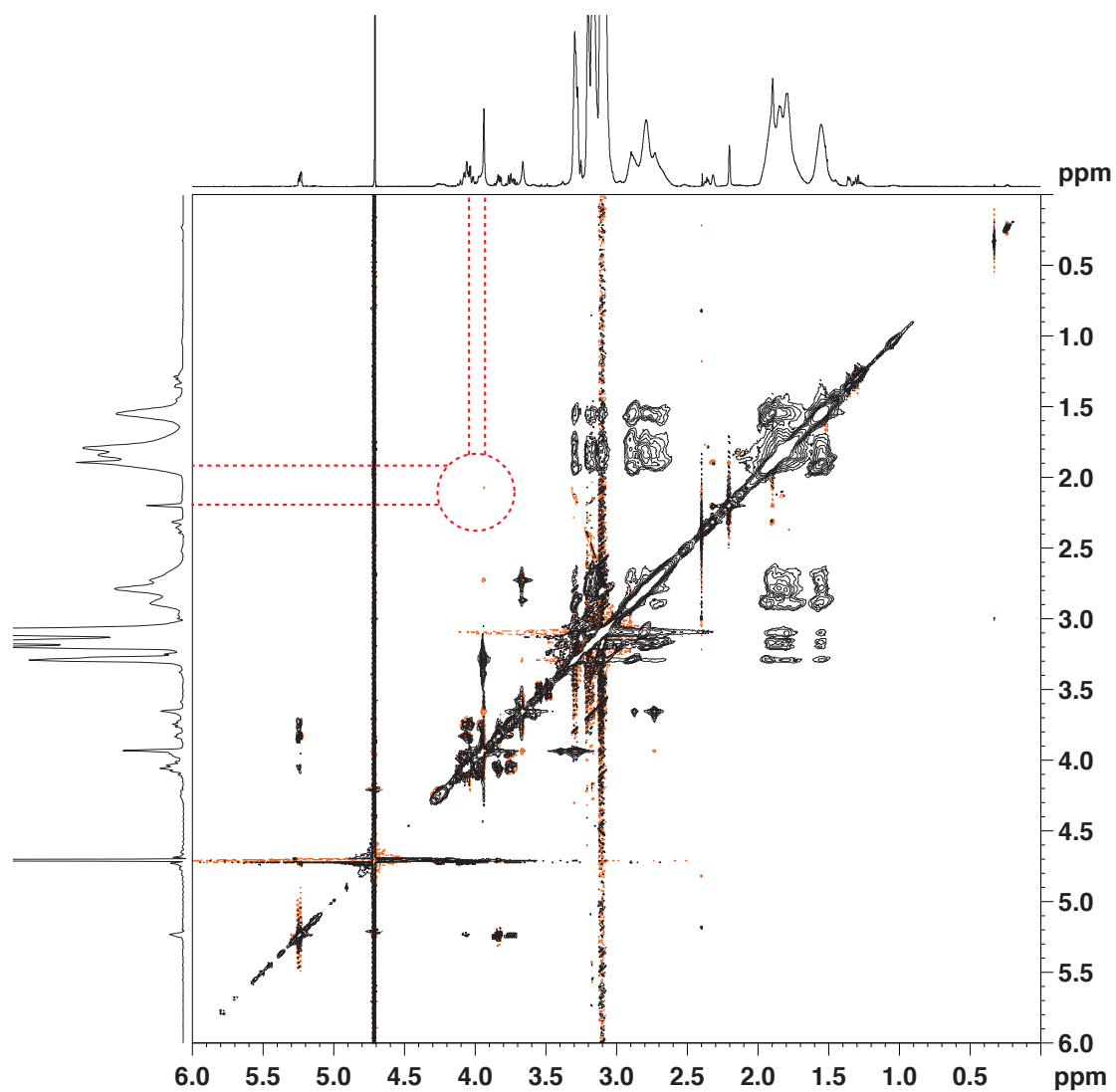
Figure 3.15 (A) Section of the NOESY NMR spectrum of β-CD-PDMAa-Ada in D_2O at 25 °C, which depicts the cross-correlation peaks arising from the CD-Ada inclusion complex. The top and left axes plot the 1D projection of the presented cross-correlation peaks. For the full spectrum see Figure 3.16. (B) Section of the NOESY NMR spectrum of β-CD-PDMAa-Ada in D_2O at 50 °C. The top and left axes plot the 1D projection of the presented cross-correlation peaks. For the full spectrum see Figure 3.17. Adapted from Reference [208] by permission of The Royal Society of Chemistry.

moiety between 1.66 ppm and 2.09 ppm and the inner CD protons between 3.71 ppm and 3.80 ppm (see Figure 3.15A and 3.16). The presence of these cross-correlation peaks evidences the close proximity of the Ada protons (a, b, c, Figure 3.16) and the inner CD protons (H3, H5, Figure 3.16), *i.e.*, formation of the inclusion complex.

Although NMR spectroscopy cannot reveal the intra- or intermolecular nature of the complex, the DLS results clearly corroborate single-chain assemblies. Due to limitations of the available NMR probehead, NOESY spectra at elevated temperatures were recorded at 50 °C instead of 70 °C. Nevertheless, even at 50 °C the absence of cross-correlation peaks (see Figure 3.15B or the full NOESY spectrum in Figure 3.17) of the inclusion complex leads to the conclusion that the chain is unfolded at 50 °C.

Figure 3.16 NOESY NMR spectrum of β-CD-PDMAa-Ada in D₂O at 25 °C. The marked cross-correlation peaks arise from the close proximity of the Ada- and inner CD-protons, thus from the formation of the inclusion complex. Reused from Reference [208] by permission of The Royal Society of Chemistry.

Figure 3.17 NOESY NMR spectrum of β-CD-PDMAa-Ada in D_2O at 50 °C. The marked area shows the absence of cross-correlation peaks. Reused from Reference [208] by permission of The Royal Society of Chemistry.

3.3 Summary

The current chapter first reported the controlled folding of single polymer chains by means of metal complexation. Macroligands were synthesized by a combination of controlled/living radical polymerization (ARGET ATRP) and modular conjugation chemistry (CuAAC). Following this strategy, two homotelechelic well-defined bis-triphenylphosphine macroligands on the basis of polystyrene with different chain lengths were generated. The formation of single-chain metal complexes (SCMCs) was induced *via* a Pd(II) precursor complex in diluted solution. Effective selective point folding was evidenced by SEC, DLS, ^{1}H and ^{31}P$\{^{1}$H$\}$ NMR spectroscopy.

It was also presented that the controlled reversible folding of an α-ω-functional polymer in water can be achieved by host/guest complexation. Therefore, a straightforward synthesis for an adamantyl-β-CD α-ω-functionalized water-soluble polymer was established, utilizing a combination of RAFT polymerization with a novel bifunctional RAFT agent and modular ligation chemistry. The reversible folding of single polymer chains, here shown on the example of poly(dimethyl acrylamide), was studied by DLS and NOESY NMR spectroscopy in diluted aqueous solution. The results evidence that the folded polymeric rings can be opened at elevated temperatures or *via* the addition of a competing guest.

The presented concepts provide an in-depth understanding of the respective folding methodology that can be applied to construct more complex architectures by combining several orthogonal binding concepts in the future.

3.4 Experimental Details

3.4.1 Synthesis of the Small Molecules

Synthesis of the Triphenylphosphine Ligand (Alkyne-Phosphine)

4-(Diphenylphosphino)benzoic acid (700 mg, 2.3 mmol, 1 equiv.) and potassium carbonate (632 mg, 4.6 mmol, 2 equiv.) were introduced into a flame-dried schlenk flask equipped with a stirring bar. The solids were dissolved in dry DMF (15 mL) before propargyl bromide (340 mg, 2.9 mmol, 1.25 equiv., 80 %(wt) in toluene) was added. The reaction mixture was stirred over night at ambient temperature. Remaining solid material was filtered off and the solvent was removed under high vacuum. The crude product was dissolved in CH_2Cl_2 and washed with deionized water twice, prior to being purified by column chromatography on silica gel (4:1 hexane/ethyl acetate, R_f=0.6). The title compound was isolated as a brown oil (385 mg, 1.1 mmol, 49 %). ^{1}H NMR (400 MHz, CDCl$_3$, 25 °C): δ/ppm = 7.92 (dd, J = 8.2, 1.2 Hz, 2H, ArH−COO), 7.34 (m, 12H, ArH), 4.92 (d, J = 2.4 Hz, 2H, CH_2C≡CH), 2.51 (t, J = 2.4 Hz, 1H, C≡CH). ^{13}C{^{1}H} NMR (100 MHz, CDCl$_3$, 25 °C): δ/ppm = 165.6 (C$_d$), 144.8 (C$_h$), 136 (C$_i$), 134 (C$_j$), 133.2 (C$_f$), 129.52 (C$_e$), 129.2 (C$_g$), 128.7 (C$_k$), 128.7 (C$_l$), 77.6 (C$_b$), 75.07 (C$_a$), 52.5 (C$_c$). ^{31}P{^{1}H} NMR (160 MHz, CDCl$_3$, 25 °C): δ/ppm = -4.91. Elemental Analysis (C$_{22}$H$_{17}$O$_2$P): Calcd.: C, 76.74; H, 4.98; Found: C, 76.81; H, 5.13. For the signal assignment of the ^{13}C NMR spectrum see Figure 3.18.

Synthesis of di(prop-2-yn-1-yl) 3,3'-disulfanediyldipropanoate

In a 500 mL Schlenk flask 3,3'-disulfanediyldipropanoic acid (6.00 g, 28.53 mmol, 1.0 equiv.), propargyl alcohol (5.1 mL, 88.25 mmol, 3.1 equiv.), and 4-DMAP (1.40 g, 11.42 mmol, 0.4 equiv.) were dissolved in anhydrous THF (240 mL). The mixture was cooled to 0 °C and a solution of DCC (17.67 g, 85.64 mmol, 3.0 equiv.) in anhydrous DCM (90 mL) was added. After one hour the solution was warmed to ambient temperature, stirred overnight, filtered, and concentrated under reduced pressure. The residual oil was purified by column chromatography on silica gel with a 6:1 mixture of *n*-hexane/ethyl acetate as the eluent that was changed gradually to 5:1. The product-containing fractions were concentrated and di(prop-2-yn-1-yl) 3,3'-disulfanediyldipropanoate was obtained as a viscous oil (6.12 g, 21.37 mmol, 75 %). ^{1}H NMR (400 MHz, CDCl$_3$, 25 °C): δ/ppm = 2.49
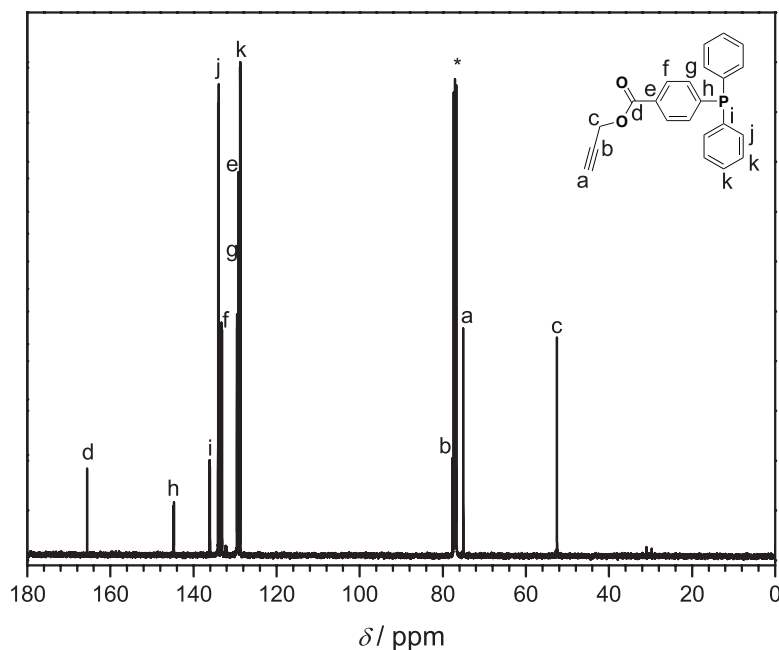
Figure 3.18 Normalized $^{13}C\{^1H\}$ NMR spectrum (100 MHz, CDCl$_3$) of prop-2-yn-1-yl 4-(diphenylphosphino)benzoate (Alkyne-Phosphine, see Scheme 3.3) at 25 °C. Adapted with permission from Reference [202] ©2013 WILEY-VCH Verlag GmbH & Co. KGaA, Weinheim.

(t, 2H, CH−C−CH$_2$), 2.79 (t, 4H, O=C−CH_2), 2.93 (t, 4H, S−CH_2), 4.71 (d, 4H, C−CH_2−O). $^{13}C\{^1H\}$ NMR (100 MHz, CDCl$_3$, 25 °C): δ/ppm = 32.9 (S−CH$_2$−CH$_2$), 34.0 (S−CH$_2$−CH$_2$), 52.4 (O−CH$_2$−C≡CH), 75.3 (CH$_2$−C≡CH), 77.5 (CH$_2$−C≡CH), 171.0 (C=O). ESI-MS: [M + Na$^+$]$_{exp}$ = 309.08 and [M + Na$^+$]$_{calc}$ = 309.02.

Synthesis of Alkyne-CTA-COOH

In a 250 mL round-bottom flask di(prop-2-yn-1-yl) 3,3'-disulfanediyldipropanoate (6.12 g, 21.37 mmol, 1.0 equiv.) and triethylamine (4.1 mL, 29.58 mmol, 1.4 equiv.) were dissolved in DCM (70 mL). The mixture was purged with argon for 30 min and DTT (4.85 g, 31.44 mmol, 1.5 equiv.) was added subsequently. The mixture was stirred at ambient temperature overnight. 1 M HCl (120 mL) was added, the organic phase was separated, washed with brine (120 mL), dried over Na$_2$SO$_4$, and filtered. After evaporation of the solvent the yellow oil was purified by column chromatography on silica gel with *n*-hexane/ethyl acetate 10:1 as eluent to give prop-2-yn-1-yl 3-mercaptopropanoate as colorless oil (3.91 g, 27.12 mmol, 64 %), which was used directly in the subsequent reaction.

Based on literature procedures,[211,212] prop-2-yn-1-yl 3-mercaptopropanoate (3.90 g, 27.04 mmol, 1.1 equiv.) was dissolved in a suspension of K_3PO_4 (7.42 g, 35.00 mmol, 1.1 equiv.) in acetone (100 mL) in a 250 mL round-bottom flask. After stirring for 20 min at ambient temperature carbon disulfide (4.5 mL, 74.47 mmol, 3.0 equiv.) was added and the solution turned yellow. 2-Bromoisobutyric acid (4.29 g, 25.15 mmol, 1.0 equiv.) was added after 20 min and the mixture was stirred at ambient temperature overnight. 1 M HCl (300 mL) was added and the aqueous phase was extracted with DCM (2 × 200 mL). The combined organic extracts were washed with deionized H_2O (200 mL), brine (200 mL), dried over Na_2SO_4, and filtered. After evaporation of the solvent the yellow oil was purified *via* column chromatography on silica gel with *n*-hexane/ethyl acetate as eluent that was gradually changed from 5:1 to 3:1 to give Alkyne-CTA-COOH as a yellow solid (3.59 g, 11.72 mmol, 47 %). ^{1}H NMR (400 MHz, $CDCl_3$, 25 °C): δ/ppm = 1.72 (s, 6H, 2 × C−CH_3), 2.49 (t, 1H, CH−C−CH$_2$), 2.80 (t, 2H, O=C−CH_2), 3.56 (t, 2H, S−CH_2), 4.70 (d, 2H, C−CH_2−O). ^{13}C{^{1}H} NMR (100 MHz, $CDCl_3$, 25 °C): δ/ppm = 25.3 (2 × CH$_3$−C), 31.1 (S−CH$_2$−CH$_2$), 33.0 (S−CH$_2$−CH$_2$), 52.5 (C(CH$_3$)$_2$), 56.0 (O−CH$_2$−C≡CH), 75.4 (CH$_2$−C≡CH), 77.4 (CH$_2$−C≡CH), 170.8 (C=O), 178.7 (C=O), 220.2 (C=S). ESI-MS: [M + Na$^+$]$_{exp}$ = 329.33 and [M + Na$^+$]$_{calc}$ = 328.99.

Synthesis of Alkyne-CTA-Ada

Alkyne-CTA-COOH (1 g, 3.26 mmol, 1 equiv.), *N*-(adamantan-1-yl)-6-hydroxyhexanamide (1.3 g, 4.89 mmol, 1.5 equiv.),[213,214] and DMAP (40 mg, 0.33 mmol, 0.1 equiv.) were dissolved in dry DCM (20 mL) in a flame-dried Schlenk flask and cooled to 0 °C. EDC·HCl (937 mg, 4.89 mmol, 1.5 equiv.) was added and the mixture was stirred over night at ambient temperature. Subsequently, the reaction mixture was washed with NaHCO$_3$ solution (100 mL). The aqueous phase was extracted with DCM (2 × 50 mL). The combined organic layers were successively washed with 1 M HCl, deionized H_2O, and brine (100 mL each) and dried over Na_2SO_4. Alkyne-CTA-Ada was isolated as a yellow oil (638 mg, 1.15 mmol, 35 %) by column chromatography on silica gel with *n*-hexane/ethyl acetate (4:1) as the eluent. For the ^{1}H NMR spectrum and signal assignment see Figure 3.19. See Figure 3.20 for the ^{13}C NMR spectrum. ^{1}H NMR (400 MHz, $CDCl_3$, 25 °C): δ/ppm = 1.34 (quin, 2H, H$_h$), 1.54 - 1.75 (m, 16H, H$_{e,g,i,m}$), 1.99 (s, 6H, H$_k$), 2.00 - 2.14
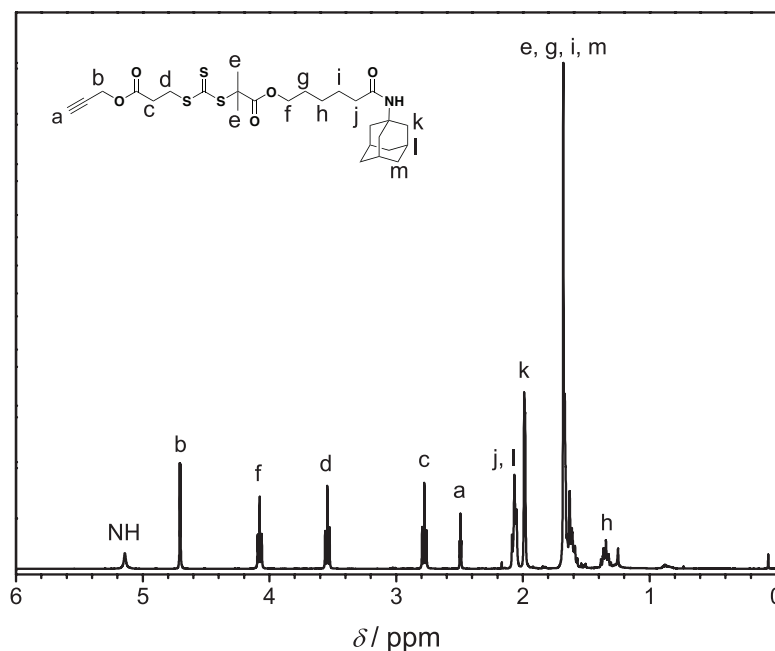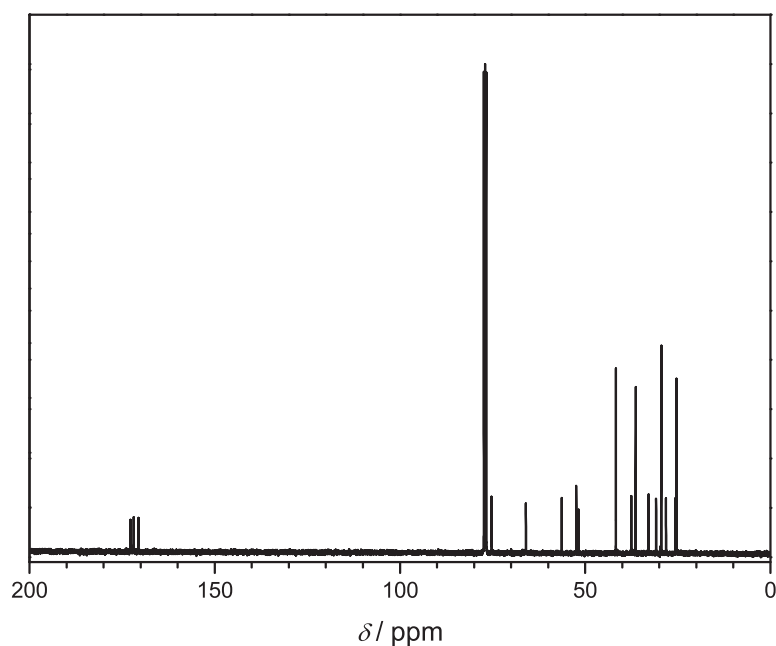
Figure 3.19 Normalized ^{1}H NMR spectrum (400 MHz, CDCl$_3$) of Alkyne-CTA-Ada at 25 °C. Adapted from Reference [208] by permission of The Royal Society of Chemistry.

(m, 5H, H$_{j,l}$), 2.49 (s, 1H, H$_a$), 2.78 (t, 2H, H$_c$), 3.54 (t, 2H, H$_d$), 4.08 (t, 2H, H$_f$), 4.70 (s, 2H, H$_b$), 5.14 (bs, 1H, NH). ^{13}C{^{1}H} NMR (100 MHz, CDCl$_3$, 25 °C): δ/ppm = 25.3, 25.6, 28.2, 29.5, 30.9, 32.9, 36.4, 37.5, 41.7, 51.9, 52.4, 56.4, 66.0, 75.3, 77.3, 170.6, 172.0, 172.8, 220.6. ESI-MS: [M + Na$^+$]$_{exp}$ = 576.19 and [M + Na$^+$]$_{calc}$ = 576.16.

3.4.2 Synthesis of the Parent Polymers

Synthesis of Symmetrical Dibromo-Polystyrene ([Br-PS-Br]1, [Br-PS-Br]2) and Subsequent End-Group Transformation to the Azide Moiety ([N$_3$-PS-N$_3$]1, [N$_3$-PS-N$_3$]2)

A general procedure is provided, for the reaction details refer to Table 3.4. The ARGET ATRP of styrene was conducted in the presence of ethylene bis(2-bromoisobutyrate) as the initiator, CuBr$_2$/tris(2-aminoethyl)amine (Me$_6$TREN) as the catalytic system and tin(II) 2-ethylhexanoate (Sn(EH)$_2$) as the reducing agent. The initiator and Sn(EH)$_2$ were each dissolved in anisole (2 mL) in separate round bottom flasks and purged with argon for 30 min. In a schlenk flask, equipped with a stirring bar, styrene, CuBr$_2$ and Me$_6$TREN were dissolved in anisole (1 mL) and also purged with argon for 30 min. Afterwards, the

Figure 3.20 Normalized $^{13}C\{^1H\}$ NMR spectrum (100 MHz, CDCl$_3$) of Alkyne-CTA-Ada at 25 °C. Reused from Reference [208] by permission of The Royal Society of Chemistry.

initiator- and reducing agent-solution were transferred to the reaction flask *via* a cannula. The flask was subsequently placed into an oil bath tempered at 90 °C for the appropriate reaction time (refer to Table 3.4). To stop the polymerization process, the mixture was cooled to ambient temperature in a water bath and opened to the atmosphere. The copper catalyst was removed by passing the solution over a short column of basic alumina oxide. The purified polymer was obtained by twofold precipitation into cold methanol (200 mL). The end-group transformation from bromine to azide was accomplished following a literature procedure.[215] ^{1}H NMR Br$-$PS$-$Br (400 MHz, CDCl$_3$, 25 °C): δ/ppm = 7.41 - 6.20 (m, ArH of PS), 4.66 - 4.30 (m, 2H, CHBr), 3.50 - 3.01 (m, 4H, 2 × CH_2 of initiator), 2.58 - 1.03 (m, aliphatic protons of PS). SEC (THF, RI): Refer to Table 3.5. ^{1}H NMR N$_3$$-PS-N_3$ (400 MHz, CDCl$_3$, 25 °C): δ/ppm = 7.39 - 6.26 (m, ArH of PS), 4.10 - 3.82 (m, 2H, CHN$_3$), 3.51 - 3.02 (m, 4H, 2 × CH_2 of initiator), 2.49 - 1.06 (m, aliphatic protons of PS). SEC (THF, RI): Refer to Table 3.5.

Table 3.4 Experimental details of the ARGET ATRPs of styrene with the initiator ethylene bis(2-bromoisobutyrate) in the presence of $CuBr_2/Me_6TREN$ and $Sn(EH)_2$ in anisole. The ratio of $CuBr_2/Me_6TREN$ and $Sn(EH)_2$ was kept constant at 0.1 equiv./0.1 equiv. and 0.5 equiv., respectively.

	Monomer/equiv.	Initiator/equiv.	$n_{Initiator}$/mmol	Time/h
1	200	1	0.44	5.0
2	400	1	0.44	7.5

Synthesis of the Homotelechelic Bis-triphenylphosphine Macroligands (ML1, ML2)

The CuAAC of the diazido-polystyrene and prop-2-yn-1-yl 4-(diphenylphosphino)benzoate in the presence of CuBr/PMDETA as the catalytic system in DMF was conducted by the following general procedure. The diazido-polymer (1 equiv.) and prop-2-yn-1-yl 4-(diphenylphosphino)benzoate (4 equiv.) were dissolved in DMF before PMDETA (10 equiv.) was added. After the mixture was degassed by three consecutive freeze-pump-thaw cycles, CuBr (10 equiv.) was added and the reaction mixture was stirred over night at ambient temperature. To remove the copper catalyst, the solution was passed over a short column of neutral alumina oxide. Subsequently, the solvent was removed under high vacuum. The remainder was dissolved in THF and precipitated into cold methanol (80 mL). The precipitate was filtered off and dried under high vacuum to afford the macroligands as white powders. ^1H NMR (400 MHz, $CDCl_3$, 25 °C): δ/ppm = 8.21 - 7.27 (m, 28H, Ar*H* of PPh_2), 7.28 - 6.24 (m, Ar*H* of PS), 5.49 - 5.20 (m, 4H, C*H$_2$*-Triazole), 5.19 - 4.86 (m, 2H, C*H*-Triazole), 3.50 - 3.01 (m, 4H, 2 × C*H$_2$* of initiator), 2.32 - 1.02 (m, aliphatic protons of PS). $^{31}P\{^1H\}$ NMR (160 MHz, $CDCl_3$, 25 °C): δ/ppm = 28.31 (s, 2P, P=O), -4.99 (s, 2P, PPh_2). SEC (THF, RI): Refer to Table 3.5.

RAFT Polymerization of DMAa with Alkyne-CTA-Ada for ^1H NMR and ESI-MS Analysis

Alkyne-CTA-Ada (38.77 mg, 0.07 mmol, 1 equiv.), AIBN (2.13 mg, 0.013 mmol, 0.2 equiv.), DMAa (200 mg, 2 mmol, 30 equiv.), and DMF (2 mL) were added into a Schlenk tube. After three freeze-pump-thaw cycles, the tube was backfilled with argon and placed into an oil bath for 4 h at 60 °C. The polymerization was stopped by cooling the reaction mixture in liquid nitrogen and opening the tube to the atmosphere. The mixture was

dialyzed against deionized water with a SpectraPor3 membrane (MWCO = 1000 Da) for three days at ambient temperature. The solvent was removed *in vacuo* at a freeze-drier to yield the polymer Alkyne-PDMAa-Ada as a yellow solid (29 mg, 0.006 mmol). SEC (DMAC, RI): $M_{\mathrm{n,SEC}} = 5000\,\mathrm{g\,mol^{-1}}$, $M_{\mathrm{m,SEC}} = 5250\,\mathrm{g\,mol^{-1}}$, $Đ = 1.06$. The NMR number-average molar mass ($M_{\mathrm{n,NMR}}$) was calculated from the integrals of the resonances at 2.27 - 2.75 ppm and 4.67 - 4.74 ppm. $M_{\mathrm{n,NMR}} = 4000\,\mathrm{g\,mol^{-1}}$.
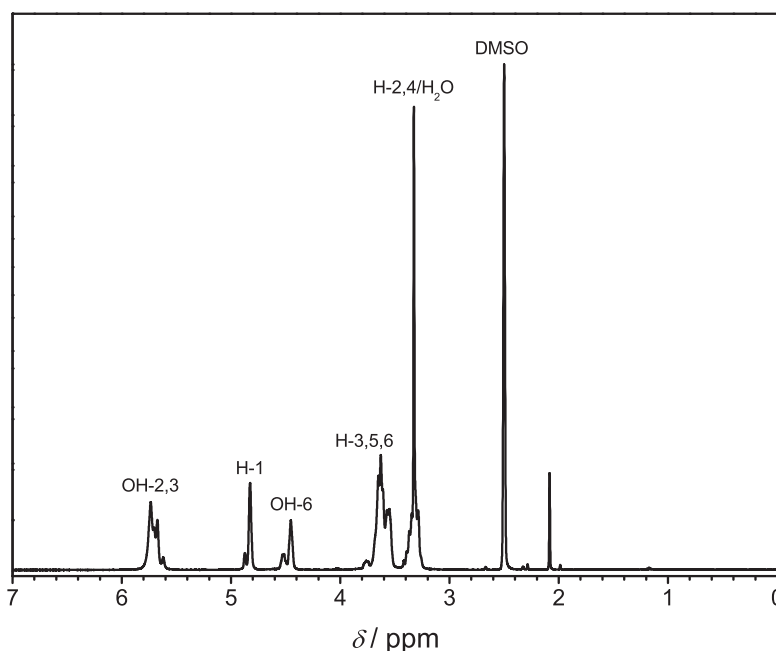
RAFT Polymerization of DMAa with Alkyne-CTA-Ada

Alkyne-CTA-Ada (124.2 mg, 0.22 mmol, 1 equiv.), AIBN (7.4 mg, 0.045 mmol, 0.2 equiv.), DMAa (2 g, 20.18 mmol, 90 equiv.), and DMF (20 mL) were added into a Schlenk tube. After three freeze-pump-thaw cycles, the tube was backfilled with argon and placed into an oil bath for 4 h at 60 °C. The polymerization was stopped by cooling the reaction mixture in liquid nitrogen and opening the tube to the atmosphere. The solution was dialyzed against deionized water with a SpectraPor3 membrane (MWCO = 1000 Da) for three days at ambient temperature. The solvent was removed *in vacuo* at a freeze-drier to yield the polymer Alkyne-PDMAa-Ada as a yellow solid (806.5 mg, 0.073 mmol). SEC (DMAC, RI): $M_{\mathrm{n,SEC}} = 11\,000\,\mathrm{g\,mol^{-1}}$, $M_{\mathrm{m,SEC}} = 13\,100\,\mathrm{g\,mol^{-1}}$, $Đ = 1.19$. The NMR number-average molar mass ($M_{\mathrm{n,NMR}}$) was calculated from the integrals of the resonances at 2.27 - 2.75 ppm and 4.67 - 4.74 ppm. $M_{\mathrm{n,NMR}} = 16\,900\,\mathrm{g\,mol^{-1}}$.

Synthesis of the β-CD-PDMAa-Ada α,ω-functional Polymer

For the following end group conversion, β-CD-N$_3$ was synthesized according to a literature procedure.[216] See Figure 3.21 for the ^{1}H NMR spectrum and the ESI-MS data in the corresponding caption.

In a flame-dried Schlenk tube, Alkyne-PDMAa-Ada (50 mg, 0.0046 mmol, 1 equiv.), β-CD-N$_3$ (26.34 mg, 0.023 mmol, 5 equiv.) and DIPEA (0.8 µL, 0.0046 mmol, 1 equiv.) were dissolved in DMF (2 mL). The mixture was degassed by three consecutive freeze-pump-thaw cycles, before copper(I) iodide (0.87 mg, 0.0046 mmol, 1 equiv.) was added. Subsequently, two freeze-pump-thaw cycles were performed, the tube backfilled with argon and the mixtures stirred at ambient temperature for 24 h. EDTA-solution (5 wt.% in water, 1 mL) was added and the residue was dialyzed against deionized water with a

Figure 3.21 Normalized ^{1}H NMR spectrum (400 MHz, DMSO$-d_6$) of the employed β-CD-azide at 25 °C. ESI-MS: $[M + Na^+]_{exp} = 1182.42$ and $[M + Na^+]_{calc} = 1182.37$. Reused from Reference [208] by permission of The Royal Society of Chemistry.

SpectraPor3 membrane (MWCO = 2000 Da) for 3 days at ambient temperature. The solvent was removed *in vacuo* at a freeze-drier to yield the polymer β-CD-PDMAa-Ada as a white solid (26.4 mg, 0.0023 mmol). SEC (DMAC, RI): $M_{n,SEC} = 11\,600\,\mathrm{g\,mol^{-1}}$, $M_{m,SEC} = 14\,000\,\mathrm{g\,mol^{-1}}$, $Đ = 1.20$.

3.4.3 Synthesis of the Single-Chain Structures

Synthesis of the Single-Chain Metal Complexes (SCMC1, SCMC2)

In a flame-dried schlenk flask, equipped with a dropping funnel and a stirring bar, $[Pd(COD)Cl_2]$ (1 equiv.) was dissolved in dry dichloromethane (50 mL). To this mixture, a solution of the macroligand (100 mg, 1 equiv.) in dry dichloromethane (50 mL) was added over the course of 5 h. Subsequently, the reaction mixture was left to stir over night. To afford the single-chain metal complexes, the mixture was concentrated under reduced pressure and then precipitated into cold methanol (80 mL). The precipitate was filtered off and dried under high vacuum, yielding the SCMC as a pale yellow powder. ^{1}H NMR (400 MHz, CDCl$_3$, 25 °C): δ/ppm = 8.06 - 7.30 (m, 28H, Ar*H* of PPh$_2$), 7.29 - 6.22 (m, Ar*H* of PS), 5.49 - 5.21 (m, 4H, C*H*$_2$-Triazole), 5.18 - 4.82 (m, 2H, C*H*-Triazole),

Table 3.5 SEC (THF, RI) data for the ARGET ATRP polymers [Br-PS-Br]1 and [Br-PS-Br]2, the macroligands ML1 and ML2 and the corresponding single-chain metal complexes SCMC1 and SCMC2.

Species	$M_n/\mathrm{g\,mol^{-1}}$	$M_m/\mathrm{g\,mol^{-1}}$	Đ
[Br-PS-Br]1	5900	6300	1.07
ML1	6600	7000	1.07
SCMC1	5600	6000	1.07
[Br-PS-Br]2	12000	12700	1.06
ML2	12800	13500	1.06
SCMC2	10300	11000	1.08

3.55 - 2.94 (m, 4H, 2 × CH_2 of initiator), 2.78 - 1.16 (m, aliphatic protons of PS). ^{31}P{^{1}H} NMR (160 MHz, CDCl$_3$, 25 °C): δ/ppm = 28.32 (s, 2P, P=O), 23.53 (s, 2P, PPh$_2$). SEC (THF, RI): Refer to Table 3.5.
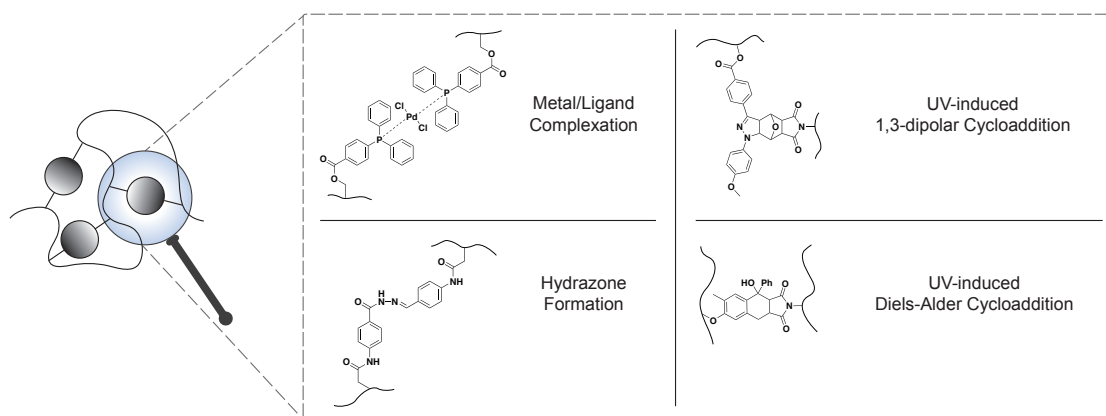
4 | The Repeating Unit Approach

Applying the repeating unit approach allows endowing a single polymer chain with a compacted structure, resulting in so-called single-chain nanoparticles (SCNPs). The synthesis of SCNPs constitute the majority of contributions to the field of single-chain technology. The following chapter investigates new mild and effective crosslinking methodologies for the straight forward synthesis of application oriented SCNPs.

Based on the established concept in Section 3.1, it will be investigated if the collapse of single polymer chains by metal-ion complexation can lead to catalytically active SCNPs. In addition, two photochemical processes will be evaluated as tools for the efficient synthesis of well-defined, functional SCNPs. The last section will address the synthesis of water-soluble, stimulus-responsive SCNPs with potential applicability in drug delivery systems. A summary of the employed crosslinking methodologies is presented in Scheme 4.1.
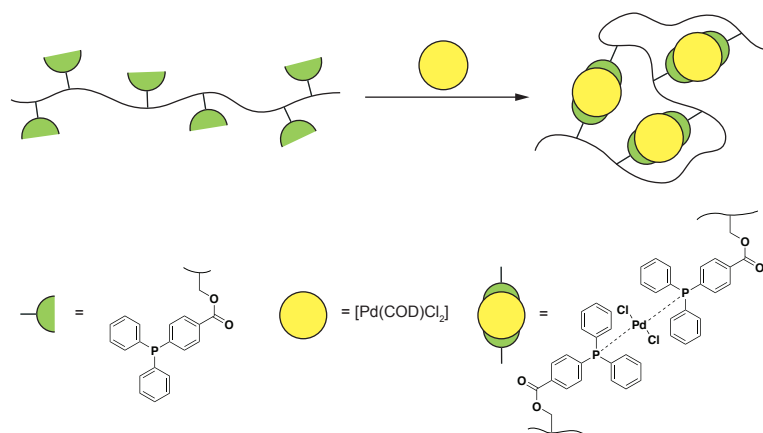

Scheme 4.1 Illustrative summary of the repeating unit approach strategies that are investigated in the current chapter.
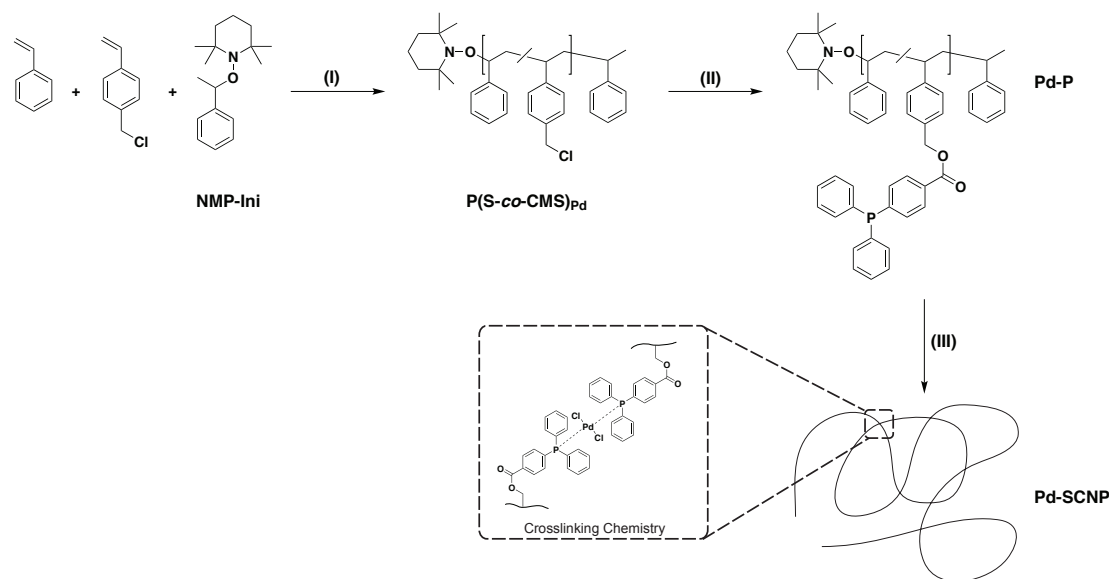
4.1 Metal Complexation Driven Formation of Single-Chain Nanoparticles

Inspired by enzymes, which act as highly efficient catalysts in nature, the current section will explore the efficient synthesis of metal-ion containing single-chain nanoparticles for the application in homogeneous catalysis. Since Section 3.1 already studied the selective point folding by metal complexation, the established concept can be transferred to the preparation of palladium(II) containing single-chain nanoparticles (Pd-SCNPs) in the current section (see Scheme 4.2).[‡] The presented procedure to synthesize SCNPs entails the advantage that the crosslinking process directly incorporates the catalytically active sites $(Pd(PPh_2Ar)_2Cl_2)$ within the Pd-SCNP structure. The palladium(II) containing single-chain nanoparticles were characterized in-depth using ^1H NMR spectroscopy, $^{31}P\{^1H\}$ NMR spectroscopy, dynamic light scattering (DLS), size exclusion chromatography (SEC), ^1H spin-spin relaxation time (T_2) analysis, X-ray photoelectron spectroscopy (XPS), and log-normal distribution (LND) simulations. Finally, the applicability of the Pd-SCNPs as catalyst in the Sonogashira coupling was exemplified.

Scheme 4.2 Illustration of the Pd-SCNP formation *via* the intramolecular crosslinking of functional, linear precursor copolymers by metal-ligand complexation in diluted solution (schematic view, in which a *trans*-configuration of the Pd-atoms is suggested, see text).
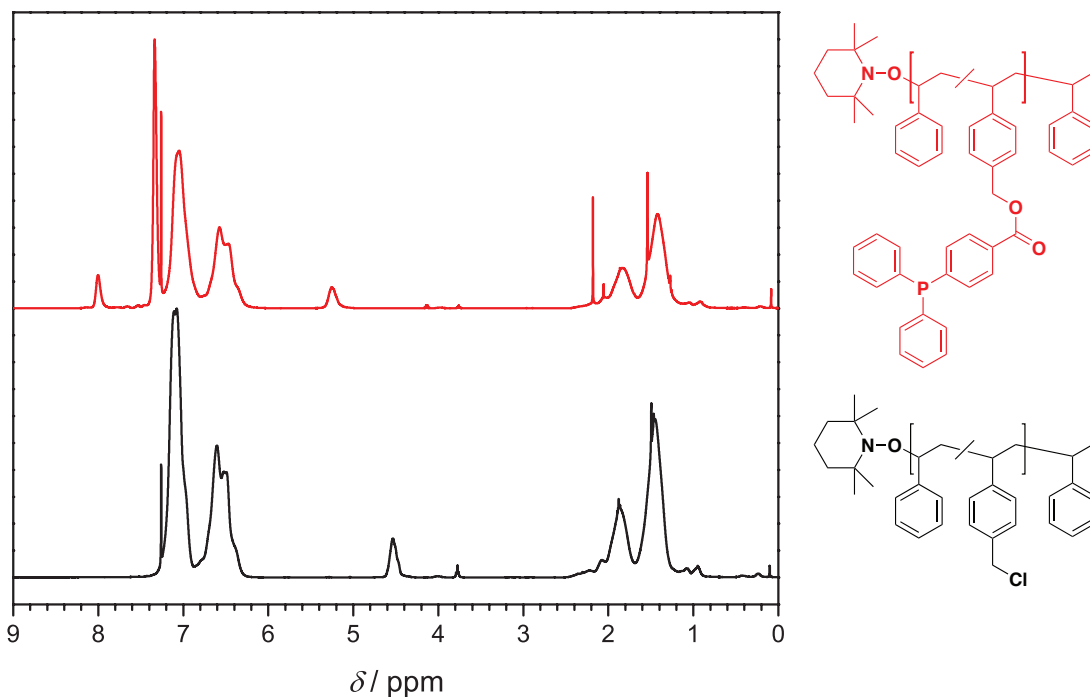
Scheme 4.3 Synthetic strategy for the preparation of palladium(II) crosslinked single-chain nanoparticles (Pd-SCNPs). (I) bulk, 125 °C, 5 h; (II) 4-(diphenylphosphino)benzoic acid, K_2CO_3, DMF (dry), 50 °C, 16 h; (III) Pd(COD)Cl$_2$, DCM (dry), a.t., 21 h (the crosslinking chemistry presents a schematic view, in which a *trans*-configuration of the Pd-atoms is suggested, see text). Adapted from Reference [217] - Published by The Royal Society of Chemistry.

Synthesis of the Linear Precursor Polymer

In a facile three step synthesis, the functional linear precursor polymers were initially generated in a random copolymerization of styrene and 4-chloromethylstyrene by nitroxide mediated polymerization (NMP), and subsequently post-modified with 4-(diphenylphosphino)-benzoic acid (see Scheme 4.3).

The random copolymerization of styrene and 4-chloromethyl styrene was conducted using a feed ratio of 9:1. The resultant styrene-*co*-chloromethylstyrene polymer P(S-*co*-CMS)$_{Pd}$ exhibits a narrow molecular weight distribution with a dispersity of $Đ = 1.17$ and a number-weighted molar mass of $M_{n,SEC} = 10\,200\,\mathrm{g\,mol^{-1}}$ according to SEC (THF, RI). The ^{1}H NMR spectrum shows the aromatic as well as the aliphatic signals for the polystyrene backbone. In addition, a broad resonance between 4.39 and 4.65 ppm can be assigned to the methylene bridge of the CMS units (see Figure 4.1).

The copolymer composition of P(S-*co*-CMS)$_{Pd}$ was calculated by utilizing the integral values for the proton resonances at 6.22 - 7.28 ppm (aromatic protons) and the resonance close to 4.51 ppm (CH$_2$Cl) (see Figure 4.1). A value of 12 % CMS units was calculated, which closely resembles the copolymerization feed ratio. The molar number
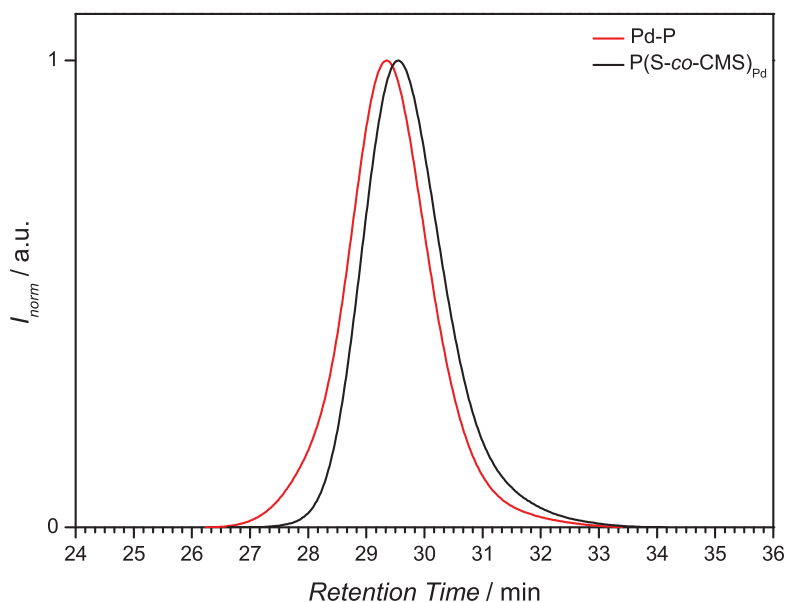
Figure 4.1 ^{1}H NMR spectra (400 MHz, CDCl$_3$) at 25 °C of the poly(styrene-*co*-chloromethylstyrene) copolymer P(S-*co*-CMS)$_{Pd}$ (bottom) and the functional, linear precursor Pd-P (top). Reused from Reference [217] - Published by The Royal Society of Chemistry.

of triphenylphosphine ligands n(L) in a given amount m of the functionalized, linear precursor polymer was calculated from Equation 4.1, where M(L) = 422.5 g mol^{-1} and M(S) = 104.2 g mol^{-1} are the molecular weights of the triarylphosphin repeating unit and the styrene repeating unit, respectively.

$$n(L) = \%L\frac{m}{\%LM(\text{L}) + (1 - \%L)M(\text{S})} \tag{4.1}$$

In order to attach the ligand moieties onto the linear precursor polymer, P(S-*co*-CMS)$_{Pd}$ was treated with a slight excess of 4-(diphenylphosphino) benzoic acid per CMS unit in the presence of the base K$_2$CO$_3$. In a simple substitution reaction, the triarylphosphine ligands were grafted onto the polymer backbone *via* an ester bond. The shift of the methylene bridge resonance from 4.54 ppm to 5.25 ppm in the ^{1}H NMR spectrum of Pd-P evidences full conversion of the CMS to ligand units (see Figure 4.1). New resonances found in the range of 7.19 and 7.99 ppm can be assigned to the aromatic protons of the triarylphosphine moiety. The ^{31}P{^{1}H} NMR spectrum of Pd-P shows a single resonance at -5.06 ppm, representing trivalent uncoordinated triarylphosphine. An additional indication for the

Figure 4.2 Normalized SEC traces (THF, RI) of the poly(styrene-*co*-chloromethylstyrene) copolymer P(S-*co*-CMS)$_{\text{Pd}}$ (black) and the functional linear precursor Pd-P (red). Adapted from Reference [217] - Published by The Royal Society of Chemistry.

successful transformation is the increase in molar mass of Pd-P to $M_{\text{n,SEC}} = 12\,300\,\text{g\,mol}^{-1}$ according to SEC (see Figure 4.2). The above described design strategy represents a universal approach for the facile introduction of functional groups into the precursor structure.

Preparation of the Palladium(II) Crosslinked SCNPs

The palladium(II) crosslinked single-chain nanoparticles (Pd-SCNPs) were prepared by intramolecularly crosslinking the linear precursor polymer Pd-P in diluted solution with a suitable palladium(II) source (see Scheme 4.3). Dichloro(1,5-cyclooctadiene)palladium(II) ([Pd(COD)Cl$_2$]) has proven to be an ideal candidate, since the COD ligand is an outstanding leaving group in the ligand exchange reaction with the triarylphosphine moieties along the polymer. Intermolecular reactions always pose a problem during the preparation of SCNPs, since they lead to multi-chain aggregates. To circumvent such by-products, highly diluted conditions need to be applied. Feeding the polymer precursor into the Pd(II)-solution overcomes the need for dilute conditions as long as the feeding rate is rate determining. A solution of the precursor polymer Pd-P ($c_{\text{Pd-P}} = 0.2\,\text{mmol\,mL}^{-1}$) was added dropwise ($1\,\text{mL\,h}^{-1}$) to a solution of [Pd(COD)Cl$_2$] *via* a syringe pump. The

Figure 4.3 SEC and DLS results of the Pd-SCNP formation. (A) Normalized SEC traces (DMAc, RI) of the linear precursor polymer Pd-P (solid line) and the Pd-SCNP (dashed line). (B) Number-averaged size distributions of the linear precursor Pd-P (solid line) and the Pd-SCNP (dashed line) in THF ($c = 4\,\mathrm{mg\,mL^{-1}}$) at 25 °C. Adapted from Reference [217] - Published by The Royal Society of Chemistry.

ratio of Pd(II)-crosslinker to ligand moieties along the polymer chain was chosen to be 1:2 to achieve the highest amount of crosslinking. During the intermolecular crosslinking of single polymer chains, the hydrodynamic volume decreases due to the transition from a random coil to a more compact structure. The change in hydrodynamic volume can readily be observed and quantified *via* size exclusion chromatography. The decreased hydrodynamic volume leads to a shift of the SEC trace to longer retention times (see Figure 4.3A), expressed in peak molar masses the shift is $\Delta M_{\mathrm{p}} = 3850\,\mathrm{g\,mol^{-1}}$, which equals a molecular weight change of $\sim$21 %. The actual hydrodynamic diameter of the Pd-SCNP can be determined by dynamic light scattering and has a value of $D_{\mathrm{h}} = 5.4\,\mathrm{nm}$. Compared with the linear precursor Pd-P ($D_{\mathrm{h}} = 8.8\,\mathrm{nm}$), the difference is $\Delta D_{\mathrm{h}} = 3.3\,\mathrm{nm}$ (see Figure 4.3B), which equals a change of $\sim$37 %.

Chemical evidence for the crosslinking reaction was obtained from ^{1}H and ^{31}P$\{^{1}$H$\}$ NMR spectroscopy. Upon complexation by Pd(II)-ions, the proton resonances of the triarylphosphine functional groups are shifted to a lower field (see Figure 4.4A). The resonance for the phosphorus atom of the free ligand at δ = -5.06 ppm shifts downfield to δ = 23.54 ppm upon coordination to the metal atom (see Figure 4.4B). A complete shift of the phosphorus resonance indicates – within the boundaries of ^{31}P$\{^{1}$H$\}$ NMR spectroscopy – a quantitative coordination of the free ligands to the metal atoms. As additional evidence for the correct interpretation of the NMR data, some metal complexes were
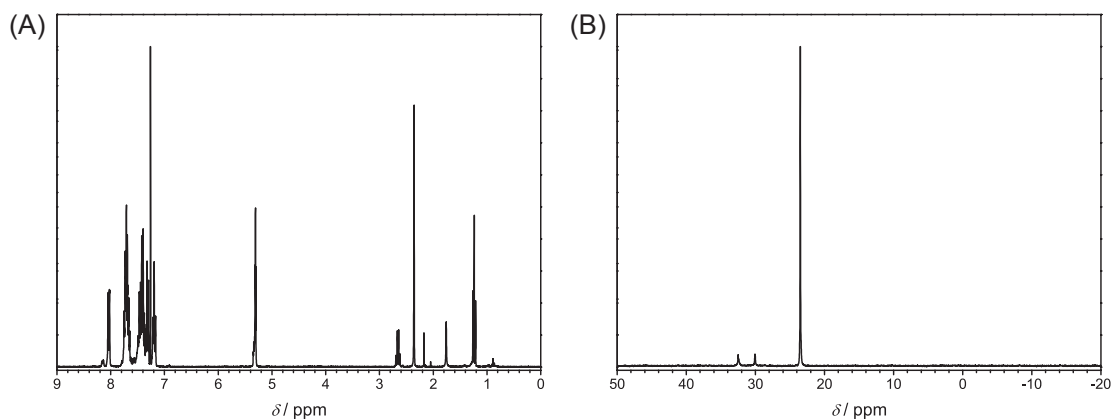
Figure 4.4 Intramolecular crosslinking by metal-ligand complexation monitored by ^{1}H NMR (A) and ^{31}P{^{1}H} NMR spectroscopy (B) in CDCl₃ at 25 °C. The complete shift of the proton and phosphorus resonances indicates quantitative complexation (the crosslinking chemistry presents a schematic view, in which a *trans*-configuration of the Pd-atoms is suggested, see text). Adapted from Reference [217] - Published by The Royal Society of Chemistry.

synthesized as model compounds for Pd-SCNP. As model ligands for the polymer Pd-P, 4-methylbenzyl-4-(diphenylphosphino) benzoate (L1) and 4-ethylbenzyl-4-(diphenylphosphino) benzoate (L2) were synthesized. The ^{31}P{^{1}H} NMR spectra of the complexes [Pd(L₁)₂Cl₂] and [Pd(L₂)₂Cl₂] (obtained from [Pd(COD)Cl₂] and L1 or L2) showed a chemical shift of $\delta = 23.5$ ppm, which is very similar to the shift observed for Pd-SCNP. [Pd(L₁)₂Cl₂] and [Pd(L₂)₂Cl₂] were fully characterized and the solid state structures of [Pd(L₁)₂Cl₂] and [Pd(L₂)₂Cl₂] were established by single crystal X-ray diffraction (see Figure 4.34 and 4.35). Like [Pd(PPh₃)₂Cl₂], [Pd(L₁)₂Cl₂] and [Pd(L₂)₂Cl₂] adopt a *trans*-configuration in the solid state.[205,206] Since Pd-P can form large rings upon crosslinking, a *trans*-configuration of the palladium atoms in Pd-SCNP is suggested. Since the phosphorus atoms in Pd-SCNP are not in all cases chemically equivalent due to the crosslinking, next the related ligands L1 and L2 were mixed with [Pd(COD)Cl₂] in a 1:1:1 ratio. Statistically, a 1:2:1 mixture of [Pd(L₁)₂Cl₂], [Pd(L₁)(L₂)Cl₂], and [Pd(L₂)₂Cl₂] is expected. In comparison to [Pd(L₁)₂Cl₂], a slightly broadened signal but no coupling is observed in the ^{31}P{^{1}H} NMR spectrum of the statistical mixture of [Pd(L₁)₂Cl₂], [Pd(L₁)(L₂)Cl₂], and [Pd(L₂)₂Cl₂] (see Figure 4.5). This data clearly shows that slight differences in the polymer backbone of the triarylphosphine functional group of Pd-SCNP have only a minor influence on the ^{31}P{^{1}H} NMR signals.

Additional information on the intramolecular crosslinking can be obtained from the ^{1}H spin-spin relaxation time (T_2), as T_2 is sensitive to molecular motion.[114] T_2 decay curves for the resonance of the methylene bridge (~ 5.25 ppm) in Pd-P and Pd-SCNP

Figure 4.5 ^{1}H NMR (A) and ^{31}P$\{^1$H$\}$ NMR (B) spectra of a statistical mixture of [Pd(L$_1$)$_2$Cl$_2$], [Pd(L$_1$)(L$_2$)Cl$_2$], and [Pd(L$_2$)$_2$Cl$_2$] in CDCl$_3$ at 25 °C. Adapted from Reference [217] - Published by The Royal Society of Chemistry.

(see Figure 4.6) were mearsured *via* the Car-Purcel-Meiboom-Gill (CPMG) echo train acquisition in THF-d$_8$.

Figure 4.6 T_2 decay curves for the methylene bridge protons of the linear precursor polymer Pd-P (dots) and the Pd-SCNP (open dots). The red curves represent mono exponential decay functions that have been fitted to the data points. Adapted from Reference [217] - Published by The Royal Society of Chemistry.

Since the intramolecular crosslinking reduces the mobility of the chain-segments, T_2 should decrease in Pd-SCNP compared to Pd-P. Analysis of the decay curves *via* a mono exponential decay function reveals $T_2 = 147$ ms for Pd-P (see Figure 4.7) and $T_2 = 70$ ms for Pd-SCNP (see Figure 4.8). These results clearly show the transformation from a

Figure 4.7 T_2 decay curve for the protons of the methylene bridge in the linear precursor Pd-P. Adapted from Reference [217] - Published by The Royal Society of Chemistry.

Figure 4.8 T_2 decay curve for the protons of the methylene bridge in the palladium(II) crosslinked single-chain nanoparticle. Adapted from Reference [217] - Published by The Royal Society of Chemistry.

random coil to a compacted, crosslinked structure. Furthermore, the transition from the linear precursor Pd-P to the more compacted structure in Pd-SCNP was analyzed by log-normal distribution (LND) simulations of the corresponding SEC traces. Therefore, the log-normal distribution (LND) based on a Gaussian function was used to model the experimental molecular weight distribution (MWD) before and after the intramolecular crosslinking. In particular, the weight distribution was used, since the weight of polymer before and after chain collapse does not change, whereas the number distribution will be very different.[166] The following equations for the LND simulations (see Reference [167] for more details) were employed:

$$w(M) = \frac{exp(-\frac{(ln M - ln \overline{M})^2}{2\sigma^2})}{\sqrt{M(2\pi\sigma^2)}}$$

$$\overline{M} = \sqrt{(M_n M_w)} \tag{4.2}$$

$$\sigma^2 = ln Đ$$

Equation 4.2 is the Gaussian distribution function of $w(M)$ (the weight distribution of the SEC trace), M_n is the number-average molecular weight, M_w is the weight-average molecular weight, and the dispersity $Đ = M_w/M_n$. An experimental distribution (*e.g.*, the black trace in Figure 4A) can now be fit multiple distributions, each distribution produced from Equation 4.2 with a pre-determined M_n and $Đ$. The final simulated distribution can be determined by accounting for the weight fraction of each distribution according to Equation 4.3,

$$w(M)_{final} = \sum_i w_{p,i} w(M)_i \tag{4.3}$$

where $w_{p,i}$ is the weight fraction of distribution i and $w(M)_i$ is the weight at molecular weight *M*. The SEC chromatogram for Pd-P was excellently fitted using Equations 4.2 and 4.3 above (see Figure 4.9A). To arrive at this fit, the main linear peak (Pd-P, $M_n = 17\,200\,\mathrm{g\,mol^{-1}}$, $Đ = 1.1$) consisted of a weight fraction of 0.858, a peak with a weight fraction of 0.069, corresponding to dead polymer formed through bimolecular

Table 4.1 Different distributions and their corresponding number-average molar mass (M_n), dispersity ($Đ$), and weight fractions (w_p) for the log-normal distribution (LND) simulations of Pd-P.

Distribution	$M_\mathrm{n}/\mathrm{g\,mol^{-1}}$	$Đ$	w_p
Pd-P	17200	1.1	0.858
Dead Pd-P	34400	1.1	0.069
Lower M_1	8600	1.1	0.056
Lower M_2	5730	1.2	0.017

radical termination ($M_\mathrm{n} = 34\,400\,\mathrm{g\,mol^{-1}}$, $Đ = 1.1$), and two lower molecular weight peaks with a combined weight fraction of 0.073 (see Table 4.1). Each LND distribution for the polymers in Table 4.1 is given in Figure 4.9A. After metal complexation forming the more compact Pd-SCNPs, it was determined that all the linear Pd-P and the dead polymer formed lower molecular weight species, suggesting ~100 % intramolecular coupling. There are many possibilities for the number of crosslinked products. Here, only seven different crosslinked products were used, but more species cannot be ruled out (see Table 4.2). The fit using the LND model was again excellent (see Figure 4.9B). The information suggests especially for the low molecular weight species that the change in hydrodynamic volume (HDV) can be as low as 0.2 that of the molecular weight of linear Pd-P. This low HDV suggests a very compact nature, which most probably consists of a single polymer chain.
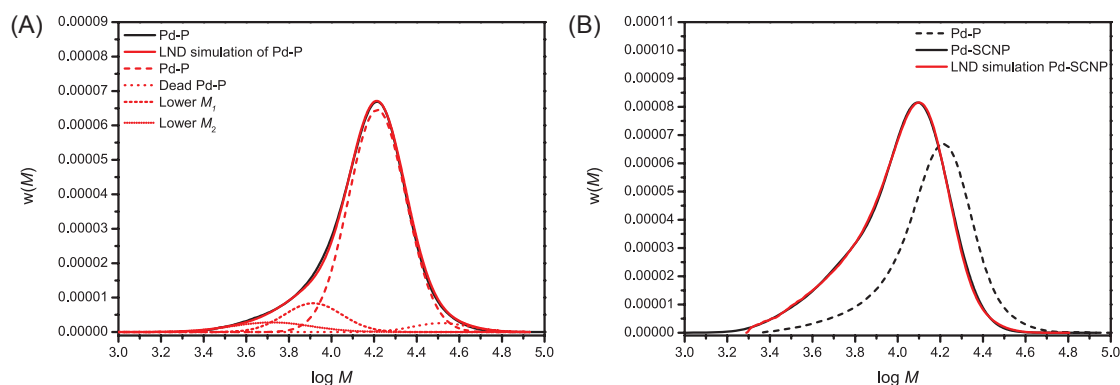
Figure 4.9 Experimental SEC (DMAc, RI) data and corresponding log-normal distribution (LND) simulations. (A) Black trace: experimental Pd-P, red trace: LND fit of Pd-P using 4 distributions, namely Pd-P (red dashed), dead Pd-P (red dotted), lower M_1 (red short dashed), and lower M_2 (red short dotted). (B) Black trace: experimental Pd-SCNP, red trace: LND fit of Pd-SCNP using 7 distributions, black dashed trace: experimental Pd-P for comparison. Adapted from Reference [217] - Published by The Royal Society of Chemistry.

Table 4.2 Different distributions and their corresponding number-average molar mass (M_n), dispersity ($Đ$), and weight fractions (w_p) for the log-normal distribution (LND) simulations of Pd-SCNP.

Distribution	$M_n/\mathrm{g\,mol}^{-1}$	$Đ$	w_p
Pd-P	17200	1.1	0
Dead Pd-P	34400	1.1	0
Lower M_1	8600	1.1	0
Lower M_2	5730	1.2	0
Pd-SCNP 1	3440	1.1	0.015
Pd-SCNP 2	5160	1.1	0.024
Pd-SCNP 3	6880	1.1	0.101
Pd-SCNP 4	12212	1.1	0.385
Pd-SCNP 5	13416	1.1	0.179
Pd-SCNP 6	14964	1.1	0.083
Pd-SCNP 7	15480	1.1	0.213

In order to determine the nature of the Pd-complexes of the SCNPs, Pd-P, Pd-SCNP and the model complex [Pd(PPh$_3$)$_2$Cl$_2$] were subjected to X-ray photoelectron spectroscopy (XPS) analysis. The spectrum of Pd-P exhibits a peak at 131.1 eV, which is attributed to the triarylphosphine ligand. The signal amounts to 1.1 atomic% (2.7 wt%, 0.0009 mmol mg^{-1}), agreeing perfectly with the ^{1}H NMR estimations (0.0008 mmol mg^{-1}). The obtained XPS data of all metal containing samples ([Pd(PPh$_3$)$_2$Cl$_2$], and Pd-SCNP) was not fully conclusive. Some decomposition of the metal complexes during the XPS process is anticipated, since besides the expected Pd signal (at 338.2 eV) a second Pd-species with a binding energy of 336.4 eV was observed (see Fig.4.10). However, the XPS-spectrum of Pd-SCNP shows signals at 131.6 eV, 198.3 eV and 338.2 eV, which are assigned to the phosphorus, chlorine and palladium species, respectively. The peak areas correspond to 0.6 atomic% for phosphorus and chlorine and to 0.3 atomic% for palladium. The ratio P:Cl:Pd of 2:2:1 thus matches the proposed structure of the Pd-complexes in the Pd-SCNPs. In addition, the binding energy of the main Pd-species in Pd-SCNP (see Figure 4.10) and of chlorine and phosphorus (not shown here) are in excellent accordance with the measured binding energy in Pd(PPh$_3$)$_2$Cl$_2$. Furthermore, the found binding energies are comparable with literature values for PdCl$_2$.[218,219]

In order to ascertain the true number of Pd-centers in Pd-SCNP, additional NMR experiments were performed. For [Pd(PPh$_3$)$_2$Cl$_2$] and Pd-SCNP ^{31}P{^{1}H} NMR samples with an inlet containing an internal standard were prepared. [Pd(PPh$_3$)$_2$Cl$_2$] was chosen as
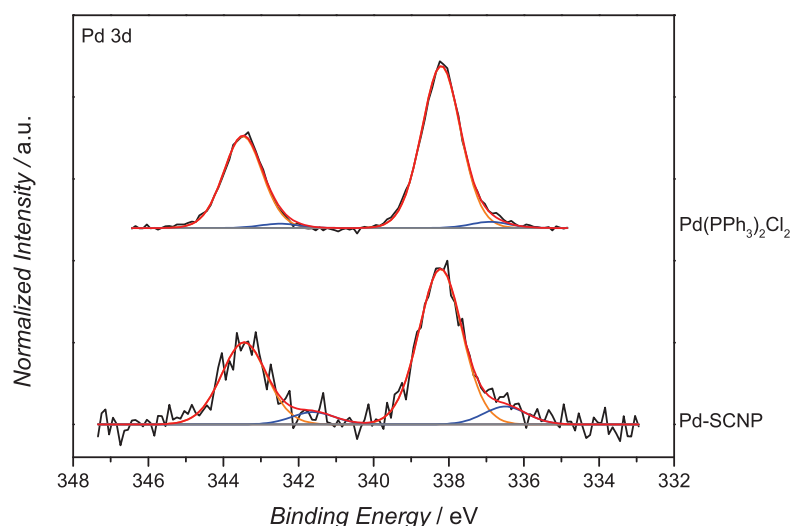
Figure 4.10 Pd 3d XPS spectra of Pd-SCNP (bottom) and [Pd(PPh$_3$)$_2$Cl$_2$] (top). The comparison of the prepared SCNPs with the model complex shows that the binding energy of the main Pd-species at 338.2 eV in Pd-SCNP is in excellent agreement with the binding energy in [Pd(PPh$_3$)$_2$Cl$_2$]. Adapted from Reference [217] - Published by The Royal Society of Chemistry.

the internal standard for Pd-P, whereas PPh$_3$ was chosen for Pd-SCNP. By utilizing inlets, it was assured that the internal standards do not chemically interfere with the samples measured. These experiments delivered phosphorus contents of 0.0009 mmol mg^{-1} for Pd-SCNP and 0.0011 mmol mg^{-1} for Pd-P. The determined values are in good agreement with the estimates from the ^{1}H NMR spectra.

As a proof of principle, the Pd-SCNPs were utilized as a novel type of catalyst for the Sonogashira coupling of terminal alkynes and aryl halides. In an exemplary reaction, 2-bromopyridine and phenylacetylene were coupled in diethylamine, employing CuI as co-catalyst. The coupling reaction was performed at two ratios of substrate to catalyst. It was observed that an increase in the amount of catalyst improved the yield of the reaction under otherwise identical conditions. To benchmark the Pd-SCNPs against a well-known system, the same coupling reaction was also conducted with the model complex [Pd(PPh$_3$)$_2$Cl$_2$], this time keeping the substrate to catalyst ratio constant. Under these same conditions the model complex delivered a higher conversion of about 75 % (see Table 4.3).

Further studies are required to gain a better understanding of the differences in conversion during the catalysis, since here only preliminary model reactions were performed. It might be assumed, however, that the accessibility of the catalytic sites for the substrates is

Table 4.3 Substrate to catalyst ratios and conversions after 24 h of the Pd-SCNP catalyzed Sonogashira coupling reactions of 2-bromopyridine and phenylacetylene.

Reaction	Catalyst	Substrate to Catalyst Ratio	Conversion
1	5 mg Pd-SCNP	2222 : 1	26 %
2	10 mg Pd-SCNP	1111 : 1	45 %
3	3.2 mg [Pd(PPh$_3$)$_2$Cl$_2$]	1111 : 1	75 %

better in [Pd(PPh$_3$)$_2$Cl$_2$] than in Pd-SCNP, which as a consequence could lead to the lower activity. A major advantage that catalytically active M-SCNPs might bring in the future is the facile seperation of the catalyst from the reaction by simple precipitation of the M-SCNPs. Thus, the M-SCNPs may be able to combine the advantages of homogeneous and heterogeneous catalysis. Unfortunately, initial trials with the herein presented Pd-SCNPs were not successful in this regard. Although a polymeric species could be precipitated, SEC and NMR analysis of the precipitate indicated that only the linear precursor with oxidized phosphine ligands was recovered. These findings led to the assumption that the Pd-SCNPs unfold during the course of the catalysis and the ligand moieties are oxidized in the presence of the Cu(I) species during the workup, which prevents the SCNPs from forming again. The unfolding of the SCNPs may be inhibited by employing a secondary crosslinking strategy to lock the SCNP structure in place, or by refining the reaction conditions for the Sonogashira coupling, *e.g.*, a copper-free variant.[220]

4.2 Photoinduced Formation of Single-Chain Nanoparticles *via* NITEC Crosslinking

Applying photochemical processes for the intramolecular crosslinking of single polymer chains allows for the efficient synthesis of SCNPs under mild reaction conditions. The following section thus reports the facile ambient temperature generation of size tunable and well-defined (pro)fluorescent single-chain nanoparticles (SCNPs) *via* the photo-induced nitrile imine-mediated intramolecular crossligation of linear precursor polymers, constituting a platform technology as potential new transporting agents (see Scheme 4.4).[§] The (pro)fluorescent single-chain nanoparticles were in-depth characterized by ^{1}H NMR spectroscopy, dynamic light scattering (DLS), size exclusion chromatography (SEC), and atomic force microscopy (AFM), as well as UV/vis and fluorescence spectroscopy. As a proof of principle, the functionalization ability of the (pro)fluorescent SCNPs is demonstrated by tethering the SCNPs to maleimide-functional microspheres *via* remaining tetrazole moieties.
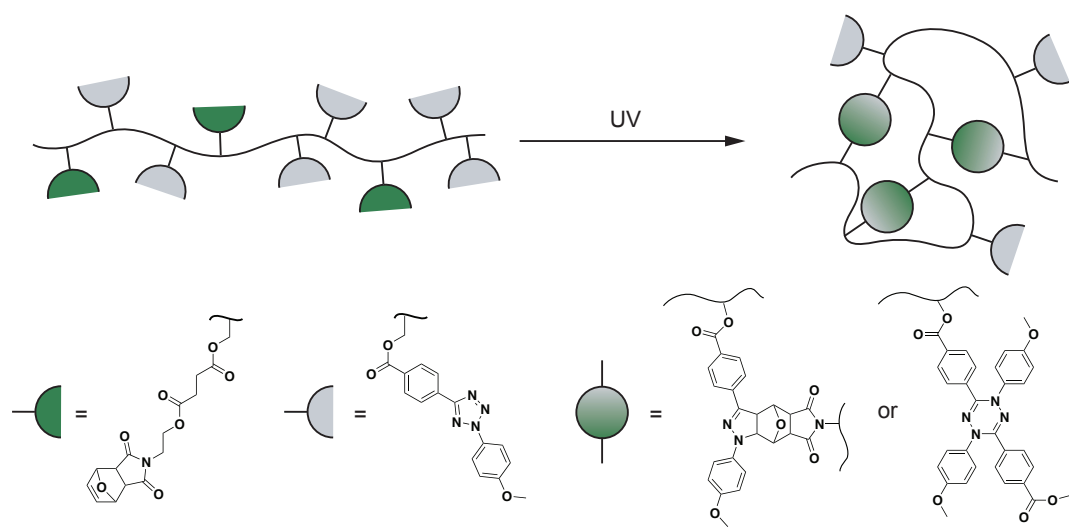
Scheme 4.4 Design strategy for the photochemical preparation of functional, (pro)fluorescent single-chain nanoparticles.

Synthesis of the Linear Precursor Polymers

The synthesis strategy for the (pro)fluorescent SCNP generation is depicted in Scheme 4.5. The functional linear precursor polymers NITEC-P1 - NITEC-P3 for the single-chain nanoparticle formation were prepared *via* postpolymerization modification of a random poly(styrene-*co*-chloromethylstyrene) copolymer (P(S-*co*-CMS)$_{\text{NITEC}}$, see Scheme 4.5A). The copolymer was synthesized by NMP of styrene and 4-(chloromethyl)styrene with 2,2,6,6-tetramethyl-1-(1-phenylethoxy)piperidine (NMP-Ini, Scheme 4.5A) as the initiator at 125 °C and was subsequently characterized by ^{1}H NMR spectroscopy.

The integral values for the proton resonances at 6.22 - 7.28 ppm (aromatic protons) and at 4.51 ppm (CH$_2$Cl) were utilized to determine the content of CMS in the copolymer, which was calculated to be 24 % (see Figure 4.11). In a one-pot postpolymerization modification, the lateral chlorine atoms were substituted by a protected maleimide derivative (PG-Mal-COOH, Scheme 4.5A) and a tetrazole species (Tet-COOH, Scheme 4.5A) in various ratios. The incorporated ratio was calculated with the aid of the integral values for the resonances at 4.24, 5.01, and 5.26 ppm (resonances g, h, k, and p) in the proton NMR spectra of the functionalized polymers (see Figure 4.11).
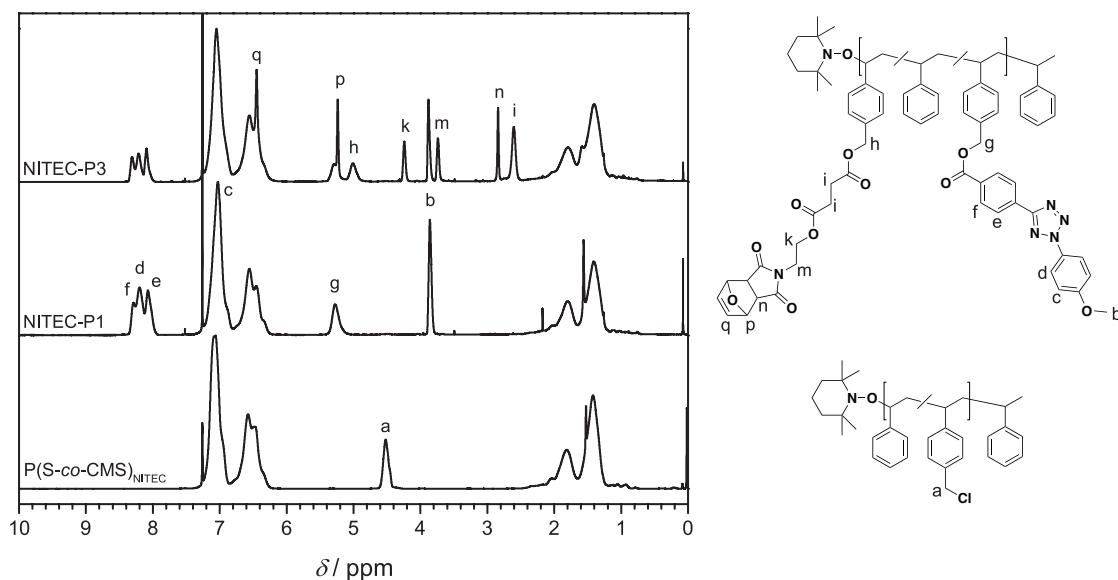
Figure 4.11 ^{1}H NMR spectra (400 MHz, CDCl$_3$) at 25 °C of P(S-*co*-CMS)$_{\text{NITEC}}$ (bottom), the functional linear precursor NITEC-P1 (100 % Tet) (middle), and the functional linear precursor NITEC-P3 (50 % Tet, 50 % PG-Mal) (top). Adapted with permission from Reference [221]. Copyright 2014 American Chemical Society.
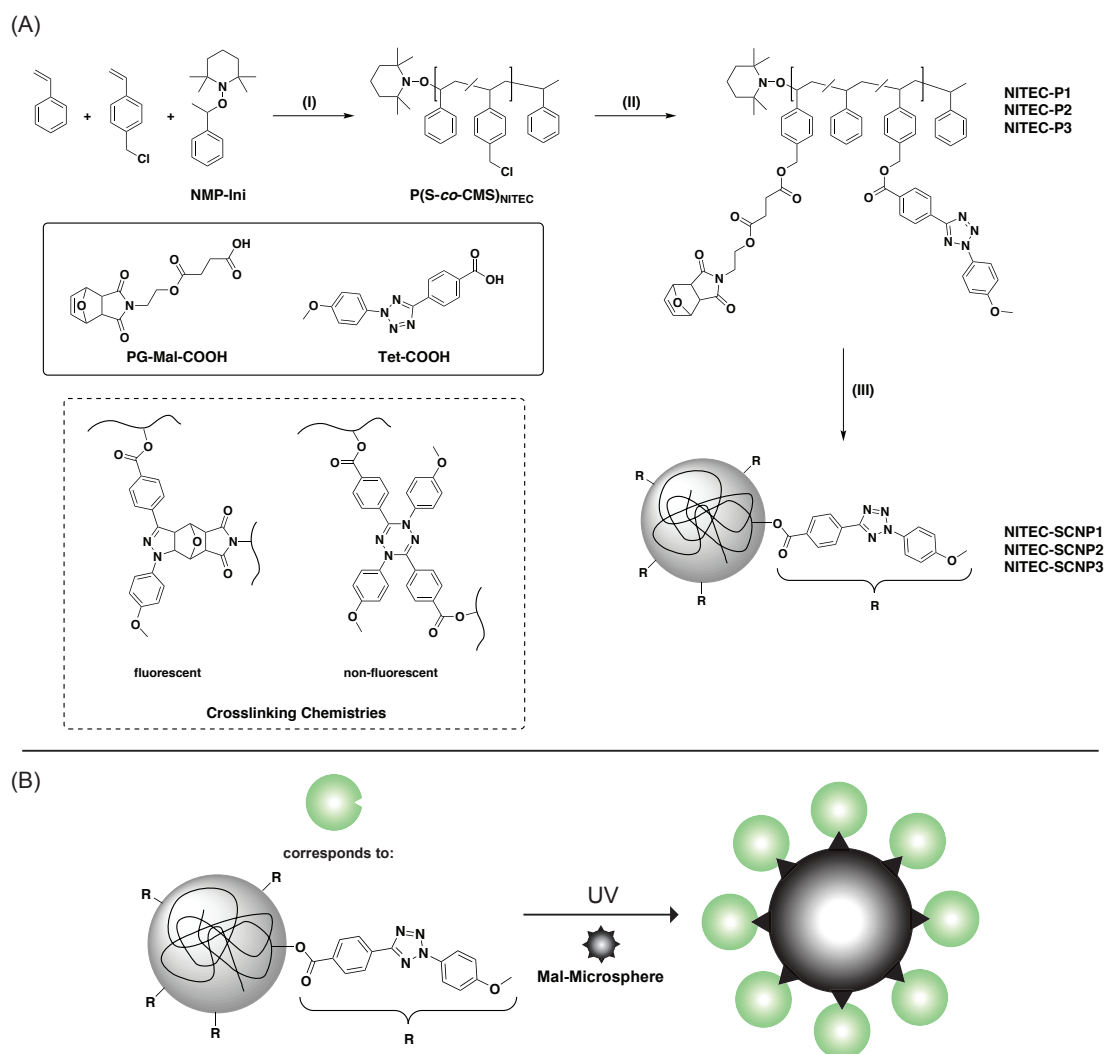
Scheme 4.5 (A) Synthetic route to the functional linear precursors NITEC-P1 - NITEC-P3 and for the preparation of the (pro)fluorescent single-chain nanoparticles NITEC-SCNP1 - NITEC-SCNP3; (I) bulk, 125 °C, 6 h; (II) PG-Mal-COOH, Tet-COOH, Cs_2CO_3, DMF, 40 °C, 2 d; (III) $h\nu$, THF. (B) Synthetic scheme for the proof of principle reaction of the profluorescent NITEC-SCNP1 with maleimide-functional microspheres (Mal-Microsphere); residual tetrazole moieties of the intramolecular crosslinking are utilized to tether NITEC-SCNP1 to the Mal-Microspheres. Adapted with permission from Reference [221]. Copyright 2014 American Chemical Society.

Table 4.4   Ratio of Tet and PG-Mal incorporation (as determined by ^{1}H NMR spectroscopy) in the linear precursors and SEC characterization data (THF, RI).

Polymer	%Tet	%PG-Mal	$M_{\text{n,SEC}}/\text{g mol}^{-1}$	$Đ$
NITEC-P1	100	0	14000	1.19
NITEC-P2	70	30	14400	1.24
NITEC-P3	50	50	14000	1.30

Table 4.5   Stoichiometries for the postpolymerization modification of P(S-*co*-CMS)$_{\text{NITEC}}$.

Polymer	Equiv. CMS	Equiv. Tet	Equiv. PG-Mal
NITEC-P1	1	1.05	0
NITEC-P2	1	0.75	0.3
NITEC-P3	1	0.55	0.5

The specific functionality ratios, as well as the SEC characterization data of the linear, functional precursor polymers NITEC-P1 - NITEC-P3 are collated in Table 4.4. A slight excess of Tet is necessary to reach the desired Tet/PG-Mal ratio and full conversion of the chlorine atoms (see Table 4.5).

Photochemical Preparation of (Pro)Fluorescent SCNPs

Contrary to common perception,[91] it was found that the electron-rich double bond of the PG-Mal moiety is still sufficiently reactive toward the nitrile imine and displays an increased performance in the intramolecular crosslinking reaction compared to the electron-deficient double bond of the deprotected maleimide. Initial attempts of the intramolecular crosslinking of the polymer to form SCNPs with the deprotected maleimide led to poorer results, mostly to intermolecular crosslinking. Thus, the procedure was altered utilizing the protected maleimide moieties for the light-induced intramolecular crosslinking reactions, which significantly reduces the synthetic effort required for the linear precursor preparation (see Scheme 4.5A). The intramolecular crosslinking of the linear precursors was carried out in highly diluted solutions ($c_{\text{precursor}} = 0.017\,\text{mg mL}^{-1}$) to afford the single-chain nanoparticles NITEC-SCNP1 - NITEC-SCNP3. Due to the fluorescent nature of NITEC-SCNP2 and NITEC-SCNP3, the kinetics of the intramolecular crosslinking process could be readily monitored by online fluorescence spectroscopy (see Figure 4.12).
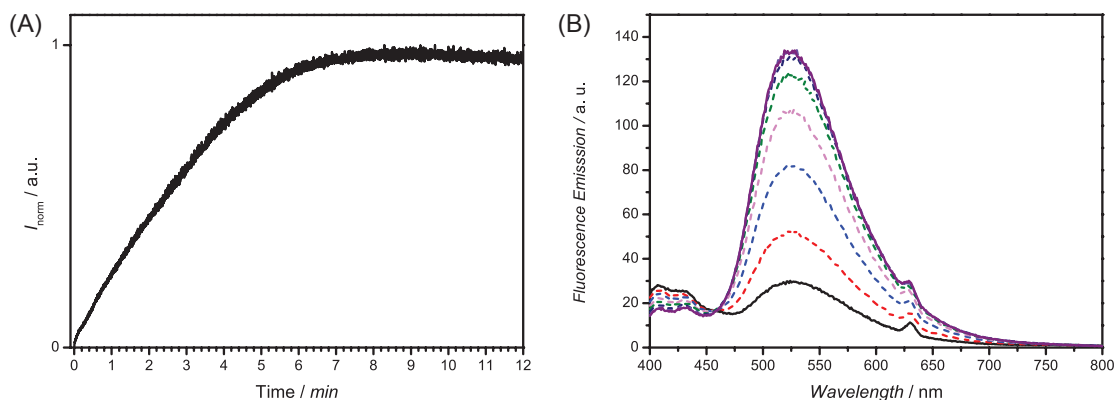
Figure 4.12 (a) Kinetic investigation of the intramolecular crosslinking of NITEC-P2 ($c_{\mathrm{precursor}} = 0.017\,\mathrm{mg\,mL^{-1}}$) in THF *via* fluorescence spectroscopy ($\lambda_{\mathrm{exc}} = 315$ nm, detection at $\lambda_{\mathrm{em}} = 535$ nm). The normalized fluorescence is plotted against time and reaches its maximum after approximately 7 min. (b) Fluorescence spectra of NITEC-SCNP2 recorded consecutively with continuous irradiation ($\lambda_{\mathrm{exc}} = 315$ nm). Adapted with permission from Reference [221]. Copyright 2014 American Chemical Society.

To achieve the best compromise between a good excitation of the photo-reactive tetrazole and the fluorescence of the resulting pyrazoline derivative, an excitation wavelength of $\lambda_{\mathrm{exc}} = 315$ nm was chosen for the irradiation of a diluted solution of NITEC-P2 in THF ($c = 0.017\,\mathrm{mg\,mL^{-1}}$). No further significant change in the fluorescence intensity occurs after 7 min, indicating that all accessible PG-Mal moieties have been consumed (see Figure 4.12). Chemical evidence for the successful intramolecular crosslinking was obtained by ^{1}H NMR spectroscopy (see Figure 4.13 for an exemplary spectrum).

The formation of the pyrazoline cycloadduct leads to a decrease in intensity of the resonances corresponding to the PG-Mal moiety (resonances a and b, Figure 4.13) and a shift of the resonances corresponding to the aromatic protons of the Tet moiety to higher field (resonances c, d, e, Figure 4.13). Additional support for the intramolecular crosslinking comes from the overall broadening of the resonances in the ^{1}H NMR spectrum. The broadening is caused by the loss of degrees of freedom during the crosslinking process.[199]

Visualization of the SCNPs can be achieved by atomic force microscopy (AFM). Therefore, the SCNPs were drop-cast onto a freshly cleaved muscovite disc from diluted dichloromethane solution and vacuum-dried. During the casting process, dewetting phenomena and evaporative self-assembly may lead to aggregation of the SCNPs.[196,197] Thus, as discussed in the introductory section on the characterization of SCNPs by AFM, it
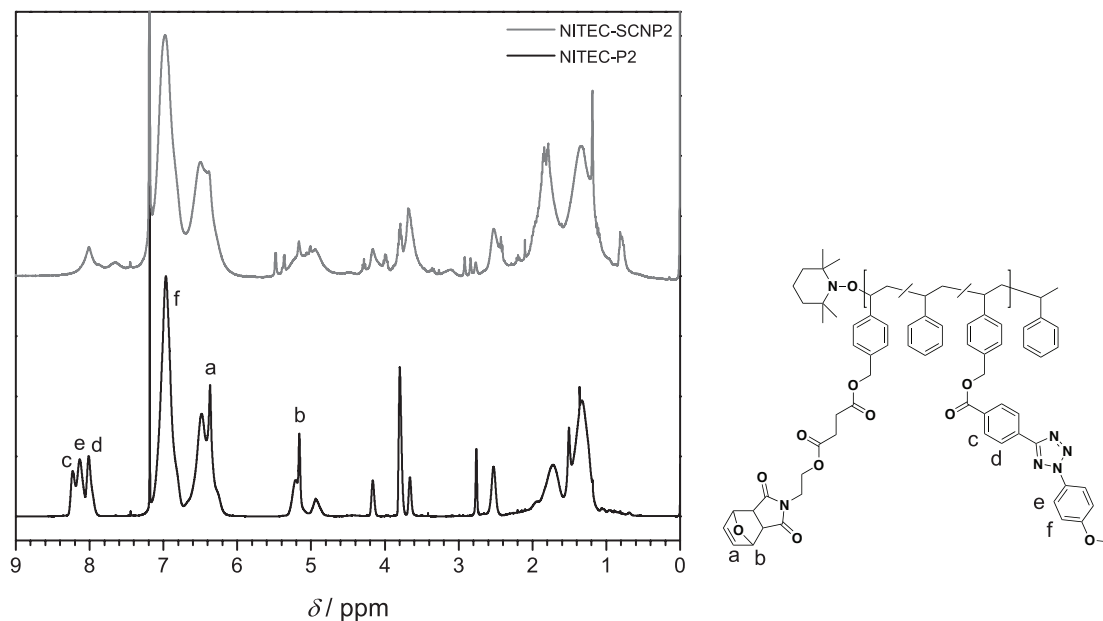
Figure 4.13 Normalized ^{1}H NMR spectra (400 MHz, CDCl$_3$) at 25 °C of NITEC-P2 (bottom) and NITEC-SCNP2 (top). Adapted with permission from Reference [221]. Copyright 2014 American Chemical Society.

should be noted that AFM can only act as a supporting analysis method and that SEC and DLS are the more reliable analytical tools.[222] Nevertheless, the particles (NITEC-SCNP2) that were exemplary analyzed by AFM may indeed be SCNPs, as their average height of 5.5 nm, which was gathered from analysis of 26 individual particles with the NanoScope Analysis 1.40 software (Bruker), is in the typical range for SCNPs.[125]
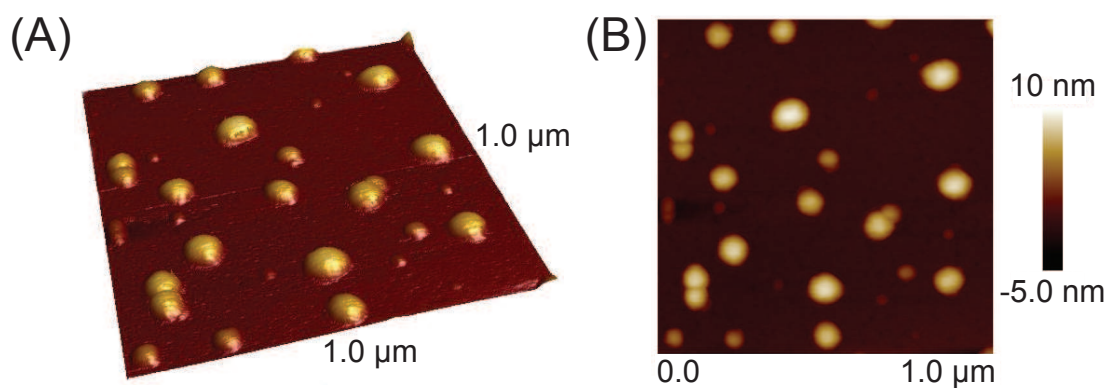
Figure 4.14 Three-dimensional (A) and two-dimensional (B) AFM topography images of NITEC-SCNP2 on freshly cleaved muscovite (scan size: 1 µm × 1 µm). Reused with permission from Reference [221]. Copyright 2014 American Chemical Society.

Table 4.6 SEC results (THF, RI) of the functional linear precursor polymers (NITEC-P) and the corresponding single-chain nanoparticles (NITEC-SCNP).

Species	M_{p}(NITEC-P)/g mol^{-1}	M_{p}(NITEC-SCNP)/g mol^{-1}	change/%
1	19500	8400	57
2	17800	11300	37
3	17000	12400	27

Table 4.7 Estimation of the hydrodynamic diameters ($D_{\mathrm{h,SEC}}$) based on the SEC data *via* Fetters' power law.

Species	$D_{\mathrm{h,SEC}}$(NITEC-P)/nm	$D_{\mathrm{h,SEC}}$(NITEC-SCNP)/nm
1	7.3	4.6
2	7.0	5.4
3	6.8	5.7

The AFM topography images depicted in Figure 4.14 display particles with a certain dispersity in size, which can be attributed to the already (limited) disperse nature of the linear precursors. Due to tip-convolution effects, the diameter determined by AFM is beset with an error, yet under the assumption of spherical particles at least the obtained height can be interpreted as an approximate estimation for the size of the SCNPs. Although it appears compelling to compare the AFM and DLS results, it is not advisable to do so, since the SCNPs are in the solid state during AFM analysis and solvated during DLS measurements.

The coil-to-particle transition taking place during the intramolecular crosslinking process can be readily evidenced by size exclusion chromatography (SEC), since the SEC columns separate the analyte according to its hydrodynamic volume. Thus, the SCNP formation manifests itself in a shift of the SEC trace to longer retention times in comparison to the linear precursor (see Figure 4.15, also Figure 4.16). Consequently, the apparent molar mass of the SCNP decreases in comparison to the parent polymer (see Table 4.6).

With increasing tetrazole content (%Tet), the shift to longer retention times becomes more pronounced, which correlates with the assumption that the intramolecular crosslinking is mainly driven by the nitrile imine dimerization. An estimation of the hydrodynamic diameter of the precursor polymers and the SCNPs can be performed by employing a power law, which was established by Fetters *et al.* (see Table 4.7).[164]
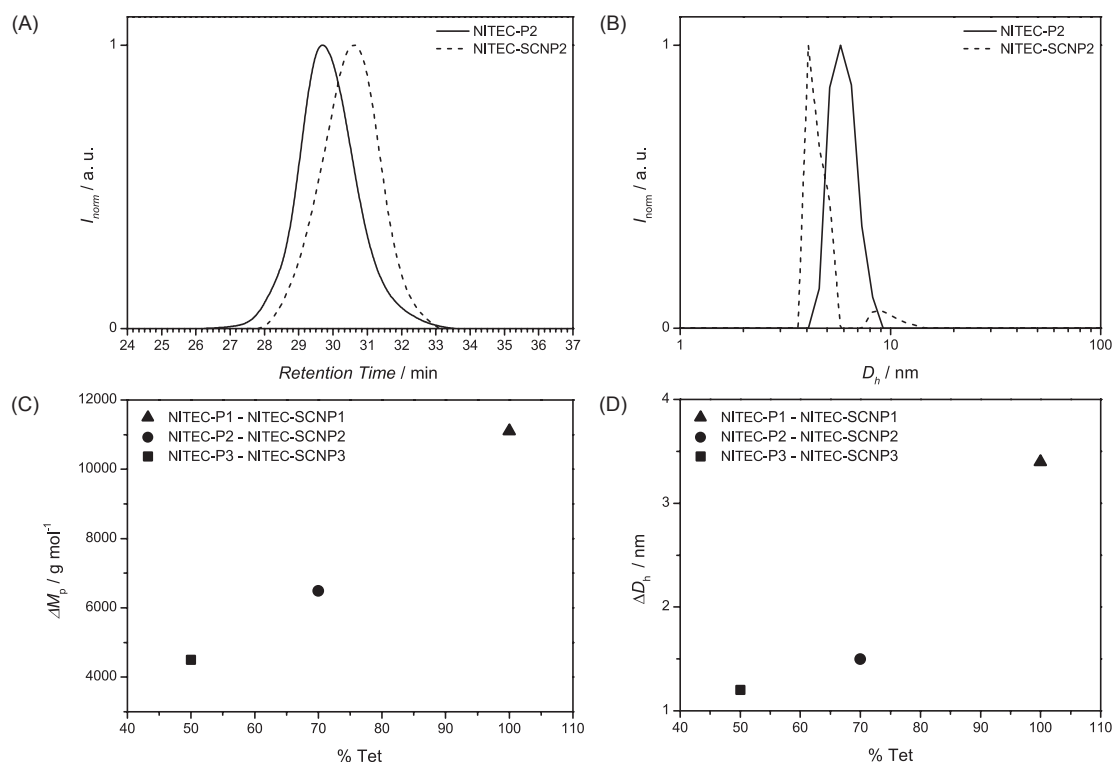
Figure 4.15 (A) Exemplary normalized SEC traces (THF, RI) of the linear precursors and single-chain nanoparticles (NITEC-P2, NITEC-SCNP2). (B) Exemplary number-weighted size distributions of the linear precursors and single-chain nanoparticles as determined by DLS (NITEC-P2, NITEC-SCNP2). (C) Change in peak molar mass (ΔM_p) after the single-chain collapse plotted against the tetrazole content (%Tet, relative to the number of initial CMS groups in the parent copolymer) of the linear precursor. (D) Change in mean hydrodynamic diameter (ΔD_h) after the single-chain collapse plotted *vs.* the tetrazole content (%Tet, relative to the number of initial CMS groups in the parent copolymer) of the linear precursor (refer to Figure 4.16 for the SEC and DLS results of the other samples). Adapted with permission from Reference [221]. Copyright 2014 American Chemical Society.

Table 4.8 DLS results of the functional linear precursor polymers (NITEC-P) and the corresponding single-chain nanoparticles (NITEC-SCNP).

Species	D_h(NITEC-P)/nm	D_h(NITEC-SCNP)/nm	collapse/%
1	6.1	3.1	49
2	6.0	4.5	25
3	7.0	5.7	19
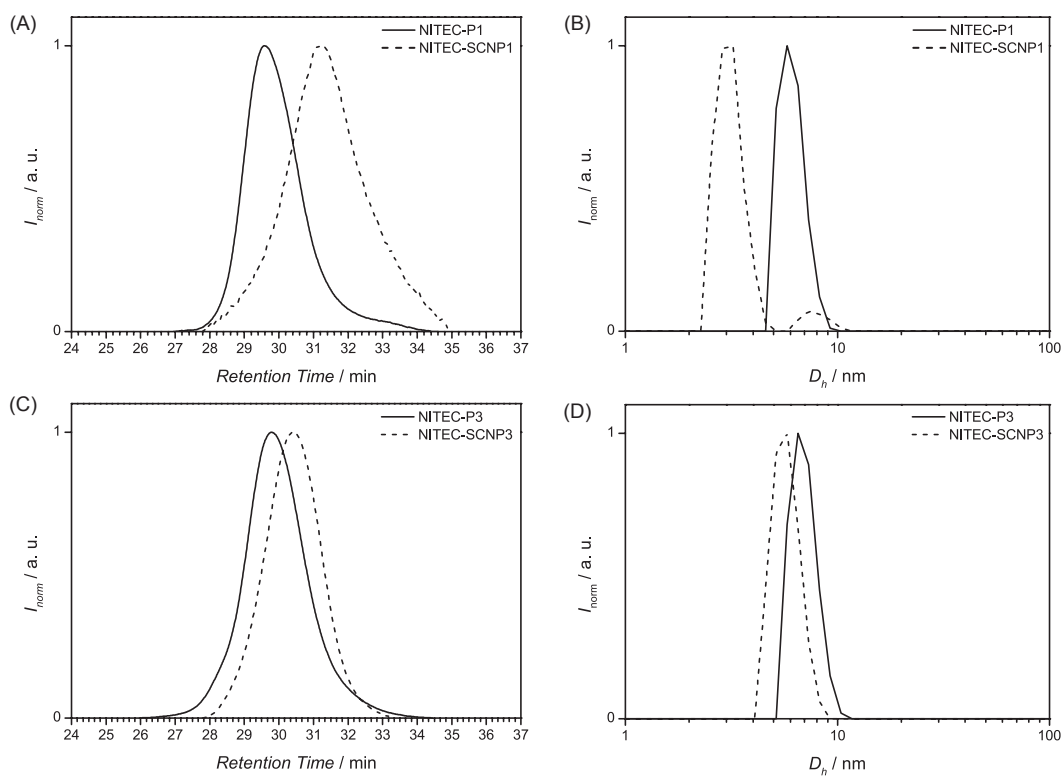
Figure 4.16 Normalized SEC traces (THF, RI) of NITEC-P1/NITEC-SCNP1 (A) and NITEC-P3/NITEC-SCNP3 (C) and number-weighted size distributions of NITEC-P1/NITEC-SCNP1 (B) and NITEC-P3/NITEC-SCNP3 (D) as determined by DLS. Adapted with permission from Reference [221]. Copyright 2014 American Chemical Society.

Since the power law is based on empirical data, the obtained values should only serve as an approximation. Information on the actual hydrodynamic diameter of the SCNPs and the corresponding linear precursors was gathered by dynamic light scattering (DLS). The DLS results corroborated in Table 4.8 clearly support the trend that has already been observed in the SEC traces: The hydrodynamic diameter of the SCNP decreases with increasing tetrazole content (see also Figure 4.15 and Figure 4.16). It should be noted that the DLS traces of NITEC-SCNP1 and NITEC-SCNP2 exhibit a small secondary population at larger hydrodynamic diameters, which might be attributed to residual linear polymer or the product of intermolecular crosslinks. The DLS and SEC results combined showcase that the size of the SCNPs can be fine-tuned by varying the ratio of functional groups along the backbone of the precursor polymer (see Table 4.6 and 4.8). In addition to finely controlling the SCNPs' size, the current approach for SCNP formation allows for adjusting the fluorescence properties of the SCNPs by increasing the content of enes (%PG-Mal) among the crosslinking moieties with equal ease. With increasing PG-Mal content the probability of pyrazoline derivative formation during the intramolecular crosslinking also increases, leading to an increased fluorescence intensity. Contrary to the pyrazoline derivative, the product of the nitrile imine dimerization does not exhibit fluorescence when excited at 415 nm. Exactly this trend is observed when examining the fluorescence properties of NITEC-SCNP1 to NITEC-SCNP3 (see Figure 4.17A,B).

The excitation maximum (λ_{max}) of the pyrazoline derivative is close to 415 nm. When excited at λ_{max}, the maximum of the broad fluorescence emission band lies at 558 nm, therefore, in the bio-compatible visible range. Thus, the particles are perfectly suitable for imaging of biological processes, since, for example, DNA and other large biomolecules are UV-sensitive. The profluorescent nature of NITEC-SCNP1 makes these single-chain nanoparticles the ideal candidate to showcase the functionalization ability of the presented SCNPs, since the success of the conjugation reaction leads to a fluorescent linkage, whereas the particles themselves do not fluoresce. In the current approach to functional SCNPs, residual tetrazole moieties after the single-chain crosslinking are utilized to attach the profluorescent NITEC-SCNP1 to maleimide-functional microspheres (see Scheme 4.5B) to showcase their powerful ligation capability. The conjugation of the tetrazole-functional single-chain nanoparticles to the maleimide-functional microspheres (Mal-Microsphere) was selected as a proof of principle, since the successful reaction can be readily monitored by
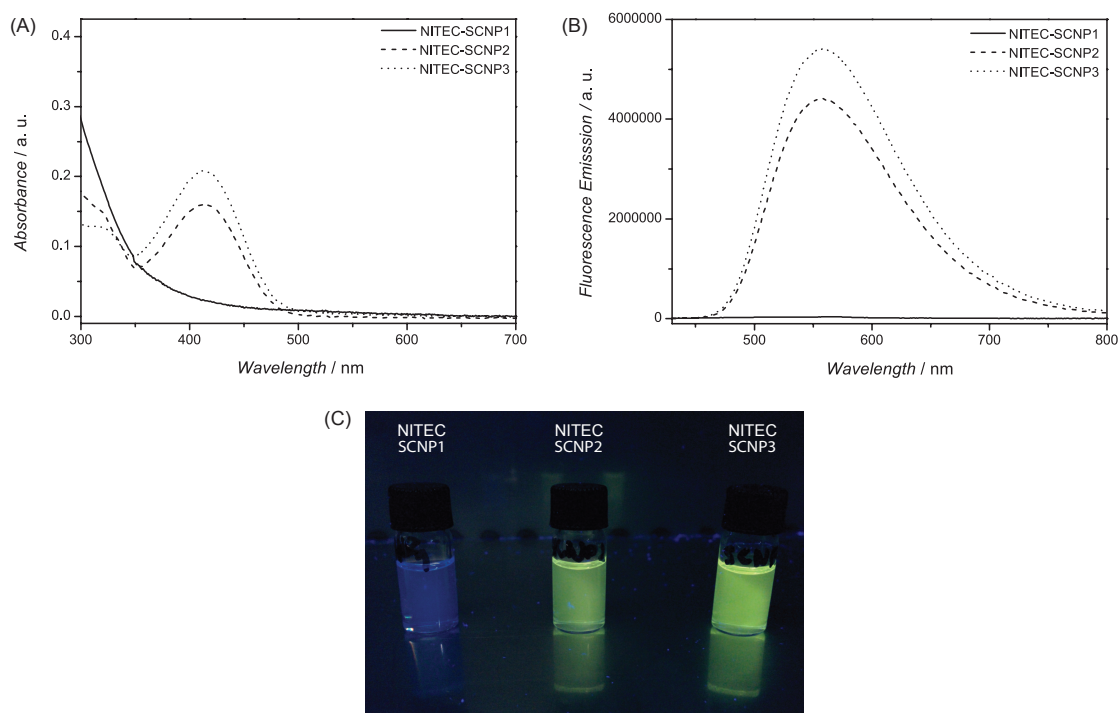
Figure 4.17 (A) UV/vis spectra of NITEC-SCNP1 - NITEC-SCNP3 in DMF. (B) Fluorescence emission in DMF at an excitation wavelength of λ_{exc} = 415 nm. (C) Image of solutions of NITEC-SCNP1 - NITEC-SCNP3 in THF irradiated with a hand-held UV-lamp (λ = 366 nm). Adapted with permission from Reference [221]. Copyright 2014 American Chemical Society.
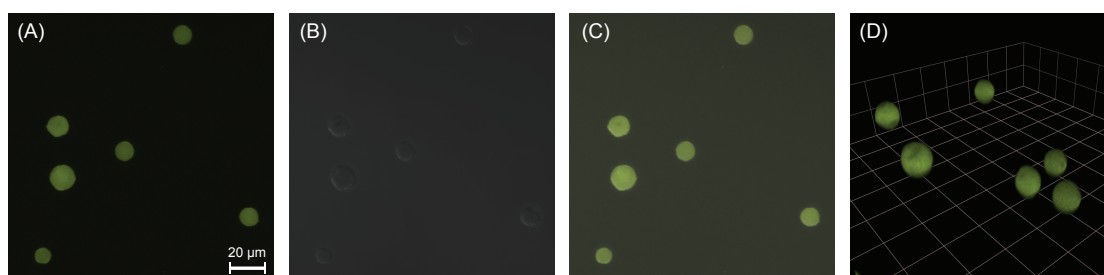
Figure 4.18 (A) Fluorescence microscopy image (142.86 μm×142.86 μm) of the SCNP-functionalized microspheres (λ_{exc} = 405 nm, fluorescence detection from 530 to 600 nm). (B) Differential interference contrast (DIC) image of the same area. (C) Overlay of images (A) and (B). (D) Three-dimensional reconstruction of a confocal image stack showing the functionalized microspheres (1 unit = 14.3 μm). Adapted with permission from Reference [221]. Copyright 2014 American Chemical Society.

fluorescence microscopy. After the irradiation, all microspheres are completely decorated with SCNPs (see Figure 4.18A-D). The employed maleimide-functional microspheres were synthesized from poly(glycidyl methacrylate) (PGMA) microspheres with a PGMA content of 80 % and pore size of 1000 and have been thoroughly characterized in an earlier publication.[98]

4.3 Photoinduced Formation of Single-Chain Nanoparticles *via* Photoenol Crosslinking

An alternative photochemical ligation technique, the photoenol reaction, will be investigated as new methodology for the intramolecular crosslinking of single polymer chains in the current section. The current UV-light-triggered Diels–Alder (DA) betwenn the photoenol and a maleimide enables a new ambient temperature synthetic approach for the preparation of mono-functional single-chain nanoparticles (SCNPs) under mild conditions (see Scheme 4.6).[¶] The formation of SCNPs was followed by size exclusion chromatography (SEC), nuclear magnetic resonance (NMR) spectroscopy, dynamic light scattering (DLS), and atomic force microscopy (AFM). Employing the single alkyne functionality, it is possible to fabricate mono-functionalized SCNPs for example by CuAAC ligation, which was exemplary shown in the synthesis of tadpole-like SCNPs.
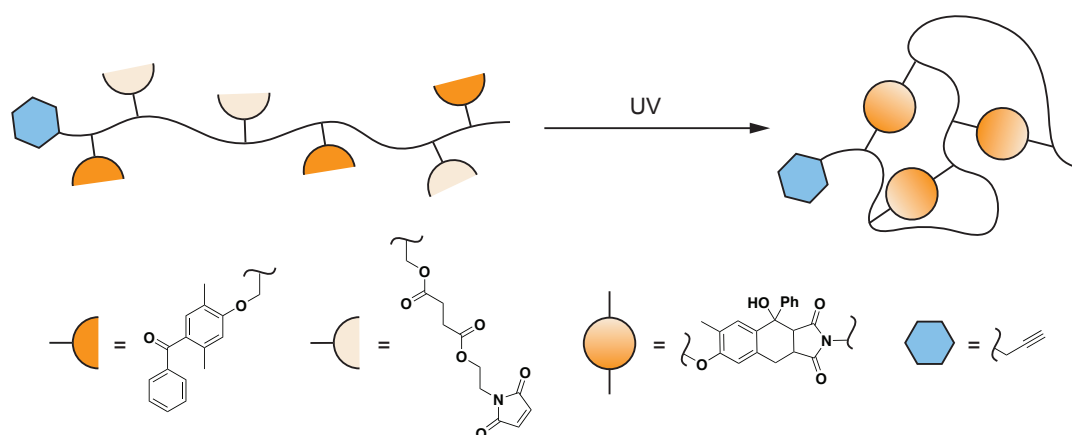
Scheme 4.6 General concept for the preparation of mono-functional single-chain nanoparticles *via* intramolecular, UV-induced Diels–Alder crosslinking.

Table 4.9 Results of the random copolymerization of styrene (S) and 4-chloromethylstyrene (CMS) *via* nitroxide-mediated radical polymerization (NMP) in the presence of Alkyne-NMP-Ini (see Scheme 4.7) and an initial monomer to initiator ratio of $[\text{M}_0]/[\text{I}_0] = 200$. Feed corresponds to the monomer feed during the polymerization, and Comp. corresponds to the final copolymer composition according to NMR calculations (see text).

Polymer	$M_{\text{n,SEC}}/\text{g mol}^{-1}$	$Đ$	Feed/%CMS	Comp./%CMS
Alkyne-P(S-*co*-CMS)1[a]	14900	1.16	8	9
Alkyne-P(S-*co*-CMS)2[a]	14900	1.22	15	17
Alkyne-P(S-*co*-CMS)3[b]	14700	1.27	30	34

[a] 6 h reaction time   [b] 4.5 h reaction time

Synthesis of the Monofunctional Linear Photoreactive Precursor Copolymers

For the synthesis of chloromethyl functionalized copolymers, a series of poly(styrene-*co*-chloromethylstyrene)s were prepared *via* nitroxide mediated polymerization (NMP) of 4-chloromethylstyrene (CMS) and styrene (S) in the presence of Alkyne-NMP-Ini at 125 °C (see Scheme 4.7).

The composition of the copolymer was determined *via* ^{1}H NMR spectroscopy. The mole fractions of CMS and S were deduced from the integrals of the peak area close to 4.51 ppm (y), corresponding to the two proton resonances of the methylene unit of CMS and the total area between 6.22 and 7.28 ppm (x), which is associated with the aromatic proton resonances of all repeating units. The percentage of CMS repeating units in the polymer was calculated using Equation 4.4.

$$\%CMS = \frac{5y}{2x + y} \tag{4.4}$$

As evidenced in Table 4.9, it was possible to finely control the functional group density of the random copolymers by varying the monomer feed utilized in the copolymerization processes. Owing to the nature of the NMP mechanism, the polymer chains should have the same composition due to a simultaneous initiation of all chains and also feature narrow dispersities. The ^{1}H NMR spectra of Alkyne-P(S-*co*-CMS)1 - Alkyne-P(S-*co*-CMS)3 display the characteristic aromatic proton resonances for the polystyrene units between 7.05 and 6.54 ppm as well as the resonances of the benzylic protons of CMS ($-$CH$_2$Cl) and the alkyne protons of the initiator ($-$OCH$_2$CCH), which appear at 4.62 and 4.50 ppm (see Figure 4.19). The CMS moieties of copolymers Alkyne-P(S-*co*-CMS)1-3 with different
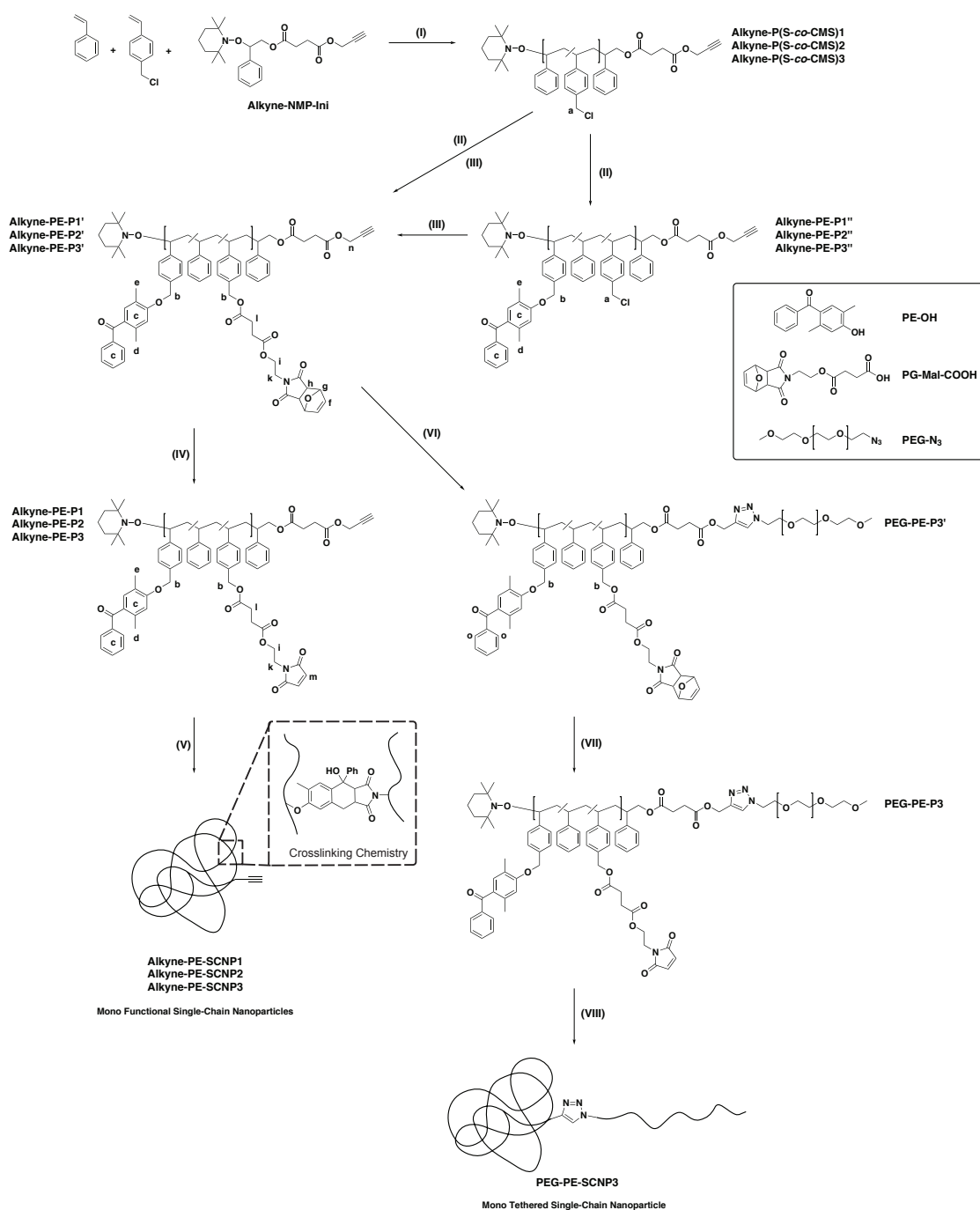
Scheme 4.7 Synthetic strategy for the preparation of monofunctional single-chain nanoparticles. (I) 125 °C, 6 h; (II) DMF, K$_2$CO$_3$, PE-OH, 70 °C, 24 h; (III) DMF, K$_2$CO$_3$, PG-Mal-COOH, a.t., 24 h; (IV) toluene, 100 °C, 15 h; (V) CH$_2$Cl$_2$, $h\nu$, 30 min; (VI) DMF, CuBr/PMDETA, PEG-N$_3$, a.t., 24 h; (VII) toluene, 100 °C, 15 h; (VIII) CH$_2$Cl$_2$, $h\nu$, 30 min. Adapted with permission from Reference [222]. Copyright 2013 American Chemical Society.
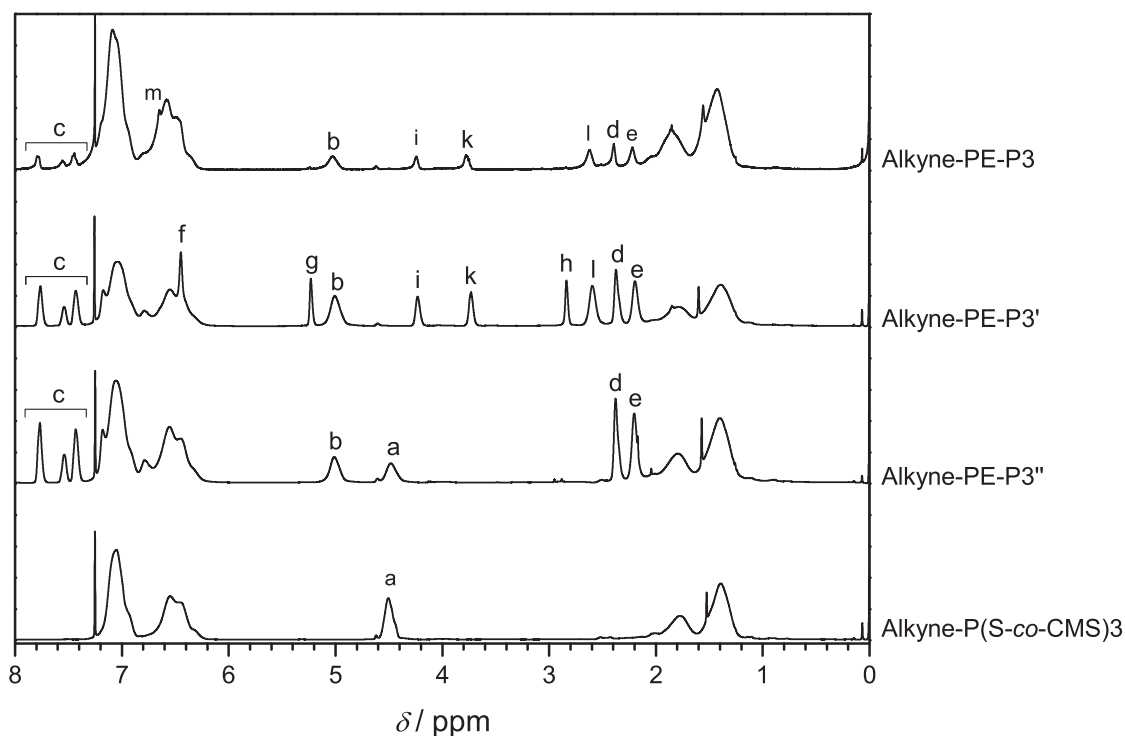
Figure 4.19 Functionalization process from poly(styrene-*co*-chloromethylstyrene) to a photo-reactive single-chain nanoparticle precursor polymer followed by [^1]H NMR spectroscopy (400 MHz, CDCl$_3$) at 25 °C. To best showcase the course of functionalization, the spectra of polymers Alkyne-P(S-*co*-CMS)3 to Alkyne-PE-P3 (34% FGD) are depicted, as these offer the most intense resonances for the pendant reactive groups. For signal assignment refer to Scheme 4.7. Adapted with permission from Reference [222]. Copyright 2013 American Chemical Society.

mole fractions of CMS (9-34 mol%) were quantitatively – as can be judged within the limits of the experimental uncertainty of ^{1}H NMR spectroscopy – converted to the corresponding reactive groups for the UV-light-triggered Diels–Alder reaction in a one-pot/two-step process. The functionalization progress of the polymer backbone could readily be monitored by ^{1}H NMR spectroscopy as illustrated in Figure 4.19.

Initially, the lateral polymer chain was functionalized with 4-hydroxy-2,5-dimethylbenzo-phenone as the photo-reactive precursor. Under basic conditions the hydroxy group was deprotonated followed by a quantitative – as can be judged within the boundaries of the experimental uncertainty of ^{1}H NMR spectroscopy – nucleophilic substitution of the chlorine atom at 70 °C. The ^{1}H NMR spectrum (see Figure 4.19) of Alkyne-P(S-*co*-CMS)3" displays a decrease in intensity of the resonances associated with the −CH$_2$Cl protons at 4.50 ppm and features new resonances corresponding to the 4-hydroxy-2,5-dimethylbenzophenone protons at 7.77 - 7.43, 2.38, and 3.80 ppm. To incorporate a maleimide motif into the

polymer chain, a carboxyl functional maleimide compound (PG-Mal-COOH) was synthesized, which was subsequently reacted with polymers Alkyne-PE-P1" - Alkyne-PE-P3" in the presence of K_2CO_3 in DMF to obtain the functionalized copolymers Alkyne-PE-P1' - Alkyne-PE-P3'. Employing the same reaction conditions as used for the functionalization with the photoenol precursor, unexpectedly led to crosslinked material. Most likely the crosslinking process is correlated to an unintentional removal of the furan protective group and successive reaction of the maleimide with residual chlorine atoms. As a consequence, milder conditions were applied, and the reaction proceeded to high conversion at ambient temperature within 24 h. The ^{1}H NMR spectrum of Alkyne-PE-P3' indicates that the signal corresponding to the $-CH_2Cl$ protons disappears and new resonances for the maleimide motif can be observed at 6.50, 5.23, 4.23, 3.73, 2.84, and 2.60 ppm (see Figure 4.19). Further investigations to improve the preparation procedure showed that a one-pot reaction with the sequential addition of 4-hydroxy-2,5-dimethylbenzophenone and the maleimide derivative, saving one work-up step and material, is the most effective synthesis route. Confirmed by ^{1}H NMR spectroscopy, the resonances for the 4-hydroxy-2,5-dimethylbenzophenone and the maleimide moiety are observed with the above-discussed chemical shifts, and the resonance for the $-CH_2Cl$ protons is no longer detected at 4.50 ppm (see Figure 4.19). The furan protecting group was quantitatively removed in a retro-DA-reaction at 100 °C, as the disappearance of the diagnostic resonances of the protecting group (g and f, Figure 4.19) in the NMR spectrum clearly shows.

Synthesis of the Monofunctionalized Linear Photoreactive Precursor Copolymers

As a proof of principle, copolymer Alkyne-PE-P3' was tethered to PEG-azide utilizing the CuBr/PMDETA supported copper(I)-catalyzed azide-alkyne cycloaddition (see Scheme 4.7). The SEC trace of polymer PEG-PE-P3' is – compared to the trace of starting material Alkyne-PE-P3' – clearly shifted to lower retention times (*i.e.*, higher molar mass) and features a monomodal distribution (see Figure 4.20).

Inspection of the ^{1}H NMR spectrum of PEG-PE-P3' reveals full conversion of the terminal alkyne as the corresponding resonance at 4.62 ppm disappears completely while new signals, corresponding to the repeating unit of PEG, emerge at 3.58 ppm (see
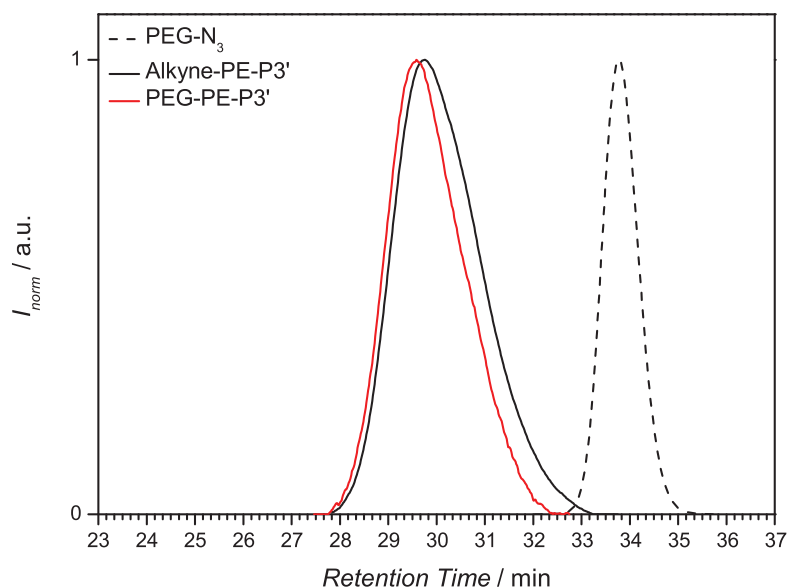
Figure 4.20 Normalized SEC traces (THF, RI) of the alkyne bearing monofunctional polymer Alkyne-PE-P3', the PEG-azide (see Scheme 4.7), and the corresponding monofunctionalized block copolymer PEG-PE-P3'. Adapted with permission from Reference [222]. Copyright 2013 American Chemical Society.

Figure 4.21). The deprotection of the *N*-maleimide motif was again carried out at $100\,°C$ and proceeded quantitatively.

Photochemical Synthesis of Monofuntional SCNPs

In order to identify optimum reaction conditions for the UV-triggered SCNP formation variable concentrations, solvents and reaction times were investigated. The polymer Alkyne-PE-P2 was employed for the following investigations. First, the solvent system dichloromethane/acetonitrile (1:3, v/v) ($c_{\mathrm{Alkyne\text{-}PE\text{-}P2}} = 1\,\mathrm{mg\,mL^{-1}}$), and a reaction time of 2 h was applied. Under these conditions intermolecular crosslinking occurred because of the limited solubility and/or a too concentrated solution, which led to an insoluble product. Thus, all further reactions were conducted in dichloromethane (DCM) due to the good solubility of the polymer. Concentrations of 0.133, 0.067, 0.033, and $0.0117\,\mathrm{mg\,mL^{-1}}$ were investigated. Only the lowest concentration of $0.0117\,\mathrm{mg\,mL^{-1}}$ led to a clean shift of the SEC trace with no shoulder at shorter retention times or bimodal distribution (see Figure 4.22).

Having identified the optimum concentration and solvent, a kinetic study was performed with polymer Alkyne-PE-P1 to find the optimal reaction time. Samples were taken from
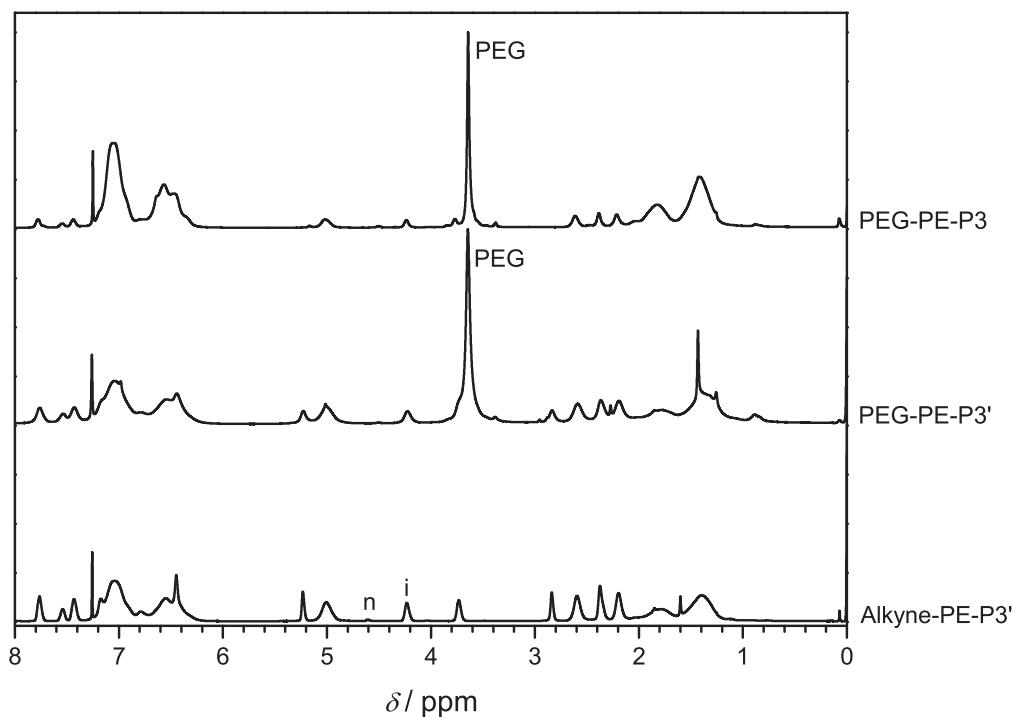
Figure 4.21 Functionalization process from the monofunctional polymer Alkyne-PE-P3' to the monofunctionalized linear precursor copolymer PEG-PE-P3 followed by ^{1}H NMR spectroscopy (400 MHz, CDCl$_3$) at 25 °C. For signal assignments refer to Scheme 4.7. Adapted with permission from Reference [222]. Copyright 2013 American Chemical Society.
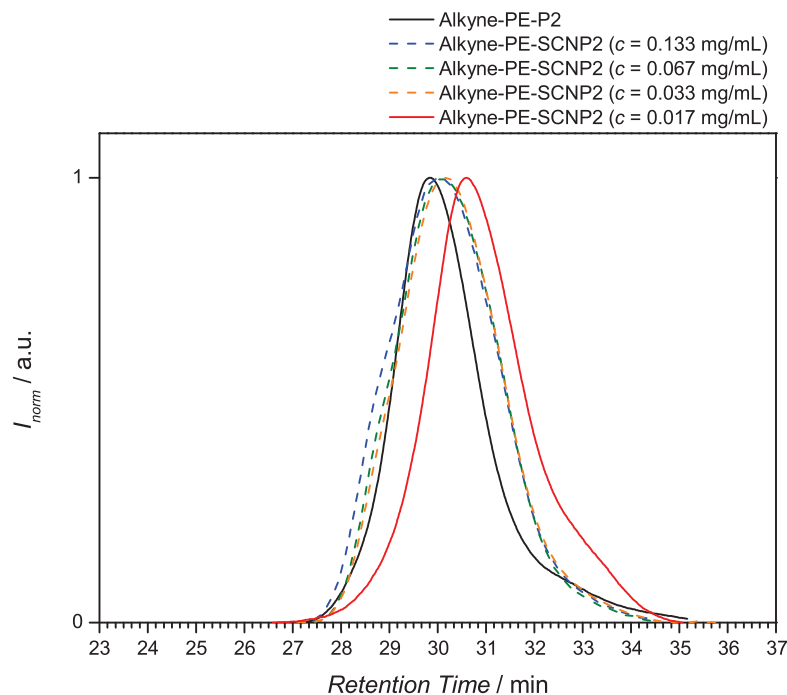
Figure 4.22 Normalized SEC traces (THF, RI) of the concentration study carried out with polymer Alkyne-PE-P2 in DCM. Adapted with permission from Reference [222]. Copyright 2013 American Chemical Society.
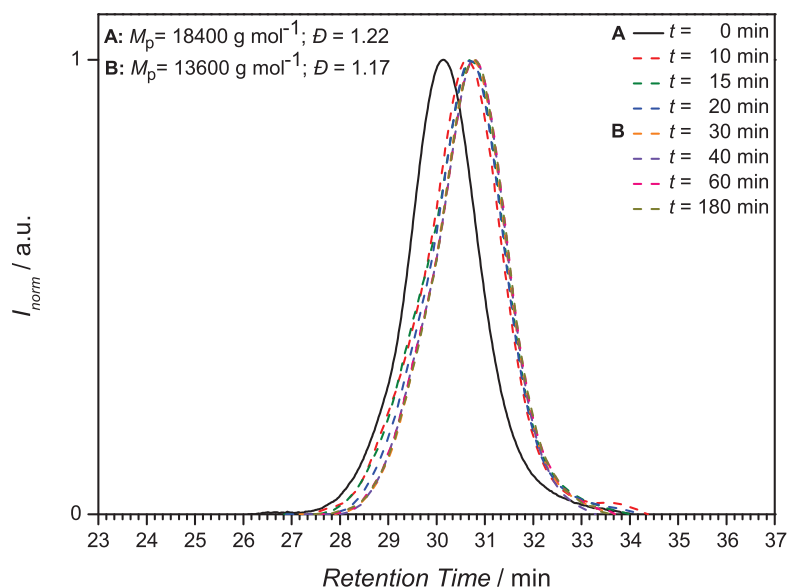
Figure 4.23 Normalized SEC traces (THF, RI) of the single-chain crosslinking kinetics study carried out with polymer Alkyne-PE-P1 in DCM. Adapted with permission from Reference [222]. Copyright 2013 American Chemical Society.

the reaction mixture in several time intervals. The results (see Figure 4.23) indicate that the single chain collapse was completed after 30 min (indicated in Figure 4.23 by the label 'B', which is associated with a final molecular weight of $13\,600\,\mathrm{g\,mol^{-1}}$), since the SEC trace remains invariant at longer reaction times. For reaction times shorter than 30 min, a small shoulder in the higher molar mass region is observed, which might be attributed to remaining linear precursor copolymer. After 30 min of UV irradiation, the SEC trace is completely shifted to higher retention times (*i.e.*, lower molar mass) and does not display a shoulder in the higher molar mass region, evidencing that no intermolecular coupling occurred during the single-chain crosslinking process.

The formation of the SCNPs was monitored by ^{1}H NMR spectroscopy, SEC, DLS, and AFM. For the ^{1}H NMR analysis, only the polymer with the highest FGD was chosen, since these spectra show the strongest signals for the reactive side groups. The most obvious sign of SCNP formation is the quality of the spectrum. When intramolecularly crosslinked, the polymers loose degrees of freedom, which leads to a significant broadening of all signals (see Figure 4.24).[199,200]

Chemical evidence was gathered from the photoenol precursor's aromatic proton resonances. As discussed in previous publications,[106,107] the aromatic protons of the photoenol precursor shift to higher field and disappear below the signal of the aromatic protons
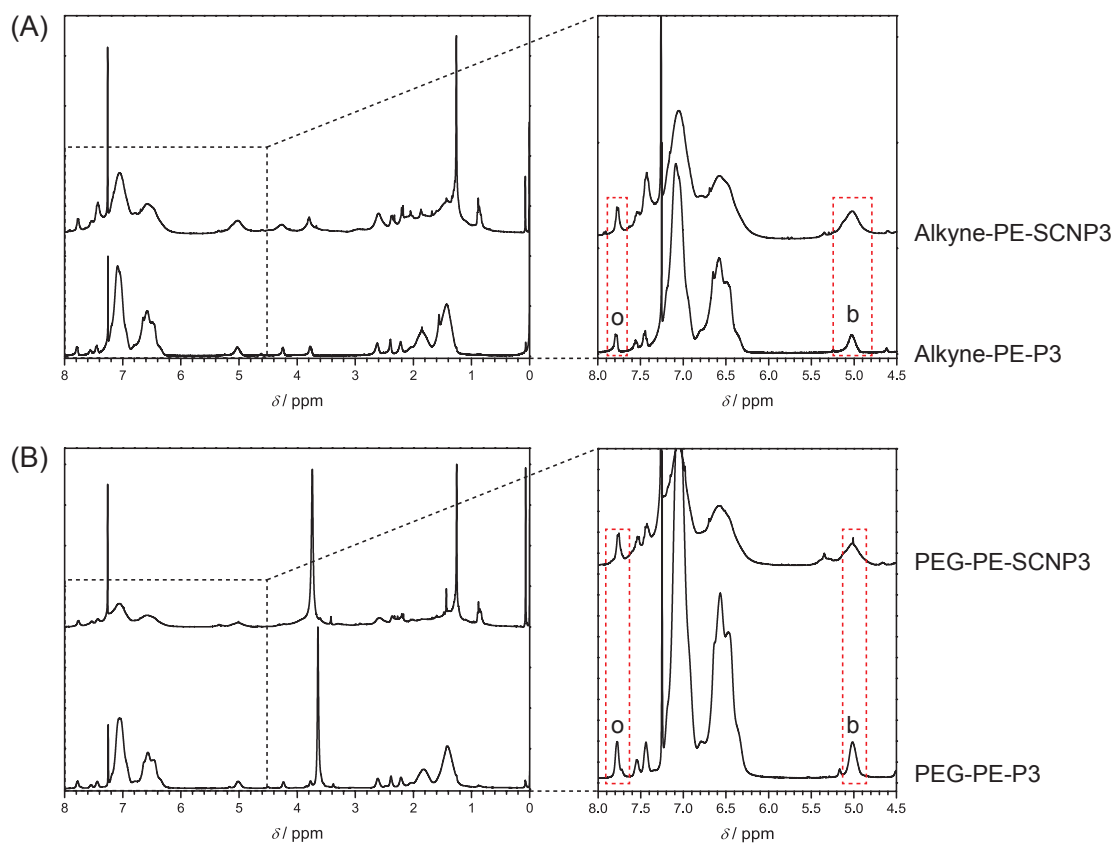
Figure 4.24 ^{1}H NMR spectra (400 MHz, CDCl$_3$) at 25 °C of the linear precursor copolymers and the corresponding SCNPs. (A) Monofunctional precursor polymer Alkyne-PE-P3 and the respective Alkyne-PE-SCNP3. (B) Monofunctionalized precursor copolymer PEG-PE-P3 and the respective monotethered PEG-PE-SCNP3. For the signal assignment refer to Scheme 4.7. Adapted with permission from Reference [222]. Copyright 2013 American Chemical Society.

Table 4.10 Comparison of the integral ratios of the resonances for the benzylic protons (set to 1) along the backbone ($\sim$ 5.0 ppm) and the two aromatic protons in the *ortho*-position to the carbonyl functionality of the photoenol precursor ($\sim$ 7.8 ppm) for the linear precursor polymers Alkyne-PE-P3 and PEG-PE-P3, and the respective SCNPs Alkyne-PE-SCNP3 and PEG-PE-SCNP3.

Polymer	Ratio	Polymer	Ratio
Alkyne-PE-P3	1/0.56	PEG-PE-P3	1/0.57
Alkyne-PE-SCNP3	1/0.39	PEG-PE-SCNP3	1/0.41

of the polystyrene backbone. The functionalization process of the polymers Alkyne-P(S-*co*-CMS)1-3 to the polymers Alkyne-PE-P1' - Alkyne-PE-P3' was quantitative as determined within the experimental error of ^{1}H NMR spectroscopy, yet the ratio of the reactive groups was likely not exactly 50:50. Thus, there will always be remaining photoenol precursor and/or maleimide moieties in the SCNPs. Additionally, the intramolecular crosslinking might also separate two reactive groups in such a way that they are no longer able to react with each other, which will again lead to residual reactive groups within the SCNPs. On the basis of these facts, it was not expected that the aromatic protons of the photoenol precursor would disappear completely, but instead decrease in their intensity. To evaluate the decrease, the integral ratios of the signals for the benzylic protons along the backbone ($\sim$5.0 ppm) and the resonances of the two aromatic protons in the *ortho*-position to the carbonyl functionality of the photoenol precursor ($\sim$7.8 ppm) are compared before and after the intramolecular crosslinking (the signals are marked with red boxes in Figure 4.24). The results, collated in Table 4.10, underpin a decrease for both the monofunctional SCNP (Alkyne-PE-SCNP3) and the monofunctionalized SCNP (PEG-PE-SCNP3). The presented values suggest an approximate conversion of the photoenol of close to 30 %.

Size exclusion chromatography (SEC) again proved to be a convenient method to monitor the changes in hydrodynamic volume from the collapse of the linear precursor polymer to an intramolecular crosslinked polymeric nanoparticle, since the SEC columns separate analytes based on their hydrodynamic volume.[39,121] For all precursor polymers, SEC demonstrates that the hydrodynamic volumes of the respective SCNPs are significantly smaller than the starting linear macromolecules, which results in higher retention times for the SCNPs (see Figure 4.25).
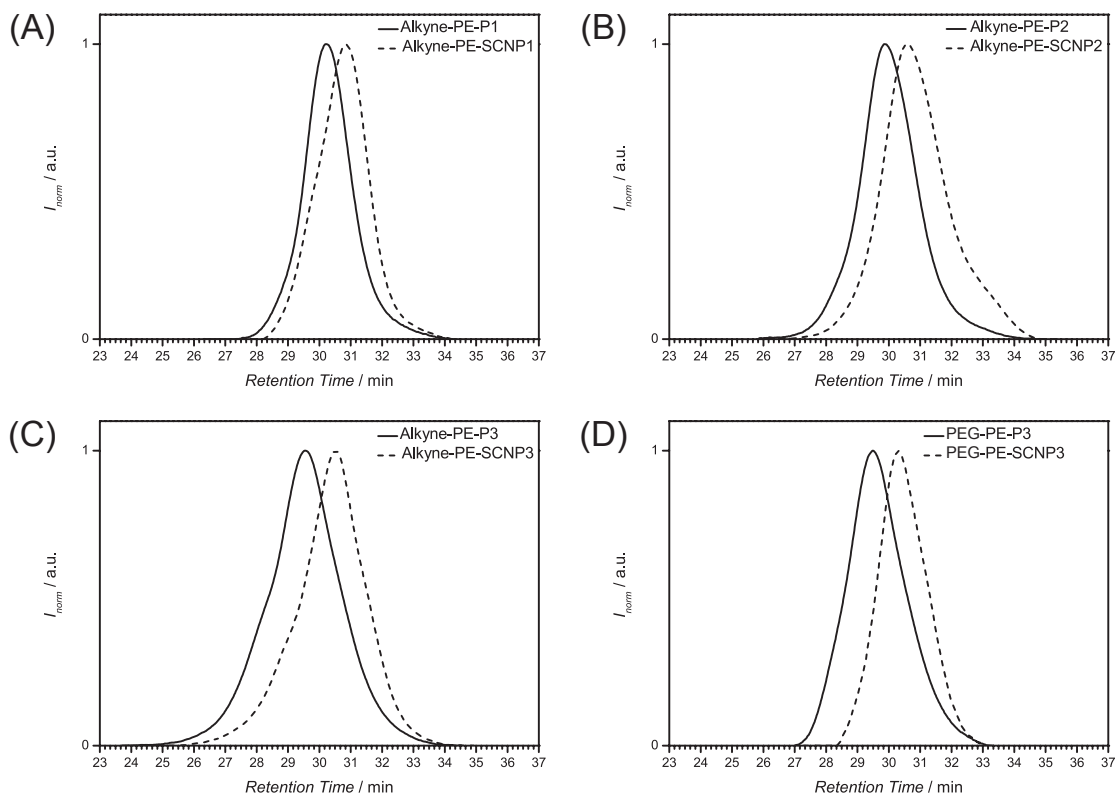
Figure 4.25 Normalized SEC traces (THF, RI) confirm the efficient formation of single-chain nanoparticles (SCNPs). The solid curves represent the linear precursor polymers and the dashed curves the respective SCNPs. (A) Polymer with 9% functional group density (FGD). (B) Polymer with 17% FGD. (C) Polymer with 34% FGD. (D) PEG-functional polymer with 34% FGD. Adapted with permission from Reference [222]. Copyright 2013 American Chemical Society.
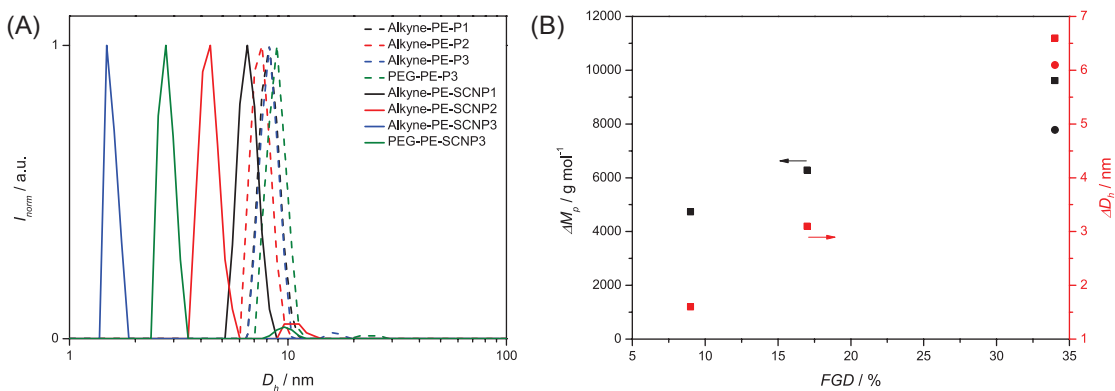
Figure 4.26 Dynamic light scattering (DLS) results and a comparison with SEC data. (A) Number-averaged size distributions of the linear precursor polymers and their respective SCNPs. (B) Change in peak molar mass (ΔM_{p}), measured by SEC, and change in hydrodynamic diameter (ΔD_{h}), measured by DLS, plotted against the functional group density (FGD). In (B) the squares are associated with the alkyne functional polymers, whereas the circles are associated with the PEG-functional polymers. Adapted with permission from Reference [222]. Copyright 2013 American Chemical Society.

The change in the apparent peak molar mass (ΔM_p), measured by SEC against polystyrene standards, can be correlated to the degree of collapse after intramolecular crosslinking. The fact that the precursor polymer with the lowest functional group density (FGD) has the smallest ΔM_p and the one with the highest FGD features the highest ΔM_p suggests that the size of the SCNP can indeed be controlled by varying the FGD along the polymeric backbone (see Figure 4.26B). Convincingly, the trend observed for ΔM_p is also observed when measuring the number-weighted mean hydrodynamic diameters D_h. Such measurements of the SCNPs and the linear precursor copolymers in THF solution were performed on a dynamic light scattering (DLS) instrument. DLS is a procedure used to determine the size distribution profile of small particles in suspension or polymers in solution, capable to detect molecules in the size range of a few nanometers up to several micrometers. The DLS results (refer to Figure 4.26A) show that all single polymer chains (functional and nonfunctional) undergo a size reduction upon the photochemically induced collapse. The largest change in hydrodynamic diameter (ΔD_h) was recorded for the polymer with the highest FGD, the smallest accordingly for the polymer with the lowest FGD (refer to Figure 4.26B). The DLS results for Alkyne-PE-SCNP2 and PEG-PE-SCNP3 show small amounts of particles with larger D_h, which might be attributed to remaining linear precursor polymers or products of the intermolecular reaction of two polymer chains. A very limited amount of particles with higher D_h is also observed in the DLS results for the linear precursor polymers Alkyne-PE-P3 and PEG-PE-P3, which were most probably a matter of aggregation.

Finally, the single-chain nanoparticles were visualized by atomic force microscopy (AFM). Therefore, Alkyne-PE-SCNP1 was adsorbed onto freshly cleaved mica disks from diluted dichloromethane solutions. A height map image of the cast surface with a scan size of 1 µm is presented in Figure 4.27. Panel A shows a sample containing Alkyne-PE-SCNP1, panel B shows the mica surface, and panel C shows a control sample, containing the linear precursor polymer Alkyne-PE-P1. The AFM image of the control sample shows a thin film consisting of the linear precursor polymer and some areas where the mica surface (dark spots) is exposed. In combination with the images in panels B and C, the AFM image of Alkyne-PE-SCNP1 in panel A further supports the efficient formation of crosslinked particles, of which some could present single chain particles. A direct comparison with the diameters observed *via* DLS in solution is not advisible, as certainly different diameters
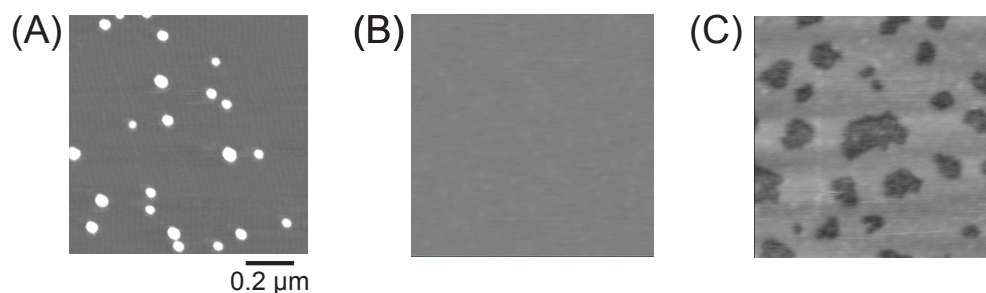
Figure 4.27 AFM topography images (1 µm × 1 µm scan size). (A) Sample containing Alkyne-PE-SCNP1. (B) Freshly cleaved mica disk. (C) Sample containing linear precursor polymer Alkyne-PE-P1. Adapted with permission from Reference [222]. Copyright 2013 American Chemical Society.

will be observed in the solid state *vs.* solution, and the AFM observation leads to an enhanced width of the SCNPs due to the broadness of the AFM tip. For this very reason, it is also not possible to observe different SCNP sizes for different FDGs as in Figure 4.26A *via* DLS. Nevertheless, the AFM images may suggest the presence of SCNPs as well as some larger aggregates.[125,196–198,209] The formation of aggregates during the casting process due to dewetting effects and evaporative self-assembly, which has been described in the literature, made the sample preparation a complex task.[196,197] To explore whether some of the smaller particles could indeed present SCNPs (and not aggregates), a height cross-section analysis (see Figure 4.28) with a focus on some of the smallest species in panel A of Figure 4.27 was carried out.

Inspection of Figure 4.28 shows that the particles feature a height of approximately 3 nm, which are similar in size to other SCNPs reported in the literature.[125] This observation leads to the conclusion that at least the smallest particles are indeed SCNPs. A dilution series also led to aggregated species (alongside smaller species), which suggests that the herein produced materials tend to aggregate when casted. Thus, the SEC and DLS data are more reliable indicators for the true single chain nature of the nanoparticles than AFM, which can only serve as a supporting analysis.
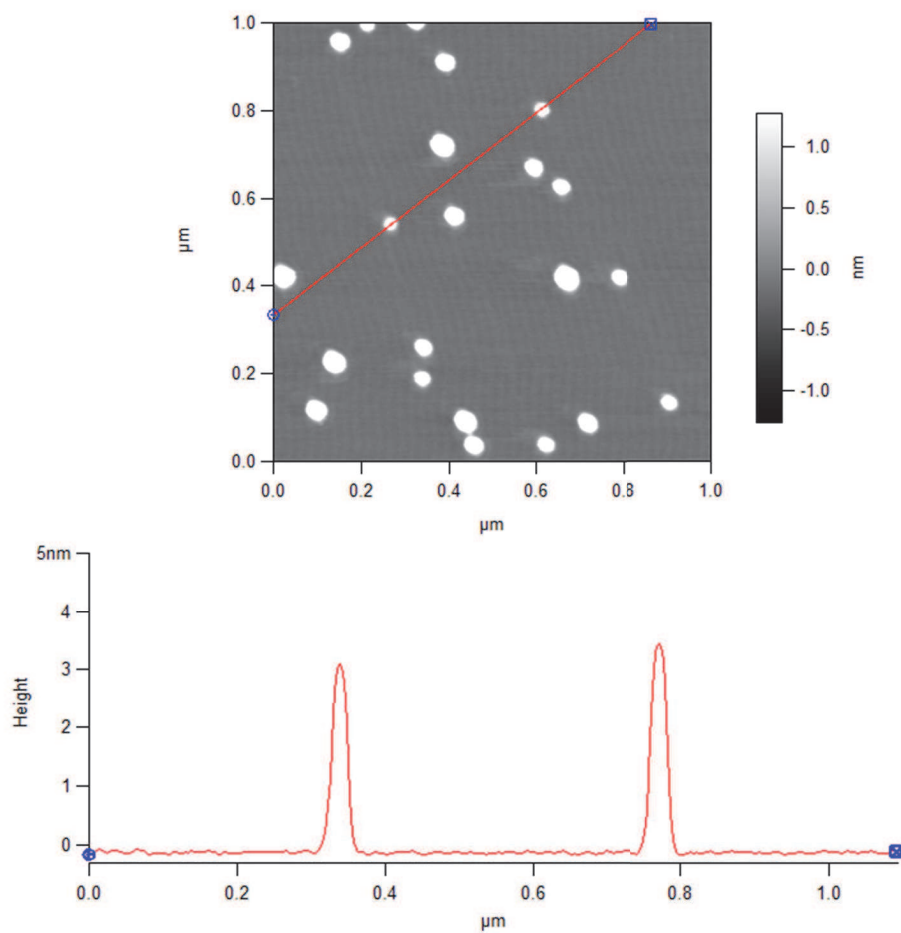
Figure 4.28 Heigt cross-section determined by AFM of two of the particles. The red line in the topography image depicts which particles have been analyzed. Adapted with permission from Reference [222]. Copyright 2013 American Chemical Society.

4.4 pH-Responsive Single-Chain Nanoparticles *via* Hydrazone Crosslinking in Water

The final section presents an approach for the formation of single-chain nanoparticles in water. A dynamic covalent chemistry (DCC) strategy for the intramolecular crosslinking was envisioned, thus making the SCNPs stimulus responsive (see Scheme 4.8). A well studied representative for DCC is the formation of hydrazones.[110] The condensation between an aldehyde and a hydrazine to the hydrazone is pH responsive, which renders the SCNPs applicable for a trigger responsive payload release. The resulting SCNPs have so far been characterized by dynamic light scattering (DLS), and diffusion ordered spectroscopy (DOSY) at acidic and basic conditions.
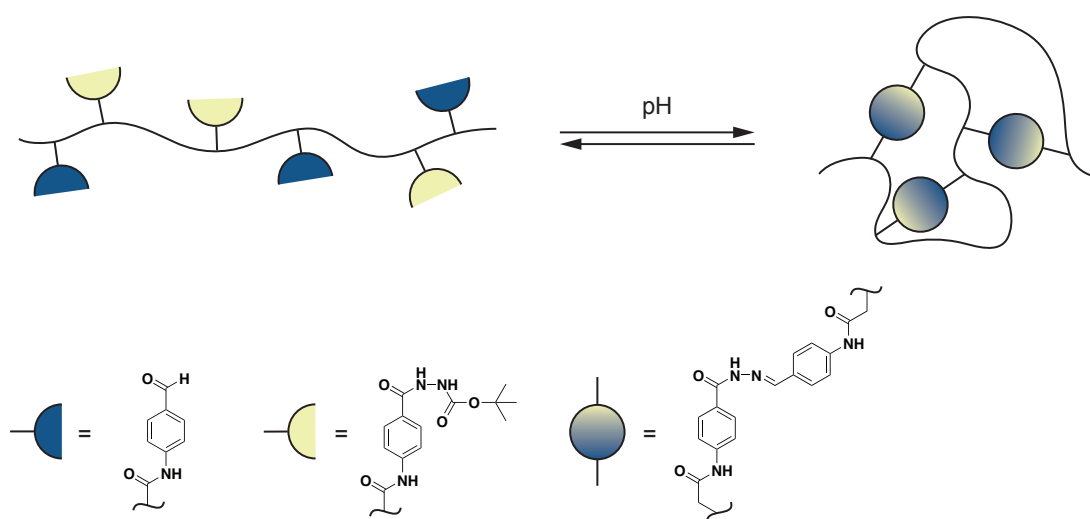
Scheme 4.8 Illustration of the formation of water soluble single-chain nanoparticles, crosslinked by dynamic-covalent hydrazone bonds. The intramolecular hydrazone bonds are responsive to changes in pH.

Synthesis of the Linear Precursor Copolymer

The synthetic pathway of the study is depicted in Scheme 4.9. At first, two novel acrylamide-based monomers were synthesized that carry either an aldehyde or a Boc-protected hydrazine functionality. Both monomers were prepared in two steps, of which each was characterized by ^{1}H and ^{13}C NMR spectroscopy as well as ESI-MS. The aldehyde-functional monomer (Aldehyde-Aa) was synthesized starting from 4-aminobenzyl alcohol.
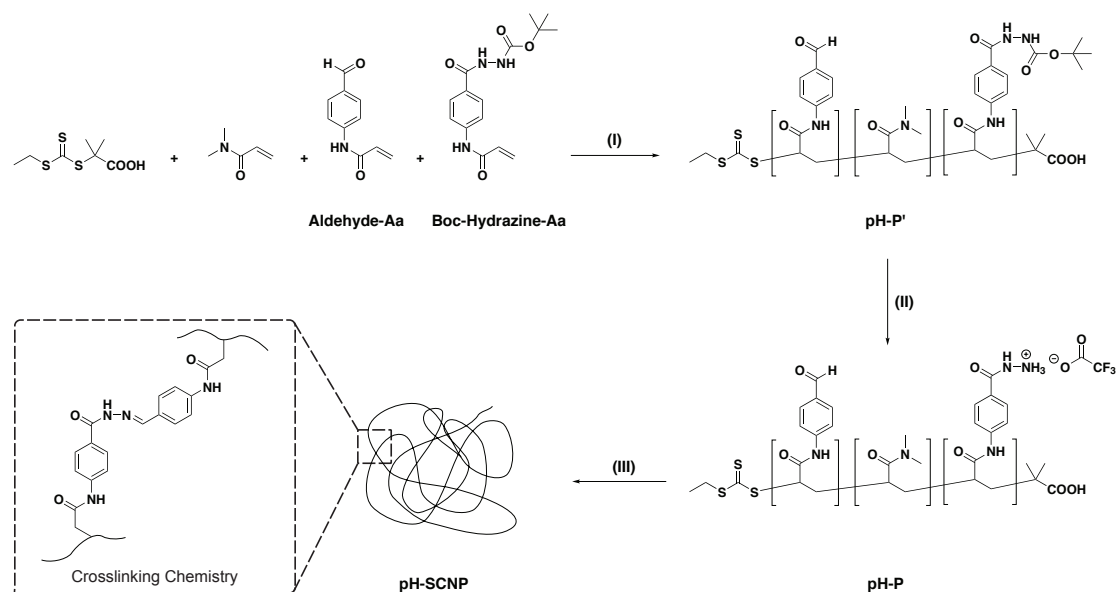
Scheme 4.9 Synthetic pathway for the preparation of water soluble, dynamic-covalently crosslinked SCNPs. (I) AIBN, DMF, 60 °C, 15 h; (II) TFA/H$_2$O, a.t., 24 h; (III) diluted solution, for details see text.

After amidation of the amine in a Schotten–Bauman reaction with acryloyl chloride, the alcohol moiety was selectively oxidized to the aldehyde in the presence of MnO$_2$. The ^{1}H and ^{13}C NMR of the Aldehyde-Aa monomer and its precursor are presented in Figure 4.29. The ESI-MS data can be found in the figure caption.

As for the protected hydrazine-functional monomer (Boc-Hydrazine-Aa), the synthesis commenced with an amidation of 4-aminobenzoic acid with Boc-carbazate. Afer having successfully introduced the Boc-protected hydrazine, the amine moiety was again reacted with acryloyl chloride in a Schotten–Bauman reaction. The ^{1}H and ^{13}C NMR of the Boc-Hydrazine-Aa monomer and its precursor are presented in Figure 4.30. The ESI-MS data can again be found in the figure caption. Inspection of the proton NMR spectra of both novel acrylamide monomers (Figure 4.29B and Figure 4.30B) shows the characteristic resonances of the vinylic protons (between 5.5 and 6.5 ppm), and diagnostic signals for the aldehyde functionality (a in Figure 4.29B) as well as the protected hydrazine (b, c in Figure 4.30B).

A random copolymer of *N*,*N*-dimethylacrylamide (DMAa), Aldehyde-Aa, and Boc-Hydrazine-Aa was subsequently prepared by RAFT polymerization with EMP as the chain transfer agent and AIBN as initiator. Polymerization for 15 h in DMF at 60 °C led
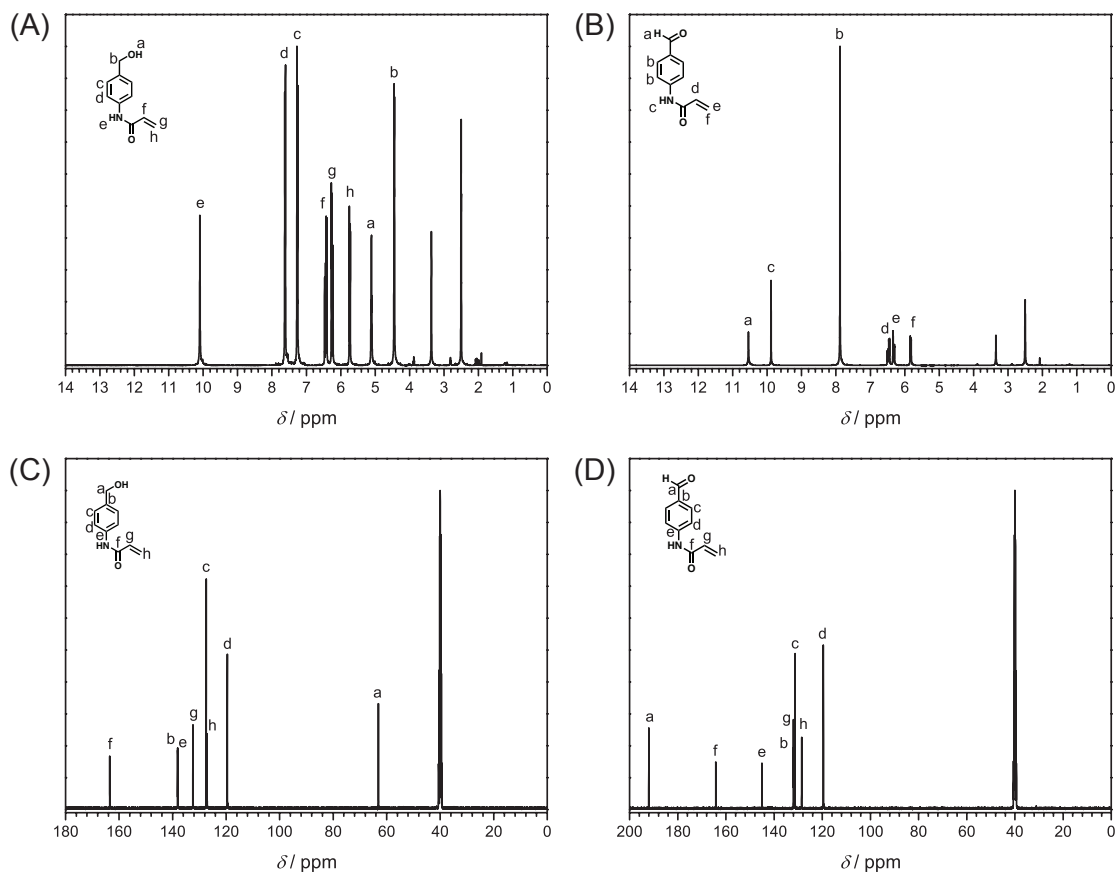
Figure 4.29 NMR spectra of the Aldehyde-Aa monomer and its precursor in DMSO-d$_6$ at 25 °C. (A) ^{1}H NMR spectrum of *N*-(4-(hydroxymethyl)phenyl)acrylamide, ESI-MS: [M + Na$^+$]$_{exp}$ = 200,0676 and [M + Na$^+$]$_{calc}$ = 200,0687; (B) ^{1}H NMR spectrum of Aldehyde-Aa, ESI-MS: [M + Na$^+$]$_{exp}$ = 198,0522 and [M + Na$^+$]$_{calc}$ = 198,0531; (C) ^{13}C NMR spectrum of *N*-(4-(hydroxymethyl)phenyl)acrylamide; (D) ^{13}C NMR spectrum of Aldehyde-Aa.
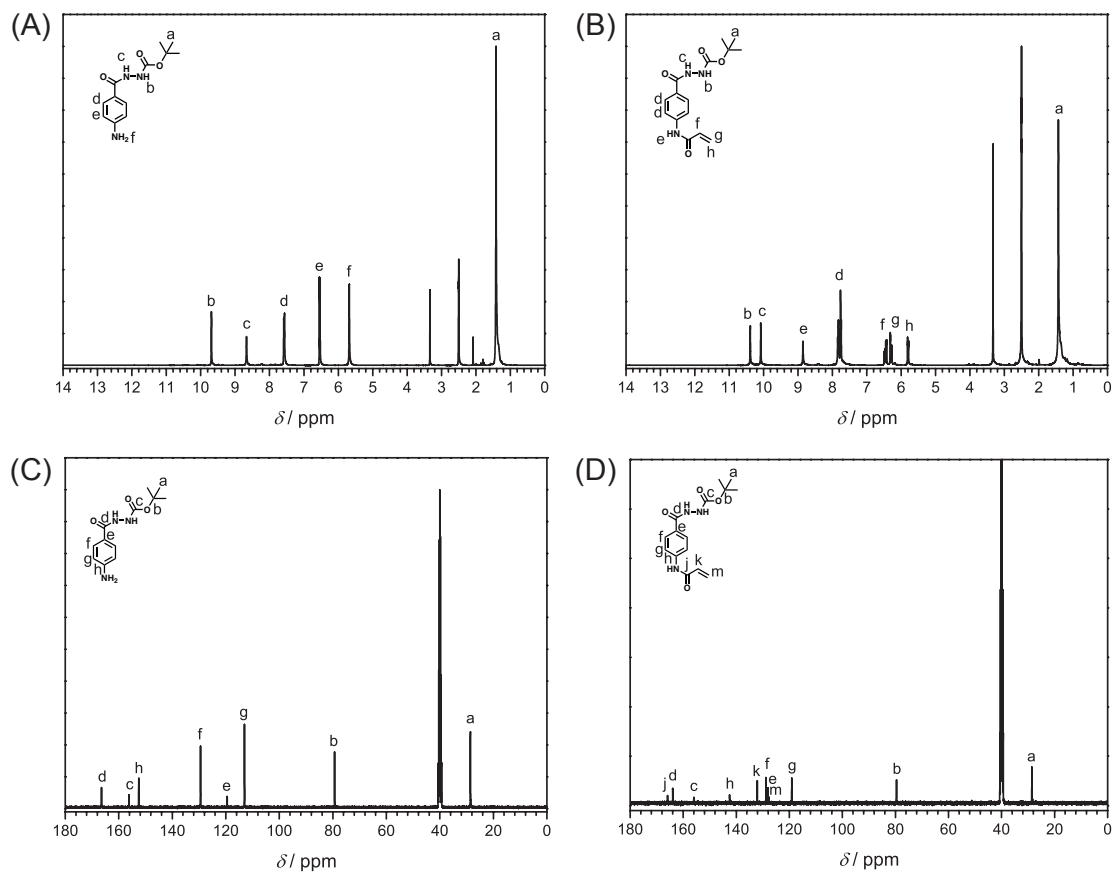
Figure 4.30 NMR spectra of the Boc-Hydrazine-Aa monomer and its precursor in DMSO-d_6 at 25 °C.(A) ^{1}H NMR spectrum of tert-butyl 2-(4-aminobenzoyl)hydrazine-1-carboxylate, ESI-MS: [M + Na$^+$]$_{exp}$ = 274,1155 and [M + Na$^+$]$_{calc}$ = 274,1168; (B) ^{1}H NMR spectrum of Boc-Hydrazine-Aa, ESI-MS: [M + Na$^+$]$_{exp}$ = 328,1273 and [M + Na$^+$]$_{calc}$ = 328,1273; (C) ^{13}C NMR spectrum of tert-butyl 2-(4-aminobenzoyl)hydrazine-1-carboxylate; (D) ^{13}C NMR spectrum of Boc-Hydrazine-Aa.
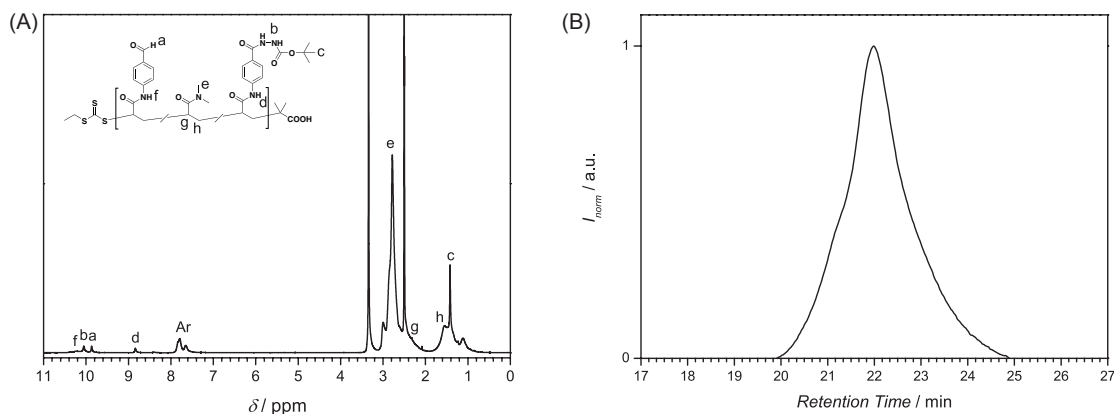
Figure 4.31 (A) ^{1}H NMR spectrum (400 MHz, DMSO-d$_6$) at 25 °C of pH-P'. (B) Normalized SEC chromatogramm (DMAc, RI) of pH-P'.

to a conversion of 79.4 %, which was calculated from NMR samples that were taken from the polymerization mixture before and after the polymerization, using the solvent signal as reference. The ^{1}H NMR spectrum of pH-P' features resonances for every employed monomer (see Figure 4.31A). In addition, the ratio of the integral of the aromatic proton resonances for the functional monomers to the integral of the methyl resonances of DMaa is 2:18, which exactly resembles the comonomer feed of 1:1:18. Size exclusion chromatography analysis provided information about the molecular weight ($M_{n,SEC} = 29\,400\,\mathrm{g\,mol^{-1}}$) and the dispersity of the molecular weight distribution ($Đ = 1.39$), which is sufficiently narrow for the targeted purpose (see Figure 4.31B).

The content of functional monomers was intentionally kept relatively low (10 %) at a comparatively high molar mass of the copolymer to ensure solubility in water. The deprotection of the hydrazine moiety was achieved by simply stirring a solution of pH-P' in a 1:1 (v/v) mixture of TFA and deionized water. The parent polymer pH-P forms a stable solution after the deprotection at a concentration of $c = 7.5\,\mathrm{mg\,mL^{-1}}$.

Synthesis of the pH-Responsive SCNPs

Aliquots of the solution of pH-P in the TFA/H$_2$O mixture were used without further purification for the formation of the hydrazone crosslinked single-chain nanoparticles. It was found that SCNPs with uniform size can be fabricated by slowly adding the pH-P solution ($c = 7.5\,\mathrm{mg\,mL^{-1}}$) into deionized water to reach a final concentration of $c = 0.375\,\mathrm{mg\,mL^{-1}}$. The resulting solution was stirred for 24 h to achieve good mixing.

Table 4.11 Compilation of mean hydrodynamic diameters as determined by DLS ($D_{\mathrm{h,DLS}}$) and diffusion coefficients (D) according to DOSY. The Stokes–Einstein equation was employed to calculate $D_{\mathrm{h,DLS}}$.

Sample	$D_{\mathrm{h,DLS}}/\mathrm{nm}$	$D_{\mathrm{h,DOSY}}/\mathrm{nm}$	$D/10^{-11}\,\mathrm{m^2\,s^{-1}}$
pH-P'	7.4	9.7	4.78
pH-SCNP at pH = 4.75	9.9	9.1	4.39
pH-SCNP at pH = 9.2	10.7	8.5	4.68
pH-SCNP + TFA	24.4	24.2	1.65

Subsequently, the pH of the solution was adjusted to basic conditions with NaOH granules. The addition of NaOH has multiple beneficial effects. It neutralizes the residual TFA, it deprotonates the hydrazine, and it shifts the equilibrium of the hydrazone formation to the product side. Two hours after NaOH addition, the SCNPs are purified by dialysis (MWCO = 1000 Da) against deionized water for one day. After lyophilization, the SCNPs can be dissolved in the appropriate solvent for analysis.

The SCNPs were synthesized in portions of 3.75 mg, so they could conveniently be dissolved in 1 mL of deuterated acetate (pH = 4.75) or ammonia (pH = 9.2) buffer solution for DLS and DOSY analysis. A sample of the pH-P' polymer in D_2O and a sample of the SCNPs in D_2O with excess TFA were analyzed as well. The number-weighted size distributions presented in Figure 4.32 show that pH-P' can not provide a comparison for the open chain status, since it shows the smallest hydrodynamic diameter. The small size might be attributed to the lower solubility of the polymer with the bulky, hydrophobic Boc-groups in the side chain. In addition, the size of the pH-SCNPs does not change when the pH is raised from 4.75 to 9.2. Only the sample with excess TFA lead to an observation of a larger hydrodynamic diameter. The mean hydrodynamic diameters ($D_{\mathrm{h,DLS}}$ and $D_{\mathrm{h,DOSY}}$), and the respective diffusion coefficients are collated in Table 4.11. It can be seen that the DLS and DOSY values correlate excellently.

The situation inside the pH-SCNPs at different pH values is illustrated in Scheme 4.10. At very acidic conditions (*e.g.*, in the presence of excess TFA), the hydrazones are protonated and will not react to the hydrazone. At a pH of around 4 to 5, the hydrazone bond is in a dynamic equilibrium and the reaction partners shuffle quickly inside the single-chain nanoparticle. A further increase of the pH to neutral or even basic conditions shifts the equilibrium to the (closed) hydrazone side. Such a behavior explains the similar
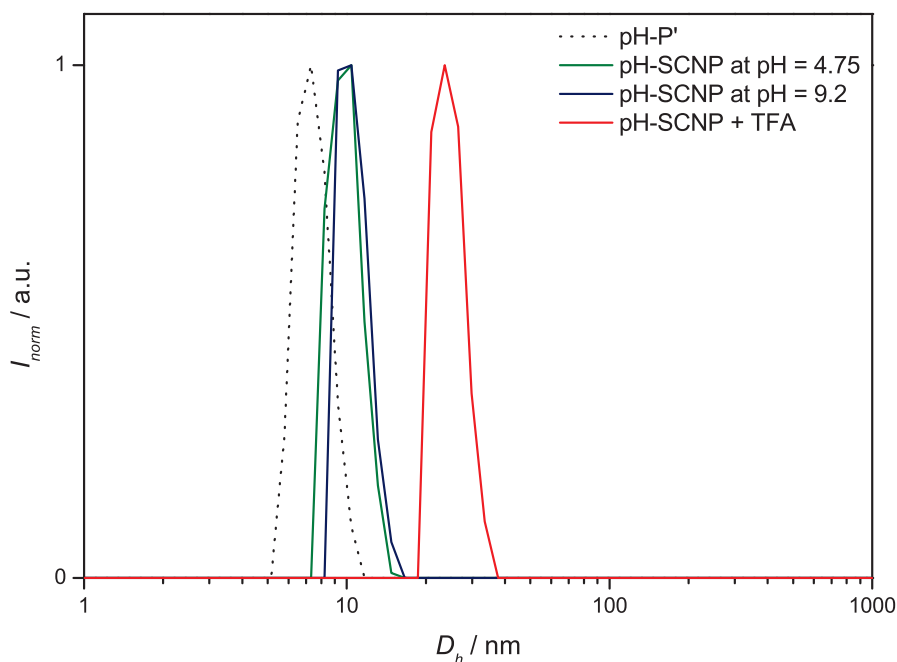
Figure 4.32 Number-weighted size distributions according to DLS of pH-P' and of the pH-SCNPs at different pH values.

hydrodynamic diameters in DLS or DOSY experiments at acidic and basic pH values. Although the pH-SCNPs will not return to the open chain structure at pH = 4.75, the dynamic nature of the hydrazone bond at the given pH can still be exploited for a trigger-responsive payload release. To round of the current study, a small molecule model probe (*e.g.*, a hydrazine, or an aldehyde) will be incorporated into the pH-SCNP structure during the formation of the single-chain nanoparticles. In acidic medium the release of the model payload can then hopefully be monitored by high performance liquid chromatography (HPLC).
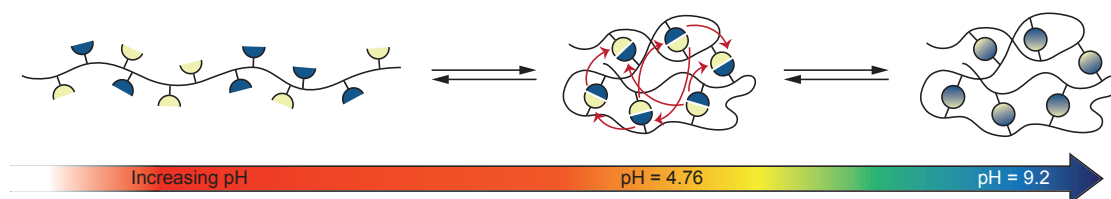
Scheme 4.10 Illustration of the behavior of the dynamic covalent hydrazone bond in the pH-SCNPs at varying pH values. At very acidic conditions (*e.g.*, in the presence of excess TFA) the hydrazones are protonated and will not react to the hydrazone (left). At a pH of around 4 to 5, the hydrazone bond is in a dynamic equilibrium and the reaction partners shuffle quickly inside the SCNP (middle). A further increase of the pH to neutral or even basic conditions shifts the equilibrium to the (closed) hydrazone side (right).

4.5 Summary

The current chapter presented various crosslinking methodologies for the preparation of application oriented SCNPs. First, the preparation and in-depth characterization of well defined, palladium(II) crosslinked single-chain nanoparticles on polystyrene basis was demonstrated. Therefore, linear precursor polymers were synthesized by the nitroxide mediated random copolymerization of styrene and 4-(chloromethyl)styrene, and a subsequent substitution reaction of the lateral chlorine atoms by the triarylphosphine ligands. A subsequent ligand exchange reaction with a Pd(II)-precursor lead to the Pd-SCNPs in diluted solution. The effective SCNP formation was confirmed by ^{1}H and ^{31}P{^{1}H} NMR spectroscopy, DLS, SEC, ^{1}H spin-spin relaxation time (T_2) analysis, and XPS. The design strategy for the linear precursor polymers entails the possibility to easily introduce variable functional groups. In the case at hand, Pd-SCNPs with a hydrodynamic diameter of 5.4 nm were fabricated. The underlying intramolecular crosslinking process directly leads to catalytically active Pd-SCNPs, which was exemplarily demonstrated in a Sonogashira coupling reaction. Employing different precursor complexes (*e.g.*, with Rh-, Ir- or Ni-ion centers) might open the door to various other catalysts. In addition, a novel procedure for interpreting the SEC chromatograms of SCNPs by log-normal distribution (LND) simulations was introduced. Thus, it was shown that all linear precursor polymers were converted to the more compact SCNP structure.

In the following sections, two synthetic approaches for the preparation of SCNPs on the basis of photochemical crosslinking were investigated.

For one, a powerful and facile to operate technology platform for the photo-induced preparation of functional, (pro)fluorescent single-chain nanoparticles (SCNPs) *via* photo-triggered nitrile imine-based intramolecular crosslinking of linear precursor polymers as novel transporting agents was presented. The precursor polymers were synthesized by nitroxide mediated random copolymerization of styrene and 4-(chloromethyl)styrene followed by a subsequent one-pot postpolymerization modification with a protected maleimide (PG-Mal) and tetrazole (Tet) moiety. The photo-triggered NITEC reaction in extremely dilute solution led to the effective formation of (pro)fluorescent SCNPs. It was unambiguously demonstrated by SEC, DLS, UV/vis-, and fluorescence spectroscopy that by varying the ratio of functional group density, the size, as well as the fluorescence

properties, of the SCNPs could be finely adjusted. In addition, an exemplary reaction evidenced that the residual (surface expressed) Tet moieties can be employed for further functionalization of the SCNPs. This, in combination with the fact that the SCNPs feature a broad fluorescence band (500-700 nm) in biocompatible excitation ranges (>400 nm), makes them ideal candidates for intracellular transport imaging applications for, *e.g.*, si-RNA or DNA delivery.

On the other hand, intramolecular UV-light-triggered Diels–Alder (DA) reactions were utilized for the fabrication of mono-functional SCNPs under mild conditions. NMP was employed to prepare well-defined random copolymers of styrene and 4-(chloromethyl)styrene with an alkyne terminal group. The backbone of the linear polymer chains was modified *via* a one-pot/two-step substitution process using 4-hydroxy-2,5-dimethylbenzophenone (DMBP) and a protected *N*-maleimide (Mal) compound. The DMBP and Mal functionalized linear precursor copolymers were irradiated with UV-light at 320 nm in diluted solution, leading to the efficient formation of SCNPs *via* photo-induced intramolecular crosslinking. The size of the SCNPs could be controlled by varying the functional group density along the polymeric backbone. The CuAAC conjugation of one of the mono-functional parent copolymers with PEG-azide evidenced the targeted principle and led to mono-tethered tadpole-like SCNPs. The successful formation of SCNPs was evidenced by SEC, NMR spectroscopy, DLS, as well as AFM. The present results unambiguously prove that the formation of SCNPs on a very well-defined level is indeed possible, employing high precision mild photochemical macromolecular design strategies.

Finally, water-soluble SCNPs were synthesized by exploiting the dynamic covalent hydrazone bond formation for the intramolecular crosslinking of linear precursor polymers. Therefore, parent polymers on the basis of dimethylacrylamide and aldehyde and Boc-protected hydrazine acrylamide monomers was prepared *via* the RAFT process. After deprotection of the hydrazine moiety by TFA, the pH-SCNPs were prepared in diluted solution. The SCNP formation was so far investigated by DLS and DOSY in acidic as well as basic conditions. Due to the dynamic covalent nature of the hydrazone bond, such SCNPs can potentially be applied for a trigger-responsive payload release.

4.6 Experimental Details

4.6.1 Synthesis of the Small Molecules

Compounds 2-(((ethylthio)carbonothioyl)thio)-2-methylpropanoic acid (EMP),[211,212] PG-Mal-COOH (Scheme 4.5),[223] Tet-COOH (Scheme 4.5),[224] PE-OH (Scheme 4.7),[105] PEG-N$_3$ ($M_{\text{n,SEC}}$ = 3200 g mol^{-1}, Đ = 1.04) (Scheme 4.7),[225] NMP-Ini (Scheme 4.5, 4.3),[226] and Alkyne-NMP-Ini (Scheme 4.7) were synthesized according to literature protocols.[37]

Synthesis of 4-Methylbenzyl 4-(diphenylphosphino)benzoate (L1)

To a solution of 4-(diphenylphosphino)benzoic acid (204 mg, 0.57 mmol, 1 equiv.) in DCM (10 mL), 4-methylbenzyl alcohol (81.4 mg, 0.67 mmol, 1 equiv.) and 4-DMAP (18.7 mg, 0.15 mmol, 0.23 equiv.) was added. Then a solution of diisopropylcarbodiimide (0.11 mL, 88.3 mg, 0.7 mmol, 1.05 equiv.) in dichloromethane was slowly added over the course of 5 min. The resulting yellow suspension was stirred under inert atmosphere at room temperature for 24 h. The reaction mixture was filtered and the solvent was removed under reduced pressure. The filtrate was diluted with ethyl acetate (20 mL) and washed consecutively with aqueous 10 % HCl (10 mL), aqueous saturated NaHCO$_3$ (10 mL) and brine (10 mL). The organic phase was separated and dried over MgSO$_4$, filtered and dried under reduced pressure. 4-Methylbenzyl 4-(diphenylphosphino)benzoate was obtained after flash chromatography on silica gel (5 % ethylacetate/*n*-pentane) as a slightly yellow oil (215 mg, 0.52 mmol, 79 %). ^{1}H NMR (300 MHz, CDCl$_3$, 25 °C): δ/ppm = 8.03 - 7.96 (m, 2H, Ph), 7.42 - 7.14 (m, 16H, Ph), 5.31 (s, 2H, C*H*$_2$OC=O), 2.36 (s, 3H, C*H*$_3$Ph). ^{13}C{^{1}H} NMR (75 MHz, CDCl$_3$, 25 °C): δ/ppm = 166.4 (s, 1C, *C*OOR), 144.1 (d, $^1J_{\text{C-P}}$ = 13.6 Hz, 1C, P*Ph*COO$_{\text{(ipso)}}$), 138.3 (s, 1C, Ph), 136.2 (d, $^1J_{\text{C-P}}$ = 10.0 Hz, 2C, P*Ph*$_{2\text{(ipso)}}$), 134.1 (d, $^2J_{\text{C-P}}$ = 19.9 Hz, 4C, P*Ph*$_{2\text{(ortho)}}$), 133.3 (d, $^2J_{\text{C-P}}$ = 18.7 Hz, 2C, P*Ph*COO$_{\text{(ortho)}}$), 133.1 (s, 1C, Ph), 130.3 (s, 1C, P*Ph*COO$_{\text{(para)}}$), 129.6 (d, $^3J_{\text{C-P}}$ = 6.4 Hz, 2C, P*Ph*COO$_{\text{(meta)}}$), 129.4 (s, 2C, Ph), 129.3 (s, 2C, P*Ph*$_{2\text{(para)}}$), 128.8 (d, $^3J_{\text{C-P}}$ = 7.2 Hz, 4C, P*Ph*$_{2\text{(meta)}}$), 128.5 (s, 2C, Ph), 66.9 (s, 1C, *C*H$_2$OC=O), 21.4 (s, 1C, *C*H$_3$Ph). ^{31}P{^{1}H} NMR (121 MHz, CDCl$_3$, 25 °C): δ/ppm = -5.0 (s, 1P, *P*Ph$_2$Ar).

Synthesis of 4-Ethylbenzyl 4-(diphenylphosphino)benzoate (L2)

The desired product was prepared from 4-(diphenylphosphino)benzoic acid (254 mg, 0.83 mmol, 1 equiv.) and ethylbenzyl alcohol (113 mg, 0.83 mmol, 1 equiv.) according to the above procedure for the synthesis of L1. 4-Ethylbenzyl 4-(diphenylphosphino)benzoate was obtained after flash chromatography on silica gel (5 % ethyl acetate/n-pentane) as a colourless oil (209 mg, 0.45 mmol, 59 %). ^{1}H NMR (300 MHz, CDCl$_3$, 25 °C): δ/ppm = 8.04 - 7.97 (m, 2H, Ph), 7.40 - 7.16 (m, 16H, Ph), 5.32 (s, 2H, CH_2OC=O), 2.66 (q, $^3J_{\text{H-H}}$ = 7.6 Hz, 2H, CH_2Ph), 1.24 (t, $^3J_{\text{H-H}}$ = 7.6 Hz, 3H, CH_3). ^{13}C{^{1}H} NMR (75 MHz, CDCl$_3$, 25 °C): δ/ppm = 166.4 (s, 1C, COOR), 144.6 (s, 1C, Ph), 144.2 (d, $^1J_{\text{C-P}}$ = 13.6 Hz, 1C, PPhCOO$_{\text{(ipso)}}$), 136.2 (d, $^1J_{\text{C-P}}$ = 10.0 Hz, 2C, P$Ph_2$$_{\text{(ipso)}}$), 134.1 (d, $^2J_{\text{C-P}}$ = 19.9 Hz, 4C, P$Ph_2$$_{\text{(ortho)}}$), 133.3 (s, 1C, Ph), 133.3 (d, $^2J_{\text{C-P}}$ = 18.7 Hz, 2C, PPhCOO$_{\text{(ortho)}}$), 130.3 (s, 1C, PPhCOO$_{\text{(para)}}$), 129.6 (d, $^3J_{\text{C-P}}$ = 6.5 Hz, 2C, PPhCOO$_{\text{(meta)}}$), 129.3 (s, 2C, PPh2$_{\text{(para)}}$), 128.8 (d, $^3J_{\text{C-P}}$ = 7.2 Hz, 4C, P$Ph_2$$_{\text{(meta)}}$), 128.6 (s, 2C, Ph), 128.2 (s, 2C, Ph), 66.9 (s, 1C, CH$_2$OC=O), 28.8 (s, 1C, CH$_2$Ph), 15.7 (s, 1C, CH$_3$). ^{31}P{^{1}H} NMR (121 MHz, CDCl$_3$, 25 °C): δ/ppm = -5.1 (s, 1P, PPh2Ar).

Synthesis of the complex [Pd(L$_1$)$_2$Cl$_2$]

To a solution of dichloro(1,5-cyclooctadiene)palladium(II) (16.2 mg, 0.06 mmol, 1 equiv.) in dichloromethane (5 mL), a solution of 4-methylbenzyl 4-(diphenylphosphino)benzoate (L1) (46.5 mg, 0.11 mmol, 2 equiv.) in dichloromethane (5 mL) was added. The resulting reaction mixture was stirred under inert atmosphere at room temperature for 16 h. Subsequently, the solution was concentrated under vacuum and after the addition of n-pentane (10 mL) a yellow solid precipitated. The solid was washed with n-pentane (10 mL) and dried under high vacuum to afford the product [Pd(L$_1$)$_2$Cl$_2$] as a yellow solid. Yellow crystals (49 mg, 0.05 mmol, 86 %) were obtained by diffusion of n-pentane into a solution of the yellow powder in dichloromethane. ^{1}H NMR (300 MHz, CDCl$_3$, 25 °C): δ/ppm = 8.09 - 7.99 (m, 4H, Ph), 7.80 - 7.14 (m, 32H, Ph), 5.31 (s, 4H, CH_2OC=O), 2.35 (s, 6H, CH_3Ph). ^{31}P{^{1}H} NMR (121 MHz, CDCl$_3$, 25 °C): δ/ppm = 23.5 (s, 2P, PPh$_2$Ar−PdCl$_2$−PPh$_2$Ar).

Synthesis of the complex [Pd(L₂)₂Cl₂]

The desired complex was prepared from dichloro(1,5-cyclooctadiene)palladium(II) (19.8 mg, 0.07 mmol, 1 equiv.) and 4-ethylbenzyl 4-(diphenylphosphino)benzoate (L2) (58.9 mg, 0.14 mmol, 2 equiv.) according to the procedure described above for the synthesis of [Pd(L₁)₂Cl₂]. The complex [Pd(L₂)₂Cl₂] was obtained as yellow crystals (62 mg, 0.06 mmol, 87 %) by diffusion of *n*-pentane into a solution of the yellow powder in dichloromethane. ^{1}H NMR (300 MHz, CDCl₃, 25 °C): δ/ppm = 8.10 - 8.00 (m, 4H, Ph), 7.79 - 7.16 (m, 32H, Ph), 5.32 (s, 4H, C*H₂*OC=O), 2.66 (q, $^{3}J_{\text{H-H}}$ = 7.6 Hz, 4H, C*H₂*Ph), 1.24 (t, $^{3}J_{\text{H-H}}$ = 7.6 Hz, 6H, C*H₃*). ^{31}P{^{1}H} NMR (121 MHz, CDCl₃, 25 °C): δ/ppm = 23.5 (s, 2P, *P*Ph₂Ar−PdCl₂−*P*Ph₂Ar).

Mixing Experiment

In addition, a statistical mixture (1:2:1) of the complexes [Pd(L₁)₂Cl₂], [Pd(L₁)(L₂)Cl₂] and [Pd(L₂)₂Cl₂] was synthesized in order to examine the effects on the resulting ^{31}P{^{1}H} NMR spectrum. Therefore, a solution of the synthesized ligands L1 (72.5 mg, 0.18 mmol, 1 equiv.) and L) (75.0 mg, 0.18 mmol, 1 equiv.) in dichloromethane (5 mL) was added simultaneously over the course of 5 min to a solution of dichloro(1,5-cyclooctadiene)palladium(II) (50.4 mg, 0.18 mmol, 1 equiv.) in dichloromethane (10 mL). The remaining preparation followed the procedure described above for the synthesis of [Pd(L₁)₂Cl₂]. The corresponding ^{1}H NMR spectrum shows the expected signals of both ligands L1 and L2 in almost the same ratio, which implies that they coordinate to the Pd-center to the same extent. In the ^{31}P{^{1}H} NMR spectrum a singulett signal at δ = 23.5 ppm is observed, analogously to the complexes [Pd(L₁)₂Cl₂] and [Pd(L₂)₂Cl₂]. The signal is slightly broadened, but no coupling is observed in the ^{31}P{^{1}H} NMR spectrum.

Synthesis of the NMP Initiator (NMP-Ini)

According to literature,2 a solution of copper(I) bromide (0.660 g, 4.60 mmol, 1.2 equiv.) and PMDETA (0.798 g, 4.60 mmol, 1.2 equiv.) in dry toluene (13 mL) was added to a solution of (1-bromoethyl) benzene (0.710 g, 3.84 mmol, 1.0 equiv.) and TEMPO (0.659 g, 4.22 mmol, 1.1 equiv.) in dry toluene (13 mL) under dry and oxygen free conditions. The reaction mixture was stirred at 50 °C for 1 h and subsequently filtered. The solvent was

removed under reduced pressure and the residue was purified by column chromatography on silica gel using toluene as eluent. The product was crystallized in the cold (5 °C) yielding NMP-Ini (0.765 g, 2.93 mmol, 76 %). ^{1}H NMR (400 MHz, CDCl$_3$, 25 °C): δ/ppm = 7.24 - 7.21 (m, 5 H), 4.70 (q, J = 6.5 Hz, 1 H), 1.49 - 0.95 (m, 18 H), 0.58 (br s, 3 H).

Synthesis of the Aldehyde Funtional Acrylamide Monomer (Aldehyde-Aa)

In a two step synthesis, first N-(4-(hydroxymethyl)phenyl)acrylamide was prepared. 4-Aminobenzyl alcohol (2 g, 16.2 mmol, 1 equiv.) was dissolved in a 1:1 (v/v) mixture of deionized water and dichloromethane (200 mL) and K$_2$CO$_3$ (5.6 g, 40.6 mmol, 2.5 equiv.) was added. The resulting mixture was stirred vigorously for 10 min, before acryloyl chloride (1.3 mL, 16.2 mmol, 1 equiv.) dissolved in dichloromethane (50 mL) was added dropwise over the course of 1 h. Afterwards, the solution was stirred at ambient temperature for 12 h. The organic phase was seperated, washed with 1 M HCl (2 × 50 mL) and dried over Na$_2$SO$_4$. After removal of the solvent, N-(4-(hydroxymethyl)phenyl)acrylamide was obtained as a pale yellow solid (2.59 g, 14.6 mmol, 90 %). ^{1}H NMR (400 MHz, DMSO-d$_6$, 25 °C): δ/ppm = 10.09 (s, 1H, H$_e$), 7.61 (d, J = 8.6 Hz, 2H, H$_d$), 7.27 (d, J = 8.6 Hz, 2H, H$_c$), 6.43 (m, 1H, H$_f$), 6.27 (m, 1H, H$_g$), 5.75 (m, 1H, H$_h$), 5.11 (t, J = 5.9 Hz, 1H, H$_a$), 4.45 (d, J = 5.4 Hz, 2H, H$_b$). ^{13}C{^{1}H} NMR (100 MHz, DMSO-d$_6$, 25 °C): δ/ppm = 163.49 (1C, C$_f$), 138.14 (1C, C$_b$), 138.08 (1C, C$_e$), 132.41 (1C, C$_g$), 127.46 (2C, C$_c$), 127.13 (1C, C$_h$), 119.57 (2C, C$_d$), 63.10 (1C, C$_a$).

ESI-MS: [M + Na$^+$]$_{exp}$ = 200,0676 and [M + Na$^+$]$_{calc}$ = 200,0687.

N-(4-formylphenyl)acrylamide (Aldehyde-Aa) was prepared by dissolving N-(4-(hydroxymethyl)phenyl)acrylamide (2.5 g, 14.1 mmol, 1 equiv.) in acetone (80 mL) and adding MnO$_2$ (24 g, 282.2 mmol, 20 equiv.). The resulting suspension was stirred at ambient temperature for 72 h. The solids were filtered of and the clear solution passed over a short column of basic alumina to remove the stabilizer that was present from the first step. After removal of the solvent N-(4-formylphenyl)acrylamide (Aldehyde-Aa) was obtained as a pale yellow solid (1.79 g, 10.21 mmol, 72 %). ^{1}H NMR (400 MHz, DMSO-d$_6$, 25 °C): δ/ppm = 10.54 (s, 1H, H$_a$), 9.89 (s, 1H, H$_c$), 7.88 (s, 4H, H$_b$), 6.47 (m, 1H, H$_d$), 6.34 (m, 1H, H$_e$), 5.84 (m, 1H, H$_f$). ^{13}C{^{1}H} NMR (100 MHz, DMSO-d$_6$, 25 °C): δ/ppm = 192.03 (1C, C$_a$), 164.17 (1C, C$_f$), 145.01 (1C, C$_e$), 131.97 (1C, C$_b$), 131.92 (1C, C$_g$), 131.31 (1C,

C_c), 128.53 (1C, C_h), 119.53 (1C, C_d). ESI-MS: $[M + Na^+]_{exp}$ = 198,0522 and $[M + Na^+]_{calc}$ = 198,0531.

Synthesis of the Boc-Hydrazine Funtional Acrylamide Monomer (Boc-Hydrazine-Aa)

In a two step synthesis, first tert-butyl 2-(4-aminobenzoyl)hydrazine-1-carboxylate was prepared. Boc-carbazate (8 g, 60.5 mmol, 2 equiv.), EDC·HCl (5.8 g, 30.2 mmol, 1 equiv.) and 4-DMAP (0.74 g, 6.04 mmol, 0.2 equiv.) were dissolved in dry dichloromethane (80 mL). The mixture was cooled to 0 °C before 4-aminobenzoic acid (4.14 g, 30.2 mmol, 1 equiv.) dissolved in dry DMF (20 mL) was added dropwise over the course of 2 h. The resulting mixture was allowed to warm to ambient temperature and was stirred for 24 h. Afterwards, the solids were filtered off and the solution was concentrated *in vacuo*. The residue was diluted with ethyl acetate (150 mL) and consecutively washed with sat. $NaHCO_3$ solution and 1 M HCl (100 mL each). The organic phase was dried over Na_2SO_4 and removed under reduced pressure. After column chromatography (silica gel, 2:1 ethyl acetate/cyclohexane, R_f = 0.3) tert-butyl 2-(4-aminobenzoyl)hydrazine-1-carboxylate was obtained as an off-white solid (4.86 g, 19.34 mmol, 64 %). ^{1}H NMR (400 MHz, DMSO-d_6, 25 °C): δ/ppm = 9.69 (s, 1H, H_b), 8.67 (s, 1H, H_c), 7.56 (d, J = 8.5 Hz, 2H, H_d), 6.55 (d, J = 8.5 Hz, 2H, H_e), 5.68 (s, 2H, H_f), 1.42 (s, 9H, H_a). ^{13}C{^{1}H} NMR (100 MHz, DMSO-d_6, 25 °C): δ/ppm = 166.45 (1C, C_d), 156.21 (1C, C_c), 152.55 (1C, C_h), 129.44 (2C, C_f), 119.50 (1C, C_e), 113.02 (2C, C_g), 79.35 (1C, C_b), 28.60 (3C, C_a). ESI-MS: $[M + Na^+]_{exp}$ = 274,1155 and $[M + Na^+]_{calc}$ = 274,1168.

tert-butyl 2-(4-acrylamidobenzoyl)hydrazine-1-carboxylate (Boc-Hydrazine-Aa) was prepared by dissolving tert-butyl 2-(4-aminobenzoyl)hydrazine-1-carboxylate (4.76 g, 18.94 mmol, 1 equiv.) in a 1:1 (v/v) mixture of deionized water and ethyl acetate (500 mL). After K_2CO_3 (6.5 g, 47.36 mmol, 2.5 equiv.) was added, the resulting mixture was stirred vigorously for 10 min, before acryloyl chloride (1.53 mL, 18.94 mmol, 1 equiv.) dissolved in ethyl acetate (50 mL) was added dropwise over the course of 1 h. Afterwards, the solution was stirred at ambient temperature for 12 h. The organic phase was seperated, washed with 1 M HCl (2 × 50 mL) and dried over Na_2SO_4. After removal of the solvent, the resulting solid was added to deionized water (100 mL) and the suspension was stirred for

24 h. tert-butyl 2-(4-acrylamidobenzoyl)hydrazine-1-carboxylate (Boc-Hydrazine-Aa) was obtained as a pale yellow solid after filtration (2.06 g, 6.8 mmol, 36 %). ^{1}H NMR (400 MHz, DMSO-d$_6$, 25 °C): δ/ppm = 10.39 (s, 1H, H$_b$), 10.08 (s, 1H, H$_c$), 8.86 (s, 1H, H$_e$), 7.79 (m, 4H, H$_d$), 6.45 (m, 1H, H$_f$), 6.32 (m, 1H, H$_g$), 5.81 (m, 1H, H$_h$), 1.43 (s, 9H, H$_a$). ^{13}C{^{1}H} NMR (100 MHz, DMSO-d$_6$, 25 °C): δ/ppm = 165.91 (1C, C$_j$), 163.94 (1C, C$_d$), 156.02 (1C, C$_c$), 142.51 (1C, C$_h$), 132.09 (1C, C$_k$), 128.79 (2C, C$_f$), 128.04 (1C, C$_e$), 127.69 (1C, C$_m$), 119.09 (2C, C$_g$), 79.60 (1C, C$_b$), 28.58 (3C, C$_a$). ESI-MS: [M + Na$^+$]$_{exp}$ = 328,1273 and [M + Na$^+$]$_{calc}$ = 328,1273.

4.6.2 Synthesis of the Parent Polymers

Synthesis of Poly(styrene-*co*-chloromethylstyrene) [P(S-*co*-CMS)$_{Pd}$]

Styrene (9 mL, 78.5 mmol, 180 equiv.), 4-(chloromethyl)styrene (1.244 mL, 8.82 mmol, 20 equiv.) and initiator 1 (114 mg, 0.438 mmol, 1 equiv.) were placed into a flame-dried Schlenk flask and deoxygenated by four consecutive freeze-pump-thaw cycles. Subsequently, the reaction mixture was placed into an oil bath tempered at 125 °C. After 5 h the polymerization was stopped by cooling the flask with liquid nitrogen and opening it to the atmosphere. The crude product was diluted with THF (20 mL) and precipitated twice into cold methanol (200 mL). The polymer P1 was afforded as a white powder by filtration and dried under high vacuum (2.6 g, 0.25 mmol). ^{1}H NMR (400 MHz, CDCl$_3$, 25 °C): δ/ppm = 7.26 - 6.20 (m, aromatic protons of PS and initiator), 4.65 - 4.39 (bs, CH_2Cl), 2.50 - 0.84 (m, aliphatic protons of PS and initiator). SEC (THF, RI): $M_{n,SEC}$ = 10 200 g mol^{-1}, $Đ$ = 1.17.

Post Modification of P(S-*co*-CMS)$_{Pd}$ with 4-(diphenylphosphino)benzoic acid (Pd-P)

P(S-*co*-CMS)$_{Pd}$ (1.0 g, 1 mmol CMS, number of CMS repeating units = 1 equiv.), 4-(diphenylphosphino) benzoic acid (459 mg, 1.5 mmol, 1.5 equiv.) and K$_2$CO$_3$ (415 mg, 3 mmol, 3 equiv.) were dissolved in dry DMF (10 mL) and stirred at 50 °C for 16 h under inert atmosphere. The reaction mixture was diluted with ethyl acetate (300 mL) and washed with brine (3×150 mL). The organic phase was separated and dried over Na$_2$SO$_4$. Subsequently, the solvent was removed under reduced pressure. The crude product

was diluted with THF (20 mL) and precipitated into cold methanol (200 mL). The functionalized linear precursor polymer Pd-P was afforded as a white solid by filtration and dried under high vacuum. (0.9 g, 0.07 mmol). ^{1}H NMR (400 MHz, CDCl$_3$, 25 °C): δ/ppm = 7.99 - 7.19 (m, aromatic protons of PPh$_2$Ar), 7.26 - 6.11 (m, aromatic protons of PS and initiator), 5.29 - 5.00 (bs, CH_2OC=O), 2.50 - 0.72 (aliphatic protons of PS and initiator). ^{31}P{^{1}H} NMR (160 MHz, CDCl$_3$, 25 °C): δ/ppm = 5.06 (s, PPh$_2$Ar). SEC (THF, RI): $M_{n,SEC}$ = 12 300 g mol^{-1}, $Đ$ = 1.16.

Synthesis of Poly(styrene-*co*-chloromethylstyrene) [P(S-*co*-CMS)$_{NITEC}$]

Styrene (6.375 g, 61.2 mmol, 160 equiv.), 4-(chloromethyl)styrene (2.335 g, 15.3 mmol, 40 equiv.) and NMP-Ini (100 mg, 0.083 mmol, 1 equiv.) were placed into a flame-dried Schlenk flask and deoxygenated by four consecutive freeze-pump-thaw cycles. Subsequently, the reaction mixture was placed into an oil bath tempered at 125 °C. After 6 h the polymerization was stopped by cooling the flask with liquid nitrogen and opening it to the atmosphere. The crude product was diluted with THF (20 mL) and precipitated twice into cold methanol (500 mL). The polymer was afforded as a white powder by filtration and dried under high vacuum (3.7 g, 0.32 mmol). ^{1}H NMR (400 MHz, CDCl$_3$, 25 °C): δ/ppm = 7.26 - 6.20 (m, aromatic protons of PS and initiator), 4.65 - 4.39 (s, CH_2Cl), 2.50 - 0.84 (m, aliphatic protons of PS and initiator). SEC (THF, RI): $M_{n,SEC}$ = 11 600 g mol^{-1}, $Đ$ = 1.20.

General Procedure for the Postpolymerization Modification of P(S-*co*-CMS)$_{NITEC}$

P(S-*co*-CMS)$_{NITEC}$, PG-Mal-COOH, Tet-COOH and Cs$_2$CO$_3$ were dissolved in DMF (15 mL) and stirred at 40 °C for 48 h. DMF was removed under reduced pressure, the remainder diluted with dichloromethane (80 mL) and washed with brine (150 mL). The organic phase was separated and dried over Na$_2$SO$_4$. Subsequently, the solvent was removed under reduced pressure. The crude product was diluted with THF (8 mL) and precipitated into cold methanol (150 mL). The functionalized linear precursor polymers NITEC-P1 - NITEC-P3 were afforded as off-white solids by filtration and dried under high vacuum. Stoichiometries and SEC (THF, RI) results for NITEC-P1 - NITEC-P3

are collated in Table 4.5. ^{1}H NMR NITEC-P1 (400 MHz, CDCl$_3$, 25 °C): δ/ppm = 8.38 - 7.89 (m, aromatic protons of Tet), 7.26 - 6.15 (m, aromatic protons of PS and initiator), 5.43 - 5.00 (s, CH_2OC=O), 3.92 - 3.77 (s, OCH_3), 2.50 - 0.72 (aliphatic protons of PS and initiator). ^{1}H NMR NITEC-P2, NITEC-P3 (400 MHz, CDCl$_3$, 25 °C): δ/ppm = 8.38 - 7.98 (m, aromatic protons of Tet), 7.23 - 6.04 (m, aromatic protons of PS and initiator), 5.42 - 5.14 (s, CH_2OC=O at Tet site and CHO of PG-Mal), 5.12 - 4.84 (s, CH_2OC=O at PG-Mal site), 4.30 - 4.17 (s, NCH$_2$CH_2O), 3.93 - 3.80 (s, OCH_3), 3.80 - 3.63 (s, NCH_2CH$_2$O), 2.90 - 2.78 (s, CH of PG-Mal), 2.69 - 2.51 (s, CH_2COO), 2.46 - 0.83 (aliphatic protons of PS and initiator).

Synthesis of Alkyne-Terminated Poly(styrene-*co*-chloromethylstyrene) (Alkyne-P(S-*co*-CMS)1-3)

P(S-*co*-CMS) copolymers, containing one alkyne functionality, with various copolymer compositions were prepared *via* the NMP of styrene (S) and 4-chloromethylstyrene (CMS) in the presence of Alkyne-NMP-Ini. The reaction mixture was degassed *via* three consecutive freeze-pump-thaw cycles and left under an argon atmosphere. The tube was subsequently placed in an oil bath tempered at 125 °C for 6 h (4.5 h for 5c). After the polymerization mixture was cooled to ambient temperature, it was diluted with THF (50 mL) and precipitated into methanol (500 mL). Next, the precipitate was filtered off and washed with methanol (2 × 50 mL). The obtained polymer was dried for 24 h under high vacuum at ambient temperature to afford a white solid. ^{1}H NMR (400 MHz, CDCl$_3$, 25 °C): δ/ppm = 7.17 - 6.15 (ArH of PS), 4.55 (s, OCH_2CCH), 4.44 (s, CH_2Cl), 3.95 (m, CHCH_2−OCO), 2.52 - 2.30 (m, OCCH_2CH_2CO), 1.78 - 1.18 (aliphatic protons of PS).

The number-average molar mass, weight-average molar mass, and the corresponding dispersity values of all of the following polymers (Alkyne-P(S-*co*-CMS) to Alkyne-PE-P) are collated in Table 4.12.

Functionalization of the Random Copolymers with the Photoenol Moiety (Alkyne-PE-P1''-3'')

Polymer Alkyne-P(S-*co*-CMS)1-3 (the number of CMS repeating units is 1 equiv.), potassium carbonate (2.5 equiv.), and 4-hydroxy-2,5-dimethylbenzophenone (PE-OH) (0.5 equiv.)

were dissolved in dry DMF (20 mL) and stirred at 70 °C for 16 h under an inert atmosphere. The reaction mixture was diluted with ethyl acetate (300 mL) and washed with brine (3 × 150 mL). The organic phase was dried over Na_2SO_4, and the solvent was removed under reduced pressure. The residue was dissolved in THF (30 mL) and precipitated into methanol (300 mL). The precipitate was filtered off and washed with methanol (2 × 30 mL). The obtained polymer was dried for 24 h under high vacuum at 25 °C to afford a white solid. ^{1}H NMR (400 MHz, CDCl$_3$, 25 °C): δ/ppm = 7.79 (s, ArH of PE-OH), 7.55 (s, ArH of PE-OH), 7.44 (s, ArH of PE-OH), 7.17 -6 .15 (ArH of PS), 5.02 (s, CH_2O), 4.55 (s, OCH_2C≡CH), 4.44 (s, CH_2Cl), 3.95 (m, CHCH_2−OCO), 2.52 (m, OCCH_2CH_2CO), 2.39 (s, CH_3), 2.22 (s, CH_3), 1.78 - 1.18 (aliphatic protons of PS).

Functionalization of the Random Copolymer with the Protected Maleimide Compound (Alkyne-PE-P1'-3')

Polymer Alkyne-PE-P1"-3" (the number of CMS repeating units is 1 equiv.), potassium carbonate (5 equiv.), and PG-Mal-COOH (0.5 equiv.) were dissolved in dry DMF (15 mL) and stirred at ambient temperature for 24 h under an inert atmosphere. The reaction mixture was diluted with ethyl acetate (300 mL) and washed with brine (3 × 150 mL). The organic phase was dried over Na_2SO_4, and the solvent was removed under reduced pressure. The residue was dissolved in THF (30 mL) and precipitated into methanol (300 mL). The precipitate was filtered off and washed with methanol (2 × 30 mL). The obtained polymer was dried for 24 h under high vacuum at 25 °C to afford a white solid. ^{1}H NMR (400 MHz, CDCl$_3$, 25 °C): δ/ppm = 7.79 (s, ArH of PE-OH), 7.55 (s, ArH of PE-OH), 7.44 (s, ArH of PE-OH), 7.17 - 6.15 (ArH of PS), 6.45 (s, C=CH of PG-Mal-COOH), 5.24 (s, OCH of PG-Mal-COOH), 5.02 (s, CH_2O), 4.55 (s, OCH_2C≡CH), 4.25 (s, CH$_2$CH_2O), 3.95 (m, CHCH_2−OCO), 3.75 (s, NCH_2CH$_2$), 2.85 (s, CH of PG-Mal-COOH), 2.61 (s,OCCH_2CH_2CO), 2.39 (s, CH_3), 2.22 (s, CH_3), 1.78 - 1.18 (aliphatic protons of PS).

One-Pot Functionalization of the Random Copolymer with the Photoenol Moiety and the Protected Maleimide Compound (Alkyne-PE-P1'-3')

Polymer Alkyne-P(S-*co*-CMS)1-3 (the number of CMS repeating units is 1 equiv.), potassium carbonate (10 equiv.), and 4-hydroxy-2,5-dimethylbenzophenone (0.5 equiv.) were

dissolved in dry DMF (20 mL) and stirred at 70 °C for 16 h. After cooling to ambient temperature, PG-Mal-COOH (0.5 equiv.) was added directly to the reaction mixture, and it was stirred at ambient temperature for an additional 24 h. The reaction mixture was diluted with ethyl acetate (300 mL) and washed with brine (3 × 250 mL). The combined organic phases were dried over Na_2SO_4, and the solvent was removed under reduced pressure. The residue was dissolved in THF (30 mL) and precipitated into methanol (300 mL). The precipitate was filtered off and washed with methanol (2 × 30 mL). The obtained polymer was dried for 24 h under high vacuum at ambient temperature to afford a white solid. ^{1}H NMR (400 MHz, CDCl$_3$, 25 °C): δ/ppm = 7.79 (s, Ar*H* of PE-OH), 7.55 (s, Ar*H* of PE-OH), 7.44 (s, Ar*H* of PE-OH), 7.17 - 6.15 (Ar*H* of PS), 6.45 (s, C=C*H* of PG-Mal-COOH), 5.24 (s, OC*H* of PG-Mal-COOH), 5.02 (s, C*H*$_2$O), 4.55 (s, OC*H*$_2$C≡CH), 4.25 (s, CH$_2$C*H*$_2$O), 3.95 (m, CHC*H*$_2$−OCO), 3.75 (s, NC*H*$_2$CH$_2$), 2.85 (s, C*H* of PG-Mal-COOH), 2.61 (s, OCC*H*$_2$C*H*$_2$CO), 2.39 (s, C*H*$_3$), 2.22 (s, C*H*$_3$), 1.78 - 1.18 (aliphatic protons of PS).

Removal of the Furan Protective Groups from the Maleimide Compounds along the Polymeric Backbone (Alkyne-PE-P1 - Alkyne-PE-P3)

Polymers Alkyne-PE-P1'-3' were dissolved in toluene (60 mL) and subsequently nitrogen was percolated through the mixture for 30 min to remove residual oxygen. The reaction mixture was stirred at 100 °C 15 h. The solvent was removed under reduced pressure. The residue was dissolved in THF (8 mL) and precipitated into methanol (40 mL). The precipitate was filtered off and washed with methanol (2 × 5 mL). The obtained polymer was dried for 24 h under high vacuum at ambient temperature to give a yellowish solid. ^{1}H NMR (400 MHz, CDCl$_3$, 25 °C): δ/ppm = 7.79 (s, Ar*H* of PE-OH), 7.55 (s, Ar*H* of PE-OH), 7.44 (s, Ar*H* of PE-OH), 7.17 - 6.15 (Ar*H* of PS), 6.65 (s, C=C*H* of Mal-COOH), 5.02 (s, C*H*$_2$O), 4.55 (s, OC*H*$_2$C≡CH), 4.25 (s, CH$_2$C*H*$_2$O), 3.95 (m, CHC*H*$_2$−OCO), 3.75 (s, NC*H*$_2$CH$_2$), 2.61 (s, OCC*H*$_2$C*H*$_2$CO), 2.39 (s, C*H*$_3$), 2.22 (s, C*H*$_3$), 1.78 - 1.18 (aliphatic protons of PS).

Table 4.12 Molar masses and dispersities for the polymers Alkyne-P(S-*co*-CMS), Alkyne-PE-P", Alkyne-PE-P', and Alkyne-PE-P as determined by SEC (THF, RI).

Polymer	M_n/g mol^{-1}	$Đ$	Polymer	M_n/g mol^{-1}	$Đ$
Alkyne-P(S-*co*-CMS)1	14900	1.16	Alkyne-PE-P1'	16000	1.15
Alkyne-P(S-*co*-CMS)2	14900	1.22	Alkyne-PE-P2'	16700	1.18
Alkyne-P(S-*co*-CMS)3	14700	1.27	Alkyne-PE-P3'	16200	1.19
Alkyne-PE-P1"	15100	1.15	Alkyne-PE-P1	15700	1.19
Alkyne-PE-P2"	15600	1.16	Alkyne-PE-P2	16500	1.33
Alkyne-PE-P3"	15000	1.18	Alkyne-PE-P3	20200	1.56

Functionalization of a Linear Precursor Copolymer *via* Copper(I)-Catalyzed Azide Alkyne Cycloaddition (PEG-PE-P3')

Alkyne-PE-P3' (1.00 g, 0.065 mmol), PEG-N$_3$ (0.26 g, 0.13 mmol), PMDETA (0.135 µL, 0.65 mmol), and CuBr (0.095 g, 0.65 mmol) were dissolved in DMF (10 mL) in a Schlenk tube, which was deoxygenated by five consecutive freeze-pump-thaw cycles. The resulting mixture was stirred at ambient temperature for 24 h before the copper catalyst was removed by passing the solution over a short column of neutral alumina. The solvent was removed under reduced pressure. The residue was dissolved in THF (10 mL) and precipitated into methanol (100 mL). The precipitate was filtered off and washed with methanol (2 × 10 mL). The obtained polymer was dried for 24 h under high vacuum at ambient temperature to give a white solid. ^{1}H NMR (400 MHz, CDCl$_3$, 25 °C): δ/ppm = 7.79 (s, Ar*H* of PE-OH), 7.55 (s, Ar*H* of PE-OH), 7.44 (s, Ar*H* of PE-OH), 7.17 - 6.15 (Ar*H* of PS), 6.45 (s, C=C*H* of PG-Mal-COOH), 5.24 (s, OC*H* of PG-Mal-COOH), 5.02 (s, C*H*$_2$O), 4.51 (s, C*H*$_2$ next to triazole), 4.25 (s, CH$_2$C*H*$_2$O), 3.95 (m, CHC*H*$_2$−OCO), 3.75 (s, NC*H*$_2$CH$_2$), 3.64 (s, PEG backbone), 3.38 (s, OC*H*$_3$), 2.85 (s, CH of 2), 2.61 (s, OCC*H*$_2$C*H*$_2$CO), 2.39 (s, C*H*$_3$), 2.22 (s, C*H*$_3$), 1.78 - 1.18 (aliphatic protons of PS). SEC (THF, RI): $M_{n,SEC}$ = 19 400 g mol^{-1}; $M_{m,SEC}$ = 22 700 g mol^{-1}; $Đ$ = 1.17.

Removal of the Furan Protective Groups from the Maleimide Compounds along the Polymeric Backbone of the PEG Functionalized Polymer (PEG-PE-P3)

The retro-Diels–Alder reaction of PEG-PE-P3' was performed in the same fashion as described for polymers Alkyne-PE-P1 - Alkyne-PE-P3. ^{1}H NMR (400 MHz, CDCl$_3$, 25 °C):

δ/ppm = 7.79 (s, ArH of PE-OH), 7.55 (s, ArH of PE-OH), 7.44 (s, ArH of PE-OH), 7.17 - 6.15 (ArH of PS), 6.65 (s, C=CH of PG-Mal-COOH), 5.02 (s, CH_2O), 4.51 (s, CH_2 next to triazole), 4.25 (s, CH$_2$CH_2O), 3.95 (m, CHCH_2−OCO), 3.75 (s, NCH_2CH$_2$), 3.64 (s, PEG backbone), 3.38 (s, OCH_3), 2.61 (s, OCCH_2CH_2CO), 2.39 (s, CH_3), 2.22 (s, CH_3), 1.78 - 1.18 (aliphatic protons of PS). SEC (THF, RI): $M_{\mathrm{n,SEC}}$ = 19 200 g mol^{-1}; $M_{\mathrm{m,SEC}}$ = 24 500 g mol^{-1}; $Đ$ = 1.28.

Synthesis of a Water-soluble Random Copolymer of DMAa, Aldehyde-Aa, and Boc-Hydrazine-Aa (pH-P')

EMP (25.1 mg, 0.112 mmol, 1 equiv.), DMAa (2 g, 20.2 mmol, 180 equiv.), Aldehyde-Aa (196.2 mg, 1.12 mmol, 10 equiv.), Boc-Hydrazine-Aa (341.9 mg, 1.12 mmol, and 2,2-azobis(2-methylpropionitrile) (AIBN) (3.7 mg, 0.022 mmol, 0.2 equiv.) were dissolved in DMF (8 mL). The yellow solution was degassed by purging it with argon for 15 min. Subsequently, a t = 0 sample for NMR analysis of the conversion was withdrawn. Then the sealed flask was emerged into an oil bath and the mixture was polymerized at 60 °C for 15 h. The polymerization was stopped by cooling with liquid nitrogen. The t = end sample for NMR analysis was withdrawn before the crude polymer was dialyzed against water (MWCO = 1000 Da) for 2 days. After lyophilization the polymer was received as a light yellow solid (954 mg). ^{1}H NMR (400 MHz, DMSO-d^6, 25 °C): δ/ppm = 10.45 - 10.10 (bs, 1H, H^{f}, NH of Aldehyde-Aa), 10.12 - 9.94 (bs, 2H, H^{b}), 9.92 - 9.74 (bs, 1H, H^{a}), 9.05 - 8.61 (bs, 1H, H^{d}, NH of Boc-Hydrazine-Aa), 7.94 - 7.39 (m, 8H, ArH of Aldehyde-Aa and Boc-Hydrazine-Aa), 3.06 - 2.58 (m, 6H, H^{e}), 2.54 - 2.13 (m, 1H, H^{g}), 1.81 - 1.03 (m, 2H, H^{h}), 1.42 (s, 9H, H^{c}). SEC (DMAc, RI): $M_{\mathrm{n,SEC}}$ = 29 400 g mol^{-1}; $M_{\mathrm{m,SEC}}$ = 41 000 g mol^{-1}; $Đ$ = 1.39.

Deprotection of the Boc-Hydrazine Units in pH-P' (pH-P)

In an examplary reaction, the pH-P' polymer (30 mg) was dissolved in deionized water (2 mL) and TFA (2 mL) was added slowly. The solution was stirred at ambient temperature for 24 h and the deprotected polymer pH-P was used for the subsequent reactions without further purification.

4.6.3 Synthesis of the Single-Chain Structures

Single-Chain Nanoparticle Formation by Intramolecular Crosslinking with Pd(II)-Ions

A solution of the functionalized, linear precursor copolymer Pd-P (50 mg, 0.04 mmol ligand moieties, 1 equiv.) in DCM (dry) ($c_{\text{precursor}} = 2.5\,\text{mg}\,\text{mL}^{-1}$) was added dropwise to a stirred solution of Pd(COD)Cl$_2$ (6 mg, 0.02 mmol, 0.5 equiv.) in 20 mL DCM (dry) by syringe pump ($1\,\text{mL}\,\text{h}^{-1}$) at ambient temperature in a flame dried Schlenk flask. After the addition the solution was stirred for an additional hour, then it was concentrated *in vacuo* and the SCNPs were precipitated in cold methanol. Filtration and drying under high vacuum afforded the product as a yellow solid (35 mg). ^{1}H NMR (400 MHz, CDCl$_3$, 25 °C): δ/ppm = 8.11 - 7.19 (m, aromatic protons of Pd—PPh$_2$Ar), 7.26 - 6.11 (m, aromatic protons of PS and initiator), 5.29 - 5.00 (bs, CH_2OC=O), 2.50 - 0.72 (aliphatic protons of PS and initiator). ^{31}P{^{1}H} NMR (160 MHz, CDCl$_3$, 25 °C): δ/ppm = 23.54 (s, PPh$_2$Ar—PdCl$_2$—PPh$_2$Ar).

General Procedure for the Photo-induced Single-Chain Nanoparticle Formation *via* NITEC

Solutions of the functionalized, parent copolymers in THF ($c_{\text{precursor}} = 0.017\,\text{mg}\,\text{mL}^{-1}$) were irradiated for 60 min in a custom build photoreactor (see Figure 4.33 for an illustration) with a 36 W compact low-pressure UV-A fluorescent lamp emitting at $\lambda_{\text{max}} = 320\,\text{nm}$. The solvent was removed under reduced pressure to afford the (pro)fluorescent single-chain nanoparticles NITEC-SCNP1 - NITEC-SCNP3, which were directly dissolved in the appropriate solvent for analysis.

Single-Chain Nanoparticles *via* Intramolecular Photoinduced Diels–Alder Cross-Linking (Alkyne-PE-SCNP1 - Alkyne-PE-SCNP3 and PEG-PE-SCNP3)

The polymers Alkyne-PE-P1 - Alkyne-PE-P3, and PEG-PE-P3 (4 mg) were each dissolved in 240 mL of CH$_2$Cl$_2$ in a round-bottom flask, sealed airtight with a septum, and flushed with nitrogen for approximately 1.5 h. The solution was subsequently irradiated for 30 min in a custom-built photoreactor with a 36 W compact low-pressure UV-A fluorescent lamp
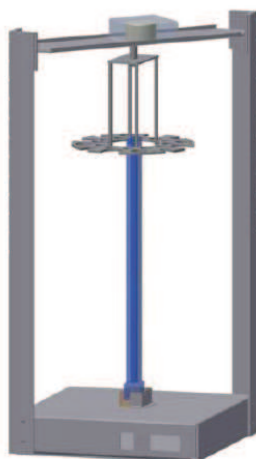
Figure 4.33 Illustration of the custom-built photoreactor employed in the current study. Reused with permission from Reference [221]. Copyright 2014 American Chemical Society.

emitting at $\lambda_{\mathrm{max}} = 320\,\mathrm{nm}$. Afterwards, the solvent was removed under reduced pressure to yield the SCNPs, which were directly dissolved in the appropriate solvent for analysis.

General Procedure for th Single-Chain Nanoparticle Formation *via* Intramolecular Hydrazone Formation (pH-SCNP)

An aliquot $0.5\,\mathrm{mL}$ of the solution of the deprotected polymer pH-P ($c = 7.5\,\mathrm{mg\,mL^{-1}}$) were slowly added to deionized water ($10\,\mathrm{mL}$) and the solution was left to stir over night at ambient temperature. Subsequently, the solution was adjusted to basic pH (≈ 12) with $\mathrm{NaOH_{(s)}}$ and then stirred for $2\,\mathrm{h}$, before the mixture was dialyzed against water ($\mathrm{MWCO} = 1000\,\mathrm{Da}$) for $24\,\mathrm{h}$. The resulting pH-SCNPs were dissolved in the appropriate solvent for analysis.

4.6.4 Miscellaneous

Sonogashira Coupling Utilizing Pd-SCNP as Catalyst

According to a modified literature procedure,[227] 2-bromopyridine ($476\,\mathrm{\mu L}$, $5\,\mathrm{mmol}$, $1\,\mathrm{equiv.}$), phenylacetylene ($549\,\mathrm{\mu L}$, $5\,\mathrm{mmol}$, $1\,\mathrm{equiv.}$) and the catalyst Pd-SCNP (see Table 4.3 for the employed amounts) were dissolved in diethylamine ($2\,\mathrm{mL}$) in a flame-dried Schlenk tube. The mixture was degassed by purging the solution with argon for $5\,\mathrm{min}$. Next, CuI ($4.8\,\mathrm{mg}$, $0.02\,\mathrm{mmol}$, $0.05\,\mathrm{equiv.}$) was added and the reaction was conducted for

24 h at ambient temperature. Subsequently, the tube was opened to the atmosphere and the mixture was diluted with Et_2O (10 mL). The organic layer was filtered and washed with distilled H_2O (2×20 mL). The organic layer was dried over Na_2SO_4 and evaporated under reduced pressure to afford the crude product. After 24 h under high vacuum the product was obtained as a brown liquid.

Functionalization of Maleimide-bearing Microspheres with NITEC-SCNP1

A solution of NITEC-P1 in THF ($c_{\mathrm{precursor}} = 0.017\,\mathrm{mg\,mL^{-1}}$) was irradiated for 5 min in a custom build photoreactor with a 36 W compact low-pressure UV-A fluorescent lamp emitting at $\lambda_{\mathrm{max}} = 320$ nm. The solvent was removed under reduced pressure and the residue redissolved in THF (1 mL). Maleimide-functional microspheres (2 mg) were added and the sample was irradiated for additional 55 min. The SCNP-functionalized microspheres were afforded by filtration and dried under high vacuum.

Preparation of the Deuterated Buffer Solutions

The 0.1 M deuterated acetate buffer was prepared by dissolving sodium acetate-d_3 (17 mg) in D_2O (2 mL) and adding acetic acid-d_4 (11.5 µL), which resulted in a pH of 4.76. The 0.1 M deuterated ammonium buffer was prepared by dissolving ND_4Cl (11.5 mg) in D_2O (1.9576 mL) and adding ND_4OD solution (25 wt.% in D_2O, 42.4 µL), which resulted in a pH of 9.2. The pH values were determined with a inoLab Level 1 pH meter (WTW) equipped with a Sentix® Mic electrode, which was calibrated by a two point method in the basic as well as the acidic regime prior to use.

4.6.5 Crystallographic Appendix

X-ray crystallographic studies: A suitable crystal was covered in mineral oil (Aldrich) and mounted on a glass fiber. The crystal was transferred directly to the cold stream of a STOE IPDS 2 diffractometer. All structures were solved by direct methods or by the Patterson method (SHELXS-2013).[228] The remaining non-hydrogen atoms were located from difference in Fourier map calculations. The refinements were carried out by using full-matrix leastsquares techniques on F, minimizing the function $(F_0 - F_c)^2$, where the weight is defined as $4F_0{}^2/2(F_0{}^2)$ and F_0 and F_c are the observed and and calculated

structure factor amplitudes using the program SHELXL-2013.[228] Carbon-bound hydrogen atom positions were calculated. The locations of the largest peaks in the final difference Fourier map calculation as well as the magnitude of the residual electron densities in each case were of no chemical significance. Crystallographic data (excluding structure factors) for the structures reported in this paper have been deposited with the Cambridge Crystallographic Data Centre as a supplementary publication no. CCDC 1060115-1060116. Copies of the data can be obtained free of charge on application to CCDC, 12 Union Road, Cambridge CB21EZ, UK (fax: (+(44)1223-336-033; email: deposit@ccdc.cam.ac.uk).
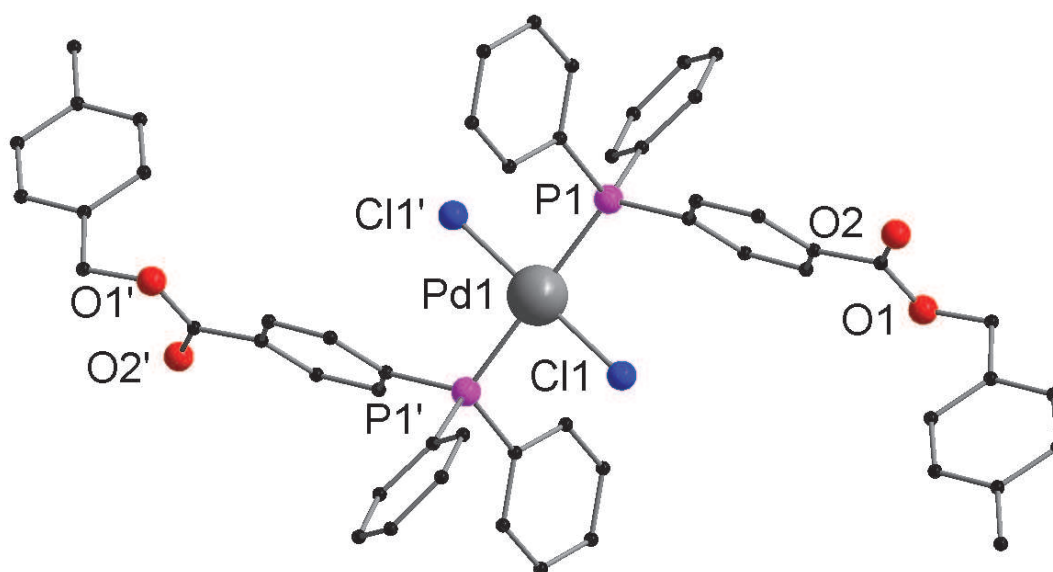
Figure 4.34 Solid-state structure of $[Pd(L_1)_2Cl_2]$. Hydrogen atoms are omitted for clarity. Reused from Reference [217] - Published by The Royal Society of Chemistry.

Table 4.13 Crystal data and structure refinement for $[Pd(L_1)_2Cl_2]$.

Empirical formula	$C_{54}H_{46}Cl_2O_4P_2Pd$
Formula weight	998.15
Temperature / K	200.15
Crystal system	triclinic
Space group	P-1
a / Å	9.5159(19)
b / Å	9.961(2)
c / Å	14.355(3)
α / °	72.77(3)
β / °	70.85(3)
γ / °	66.35(3)
Volume / Å^3	1155.9(5)
Z	1
ρ_{calc} / g cm^{-3}	1.434
μ / mm^{-1}	0.633
F(000)	512.0
Crystal size / mm^3	$0.336 \times 0.217 \times 0.071$
Radiation	MoKα ($\lambda = 0.71073$)
2Θ range for data collection / °	3.06 to 51.998
Index ranges	$-11 \leq h \leq 11$, $-12 \leq k \leq 12$, $-17 \leq l \leq 17$
Reflections collected	8439
Independent reflections	4449 [$R_{int} = 0.0455$, $R_{sigma} = 0.0529$]
Data/restraints/parameters	4449/0/287
Goodness-of-fit on F^2	0.955
Final R indexes [I>=2σ (I)]	$R_1 = 0.0315$, $wR_2 = 0.0735$
Final R indexes [all data]	$R_1 = 0.0421$, $wR_2 = 0.0756$
Largest diff. peak/hole / e Å^{-3}	0.85/-0.47

Table 4.14 Crystal data and structure refinement for [Pd(L$_2$)$_2$Cl$_2$].

|	
Empirical formula	C$_{56}$H$_{50}$Cl$_2$O$_4$P$_2$Pd
Formula weight	1026.20
Temperature / K	150.15
Crystal system	triclinic
Space group	P-1
a / Å	10.118(2)
b / Å	14.622(3)
c / Å	17.316(4)
α / °	89.46(3)
β / °	87.53(3)
γ / °	73.09(3)
Volume / Å^3	2448.8(9)
Z	2
ρ_{calc} / g cm^{-3}	1.392
μ / mm^{-1}	0.600
F(000)	1056.0
Crystal size / mm^3	0.35 × 0.194 × 0.068
Radiation	MoKα (λ = 0.71073)
2Θ range for data collection / °	3.738 to 52
Index ranges	-11 ≤ h ≤ 12, -18 ≤ k ≤ 18, -21 ≤ l ≤ 21
Reflections collected	18856
Independent reflections	9493 [R$_{int}$ = 0.0607, R$_{sigma}$ = 0.0804]
Data/restraints/parameters	9493/0/607
Goodness-of-fit on F^2	0.866
Final R indexes [I>=2σ (I)]	R$_1$ = 0.0322, wR$_2$ = 0.0654
Final R indexes [all data]	R$_1$ = 0.0556, wR$_2$ = 0.0745
Largest diff. peak/hole / e Å^{-3}	1.09/-0.54
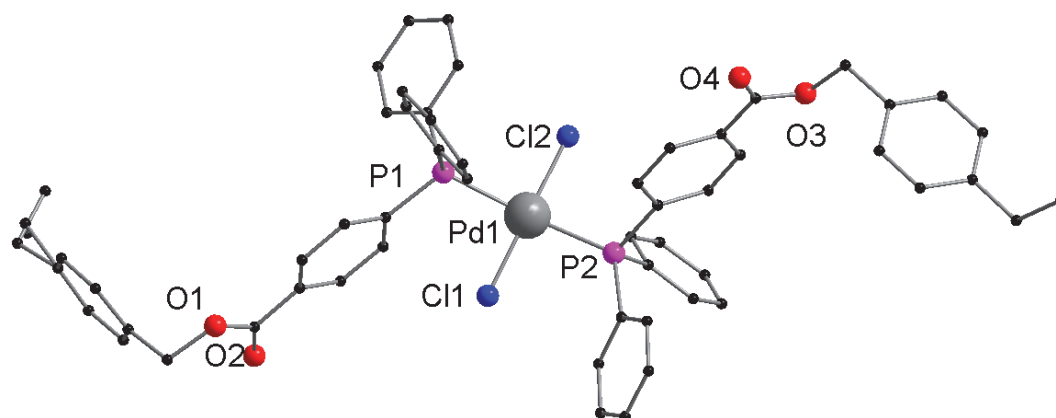
Figure 4.35 Solid-state structure of $[Pd(L_2)_2Cl_2]$. Hydrogen atoms are omitted for clarity. Reused from Reference [217] - Published by The Royal Society of Chemistry.

5 | Materials and Characterization

A list of employed materials and details about the analytical instrumentation and procedures are found in the subsequent sections.

5.1 Materials

(+)-sodium L-ascorbate (98 %, Sigma Aldrich), 1-(3-dimethylaminopropyl)-3-ethylcarbodiimide hydrochloride (EDC, >98 %, TCI), (1-bromoethyl)benzene (Merck), 1,4-dioxane (HPLC-grade, VWR), 2,2,6,6-tetramethylpiperidinooxy (TEMPO, 98 %, Acros), 2,5-dimethyl-4-hydroxybenzophenone (BASF), 2-bromoisobutyric acid (98 %, Sigma Aldrich), 2-bromopyridine (99 %, Alfa Aesar), 3,3'-disulfanediyldipropanoic acid (99 %, ABCR), 4-(diphenylphosphino)benzoic acid (97 %, Acros), 4-dimethylaminopyridine (DMAP, 99 %, Acros), anisole (99 %, extra pure, Acros), benzyl chloride (99 %, stabilized, Alfa Aesar), carbon disulfide (99.9 %, Acros), chloroform-d$_1$ (CDCl$_3$, 99.8 %, EURISO-TOP), copper(I) bromide (99 %, ABCR), copper(I) iodide (CuI, 99.999 %, PURATREM, ABCR), Cs$_2$CO$_3$ (99.9 %, Merck), cupric sulfate pentahydrate (99.5 %, Sigma Aldrich), deuterium oxide (D$_2$O, 99.9 %, EURISO-TOP), dibenzoyl peroxide (75 %, remainder water, Acros), dichloro(1,5-cyclooctadiene)palladium(II) ([Pd(COD)Cl$_2$], 99 %, ABCR), dichloromethane (DCM, 99.8 %, extra dry, over molecular sieve, stabilized, Acros), diethylamine (>99 %, extra pure, Acros), dimethyl sulfoxide-d$_6$ (DMSO-d$_6$, 99.8 %, EURISO-TOP), dithiothreitol (DTT, ABCR), ethanol amine (Sigma Aldrich), ethylene bis(2-bromoisobutyrate) (Sigma Aldrich), ethylenediaminetetraacetic acid disodium salt (EDTA, 99 %, ABCR), furane (Acros), HCl (37 %, Carl Roth), K$_2$CO$_3$ (99 %, Merck), maleic anhydride (99 %, Acros), N,N'-dicyclohexylcarbodiimide (DCC, 99 %, ABCR), N,N-diisopropylethylamine (DIPEA, >99.5 %, Acros), N,N-dimethylformamide (DMF, 99 %, extra pure, Acros), N,N-dimethylformamide (DMF, 99.8 %, extra dry, Acros), Na$_2$SO$_4$ (99 %, Carl Roth),

NaNO$_2$ (98 %, Alfa Aesar), NaOH (Carl Roth), oxalyl chloride (98 %, Acros), *p*-anisidine (99 %, ABCR), phenylacetylene (98 %, pure, Acros), potassium phosphate monohydrate (puriss., Sigma Aldrich), propargyl alcohol (99 %, Alfa Aesar), propargyl bromide solution (80 wt.% in toluene, Alfa Aesar), p-toluene sulfonyl hydrazide (98 %, Alfa Aesar), *p*-toluenesulfonic acid monohydrate (99 %, Sigma Aldrich), pyridine (99 %, ABCR), silica gel (Geduran SI60 0.063-0.200 mm, Merck), sodium azide (99 %, Acros), succinic anhydride (99 %, Sigma Aldrich), tetrahydrofuran-d$_8$ (THF-d$_8$, 99.5 %, EURISO-TOP), tin(II) 2-ethylhexanoate (Sn(EH)$_2$, 95 %, Sigma Aldrich), triethylamine (99 %, Acros), and tris(2-aminoethyl)amine (Me$_6$TREN, 96 %, Sigma Aldrich) were used as received.

2,2'-Azobis(2-methylpropionitrile) (AIBN, 99 %, Fluka) was recrystallized twice from methanol. 4-chloromethyl styrene (Acros) was distilled prior to usage and stored at $-19\,°$C. *N,N*-dimethylacrylamide (DMAa, 99 %, TCI) was passed over a short column of basic alumina prior to usage. Styrene (Sigma Aldrich) was passed over a column of basic alumina (Acros) and stored at $-19\,°$C. *N,N*-dimethylformamide, THF, DCM, diethylether, ethyl acetate, *n*-hexane, toluene, 2-propanol, ethanol, and methanol were purchased as analytical grade solvents (Sigma Aldrich) and used as received. Anhydrous DCM and THF were purchased from Acros (extra dry over molecular sieves) and used as received. All other solvents were of analytical grade and used as received.

5.2 Characterization

Atomic Force Microscopy (AFM)

AFM for NITEC-SCNP2

Sample Preparation: Freshly prepared and dried NITEC-SCNP2 ($\approx 1\,$mg) was dissolved in dichloromethane (1 mL) (VWR, Normapur). 7.5 µL of the 1:10000 stock solution (stepwise diluted with dichloromethane) were pipetted on a freshly cleaved muscovite disc of 12 mm diameter and spread-dried under a weak nitrogen gas stream. The muscovite disc was then transferred on a 12 mm diameter carbon Leit-Tab (Plano GmbH) prefixed on a 12 mm metal disc. In order to remove residual organic solvent, the samples were desiccated for 5 min in vacuum and subsequently vented with argon gas before AFM analysis.

Sample Measurements: AFM analysis was performed on a MultiMode 2 AFM (Bruker) equipped with a scanner type "E" at a scan range of 1 µm, at a scan speed of 0.5 Hz, with a resolution of 512 lines and points and a scan angle of 0°. A Silicon nitrate cantilever was used with a typical resonant frequency of 75 kHz and force constant of approximately 2.8 N m^{-1} (MikroMasch, HQ:NSC18/No Al). The image data were processed with the NanoScope Analysis 1.40 software (Bruker).

AFM for Alkyne-PE-SCNP1

Sample Preparation: Mica discs, double-sided carbon tabs and metal specimen used for particle sample preparation are purchased from TED PELLA, Inc., Redding, USA. 14 mm mica discs were freshly cleaved in dichloromethane and separately stored in dichloromethane over night, before being used as substrates for particle adsorption. 10 µL of particle suspension (8 µg mL^{-1} in DCM) were spread on N$_2$ dried substrate by a constant N$_2$ gas flow immediately after deposition. To prevent electrical charge effects during the scanning process, the samples were put on double-sided carbon tabs prefixed on a 10 mm metal specimen disc prior to force microscopy. Samples were dried for 30 min at 333 K and stored, protected from light, under vacuum until AFM analysis.

Sample Measurements: Atomic force microscopy was performed on an MFP-3D-BIO AFM (Asylum Research, Santa Barbara, USA) equipped with an electric sample holder and a standard cantilever holder. The electric sample holder was used to ground sample charges by contacting the mica sample surface with a conductive clamp. A silicone HQ:NSC18/No Al cantilever (MikroMasch, Lady's Island, USA) was used in intermittent contact mode (AC-Mode), at 1 µm scan size, 0.5 Hz scan rate and a resolution of 512 or 384 scan lines and points.

Dynamic Light Scattering (DLS)

Dynamic light scattering (DLS) was performed on a NICOMP 380 DLS spectrometer (Particle Sizing Systems, Santa Barbara, USA) with a 90 mW laser diode operating at 658 nm equipped with an avalanche photodiode detector. The sample solutions were prepared by dissolving the sample in the appropriate solvent and subsequent filtering over a 0.2 µm filter. The measurements were performed in automatic mode and evaluated

with a standard Gaussian and an advanced evaluation method, the latter using an inverse Laplace algorithm to analyze for multimodal distributions. Numbers given in the text are the number weighted average values as calculated by the NICOMP evaluation. All measurements were determined at 90° to the incident beam.

Electrospray Ionization Mass Spectrometry (ESI-MS)

Electrospray ionization-mass spectrometry (ESI-MS) spectra were recorded on a LXQmass spectrometer (ThermoFisher Scientific, San Jose, CA) equipped with an atmospheric pressure ionization source operating in the nebulizer-assisted electrospray mode. The instrument was calibrated in the m/z range 195-1822 Da using a standard containing caffeine, Met-Arg-Phe-Ala acetate (MRFA), and a mixture of fluorinated phosphazenes (Ultramark 1621) (all from Aldrich). A constant spray voltage of 4.5 kV was used, and nitrogen at a dimensionless sweep gas flow rate of 2 ($\approx$ 3 L min^{-1}) and a dimensionless sheath gas flow rate of 12 ($\approx$ 1 L min^{-1}) were applied. The capillary voltage, the tube lens offset voltage, and the capillary temperature were set to 60 V, 110 V, and 300 °C, respectively. The samples were dissolved with a concentration of 0.1 mg mL^{-1} in a mixture of THF and MeOH (3:2) containing 100 µmol of sodium triflate and infused with a flow of 10 µL min^{-1}.

ESI-MS analysis of the materials of Section 4.4 was performed on a Q Exactive (Orbitrap) mass spectrometer (Thermo Fisher Scientific, San Jose, CA, USA) equipped with an HESI II probe. The instrument was calibrated in the m/z range 74-1822 Da using premixed calibration solutions (Thermo Scientific). A constant spray voltage of 4.7 kV and a dimensionless sheath gas of 5 were applied. The capillary temperature and the S-lens RF level were set to 320 °C and 62.0, respectively. The samples were dissolved with a concentration of 0.05 mg mL^{-1} in a mixture of THF and MeOH (3:2) containing 100 µmol of sodium triflate and infused with a flow of 5 µL min^{-1}.

Fluorescence Microscopy

A drop of Mowiol (Hoechst) was applied on a microscope slide. Then 0.5 mg of the microspheres were added to the Mowiol and stirred well. Afterwards, the sample was capped with a cover slip and stored for 24 h at room temperature to let the Mowiol solidify.

The examination of the sample was performed on a confocal laser scanning microscope (LSM 510 Meta, Zeiss) with a 63x NA 1.4 objective lens. The 3D reconstruction of the confocal image stack was prepared with Volocity (version 4.3.2, Perkin Elmer).

Fluorescence Spectroscopy

Fluorescence spectra were measured on a Jobin–Yvon Fluoromax 3 fluorimeter with a step width of 1 nm and an integration time of 0.2 s. All spectra were recorded in DMF ($c = 40\,\mathrm{mg\,L^{-1}}$) at 20 °C and are corrected for Raman emission from water. Fluorescence emission spectra for the kinetic investigation were recorded in quartz cuvettes loaded with a sample volume of 230 µL on a Varian Cary Eclipse Fluorescence Spectrometer.

Nuclear Magnetic Resonance (NMR) Spectroscopy

The synthesized compounds were analyzed *via* ^{1}H, ^{13}C$\{^1$H$\}$, and ^{31}P$\{^1$H$\}$ NMR spectroscopy using a Bruker Avance 400 spectrometer (^{1}H, 400 MHz; ^{13}C, 100 MHz; ^{31}P, 160 MHz). Samples were dissolved in the appropriate solvent. The δ-scale was referenced with the solvent residual peak. Abbreviations used in the description of the materials' syntheses include singlet (s), broad singlet (bs), doublet (d), triplet (t), quartet (q), broad multiplet (bm), and unresolved multiplet (m).

The transversal relaxation time T_2 was measured by applying the Carr-Purcel-Meiboom-Gill (CPMG) echo train acquisition. The 90° pulses were 9.14 µs, the relaxation delay 3 s, and the fixed echo time 0.001 s. Processing was achieved using Topspin 3.1 with the Dynamics Center 2.0.4 software. The resulting decay curves were fitted with a mono exponential decay function to calculate T_2:

$$I(T) = I(0)exp(-\frac{t}{T_2}) \tag{5.1}$$

NOESY experiments were performed on a 600 MHz Bruker Avance III spectrometer equipped with a ^{1}H, ^{13}C, ^{15}N-TCI inversely detecting cryoprobe at a temperature of 295 K or 320 K. The mixing time was set to 200 µs. The 90° pulse was determined to be 8.7 µs. Spectra were recorded with 4k × 1k complex data points using 16 or 20 scans per t1 increment and 16 dummy scans at 25 °C and 50 °C. The spectral width was set to 8 × 8 ppm which leads to a total experiment time of 5 h, 33 min, and 43 s and 6 h,

57 min, and 4 s, respectively. After zero filling to 4k × 2k points and apodization, using a 90°-phase shifted squared sine function, the spectra were Fourier transformed.

DOSY experiments for the selective point folding system presented in Section 3.2 were performed on a 400 MHz Bruker Avance III spectrometer equipped with a broadband ^{1}H decoupling probe (PABBO) using an Eddy current compensated bipolar gradient pulse sequence (BPLED),[229] at a temperature of 298 K. Proton pulse lengths were determined to be 11.15 µs and bipolar gradients of $\delta = 4.8$ - 6.4 ms (depending on the diffusion behavior of the measured sample) length were incremented from $G = 1 \, \text{G cm}^{-1}$ to $49 \, \text{G cm}^{-1}$ in 32 steps. 8 scans with 12k complex data points were recorded for each increment with 8 dummy scans per experiment, leading to an overall experiment time of 20 min and 31 s seconds per sample. The diffusion delay Δ was set to 100 µs. Processing was achieved using Topspin 3.1 with the Dynamics Center 2.0.4. After zero filling to 24k points and apodization using an exponential window function with an additional linewidth of 0.1 Hz, 1D increment spectra were Fourier transformed and the signal decay due to gradients was fitted using Equation 5.2.

$$f(G) = I_0^2 exp(-\gamma_H^2 G^2 \delta^2 (\Delta - \frac{\delta}{3})D) \qquad (5.2)$$

with the proton gyromagnetic ratio γ_H and the full signal intensity I_0. Corresponding diffusion coefficients D of the polymer signals and the solvent are the result of the fitting procedure and are plotted against chemical shifts in Figure 3.17. As alluded to in Section 2.3, the signal attenuation needs to be slightly adjusted when the BPLED pulse sequence is used. However, the correction value of $\frac{\tau}{2}$ is negligible, since it is small compared to $\frac{\delta}{3}$.

DOSY experiments for the pH-responsive SCNPs presented in Section 4.4 were performed on a 400 MHz Bruker Avance III spectrometer equipped with a broadband ^{1}H decoupling probe (PABBO) using an Eddy current compensated bipolar gradient pulse sequence (BPLED),[229] at a temperature of 298 K. Proton pulse lengths were determined to be 9.14 µs and bipolar gradients of $\delta = 6.4$ - 11 ms (depending on the diffusion behavior of the measured sample) length were incremented from $G = 1 \, \text{G cm}^{-1}$ to $49 \, \text{G cm}^{-1}$ in 32 steps. 8 scans with 12k complex data points were recorded for each increment with 8 dummy scans per experiment, leading to an overall experiment time of 20 min and 31 s

seconds per sample. The diffusion delay Δ was set to $100\,\mu s$. Processing was achieved using Topspin 3.1 with the Dynamics Center 2.0.4. After zero filling to 24k points and apodization using an exponential window function with an additional linewidth of $0.1\,Hz$, 1D increment spectra were Fourier transformed and the signal decay due to gradients was fitted using Equation 5.2.

Size Exclusion Chromatography (SEC)

THF-SEC measurements were performed on a Polymer Laboratories PL-GPC 50 Plus Integrated System, comprising an autosampler, a PLgel $5\,\mu m$ bead-size guard column $(50 \times 7.5\,mm)$ followed by three PLgel $5\,\mu m$ Mixed-C and one PLgel $3\,\mu m$ Mixed-E columns $(300 \times 7.5\,mm)$ and a differential refractive index detector using THF as the eluent at $35\,°C$ with a flow rate of $1\,mL\,min^{-1}$. The SEC system was calibrated using linear poly(styrene) (PS) standards ranging from 474 to $2.5 \times 10^6\ g\,mol^{-1}$. Calculation of the molecular weight proceeded *via* the Mark-Houwink parameters for polystyrene, *i.e.*, $K = 14.1 \times 10^{-5}\ dL\,g^{-1}$, $\alpha = 0.70$.[230]

   DMAc-SEC measurements were performed on a Polymer Laboratories PL-GPC 50 Plus Integrated System, comprising an autosampler, a PLgel $5\,\mu m$ bead-size guard column $(50 \times 7.5\,mm)$ followed by three PLgel $5\,\mu m$ Mixed-C $(300 \times 7.5\,mm)$ and a differential refractive index detector using *N*,*N*-dimethylacetamide (DMAc) containing 0.03 wt% LiBr as the eluent at $50\,°C$ with a flow rate of $1\,mL\,min^{-1}$. The SEC system was calibrated using linear poly(styrene) (PS) standards ranging from 474 to $2.5 \times 10^6\ g\,mol^{-1}$.

Ultraviolet/Visible (UV/Vis) spectroscopy

UV-Vis spectra were measured on a Varian Cary 100 Bio spectrometer including a temperature control unit. All measurements were carried out in DMF in quartz glass cuvettes (Starna) with a thickness of $1\,cm$ at a temperature of $20\,°C$. The NITEC-SCNPs were measured in DMF $(c = 40\,mg\,L^{-1})$.

X-Ray Photoelectron Spectroscopy (XPS)

XPS measurements were performed using a K-Alpha XPS spectrometer (ThermoFisher Scientific, East Grinstead, UK). Data acquisition and processing using the Thermo

Avantage software is described elsewhere.2 All samples were analyzed using a microfocused, monochromated Al Kα X-ray source (400 µm spot size). The K-Alpha charge compensation system was employed during analysis, using electrons of 8 eV energy, and low-energy argon ions to prevent any localized charge build-up. The spectra were fitted with one or more Voigt profiles (BE uncertainty: ±0.2 eV) and Scofield sensitivity factors were applied for quantification.[231] All spectra were referenced to the C1s peak (C-C, C-H) at 285 eV binding energy controlled by means of the well-known photoelectron peaks of metallic Cu, Ag, and Au, respectively.

6 | Concluding Remarks and Outlook

Ongoing research in the field of single-chain technology requires new strategies for the folding of synthetic polymers and efficient concepts for the preparation of application oriented single-chain nanoparticles (SCNPs) in order to get closer to the ultimate goal of eventually mimicking the three dimensional structure and the function of naturally occurring proteins.

Therefore, the present thesis for the first time distinguishes the different approaches that can be followed to structure single synthetic polymer chains by introducing the terms *selective point folding* and *repeating unit approach*. Research of the current thesis on the one hand contains new synthetic platform technologies for the selective point folding approach based on metal complexation and reversible host/guest inclusion. On the other hand, efficient concepts for the preparation of application oriented SCNPs by the repeating unit approach are introduced, which employ metal complexation, advanced photochemical ligation tools, and stimulus responsive dynamic covalent chemistry for the intramolecular crosslinking. Thus, advances for both approaches are reported, opening the door for various potential applications of the single chain architectures.

Investigations regarding the selective point folding approach are discussed in Chapter 3. To showcase the viability of the targeted mode of folding, only the simplest form of folding, namely the cyclization, is addressed in the current thesis. Initially, inspired by metalloproteins, the precise folding of synthetic polymers by palladium(II) complexation is reported in Section 3.1. Therefore, α, ω-triarylphosphine functionalized styrene-based macroligands were designed, which efficiently folded into a cyclic structure in diluted solution. With the ultimate goal of mimicking the structure of proteins in mind, the selective point folding of synthetic polymers is adapted to aqueous media in Section 3.2. The recognition units employed in the study were β-cyclodextrin and adamantane, which were tethered to the chain ends of watersoluble poly(dimethylacrylamide). Single-chain

selective point folding of this polymer was achieved in diluted aqueous solution and was reversible at elevated temperatures.

The research collated in Chapter 4 addresses the synthesis of single-chain nanoparticles utilizing the repeating unit approach. The concept of metal complexation is exploited further in Section 4.1 for the fabrication of catalytically active SCNPs. A parent copolymer carrying triarylphosphine units along its backbone was reacted with a Pd(II)-precursor complex in diluted solution to prepare Pd-SCNPs. These Pd-SCNPs were found to be applicable as catalyst in the Sonogashira coupling of a terminal alkyne and an aryl halide. Due to their efficiency, two photochemical ligation techniques are employed for the synthesis of SCNPs in the current thesis. In Section 4.2, the nitrile imine-mediated tetrazole-ene cycloaddition (NITEC) is applied for the fabrication of a set of inherently (pro)fluorescent SCNPs. A versatile random copolymer of styrene and 4-chloromethyl styrene (CMS) was modified with both photo-reactive groups in a one pot substitution reaction. UV-Irradiation of the parent polymers in diluted solution led to the efficient formation of (pro)fluorescent SCNPs. Careful adjustment of the ratio of reactive groups in the parent polymer allows for fine control over the final size of the SCNPs, while simultaneously controlling the fluorescence properties. By utilizing residual (surface) exposed tetrazole units, these SCNPs can be further functionalized, which was exemplary shown in the reaction with maleimide-functional microspheres. The NITEC-SCNPs feature a broad fluorescence band (500-700 nm), which can be excited in a biocompatible range at $\lambda_{\mathrm{max}} = 415\,\mathrm{nm}$. Thus, these SCNPs might serve as inherently fluorescent transporting molecules, which can directly be monitored *via* their fluorescence. The photoenol reaction, a light-induced Diels–Alder ligation, is exploited for the synthesis of mono-functional SCNPs in Section 4.3. Therefore, a set of mono-alkyne-functional random copolymers of styrene and CMS with varying CMS content was synthesized. Equimolar amounts of the photo-reactive compounds were tethered to the backbone of the polymer in a one-pot two-step postpolymerization modification. Prior to the single-chain collapse, the maleimide moieties had to be deprotected in order to become sufficiently reactive towards the photoenol. Irradiation of the parent polymers with UV-light in diluted solution resulted in the efficient formation of mono-alkyne-funtional SCNPs. Variation of the CMS content, and consequently also the functional group density of the parent polymers, allowed for fine control over the size of the resulting SCNPs. In order to present the

functionalization ability, azide-functional poly(ethylene glycol) (PEG) was reacted with one of the precursor polymers for the proof of principle. The single-chain collapse of these linear precursors led to the formation of tadpole-like SCNPs. At last, preliminary results from the investigation of stimulus responsive, watersoluble SCNPs are presented in Section 4.4. Employing pH-responsive hydrazone bonds for the intramolecular crosslinking of dimethylacrylamide based parent polymers in diluted aqueous solution, resulted in the formation of trigger-responsive SCNPs. Due to the dynamic nature of the hydrazone bond at pH = 4.75, a triggered payload release in the acidic medium is envisiond for such SCNPs.

In summary, the present thesis describes significant advances in the field of single-chain technology. Various strategies for the selective point folding of synthetic polymer chains and concepts for the efficient synthesis of application oriented SCNPs are demonstrated. Especially the last sections of each chapter, which address single-chain architectures in the aqueous medium, entail important steps on the long route to artificial proteins.

However, synthetically establishing the highly complex structures in naturally occurring macromolecules seems still out of reach for todays chemists, regardless of the taken approach. Continuous effort is needed to close in on the ultimate goals of single-chain technology step by step. The intricate synthesis should from the first moment be guided by computer simulations and chaperoned by adequate analytical methods. In the case of the selective point folding, combinations of several mutually orthogonal, ideally dynamic, recognition unit pairs in a single polymeric backbone can lead to more complex structures. By varying the type of polymeric backbone (polar *vs.* apolar, stiff *vs.* flexible, "linear" *vs.* helical) between the recognition units, structural diversity of the folded single chain can be generated. Ultimately, reactive sites could be incorporated into the backbone, thus creating catalytic pockets inside the folded structure that might show selectivity similar to enzymes. Here, also dynamic/responsive systems should be considered to make the structures adaptable to outer stimuli. Analogous improvements could be implemented in the repeating unit approach. Selectively crosslinking different sections in multi-block copolymers might lead to multi-compartment SCNPs. Here again, various combinations of polymeric building blocks and crosslinking methodologies are conceivable. By careful design, such SCNPs could one day function as unimolecular assembly lines, hosting a cascade reaction inside the multiple compartments. Owing to the employed RDRP

protocols, current parent polymers have a certain (narrow) dispersity. Regardless of the approach, it has to be assessed how this dispersity influences the final single chain architecture and what degree of deviation from the targeted design is acceptable for a certain application. Ultimately, the artificial single chain structures may fulfill a biological function. In order to test their activity, the polymeric backbones, as well as the recognition motifs, need to be adapted to the complex biological environment.

Bibliography

[1] B. Bhushan, *Philos Trans A Math Phys Eng Sci.* **2009**, *367*, 1445–86.

[2] J. F. V. Vincent, O. A. Bogatyreva, N. R. Bogatyrev, A. Bowyer, A.-K. Pahl, *J. R. Soc., Interface* **2006**, *3*, 471–482.

[3] D. Voet, J. Voet, *Biochemistry*, John Wiley & Sons, Hoboken, 4th ed., **2011**.

[4] C. B. Anfinsen, *Science* **1973**, *181*, 223–230.

[5] C. M. Dobson, *Nature* **2003**, *426*, 884–890.

[6] I. F. Sevrioukova, H. Li, H. Zhang, J. A. Peterson, T. L. Poulos, *Proc. Natl. Acad. Sci. U. S. A.* **1999**, *96*, 1863–1868.

[7] H. Lodish, A. Berk, S. L. Zipursky, P. Matsudaira, D. Baltimore, J. Darnell, *Molecular Cell Biology*, W. H. Freeman, New York, 4th ed., **2000**.

[8] H. Gröger, Y. Asano in *Enzyme Catalysis in Organic Synthesis*, (Eds.: K. Drauz, H. Gröger, O. May), Wiley-VCH, Weinheim, 3rd ed., **2012**.

[9] G. A. Behrens, A. Hummel, S. K. Padhi, S. Schätzle, U. T. Bornscheuer, *Adv. Synth. Catal.* **2011**, *353*, 2191–2215.

[10] H. Yamada, M. Kobayashi, *Biosci., Biotechnol., Biochem.* **1996**, *60*, 1391–1400.

[11] U. Koert, *Angew. Chem.* **1997**, *109*, 1922–1923.

[12] M. Hagihara, N. J. Anthony, T. J. Stout, J. Clardy, S. L. Schreiber, *J. Am. Chem. Soc.* **1992**, *114*, 6568–6570.

[13] T. L. Sommerfeld, D. Seebach, *Angew. Chem.* **1995**, *107*, 622–623.

[14] R. J. Simon, R. S. Kania, R. N. Zuckermann, V. D. Huebner, D. A. Jewell, S. Banville, S. Ng, L. Wang, S. Rosenberg, C. K. Marlowe, *Proc. Natl. Acad. Sci. U. S. A.* **1992**, *89*, 9367–9371.

[15] F. Alsubaie, A. Anastasaki, P. Wilson, D. M. Haddleton, *Polym. Chem.* **2015**, *6*, 406–417.

[16] A. Anastasaki, V. Nikolaou, N. W. McCaul, A. Simula, J. Godfrey, C. Waldron, P. Wilson, K. Kempe, D. M. Haddleton, *Macromolecules* **2015**, *48*, 1404–1411.

[17] Y.-M. Chuang, A. Ethirajan, T. Junkers, *ACS Macro Lett.* **2014**, *3*, 732–737.

[18] T. Soejima, K. Satoh, M. Kamigaito, *ACS Macro Lett.* **2015**, *4*, 745–749.

[19] S. C. Solleder, M. A. R. Meier, *Angew. Chem., Int. Ed.* **2014**, *53*, 711–714.

[20] S. C. Solleder, K. S. Wetzel, M. A. R. Meier, *Polym. Chem.* **2015**, *6*, 3201–3204.

[21] N. Zydziak, F. Feist, B. Huber, J. O. Mueller, C. Barner-Kowollik, *Chem. Commun.* **2015**, *51*, 1799–1802.

[22] T. T. Trinh, C. Laure, J.-F. Lutz, *Macromol. Chem. Phys.* **2015**, *216*, 1498–1506.

[23] Z. Zhang, Y.-Z. You, D.-C. Wu, C.-Y. Hong, *Macromolecules* **2015**, *48*, 3414–3421.

[24] A. A. Ouahabi, M. Kotera, L. Charles, J.-F. Lutz, *ACS Macro Lett.* **2015**, 1077–1080.

[25] D. Danilov, C. Barner-Kowollik, W. Wenzel, *Chem. Commun.* **2015**, *51*, 6002–6005.

[26] V. W. Kuhn, H. Majer, *Die Makromolekulare Chemie* **1956**, *18*, 239–253.

[27] M. Kato, M. Kamigaito, M. Sawamoto, T. Higashimura, *Macromolecules* **1995**, *28*, 1721–1723.

[28] J.-S. Wang, K. Matyjaszewski, *Macromolecules* **1995**, *28*, 7901–7910.

[29] G. Moad, E. Rizzardo, *Macromolecules* **1995**, *28*, 8722–8728.

[30] C. J. Hawker, G. G. Barclay, J. Dao, *J. Am. Chem. Soc.* **1996**, *118*, 11467–11471.

[31] J. Chiefari, Y. K. Chong, F. Ercole, J. Krstina, J. Jeffery, T. P. T. Le, R. T. A. Mayadunne, G. F. Meijs, C. L. Moad, G. Moad, E. Rizzardo, S. H. Thang, *Macromolecules* **1998**, *31*, 5559–5562.

[32] S. Mavila, O. Eivgi, I. Berkovich, N. G. Lemcoff, *Chem. Rev.* **2015**, DOI 10.1021/ acs.chemrev.5b00290.

[33] C. K. Lyon, A. Prasher, A. M. Hanlon, B. T. Tuten, C. A. Tooley, P. G. Frank, E. B. Berda, *Polym. Chem.* **2015**, *6*, 181–197.

[34] M. Gonzalez-Burgos, A. Latorre-Sanchez, J. A. Pomposo, *Chem. Soc. Rev.* **2015**, *44*, 6122–6142.

[35] A. Sanchez-Sanchez, J. A. Pomposo, *Part. Part. Syst. Char.* **2014**, *31*, 11–23.

[36] A. Sanchez-Sanchez, I. Pérez-Baena, J. A. Pomposo, *Molecules* **2013**, *18*, 3339.

[37] O. Altintas, C. Barner-Kowollik, *Macromol. Rapid Commun.* **2012**, *33*, 958–971.

[38] M. Ouchi, N. Badi, J.-F. Lutz, M. Sawamoto, *Nat. Chem.* **2011**, *3*, 917–924.

[39] B. V. K. J. Schmidt, N. Fechler, J. Falkenhagen, J.-F. Lutz, *Nat. Chem.* **2011**, *3*, 234–238.

[40] O. Shishkan, M. Zamfir, M. A. Gauthier, H. G. Börner, J.-F. Lutz, *Chem. Commun.* **2014**, *50*, 1570–1572.

[41] O. Altintas, P. Gerstel, N. Dingenouts, C. Barner-Kowollik, *Chem. Commun.* **2010**, *46*, 6291–6293.

[42] O. Altintas, T. Rudolph, C. Barner-Kowollik, *J. Polym. Sci., Part A: Polym. Chem.* **2011**, *49*, 2566–2576.

[43] C. Burd, M. Weck, *Macromolecules* **2005**, *38*, 7225–7230.

[44] O. Altintas, E. Lejeune, P. Gerstel, C. Barner-Kowollik, *Polym. Chem.* **2012**, *3*, 640–651.

[45] O. Altintas, P. Krolla-Sidenstein, H. Gliemann, C. Barner-Kowollik, *Macromolecules* **2014**, *47*, 5877–5888.

[46] Z. Jia, M. J. Monteiro, *J. Polym. Sci., Part A: Polym. Chem.* **2012**, *50*, 2085–2097.

[47] H. R. Kricheldorf, *J. Polym. Sci., Part A: Polym. Chem.* **2010**, *48*, 251–284.

[48] B. A. Laurent, S. M. Grayson, *Chem. Soc. Rev.* **2009**, *38*, 2202–2213.

[49] I. Manners, *J. Polym. Sci., Part A: Polym. Chem.* **2002**, *40*, 179–191.

[50] S. K. Yang, A. V. Ambade, M. Weck, *Chem.–Eur. J.* **2009**, *15*, 6605–6611.

[51] M. Chiper, R. Hoogenboom, U. S. Schubert, *Macromol. Rapid Commun.* **2009**, *30*, 565–578.

[52] G. L. Fiore, J. L. Klinkenberg, C. L. Fraser, *Macromolecules* **2008**, *41*, 9397–9405.

[53] U. Mansfeld, A. Winter, M. D. Hager, W. Günther, E. Altuntaş, U. S. Schubert, *J. Polym. Sci., Part A: Polym. Chem.* **2013**, *51*, 2006–2015.

[54] M. A. R. Meier, B. G. G. Lohmeijer, U. S. Schubert, *Macromol. Rapid Commun.* **2003**, *24*, 852–857.

[55] A. Ambade, S. Yang, M. Weck, *Angew. Chem., Int. Ed.* **2009**, *48*, 2894–2898.

[56] M. Chiper, M. A. R. Meier, D. Wouters, S. Hoeppener, C.-A. Fustin, J.-F. Gohy, U. S. Schubert, *Macromolecules* **2008**, *41*, 2771–2777.

[57] D. Shriver, P. Atkins, *Inorganic Chemistry*, Oxford University Press, Oxford, 3rd, **1999**.

[58] Y. Lu, N. Yeung, N. Sieracki, N. M. Marshall, *Nature* **2009**, *460*, 855–862.

[59] M. Burnworth, L. Tang, J. R. Kumpfer, A. J. Duncan, F. L. Beyer, G. L. Fiore, S. J. Rowan, C. Weder, *Nature* **2011**, *472*, 334–337.

[60] B. V. K. J. Schmidt, M. Hetzer, H. Ritter, C. Barner-Kowollik, *Prog. Polym. Sci.* **2014**, *39*, 235–249.

[61] Y. Inoue, P. Kuad, Y. Okumura, Y. Takashima, H. Yamaguchi, A. Harada, *J. Am. Chem. Soc.* **2007**, *129*, 6396–6397.

[62] Y. Inoue, M. Miyauchi, H. Nakajima, Y. Takashima, H. Yamaguchi, A. Harada, *J. Am. Chem. Soc.* **2006**, *128*, 8994–8995.

[63] Z. Ji, Y. Li, Y. Ding, G. Chen, M. Jiang, *Polym. Chem.* **2015**, *6*, 6880–6884.

[64] E. Harth, B. V. Horn, V. Y. Lee, D. S. Germack, C. P. Gonzales, R. D. Miller, C. J. Hawker, *J. Am. Chem. Soc.* **2002**, *124*, 8653–8660.

[65] T. A. Croce, S. K. Hamilton, M. L. Chen, H. Muchalski, E. Harth, *Macromolecules* **2007**, *40*, 6028–6031.

[66] G. Njikang, G. Liu, S. A. Curda, *Macromolecules* **2008**, *41*, 5697–5702.

[67] J. Tao, G. Liu, *Macromolecules* **1997**, *30*, 2408–2411.

[68] F. Zhou, M. Xie, D. Chen, *Macromolecules* **2014**, *47*, 365–372.

[69] M. X. Xie, L. Jiang, Z. P. Xu, D. Y. Chen, *Chem. Commun.* **2015**, *51*, 1842–1845.

[70] S. Hecht, A. Khan, *Angew. Chem., Int. Ed.* **2003**, *115*, 6203–6206.

[71] P. G. Frank, B. T. Tuten, A. Prasher, D. Chao, E. B. Berda, *Macromol. Rapid Commun.* **2014**, *35*, 249–253.

[72] C. Tooley, S. Pazicni, E. B. Berda, *Polym. Chem.* **2015**, DOI `10.1039/C5PY01196E`.

[73] R. Huisgen, J. Sauer, H. J. Sturm, J. H. Markgraf, *Chem. Ber.* **1960**, *93*, 2106–2124.

[74] R. Huisgen, *Angew. Chem., Int. Ed.* **1963**, *2*, 565–598.

[75] J. S. Clovis, A. Eckell, R. Huisgen, R. Sustmann, *Chem. Ber.* **1967**, *100*, 60–70.

[76] P. Weinberg, M. Siegmund, C. Csongar, G. Tomaschewski, *Zeitschrift für Chemie* **1988**, *28*, 252–253.

[77] P. Weinberg, C. Csongar, M. Gessner, G. Tomaschewski, *Journal für Praktische Chemie* **1988**, *330*, 879–886.

[78] P. Weinberg, U. W. Grummt, C. Csongar, *Journal für Praktische Chemie* **1988**, *330*, 887–892.

[79] G. Bertrand, C. Wentrup, *Angew. Chem., Int. Ed.* **1994**, *33*, 527–545.

[80] W. Song, Y. Wang, J. Qu, Q. Lin, *J. Am. Chem. Soc.* **2008**, *130*, 9654–9655.

[81] W. Song, Y. Wang, J. Qu, M. M. Madden, Q. Lin, *Angew. Chem., Int. Ed.* **2008**, *47*, 2832–2835.

[82] Y. Wang, C. I. Rivera Vera, Q. Lin, *Org. Lett.* **2007**, *9*, 4155–4158.

[83] Y. Wang, W. Song, W. J. Hu, Q. Lin, *Angew. Chem., Int. Ed.* **2009**, *48*, 5330–5333.

[84] J. Wang, W. Zhang, W. Song, Y. Wang, Z. Yu, J. Li, M. Wu, L. Wang, J. Zang, Q. Lin, *J. Am. Chem. Soc.* **2010**, *132*, 14812–14818.

[85] Z. Yu, L. Y. Ho, Z. Wang, Q. Lin, *Bioorg. Med. Chem. Lett.* **2011**, *21*, 5033–5036.

[86] S. Arndt, H.-A. Wagenknecht, *Angew. Chem., Int. Ed.* **2014**, *53*, 14580–14582.

[87] M. Dietrich, G. Delaittre, J. P. Blinco, A. J. Inglis, M. Bruns, C. Barner-Kowollik, *Adv. Funct. Mater.* **2012**, *22*, 304–312.

[88] T. Tischer, C. Rodriguez-Emmenegger, V. Trouillet, A. Welle, V. Schueler, J. O. Mueller, A. S. Goldmann, E. Brynda, C. Barner-Kowollik, *Adv. Mater.* **2014**, *26*, 4087–4092.

[89] A. Hufendiek, C. Barner-Kowollik, M. A. R. Meier, *Polym. Chem.* **2015**, *6*, 2188–2191.

[90] L. Stolzer, A. Vigovskaya, C. Barner-Kowollik, L. Fruk, *Chem.–Eur. J.* **2015**, *21*, 14309–14313.

[91] C. J. Dürr, P. Lederhose, L. Hlalele, D. Abt, A. Kaiser, S. Brandau, C. Barner-Kowollik, *Macromolecules* **2013**, *46*, 5915–5923.

[92] J. O. Mueller, N. K. Guimard, K. K. Oehlenschlaeger, F. G. Schmidt, C. Barner-Kowollik, *Polym. Chem.* **2014**, *5*, 1447–1456.

[93] J. O. Mueller, D. Voll, F. G. Schmidt, G. Delaittre, C. Barner-Kowollik, *Chem. Commun.* **2014**, *50*, 15681–15684.

[94] L. Oria, R. Aguado, J. A. Pomposo, J. Colmenero, *Adv. Mater.* **2010**, *22*, 3038–3041.

[95] S. M. Mellows, P. G. Sammes, *J. Chem. Soc. D* **1971**, 21–22.

[96] T. Pauloehrl, G. Delaittre, V. Winkler, A. Welle, M. Bruns, H. G. Börner, A. M. Greiner, M. Bastmeyer, C. Barner-Kowollik, *Angew. Chem., Int. Ed.* **2012**, *51*, 1071–1074.

[97] T. Tischer, T. K. Claus, M. Bruns, V. Trouillet, K. Linkert, C. Rodriguez-Emmenegger, A. S. Goldmann, S. Perrier, H. G. Börner, C. Barner-Kowollik, *Biomacromolecules* **2013**, *14*, 4340–4350.

[98]   M. Kaupp, T. Tischer, A. F. Hirschbiel, A. P. Vogt, U. Geckle, V. Trouillet, T. Hofe, M. H. Stenzel, C. Barner-Kowollik, *Macromolecules* **2013**, *46*, 6858–6872.

[99]   C. M. Preuss, T. Tischer, C. Rodriguez-Emmenegger, M. M. Zieger, M. Bruns, A. S. Goldmann, C. Barner-Kowollik, *Journal of Materials Chemistry B* **2014**, *2*, 36–40.

[100] L. Stolzer, I. Ahmed, C. Rodriguez-Emmenegger, V. Trouillet, P. Bockstaller, C. Barner-Kowollik, L. Fruk, *Chem. Commun.* **2014**, *50*, 4430–4433.

[101] L. Stolzer, A. S. Quick, D. Abt, A. Welle, D. Naumenko, M. Lazzarino, M. Wegener, C. Barner-Kowollik, L. Fruk, *Chem. Commun.* **2015**, *51*, 3363–3366.

[102] M. Glassner, J. P. Blinco, C. Barner-Kowollik, *Macromol. Rapid Commun.* **2011**, *32*, 724–728.

[103] T. Josse, O. Altintas, K. K. Oehlenschlaeger, P. Dubois, P. Gerbaux, O. Coulembier, C. Barner-Kowollik, *Chem. Commun.* **2014**.

[104] T. Josse, J. De Winter, O. Altintas, P. Dubois, C. Barner-Kowollik, P. Gerbaux, O. Coulembier, *Macromol. Chem. Phys.* **2015**, *216*, 1227–1234.

[105] T. Gruendling, K. K. Oehlenschlaeger, E. Frick, M. Glassner, C. Schmid, C. Barner-Kowollik, *Macromol. Rapid Commun.* **2011**, *32*, 807–812.

[106] M. Glassner, K. K. Oehlenschlaeger, T. Gruendling, C. Barner-Kowollik, *Macromolecules* **2011**, *44*, 4681–4689.

[107] M. Winkler, J. O. Mueller, K. K. Oehlenschlaeger, L. Montero de Espinosa, M. A. R. Meier, C. Barner-Kowollik, *Macromolecules* **2012**, *45*, 5012–5019.

[108] K. K. Oehlenschlaeger, J. O. Mueller, N. B. Heine, M. Glassner, N. K. Guimard, G. Delaittre, F. G. Schmidt, C. Barner-Kowollik, *Angew. Chem., Int. Ed.* **2013**, *52*, 762–766.

[109] S. J. Rowan, S. J. Cantrill, G. R. L. Cousins, J. K. M. Sanders, J. F. Stoddart, *Angew. Chem., Int. Ed.* **2002**, *41*, 898–952.

[110] P. T. Corbett, J. Leclaire, L. Vial, K. R. West, J.-L. Wietor, J. K. M. Sanders, S. Otto, *Chem. Rev.* **2006**, *106*, 3652–3711.

[111] B. T. Tuten, D. Chao, C. K. Lyon, E. B. Berda, *Polym. Chem.* **2012**, *3*, 3068–3071.

[112] R. Braslau, F. Rivera Iii, C. Tansakul, *React. Funct. Polym.* **2013**, *73*, 624–633.

[113] C. Song, L. Li, l. Dai, S. Thayumanavan, *Polym. Chem.* **2015**, *6*, 4828–4834.

[114] J. He, L. Tremblay, S. Lacelle, Y. Zhao, *Soft Matter* **2011**, *7*, 2380–2386.

[115] W. Fan, X. Tong, Q. Yan, S. Fu, Y. Zhao, *Chem. Commun.* **2014**, *50*, 13492–13494.

[116] L. Buruaga, J. A. Pomposo, *Polymers* **2011**, *3*, 1673.

[117] A. Sanchez-Sanchez, D. A. Fulton, J. A. Pomposo, *Chem. Commun.* **2014**, *50*, 1871–1874.

[118] W. G. Skene, J.-M. P. Lehn, *Proc. Natl. Acad. Sci. U. S. A.* **2004**, *101*, 8270–8275.

[119] T. Ono, T. Nobori, J.-M. Lehn, *Chem. Commun.* **2005**, 1522–1524.

[120] E. Kolomiets, J.-M. Lehn, *Chem. Commun.* **2005**, 1519–1521.

[121] B. S. Murray, D. A. Fulton, *Macromolecules* **2011**, *44*, 7242–7252.

[122]   D. E. Whitaker, C. S. Mahon, D. A. Fulton, *Angew. Chem., Int. Ed.* **2013**, *52*, 956–959.

[123]   L. Brunsveld, B. J. B. Folmer, E. W. Meijer, R. P. Sijbesma, *Chem. Rev.* **2001**, *101*, 4071–4098.

[124]   E. J. Foster, E. B. Berda, E. W. Meijer, *J. Am. Chem. Soc.* **2009**, *131*, 6964–6966.

[125]   E. B. Berda, E. J. Foster, E. W. Meijer, *Macromolecules* **2010**, *43*, 1430–1437.

[126]   E. J. Foster, E. B. Berda, E. W. Meijer, *J. Polym. Sci., Part A: Polym. Chem.* **2011**, *49*, 118–126.

[127]   P. J. M. Stals, M. A. J. Gillissen, R. Nicolay, A. R. A. Palmans, E. W. Meijer, *J. Polym. Sci., Part A: Polym. Chem.* **2013**, *4*, 2584–2597.

[128]   F. Wang, H. Pu, M. Jin, H. Pan, Z. Chang, D. Wan, J. Du, *J. Polym. Sci., Part A: Polym. Chem.* **2015**, *53*, 1832–1840.

[129]   M. P. Lightfoot, F. S. Mair, R. G. Pritchard, J. E. Warren, *Chem. Commun.* **1999**, 1945–1946.

[130]   T. Mes, R. van der Weegen, A. R. A. Palmans, E. W. Meijer, *Angew. Chem., Int. Ed.* **2011**, *50*, 5085–5089.

[131]   M. A. J. Gillissen, T. Terashima, E. W. Meijer, A. R. A. Palmans, I. K. Voets, *Macromolecules* **2013**, *46*, 4120–4125.

[132]   P. J. M. Stals, M. A. J. Gillissen, T. F. E. Paffen, T. F. A. de Greef, P. Lindner, E. W. Meijer, A. R. A. Palmans, I. K. Voets, *Macromolecules* **2014**, *47*, 2947–2954.

[133]   N. Hosono, A. R. A. Palmans, E. W. Meijer, *Chem. Commun.* **2014**, *50*, 7990–7993.

[134]   T. Terashima, T. Mes, T. F. A. De Greef, M. A. J. Gillissen, P. Besenius, A. R. A. Palmans, E. W. Meijer, *J. Am. Chem. Soc.* **2011**, *133*, 4742–4745.

[135]   M. Artar, T. Terashima, M. Sawamoto, E. W. Meijer, A. R. A. Palmans, *J. Polym. Sci., Part A: Polym. Chem.* **2014**, *52*, 12–20.

[136]   E. Huerta, P. J. M. Stals, E. W. Meijer, A. R. A. Palmans, *Angew. Chem., Int. Ed.* **2013**, *52*, 2906–2910.

[137]   E. Huerta, B. van Genabeek, P. J. M. Stals, E. W. Meijer, A. R. A. Palmans, *Macromol. Rapid Commun.* **2014**, *35*, 1320–1325.

[138]   Y. Liu, T. Pauloehrl, S. I. Presolski, L. Albertazzi, A. R. A. Palmans, E. W. Meijer, *J. Am. Chem. Soc.* **2015**, *137*, 13096–13105.

[139]   M. A. J. Gillissen, I. K. Voets, E. W. Meijer, A. R. A. Palmans, *Polym. Chem.* **2012**, *3*, 3166–3174.

[140]   J. Lu, N. ten Brummelhuis, M. Weck, *Chem. Commun.* **2014**, *50*, 6225–6227.

[141]   J. Romulus, M. Weck, *Macromol. Rapid Commun.* **2013**, *34*, 1518–1523.

[142]   G. R. Whittell, M. D. Hager, U. S. Schubert, I. Manners, *Nat. Mater.* **2011**, *10*, 176–188.

[143]   A. M. Breul, J. Schäfer, C. Friebe, F. Schlütter, R. M. Paulus, G. Festag, M. D. Hager, A. Winter, B. Dietzek, J. Popp, U. S. Schubert, *Macromol. Chem. Phys.* **2012**, *213*, 808–819.

[144] J. Brassinne, E. Poggi, C.-A. Fustin, J.-F. Gohy, *Macromol. Rapid Commun.* **2015**, *36*, 610–615.

[145] J.-C. Eloi, L. Chabanne, G. R. Whittell, I. Manners, *Mater. Today* **2008**, *11*, 28–36.

[146] I. Perez-Baena, I. Loinaz, D. Padro, I. Garcia, H. J. Grande, I. Odriozola, *J. Mater. Chem.* **2010**, *20*, 6916–6922.

[147] A. Sanchez-Sanchez, A. Arbe, J. Colmenero, J. A. Pomposo, *ACS Macro Lett.* **2014**, *3*, 439–443.

[148] A. Sanchez-Sanchez, A. Arbe, J. Kohlbrecher, J. Colmenero, J. A. Pomposo, *Macromol. Rapid Commun.* **2015**, *36*, 1592–1597.

[149] Y.-H. Ng, F. di Lena, C. L. L. Chai, *Chem. Commun.* **2011**, *47*, 6464–6466.

[150] Y.-H. Ng, F. di Lena, C. L. L. Chai, *Polym. Chem.* **2011**, *2*, 589–594.

[151] J. Jeong, Y.-J. Lee, B. Kim, B. Kim, K.-S. Jung, H.-j. Paik, *Polym. Chem.* **2015**, *6*, 3392–3397.

[152] S. Mavila, C. E. Diesendruck, S. Linde, L. Amir, R. Shikler, N. G. Lemcoff, *Angew. Chem. Int. Ed. Engl.* **2013**, *52*, 5767–70.

[153] S. Mavila, I. Rozenberg, N. G. Lemcoff, *Chem. Sci.* **2014**, *5*, 4196–4203.

[154] J. Szejtli, *Chem. Rev.* **1998**, *98*, 1743–1754.

[155] A. Ikeda, S. Shinkai, *Chem. Rev.* **1997**, *97*, 1713–1734.

[156] C. J. Pedersen, *J. Am. Chem. Soc.* **1967**, *89*, 7017–7036.

[157] J. W. Lee, S. Samal, N. Selvapalam, H.-J. Kim, K. Kim, *Acc. Chem. Res.* **2003**, *36*, 621–630.

[158] E. A. Appel, J. d. Barrio, J. Dyson, L. Isaacs, O. A. Scherman, *Chem. Sci.* **2012**, *3*, 2278–2281.

[159] E. A. Appel, J. Dyson, J. del Barrio, Z. Walsh, O. A. Scherman, *Angew. Chem., Int. Ed.* **2012**, *51*, 4185–4189.

[160] M. D. Lechner, E. H. Nordmeier, K. Gehrke, *Makromolekulare Chemie*, Birkhäuser Basel, Basel, 4th ed., **2010**.

[161] K. Arndt, G. Müller, *Polymercharakterisierung*, Hanser, **1996**.

[162] C. Wu, *Handbook Of Size Exclusion Chromatography And Related Techniques*, CRC Press, New York, 2nd ed., **2003**.

[163] J. A. Pomposo, I. Perez-Baena, L. Buruaga, A. Alegría, A. J. Moreno, J. Colmenero, *Macromolecules* **2011**, *44*, 8644–8649.

[164] L. J. Fetters, N. Hadjichristidis, J. S. Lindner, J. W. Mays, *J. Phys. Chem. Ref. Data* **1994**, *23*, 619–640.

[165] S. E. Cabaniss, Q. Zhou, P. A. Maurice, Y.-P. Chin, G. R. Aiken, *Environ. Sci. Technol.* **2000**, *34*, 1103–1109.

[166] M. Gavrilov, M. J. Monteiro, *Eur. Polym. J.* **2014**, *65*, 191–196.

[167] M. J. Monteiro, *Eur. Polym. J.* **2015**, *65*, 197–201.

[168] L. H. Peebles in *Polymer Reviews*, (Eds.: H. F. Frank, E. H. Immergut), Wiley-Interscience, New York, **1971**.

[169] B. Berne, R. Pecora, *Dynamic Light Scattering: With Applications to Chemistry, Biology, and Physics*, Dover Publications, Mineola, 1st ed., **2000**.

[170] D. M. Stevens, S. Tempelaar, A. P. Dove, E. Harth, *ACS Macro Lett.* **2012**, *1*, 915–918.

[171] N. Hosono, M. A. J. Gillissen, Y. Li, S. S. Sheiko, A. R. A. Palmans, E. W. Meijer, *J. Am. Chem. Soc.* **2013**, *135*, 501–510.

[172] A. Sanchez-Sanchez, S. Akbari, A. Etxeberria, A. Arbe, U. Gasser, A. J. Moreno, J. Colmenero, J. A. Pomposo, *ACS Macro Lett.* **2013**, *2*, 491–495.

[173] I. Perez-Baena, F. Barroso-Bujans, U. Gasser, A. Arbe, A. J. Moreno, J. Colmenero, J. A. Pomposo, *ACS Macro Lett.* **2013**, *2*, 775–779.

[174] J. A. Pomposo, I. Perez-Baena, F. Lo Verso, A. J. Moreno, A. Arbe, J. Colmenero, *ACS Macro Lett.* **2014**, 767–772.

[175] H. Friebolin, *Basic One- and Two-Dimensional NMR Spectroscopy*, Wiley-VCH, Weinheim, 5th ed., **2010**.

[176] J. Keeler, *Understanding NMR Spectroscopy*, John Wiley & Sons, West Sussex, 2nd ed., **2011**.

[177] S. Meiboom, D. Gill, *Rev. Sci. Instrum.* **1958**, *29*, 688–691.

[178] E. L. Hahn, *Phys. Rev.* **1950**, *80*, PR, 580–594.

[179] K. F. Morris, C. S. Johnson, *J. Am. Chem. Soc.* **1992**, *114*, 3139–3141.

[180] N. Ormategui, I. Garcia, D. Padro, G. Cabanero, H. J. Grande, I. Loinaz, *Soft Matter* **2012**, *8*, 734–740.

[181] W. S. Price, *Concepts Magn. Reson.* **1997**, *9*, 299–336.

[182] W. S. Price, *Concepts Magn. Reson.* **1998**, *10*, 197–237.

[183] C. S. Johnson Jr, *Prog. Nucl. Magn. Reson. Spectrosc.* **1999**, *34*, 203–256.

[184] D. H. Wu, A. D. Chen, C. S. Johnson, *J. Magn. Reson., Ser. A* **1995**, *115*, 260–264.

[185] G. Wider, V. Dotsch, K. Wuthrich, *J. Magn. Reson., Ser. A* **1994**, *108*, 255–258.

[186] W. A. Anderson, R. Freeman, *J. Chem. Phys.* **1962**, *37*, 85–103.

[187] J. H. Simpson, *Organic Structure Determination Using 2-D NMR Spectroscopy*, Elsevier, Boston, 2nd ed., **2012**.

[188] T. D. W. Claridge, *High-Resolution NMR Techniques in Organic Chemistry*, Elsevier, Oxford, 2nd ed., **2009**.

[189] D. Neuhaus, M. P. Williamson, *The Nuclear Overhauser Effect in Structural and Conformational Analysis*, Wiley-VCH, Weinheim, 2nd ed., **2000**.

[190] A. A. Bothner-By, R. L. Stephens, J. Lee, C. D. Warren, R. W. Jeanloz, *J. Am. Chem. Soc.* **1984**, *106*, 811–813.

[191] A. Bax, D. G. Davis, *J. Magn. Reson.* **1985**, *63*, 207–213.

[192] G. Binnig, C. F. Quate, C. Gerber, *Phys. Rev. Lett.* **1986**, *56*, 930–933.

[193] B. Cappella, G. Dietler, *Surf. Sci. Rep.* **1999**, *34*, 1–104.

[194] J. Wen, L. Yuan, Y. Yang, L. Liu, H. Zhao, *ACS Macro Lett.* **2013**, *2*, 100–106.

[195]   C. F. Hansell, A. Lu, J. P. Patterson, R. K. O'Reilly, *Nanoscale* **2014**, *6*, 4102–4107.

[196]   E. Rabani, D. R. Reichman, P. L. Geissler, L. E. Brus, *Nature* **2003**, *426*, 271–274.

[197]   H. W. H. van Roekel, P. J. M. Stals, M. A. J. Gillissen, P. A. J. Hilbers, A. J. Markvoort, T. F. A. de Greef, *Chem. Commun.* **2013**, *49*, 3122–3124.

[198]   A. E. Cherian, F. C. Sun, S. S. Sheiko, G. W. Coates, *J. Am. Chem. Soc.* **2007**, *129*, 11350–11351.

[199]   A. R. de Luzuriaga, N. Ormategui, H. J. Grande, I. Odriozola, J. A. Pomposo, I. Loinaz, *Macromol. Rapid Commun.* **2008**, *29*, 1156–1160.

[200]   P. Wang, H. Pu, M. Jin, *J. Polym. Sci., Part A: Polym. Chem.* **2011**, *49*, 5133–5141.

[201]   X. Jiang, H. Pu, P. Wang, *Polymer* **2011**, *52*, 3597–3602.

[202]   J. Willenbacher, O. Altintas, P. W. Roesky, C. Barner-Kowollik, *Macromol. Rapid Commun.* **2013**, *35*, 45–51.

[203]   D. Schweinfurth, R. Pattacini, S. Strobel, B. Sarkar, *Dalton Trans.* **2009**, 9291–9297.

[204]   A. M. Trzeciak, H. Bartosz-Bechowski, Z. Ciunik, K. Niesyty, J. J. Ziółkowski, *Can. J. Chem.* **2001**, *79*, 752–759.

[205]   G. Ferguson, R. McCrindle, A. J. McAlees, M. Parvez, *Acta Crystallogr., Sect. B: Struct. Sci.* **1982**, *38*, 2679–2681.

[206]   S. Otsuka, *J. Organomet. Chem.* **1980**, *200*, 191–205.

[207]   V. R. Khabibulin, A. V. Kulik, I. V. Oshanina, L. G. Bruk, O. N. Temkin, V. M. Nosova, Y. A. Ustynyuk, V. K. Bel'skii, A. I. Stash, K. A. Lysenko, M. Y. Antipin, *Kinet. Catal.* **2007**, *48*, 228–244.

[208]   J. Willenbacher, B. V. K. J. Schmidt, D. Schulze-Suenninghausen, O. Altintas, B. Luy, G. Delaittre, C. Barner-Kowollik, *Chem. Commun.* **2014**, *50*, 7056–7059.

[209]   T. F. A. de Greef, G. Ercolani, G. B. W. L. Ligthart, E. W. Meijer, R. P. Sijbesma, *J. Am. Chem. Soc.* **2008**, *130*, 13755–13764.

[210]   B. V. K. J. Schmidt, M. Hetzer, H. Ritter, C. Barner-Kowollik, *Macromolecules* **2013**, *46*, 1054–1065.

[211]   J. Skey, R. K. O'Reilly, *Chem. Commun.* **2008**, 4183–4185.

[212]   B. V. K. J. Schmidt, M. Hetzer, H. Ritter, C. Barner-Kowollik, *Macromolecules* **2011**, *44*, 7220–7232.

[213]   Z. Yu, A. R. Sawkar, L. J. Whalen, C.-H. Wong, J. W. Kelly, *J. Med. Chem.* **2006**, *50*, 94–100.

[214]   B. V. K. J. Schmidt, M. Hetzer, H. Ritter, C. Barner-Kowollik, *Polym. Chem.* **2012**, *3*, 3064–3067.

[215]   K. Matyjaszewski, Y. Nakagawa, S. G. Gaynor, *Macromol. Rapid Commun.* **1997**, *18*, 1057–1066.

[216]   S. Amajjahe, S. Choi, M. Munteanu, H. Ritter, *Angew. Chem., Int. Ed.* **2008**, *47*, 3435–3437.

[217] J. Willenbacher, O. Altintas, V. Trouillet, N. Knofel, M. J. Monteiro, P. W. Roesky, C. Barner-Kowollik, *Polym. Chem.* **2015**, *6*, 4358–4365.

[218] K. Young-Inn, J. Chan-Kyou, L. Yong-Min, C. Sung-Nak, *Bull. Korean Chem. Soc.* **2002**, *23*, 1754–1758.

[219] M. Ranjbar, S. Fardindoost, S. M. Mahdavi, A. Iraji zad, N. Tahmasebi G, *Sol. Energy Mater. Sol. Cells* **2011**, *95*, 2335–2340.

[220] Z. Gu, Z. Li, Z. Liu, Y. Wang, C. Liu, J. Xiang, *Catal. Commun.* **2008**, *9*, 2154–2157.

[221] J. Willenbacher, K. N. R. Wuest, J. O. Mueller, M. Kaupp, H.-A. Wagenknecht, C. Barner-Kowollik, *ACS Macro Lett.* **2014**, 574–579.

[222] O. Altintas, J. Willenbacher, K. N. R. Wuest, K. K. Oehlenschlaeger, P. Krolla-Sidenstein, H. Gliemann, C. Barner-Kowollik, *Macromolecules* **2013**, *46*, 8092–8101.

[223] G. Mantovani, F. Lecolley, L. Tao, D. M. Haddleton, J. Clerx, J. J. L. M. Cornelissen, K. Velonia, *J. Am. Chem. Soc.* **2005**, *127*, 2966–2973.

[224] C. Rodriguez-Emmenegger, C. M. Preuss, B. Yameen, O. Pop-Georgievski, M. Bachmann, J. O. Mueller, M. Bruns, A. S. Goldmann, M. Bastmeyer, C. Barner-Kowollik, *Adv. Mater.* **2013**, *25*, 6123–6127.

[225] O. Altintas, B. Yankul, G. Hizal, U. Tunca, *J. Polym. Sci., Part A: Polym. Chem.* **2006**, *44*, 6458–6465.

[226] A. Mantel, N. Barashkov, I. Irgibayeva, A. Kiriy, V. Senkovskyy, *Polym. Prepr.* **2012**, *53*, 189.

[227] K. Sonogashira, Y. Tohda, N. Hagihara, *Tetrahedron Lett.* **1975**, *16*, 4467–4470.

[228] G. M. Sheldrick, *Acta Crystallogr., Sect. A: Found. Crystallogr.* **2008**, *64*, 112–22.

[229] J. E. Tanner, *J. Chem. Phys.* **1970**, *52*, 2523.

[230] C. Strazielle, H. Benoit, O. Vogl, *Eur. Polym. J.* **1978**, *14*, 331–334.

[231] J. H. Scofield, *J. Electron Spectrosc. Relat. Phenom.* **1976**, *8*, 129–137.

Abbreviations

Đ	Dispersity
ns-CB[10]	*nor-seco*-CB[10]
AA	Acrylic acid
AEMA	2-(Acetoacetoxy)ethyl methacrylate
AFM	Atomic Force Microscopy
AIBN	2,2'-Azoisobutyronitrile
ATRP	Atom Transfer Radical Polymerization
Bimpy	Mono(benzimidazoylmethyl)-bis(pyridylmethyl)
BiPy	2,2-Bipyridine
BiPy-BTA	3,3-Bis(acylamino)-2,2-bipyridine substituted BTA
BPLED	Bi-Polar Longitudinal Eddy Current Delay
BTA	Benzene-1,3,5-tricarboxamide
BTAMA	BTA-bearing Methacrylate
CB[*n*]; *n* = 5-8, 10	Cucurbit[*n*]uril Family
CB[8]	Cucurbit[8]uril
CD	Cyclodextrin
CMA	4-Methyl-[7-(methacryloyl)oxy-ethyl-oxy]coumarin
COE	*cis*-Cyclooctene
CPDB	2-Cyanopropyl dithiobenzoate
CPMG	Carr-Purcell-Meiboom-Gill
CRC	Cysteine–Arginine–Cysteine
CuAAC	Copper(I)-Catalyzed Azide-Alkyne Cycloaddition
DAN	Diaminonaphthyridine
DCC	Dynamic Covalent Chemistry
DCC	*N*,*N*'-Dicyclohexylcarbodiimide
DIBAL-H	Diisobutylaluminiumhydrid
DIPEA	*N*,*N*-Diisopropylethylamine
DLS	Dynamic Light Scattering
DMAa	*N*,*N*-Dimethylacrylamide
DMAc	Dimethylacetamide
DMAEMA	*N*,*N*-Dimethylaminoethyl methacrylate
DMF	*N*,*N*-Dimethylformamide
DOSY	Diffusion Ordered Spectroscopy
DTPA	Diethylenetriaminepentaacetic acid
DTT	Dithiothreitol
EDC	1-(3-Dimethylaminopropyl)-3-ethylcarbodiimide hydrochloride

EDTA	Ethylenediaminetetraacetic acid disodium salt
EMP	2-(((Ethylthio)carbonothioyl)thio)-2-methylpropanoic acid
HDA	Hetero-Diels–Alder
HDV	Hydrodynamic Volume
HPLC	High Performance Liquid Chromatography
LCST	Lower Critical Solution Temperature
LED	Longitudinal Eddy Current Delay
LMA	Lauryl methacrylate
LND	Log-Normal Distributions
MD	Molecular Ddynamics
Me$_6$TREN	Tris(2-aminoethyl)amine
MMA	Methyl methacrylate
MRI	Magnetic Resonance Imaging
M-SCNP	Metallo Single-Chain Nanoparticle
MV	Methyl viologen
MWCO	Molecular Weight Cut-Off
MWD	Molecular Weight Distribution
NIPAM	N-Isopropyl acrylamide
NITEC	Nitrile Imine-Mediated Tetrazole-Ene Cycloaddition
NMP	Nitroxide Mediated Polymerization
NMR	Nuclear Magnetic Resonance
NOE	Nuclear Overhauser Effect
NOESY	Nuclear Overhauser Enhancement Spectroscopy
Np	Naphthyl
OEG	Oligo(ethylene glycol)
OEGMA	Oligo(ethylene glycol) methacrylate
PCHO	2-(Diphenylphosphino) benzaldehyde
PDMAa	Poly(dimethyl acrylamide)
PEGMA	Poly(ethylene glycol) methyl ether methacrylate
PFG	Pulsed Field Gradient
Phen	Phenanthroline
polyCOD	Polycyclooctadiene
RAFT	Reversible Addition–Fragmentation Chain Transfer
RDRP	Reversible-Deactivation Radical Polymerization
ROESY	Rotating Frame NOE Spectroscopy
SANS	Small Angle Neutron Scattering
SAXS	Small Angle X-Ray Scattering
SCNP	Single-Chain Nanoparticle
SDP	Diphenylphosphinostyrene
SEC	Size Exclusion Chromatography
SPM	Scanning Probe Microscopy
STE	Stimulated Echo
TEM	Transmission Electron Spectroscopy
TFA	Trifluoroacetic acid
UG	Ureidoguanosine
upy	Ureido-pyrimidinone
VBOP	4-((4-Vinylbenzyl)oxy)phthalonitrile

Curriculum Vitae

Johannes Willenbacher

Luisenstr. 30

76137 Karlsruhe (Germany)

Mobile	+ 49 (0) 151 64504994
Email	johannes.willenbacher@kit.edu
Birthday	07/10/1987
Nationality	German

Academic Career

10/2012–12/2015 **Karlsruher Institut für Technologie (KIT)**
Karlsruhe (Germany)
PhD thesis, Institute for Technical Chemistry and Polymer Chemistry
under the supervision of Prof. Barner-Kowollik
Single-Chain Origami - En Route to Artificial Proteins?

04/2015–06/2015 **University of California, Santa Barbara (UCSB)**
Santa Barbara (United States)
visiting scholar in the group of Prof. Craig Hawker, Materials Research
Laboratory

02/2012–08/2012 **Karlsruher Institut für Technologie (KIT)**
Karlsruhe (Germany)
Diploma thesis, Institute for Technical Chemistry and Polymer Chemistry under the supervision of Prof. Barner-Kowollik
Elucidating the Self-Folding Behaviour of Single Polymer Chains:
Towards Emulating Natural Biomacromolecules
Diploma in Chemistry - Grade: 1.2

10/2008–08/2012 **Karlsruher Institut für Technologie (KIT)**
Karlsruhe (Germany)
Studies of pure Chemistry

10/2007–09/2008	**Johannes Gutenberg Universität** Mainz (Germany) Studies of biomedical chemistry
1999-2007	**Nordpfalzgymnasium** Kirchheimbolanden (Germany) Higher education entrance qualification, grade: 1.8

Extra Curricular Activities

04/2007–06/2007	Voluntary work at a nature reserve for "Youth Action for Peace" in Ecuador
2005–2007	Badminton instructor, TV Kirchheimbolanden
1996–2006	Altar server, parish St. Peter, Kirchheimbolanden

Skills

EDP	MS Office: Word, PowerPoint, and Excel, Adobe Illustrator, Adobe Photoshop, Origin, TopSpin
Languages	German: Mother Tongue, English: Proficient User, Spanish: Basic User

Personal Interests

Winter sports, football, badminton

Traveling (in particular Asia and South America)

Reading, music

Karlsruhe, January 12, 2016

List of Publications and Conference Contributions

Peer Reviewed Publications

[1] *Pd-Complex Driven Formation of Single-Chain Nanoparticles*
J. Willenbacher, O. Altintas, V. Trouillet, N. Knoefel, M.J. Monteiro, P.W. Roesky, C. Barner-Kowollik, *Polym. Chem.* **2015**, *6*, 4358–4365.

[2] *Photochemical Design of Functional Fluorescent Single-Chain Nanoparticles*
J. Willenbacher, K. Wuest, J.O. Mueller, M. Kaupp, H.-A. Wagenknecht, C. Barner-Kowollik, *ACS Macro Lett.* **2014**, *3*, 574–579.

[3] *Reversible Single-Chain Selective Point Folding via Cyclodextrin Driven Host/Guest Chemistry in Water*
J. Willenbacher, B.V.K.J. Schmidt, D. Schulze-Suenninghausen, O. Altintas, B. Luy, G. Delaittre, C. Barner-Kowollik, *Chem. Commun.* **2014**, *50*, 7056–7059.

[4] *Single-Chain Self-Folding of Synthetic Polymers Induced by Metal-Ligand Complexation*
J. Willenbacher, O. Altintas, P.W. Roesky, C. Barner-Kowollik, *Macromol. Rapid Commun.* **2014**, *35*, 45–51.

[5] *A Mild and Efficient Approach to Functional Single-Chain Polymeric Nanoparticles via Photoinduced Diels-Alder Ligation*
O. Altintas,‖ J. Willenbacher,‖ K. Wuest, K.K. Oehlenschlaeger, P. Krolla-Sidenstein, H. Gliemann, C. Barner-Kowollik, *Macromolecules* **2013**, *46*, 8092–8101.

‖O.A. and J.W. contributed equally.

Conference Contributions

[1] *3-D Architectures from Single Polymer Chains* (Oral Presentation)

J. Willenbacher, C. Barner-Kowollik, **249th ACS National Meeting**, March 22 - 26, **2015**, Denver, CO, **USA**.

[2] *Reversible Single-Chain Selective Point Folding via Cyclodextrin Driven Host/Guest Chemistry in Water* (Poster Presentation)

J. Willenbacher, B.V.K.J. Schmidt, D. Schulze-Suenninghausen, O. Altintas, B. Luy, G. Delaittre, C. Barner-Kowollik, **Europolymer Conference (EUPOC) on Precision Polymers: Synthesis, Folding and Function**, May 25 - 29, **2014**, Gargnano, Lago di Garda, **Italy**.

[3] *Single Polymer Chain Architectures* (Poster Presentation)

J. Willenbacher, O. Altintas, K. Wuest, K.K. Oehlenschlaeger, P. Krolla-Sidenstein, H. Gliemann, P.W. Roesky, C. Barner-Kowollik, **2nd Conference on Precision Polymer Materials**, August 25-28, **2013**, Ghent, **Belgium**.

Acknowledgements

ich danke euch für euer Engagement und eure Hilfe bei den gemeinsamen Veröffentlichungen. Bei Rouven Müller bedanke ich mich für das Aufräumen meiner chaotischen LaTeX-Vorlage und den vielen hilfreichen Vorschlägen bezüglich der Arbeit mit LaTeX. Ein weiteres riesiges Dankeschön geht an Kilian Wüst, Janin Offenloch und Hannah Rothfuß, die ihre Vertiefer-, Bachelor-, Master- oder Diplom-Arbeit unter meiner Betreuung angefertig haben. Es hat Spaß gemacht mit euch zusammenzuarbeiten, alles Gute für eure Zukunft! Außerdem danke ich Maria Schneider, Evelyn Stühring, Anja Goldmann, Peter Gerstel und Vincent Schüler für ihre organisatorischen Meisterleistungen innerhald des Arbeitskreises, ohne die eine so effektive Forschung unmöglich wäre. Weiterhin danke ich den Kollegen Michael Kaupp, Marcel Langer, Jan Müller und Matthias Eing für das Korrekturlesen von Teilen dieser Arbeit.

Since I would for sure forget somebody when listing all the people, I would like to thank each current and former member of the group who have accompanied me on my macroarc journey. My time with you at work, but also after hours, has been a great experience. Especially the Doko and Squash sessions will be kept in extremely good memory!

Die abschließenden Worte gelten meiner Frau Judit, meinen Eltern Jutta und Norbert, meinen Geschwistern Max, Franziska und Pauline, dem Rest meiner Familie, meinen Schwiegereltern Bärbel und Stefan und all meinen neuen und alten Freunden. Ihr wisst, dass ich kein Freund großer oder vieler Worte bin, genauso wisst ihr aber hoffentlich auch wie stolz ich bin Teil eures Lebens zu sein! Ihr habt mich zu dem gemacht was ich heute bin, dafür werde ich für immer dankbar sein!

Declaration

Ich erkläre hiermit, dass ich die vorliegende Arbeit im Rahmen der Betreuung durch Prof. Dr. Christopher Barner-Kowollik selbstständig verfasst und keine anderen als die angegebenen Quellen und Hilfsmittel verwendet habe. Wörtlich oder inhaltlich übernommenen Stellen sind als solche kenntlich gemacht und die Satzung des Karslruher Instituts für Technologie (KIT) zur Sicherung guter wissenschaftlicher Praxis wurde beachtet. Des Weiteren erkläre ich, dass ich mich derzeit in keinem weiteren laufenden Promotionsverfahren befinde und auch keine vorausgegangenen Promotionsversuche unternommen habe.

_____

Karlsruhe, 12. Januar 2016